THESE

Pour l'obtention du Grade de

DOCTEUR DE L'UNIVERSITE DE POITIERS

(Faculté des Sciences Fondamentales et Appliquées)
(Diplôme National - Arrêté du 25 mai 2016)

Ecole Doctorale : Chimie, Ecologie, Géosciences et Agrosciences « *Théodore Monod* »

Secteur de Recherche : Structure et évolution de la Terre et autres planètes

Présentée par:

Ali Asaad

****

Influence of particles organization and dual porosity on the diffusion of water and solutes in clayey porous media

****

Directeurs de Thèse :

Emmanuel Tertre, Fabien Hubert et Eric Ferrage

Soutenue prévue entre le 11 et 18 décembre 2021

devant la Commission d'Examen

****

JURY

Rapportrice	Jocelyne Brendlé	Professeure, IS2M, Université de Haute Alsace
Rapporteur	Christophe Tournassat	Professeur, ISTO, Université d'Orléans
Examinatrice	Delphine Roubinet	Chargé de Recherche CNRS, Géosciences Montpellier
Examinateur	Sébastien Savoye	Ingénieur de recherche expert senior, CEA, Saclay
Membre	Patricia Patrier	Professeure, IC2MP, Université de Poitiers
Membre	Fabien Hubert	Maître de conférences HDR, IC2MP, Université de Poitiers
Membre	Eric Ferrage	Directeur de Recherche CNRS, IC2MP, Université de Poitiers
Membre	Emmanuel Tertre	Professeur, IC2MP, Université de Poitiers

Acknowledgements

I'm grateful to "la Region Nouvelle Aquitaine" which allowed me to do this thesis, as well as to the CNRS interdisciplinary "Defi Needs" through its "MiPor" program (Project DARIUS), the H2020 European program EURAD through its "Future" WP, the French government program "Investissements d'Avenir" (EUR ENTREE, reference ANR-18-EURE-0010), and the European Union (ERDF) for providing financial support for this work.

First and foremost, I'm tremendously thankful to my supervisors; Prof. Emmanuel Tertre, for your guide and support, and for being able to remove the frown from my face whenever the results were a little different from what we expected, for your careful review and remarks during the writing of this manuscript and publications. Dr. Eric Ferrage, for sharing with me your immense knowledge and plentiful experience, thanks for being so patient with my ignorance of simulation, for your invaluable contributions in writing and reviewing our publications, as well as for your compassion and for our frequent personal talks. Dr. Fabien Hubert, thank you for everything, and for your unlimited technical support during the design and implementation of our experiments, none of them would have been possible without your enthusiasm and courage to test new things.

In addition, I would like to thank the following people who have helped me undertake this research: Prof. Christophe Tournassat, Prof. Jocelyne Brendlé, and Dr. Delphine Roubinet for accepting to be jury members and providing insightful feedback in the thesis and presentation. Prof. Patricia Patrier for being on the jury, and for your support and supervision through two internships during my master's degree, working with you was one of the main reasons for me to continue in the academic research field. Dr. Sebastien Savoye, for being a member of the jury, and for the collaboration and advice on the diffusion experiments, and for all our long discussions and exchange, it was great knowing you as a person and as a scientist. Dr. Erwan Paineau for helping me acquire 2D X-ray measurements, thank you for your valuable support and for your interest in this subject. Dr. Baptiste Dazas, for your overall contribution to this work, and for helping me with XRD modeling. Dr.Ahmed Abd Elmola, for your support and for being there whenever I needed your help. Professors Alain Meunier and Daniel Beaufort for all useful discussions and exchanges during coffee time. Thanks to all the Hydrasa team for all the enjoyable moments.

Finally, my biggest thanks to my family. My partner Nour, simply none of this was possible without your infinite unconditional support, patience, and love. My mother Samar and my sister Farah for all the support you have shown me. My son Julien, who was able to put a smile on my face in the most difficult times. My father Faek, whom I wish he is safe, and hope to see him soon.

Abstract

Compacted clay and clay-rich geological formations are often associated with very low hydraulic conductivity and predominant nanopores. These qualities made them ideal for the confinement of chemical and radiological species. In this respect, it is of utmost importance to understand/predict the diffusion phenomena in these systems because it is the primary conveying process of water/solutes to the surrounding environments. In such systems, clay particles control the (i) water and ions adsorption-desorption mechanisms because of their frequently sub-micrometer-sized, large specific surface area, and high reactivity for ion exchange processes, (ii) the spatial anisotropy of solutes diffusion due to their dominant platelet morphology leading to a preferred orientation when compacted. In addition, (iii) clay particles control the permeability of these formations, owing to their different porosity types (interlayer *vs.* interparticle) that can be wholly or partly accessible or inaccessible for ions and water. In this context, the present Ph.D. thesis investigates the influence of (i) the clay particles preferred orientation, (ii) the presence of different types of water and ions accessible porosities (interlayer *vs.* interparticle), and (iii) the presence of negative structural charge in some clay particles, on the diffusion of water/solutes in compacted porous clay media.

The first part of this manuscript includes a baseline study of illite du Puy (IDP) samples' mineralogical and morphological properties from three sources; IDP is a naturally occurring material used after purification and Na-saturation in several experiments reported in literature devoted to the sorption/diffusion of cations/water tracers. However, the reported properties of bulk or purified Na-IDP vary between these previous studies. For this reason, this part highlights the differences between different IDP materials. It also provides reference data through additional detailed analyses of this work's material, also used in the European Joint Programme on Radioactive Waste Management (EURAD) project.

The second part is devoted to the results of through-diffusion (TD) of water tracer (HDO) and ions (Na^+ and Cl^-) in compacted porous media from Na-vermiculite, Na-IDP, and Na-kaolinite particles using different salinity gradient values. These clay minerals were carefully chosen to display either mono porosity (i.e., interparticle; IDP, kaolinite) or dual-porosity (interlayer and interparticle; vermiculite) in water-saturated conditions. A protocol developed in this work allowed us to build samples from these minerals at variable degrees in anisotropy in particles' preferred orientation while having similar interparticle porosity volume, and with or without water and ions accessible interlayer porosity. With this approach, quantitative information was obtained on the influence of (i) particles' preferred orientation, (ii) the presence or not of accessible interlayer porosity (to HDO), on the diffusion of these tracers within the porous media made from these minerals. In this part, all TD data for HDO were compared to Brownian dynamics (BD) simulations performed on virtual porous media to assess the prediction capacity of this tool (BD simulation).

Keywords: clay minerals; porous media; anisotropy; particles orientation; water and solutes diffusion; through diffusion; Diffusion coefficient; 2D X-ray diffraction; vermiculite; illite du Puy; dual porosity.

Résumé

Les roches compactées riches en minéraux argileux sont souvent caractérisées par une conductivité hydraulique très faible et la présence de tout petits pores (nanopores). Ces caractéristiques les rendent idéales pour confiner notamment des déchets chimiques et radiologiques. Dans ces contextes de barrières ouvragées, il est important de comprendre/prédire les processus de diffusion dans ces systèmes car il s'agit du principal mécanisme de transport de l'eau/solutés vers les milieux environnants. Dans ces systèmes, les particules d'argile sont les principaux acteurs contrôlant (i) les mécanismes d'adsorption-désorption de l'eau et des ions en raison de leur taille souvent inférieure au micromètre, de leur grande surface spécifique et de leur réactivité élevée pour les processus d'échange d'ions, (ii) l'anisotropie spatiale de la diffusion des solutés dans les milieux poreux en raison de leur morphologie en plaquettes, qui conduit à une orientation préférentielle lorsqu'elles sont compactées et, (iii) la perméabilité de ces formations, en raison de leurs différents types de porosité (interfoliaire *vs.* interparticulaire) qui peuvent être totalement ou partiellement accessibles ou inaccessibles pour les ions et l'eau. Dans ce contexte, cette thèse étudie l'influence de (i) l'orientation préférentielle des particules d'argile, (ii) la présence de différents types de porosités accessibles à l'eau et aux ions (interfoliaire vs interparticulaire), et (iii) la présence d'une charge structurale négative de certaines particules d'argileuses, sur la diffusion d'eau/solutés dans des milieux argileux poreux compactés.

La première partie de ce manuscrit reporte des résultats sur les propriétés minéralogiques et morphologiques d'échantillons d'illite du Puy (IDP) provenant de trois sources différentes. L'IDP est un matériau naturel utilisé après purification et saturation en Na dans plusieurs expériences présentées dans la littérature consacrées à la sorption/diffusion de cations/traceurs d'eau. Cependant, les propriétés de ce matériau (purifié ou non) reportées dans ces études sont assez variables. Pour cette raison, cette partie met en évidence les différences entre les différents matériaux IDP utilisées. Elle fournit également des données de référence grâce à des analyses détaillées du matériau ; celui-ci étant également utilisé dans le projet EURAD (European Joint Programme on Radioactive Waste Management).

La deuxième partie est consacrée aux résultats de la diffusion d'un traceur de l'eau (HDO) et d'ions (Na^+ et Cl^-) à travers des milieux poreux compactés constitués de particules de Na-vermiculite, de Na-IDP et de Na-kaolinite sous différents gradients de salinité en utilisant un setup de through diffusion (TD). Ces minéraux argileux ont été soigneusement choisis pour fabriquer des milieux poreux caractérisés par une simple porosité (i.e., interparticulaire ; IDP, kaolinite) ou une double-porosité (i.e., interfoliaire et interparticulaire ; vermiculite) et pour des conditions saturées en eau. Un protocole développé dans ce travail nous a permis de fabriquer des milieux poreux caractérisés par des degrés variables d'anisotropie dans l'orientation préférentielle des particules tout en ayant une porosité interparticulaire similaire, et présentant une porosité interfoliaire accessible ou non à l'eau et aux ions. Cette approche a permis d'obtenir des informations quantitatives sur l'influence (i) de l'orientation préférentielle des particules et (ii) de la présence d'une porosité interfoliaire accessible (pour HDO), sur la diffusion de ces traceurs au sein des milieux poreux constitués de ces minéraux. Dans cette partie, toutes les données expérimentales obtenus pour HDO par TD ont été comparées à celles simulées par dynamique brownienne (BD) réalisée avec des milieux poreux virtuels représentatifs des échantillons expérimentaux utilisés afin d'évaluer la capacité de prédiction de cet outil (simulation en BD).

Mots clés : minéraux argileux ; milieu poreux ; anisotropie ; orientation des particules ; diffusion de l'eau et de solutés; through diffusion; coefficient de diffusion; diffraction des RX 2D; vermiculite; illite du Puy; double porosité

Contents

Acknowledgements ..... **i**

Abstract ..... **iii**

Résumé ..... **v**

General introduction **1**

Chapter I **7**

Clay minerals and clay porous clay media **7**

I.1. Clay structure and classification 7

I.1.1. The definition of clay minerals 7

I.1.2. The unit cell of clay minerals 7

I.1.3. The structure of the clay sheet 8

I.1.4. Linkage and deformation of the tetrahedral and octahedral sheets 10

I.1.5. The classification of the clay minerals 11

I.1.6. The chemical formula of the clay minerals used in this work 13

I.1.7. External surface properties and structural charge in clay minerals 14

I.1.8. The Electrical Double Layer (EDL) 16

I.2. Clay porous media 18

I.2.1. Clay particles, aggregates, and porosity types 18

I.2.2. Definition and main properties of a clayey medium 19

I.2.3 Diffusion of water and solutes in a clayey medium 20

Chapter II **23**

Material and Methods **23**

II.1. Materials 25

II.1.1. Santa Olalla vermiculite 25

II.1.2. Illite du Puy 26

II.1.3. KGa-2 kaolinite 27

II.2. Conditioning and preparation of the different size fractions 27

II.3. Building the clay porous media 29

II.3.1 Building clay media with variable anisotropy in particles organization 29

II.3.2. Induration and slicing of the clay porous media 33

II.4. Analyzing the preferred orientation of clay particles 34

II.4.1. The Orientation Distribution Function (ODF) 35

II.4.2. Two-dimensional X-ray Scattering (2D-XRS) measurements 36

II.4.3. Treatment of 2D-XRS patterns 37

II.4.4. Calculating the ⟨P2⟩ order parameter 41

II.5. Experimental techniques used to measure diffusion in the clay porous media 41

II.5.1. Through-Diffusion (TD) experiment 41

II.5.2. ^{1}H NMR pulsed Gradient Spin Echo experiments 45
Chapter III 47
Mineralogical and morphological characterization of different size fractions of Illite du Puy 47
Abstract 49
Introduction 50
III.1. Materials and Methods 52
III.1.1. Illite du Puy materials 52
III.1.2. Bulk mineral quantification using XRD refinement on randomly oriented powders 54
III.1.3. Quantification of clay mineralogy using profile modelling of XRD 00ℓ reflections 54
III.1.4. Microchemical analysis by electron microscopy 55
III.1.5. Low-pressure nitrogen and argon adsorption at 77 K 55
III.2. Results and discussion 58
III.2.1. Mineralogy comparison between V-IDP and E-IDP raw materials 58
III.2.2. Crystal-chemistry and geometrical characterization of sub-fractions from E-IDP sample 63
III.3. Concluding remarks and perspectives 70
III.4. Acknowledgements 71
III.5. References 71
III.6. Supplementary Data (S.D.) 77
Chapter IV 78
Water diffusion in Na-vermiculite, illite and kaolinite 78
IV.1. Water diffusion in Na-saturated illite du Puy (Na-IDP) 81
IV.1.1. Particle organization measurements in IDP 81
IV.1.2. Experimental challenges and modification of the diffusion cell 83
IV.1.3. Results and discussion 84
IV.2. Water diffusion in Na-Santa Olalla (SO) vermiculite 87
IV.2.1. Article; Role of interlayer porosity and particle organization in the diffusion of water in swelling clays 87
IV.2.1. Supplementary data for “Role of interlayer porosity and particle organization in the diffusion of water in swelling clays” 118
IV.3. A comparison of HDO diffusion in Na-IDP, Na-vermiculite, and Na-kaolinite 127
IV.4. Summary of Chapter IV 129
Chapter V: 132
Na^{+} and Cl^{-} diffusion in Na-vermiculite and Na-illite 132
V.I. Generalities 132
V.2 Summary of the TD experiments 133
V.3. Na^{+} and Cl^{-} diffusion in Na-saturated Illite du Puy (Na-IDP) 136

V.4. Na^+ and Cl^- diffusion in Na-Santa Olalla (SO) vermiculite 140
V.5. Summary and conclusions 142
General conclusions and perspectives 145
References 151
Appendices 167

List of figures

Chapter I

Fig. I.1: The unit cell in the clay minerals 8
Fig. I.2: Illustration of the structure of the tetrahedral sheet from the a-b plane 9
Fig. I.3: Illustration of the structure of the octahedral sheet from the a-b plane. 10
Fig. I.4: Illustration of the deformation in the clay structure from hexagonal to ditrigonal symmetry 11
Fig. I.5: Illustration of clay minerals families based on their layer structure 12
Fig. I.6: The inner and outer spheres complexation and hydration shells of the cations 16
Fig. I.7: Formation of the electrostatic diffuse double layer (EDL) on the clay basal surfaces 17
Fig. I.8: Different stacking modes of the clay layers 19

Chapter II

Fig. II.1: Illustration of the method used to prepare clay samples at a low degree of particles preferred orientation (i.e., isotropic) 31
Fig. II.2: Illustration of the protocol used to prepare clay samples at high degree of particles preferred orientation (i.e., anisotropic) 32
Fig. II.3: Images of 0.1-0.2µm Na-vermiculite samples prepared by centrifugation to obtain high anisotropy in the particles preferred orientation. 33
Fig. II.4: Illustration of the method used to endure the clay samples. 35
Fig. II.5: The orientation of an individual clay particle in Spherical coordinates 36
Fig. II.6: How particles organization is measured from thin lamella of the clayey sample. 37
Fig. II.7: Illustration of the longitudinal and transversal lamellas and their corresponding two-dimensional X-Ray Scattering (2D-XRS) diffractograms 39
Fig. II.8: Processing of the two-dimensional X-Ray Scattering (2D-XRS) diffractograms. 39
Fig. II.9: Results from particle orientation measurements for Na-vermiculite samples. 40
Fig. II.10: Illustration of the through-diffusion (TD) setup. 42
Fig. II.11**:** Pulse sequence used to perform Pulsed Gradient Spin Echo (PGSE-NMR) attenuation measurements in Na-kaolinite samples. 46

Chapter III

Fig. III.1: Experimental X-ray diffraction patterns of randomly oriented Na^+-saturated bulk powders of Velay illite du Puy (V-IDP) and EURAD illite du Puy (E-IDP) together with calculated patterns obtained by BGMN Rietveld refinement 58

Fig. III.2: Lithological section of the central zone of the Velay basin (adapted from Gabis, 1963) ... 60

Fig. III.3: Experimental X-ray diffraction patterns of oriented Ca^{2+}-saturated preparations for the different sub-fractions of illite du Puy (IDP). 62

Fig. III.4: Comparison between the experimental and calculated XRD patterns of oriented Ca^{2+}-saturated X-ray diffractions of EURAD illite du Puy (E-IDP) 64

Fig. III.5: Experimental low-pressure Ar derivative adsorption isotherms of EURAD illite du Puy (E-IDP) 69

Chapter IV

Fig. IV.1: Measurement of the degree of anisotropy in particles preferred orientation in Na-illite du Puy (IDP) samples 82

Fig. IV.2: Cross-section of the different through-diffusion (TD) cells used in this work. 84

Fig. IV.3: Experimental instantaneous flux and cumulative quantities of HDO diffusing through IDP samples. 85

Fig. IV.4: Comparison between effective diffusion coefficients (De_z) obtained from Na-illite du Puy (IDP) samples from this work and the published ones as function of the sample's total porosity. 86

Fig. IV.5: Comparison between effective diffusion coefficients (De_z) obtained from Brownian dynamics (BD) simulation performed on virtual porous media (VPMs) and TD experiments 87

Fig. 1: Illustration of the methodology used to prepare Na-vermiculite samples with a high degree of particles' preferred orientation 93

Fig. 2: Experimental measurement of the particle orientation in clayey samples using an X-ray scattering technique with a 2D-detector (2D-XRS). 97

Fig. 3: Virtual porous media with similar interparticle porosity values but different anisotropy degrees in particle orientation. 101

Fig. 4: Results from particle orientation and water tracer (HDO) through–diffusion (TD) measurements for Na-kaolinite and Na-vermiculite samples. 103

Fig. 5: Comparison between experimental and Brownian dynamics (BD) simulated water diffusion coefficients in the direction perpendicular to the preferred orientation of clay particles as a function of order parameter $\langle P_2 \rangle$ values 106

Fig .6: Influence of porosity and its distribution between interlayer and interparticle volumes on the evolution of the diffusion anisotropy ratio $De_{\overline{xy}}/De_z$ as a function of the order parameter $\langle P_2 \rangle$. 109

Fig. S1: Pulse sequence used to perform Pulsed Gradient Spin Echo (PGSE-NMR) attenuation measurements in Na-kaolinite samples 120

Fig. IV.6: Comparison between diffusion coefficients of water tracers (HDO/HTO) from this work and published data obtained from compressed samples of different clay minerals. 128

Chapter IV

Fig. V.1: Comparison between effective diffusion coefficients (De_z) of Na^+ and Cl^- obtained from Na-illite du Puy (IDP) samples from this work and the published $^{36}Cl^-$ as a function of the sample's total porosity. 136

Fig. V.2: Experimental instantaneous flux and cumulative quantities of Na^+ and Cl^- diffusing through IDP samples 138

Fig. V.3: Experimental instantaneous flux and cumulative quantities of Na^+ diffusing through IDP samples. 139

Fig. V.4: Experimental instantaneous flux (blue diamonds) and cumulative quantities (red diamonds) of Na^+ and Cl^- diffusing through Na-vermiculite samples 141

Fig. V.5: A theoretical model to interpret the co-diffusion of Na^+ and Cl^- in negatively charged clayey porous media. 142

Annexes

Fig. A.1: Experimental instantaneous flux and cumulative quantities of HDO, Sr^{2+} and Cl^- diffusing through < 0.1 µm Ca-vermiculite samples 167

Fig. A.2: Combined graph of the experimental instantaneous fluxes of HDO, Sr^{2+}, Ca^{2+} and Cl^- diffusing through < 0.1 µm Ca-vermiculite samples. 168

List of tables

Chapter I

Table I.1: Main families of clay minerals and their basic characteristics. 13

Table I.2: Morphological properties of the clay minerals used for through-diffusion experiments in this work 14

Chapter II

Table II.1: Centrifuging parameters used for size fractioning of illite du Puy (IDP), and the relative mass contribution of each fraction. 28

Chapter III

Table III.1: Centrifuging parameters were used for size fractioning of the Velay and EURAD illite du Puy (V-IDP and E-IDP, respectively) with the relative mass contribution of each fraction. 53

Table III.2: Structural parameters for the modeling of experimental 00ℓ XRD reflections of the Ca^{2+}-saturated fractions of EURAD illite du Puy (E-IDP) in air-dried condition (AD) and after ethylene glycol solvation (EG). 65

Table III.3: Structural formulas and grain densities for different fractions of EURAD illite du Puy (E-IDP). 66

Table III.4: Physio-chemical characterization of Na^{+}-saturated size fractions of EURAD illite du Puy (E-IDP) with a relative mass contribution to < 2 μm, cationic exchange capacity, and surface properties 70

Table III.S1: Main parameters obtained from the application of the DIS method to low-pressure Ar adsorption isotherms for the Na^{+}-saturated EURAD illite du Puy (Na-EIDP) size fractions. 77

Chapter IV

Table IV.1: Summary table of all diffusion experiments carried out in this work 80

Table .1: Experimental results for water tracer (HDO) in Na-kaolinite and Na-vermiculite from through-Diffusion (TD) and ^{1}H NMR pulsed gradient spin echo (PGSE-NMR) experiments 95

Table S.1: Characteristics of the 13 virtual porous media used for the Brownian dynamics simulations 125

originally blank

General introduction

Clay particles are formed from the compiling of individual layers; each one is composed of 1 or 2 tetrahedra sheets (contains mainly Si and Al atoms) and an octahedral one (contains mainly Al, Mg, and Fe atoms). This structure gives them a layered or platelet morphology (Rajec, 1999; Hassan et al., 2005; Reinholdt et al., 2013), from which their name is derived (phyllosilicate, from the Greek word "phyllon": leaf). Isomorphic substitutions in their layers give them a negative charge (Fripiat et al., 1982; Bleam, 1990; Christidis et al., 2006). In addition, most clay minerals are regarded as nanoparticles by considering the definition of nanoparticles in Fischer, (2003) as being combined material with at least one dimension size of 100 nm or less. Still, it is not uncommon to find clay particles up to 100 µm in size (usually a product of diagenetic or alteration process; see Gonzáles García and García Ramos, 1960; Meunier, 2005; Wilson, 2013).

The combination of their structure and chemical composition gives the clay minerals very interesting properties. For example; the adsorption of water and polar molecules (Ferrage et al., 2010, 2011), high cationic exchange capacity (Brigatti et al., 2013; Robin et al., 2015; Dzene et al., 2016), very large specific surface area (Tournassat et al., 2003; Hassan et al., 2005; Reinholdt et al., 2013), and preferential particles orientation (Sato, 2000; Wenk et al., 2010; Dabat et al., 2018, 2020; Ferrage et al., 2018), in addition, their suspensions display some unique rheological properties (Nuntiya and Prasanphan, 2006; Abu-Jdayil, 2011; Bailey et al., 2015).

Clays and clay minerals occur in soil horizons, marine and continental sedimentary formations, volcanic and hydrothermal deposits, and they are one of the main products of rock weathering and alteration (Bergaya and Lagaly, 2013). Although they are not the most abundant minerals in the earth's crust, their natural environments (Ito and Wagai, 2017) and low production cost (Christidis, 2013) make them a fundamental resource for various domains. For instance, clay minerals control several properties of the soils, such as their contents in nutritive cations (as Ca^{2+}, K^{+}), their permeabilities, and contaminant retention capabilities (Wilson, 1999; Hubert et al., 2012; Amundson et al., 2015; Dzene et al., 2016; Mukai et al., 2016; Ito and Wagai, 2017). They are commonly used in water treatment to adsorb organic and inorganic pollutants (Evangelou, 1998; Beall, 2003; Mukhopadhyay et al., 2020). Moreover, clay materials are widely used in building materials (bricks, tiles, thermal isolation, and ceramics),

drilling fluids, electronics, paper manufacturing, medical and cosmetic applications (Harvey and Murray, 1997; Murray, 2002; Kasthurba et al., 2007; Carretero and Pozo, 2009; Kouakou and Morel, 2009; Christidis, 2013; Bailey et al., 2015; Mahato et al., 2015; Pan et al., 2018).

Compacted clay minerals and clay-rich rocks, and owing to their particles size and morphology, are dominated with nano to meso-metric pore size (i.e., 0-50 nm). Such pore size distribution, coupled with the clay particles' swelling behavior and negative charge, gives them a very low permeability (Delay et al., 2006, 2014), high cations retention capacity, and slow diffusive transport of water and solutes. These features explain the great interest in these materials for; (i) the exploitation and conservation of natural resources (water, gas, oil, ores; Day and Gilpin, 1909; Jiang, 2012; Zhai et al., 2014; Johnston, 2018; Dill, 2020; Zhou et al., 2020; Muhammed et al., 2021), and as (ii) natural and engineered barriers used in subsurface geological repositories for the confinement of nuclear wastes and the capture of CO_2 (i.e., Opalinus, Callovo-Oxfordian, Boom clay, Argillite; Pusch, 1979; Andra, 2005; Ketzer et al., 2005; Gherardi et al., 2007; Bachu, 2008; Altmann et al., 2012, 2015; Charlet et al., 2017; Porion et al., 2018. In addition, (iii) swelling clays and swelling clay-rich materials are used to construct geosynthetic Clay Liners (GCL) and compacted Clay Liners (CCL) in landfills barriers applications (Komine and Ogata, 2004; Razakamanantsoa et al., 2012).

Given that the paramount quality of these barriers is to restrain the advective transport of the contaminant's species to the surrounding environments, the primary mass transfer of these species occurs through molecular diffusion over long time scales (Pusch, 1979; Bourg et al., 2003; Bourg and Tournassat, 2015) among others). For this reason, an extensive experimental and simulation studies were carried out to obtain diffusion coefficients of water and different ionic tracers in such environments, as in (Bourg et al., 2003; Van Loon et al., 2003; Andra, 2005; García-Gutiérrez et al., 2006; Landais, 2006; Appelo and Wersin, 2007; Bachu, 2008; González Sánchez et al., 2008b; Bruggeman et al., 2009; Glaus et al., 2010; Altmann et al., 2012; Bourg and Tournassat, 2015; Savoye et al., 2015; Bacle et al., 2016; Charlet et al., 2017; Tertre et al., 2018). Furthermore, different studies focused on the parameters that can significantly control the flux of the chemical species diffusing through compacted clayey media. These studies were driven by the need to understand and to predict such a complex process as molecular diffusion. Indeed, in addition to pressure and temperature, inert tracers (as water) are highly dependent on the geometric properties of the media, such as the total porosity, the organization and connectivity of the pore network, and the different types of porosities in swelling clay minerals (Bourg et al., 2006, 2007, 2008). While for reactive species (i.e., ions),

molecular diffusion is in addition very sensitive to the salinity of the pore water (i.e., ionic strength; Glaus et al., 2007; Savoye et al., 2015), and the negative charge of clay particles (Ochs et al., 1998, 2001; Tournassat and Steefel, 2019).

In this context, the influence of the preferred orientation of the clay particles on the diffusion properties was a subject of growing attention in the last 30 years. This preferential orientation occurs in the compacted clayey rocks formed through layer deposition (sedimentation beds) within aqueous environments. In such environments, platelet-shaped clay particles tend to settle on their basal surface in a direction parallel to sedimentation beds (Bennett et al., 1981). This property is known to increase with increasing compaction degree (i.e., decreasing the porosity) of these rocks (Velde, 1996; Bolton et al., 2000). Because preferred orientation creates an anisotropy in the shape and spatial distribution of the pore space, the pathway length of the diffusive species will vary depending on the direction of diffusion (i.e., parallel or perpendicular to the sedimentation beds).

In 1992, Sato et al. (1992) reported considerable decrease in the effective diffusion coefficient (*D*e) of different radionuclides with increasing the dry density of bentonite samples (i.e., by increasing compaction). In the following years, further investigations of the spatial anisotropy of the diffusion of different tracers were carried out in such media, either by *through-diffusion* (TD) experiments or by analyzing the 3D distribution of the tracer. As a result, many authors (Farver and Yund, 1999; Sato, 2000; Sato and Suzuki, 2003; Suzuki et al., 2004; Van Loon et al., 2004; García-Gutiérrez et al., 2006; Wenk et al., 2008; Wittebroodt et al., 2012; Xiang et al., 2013; Dagnelie et al., 2017; Jacops et al., 2017) reported a significant decrease in the effective diffusion coefficients (*D*e) of these tracers in the direction perpendicular to the sedimentation beds in comparison to the parallel direction. This observation was attributed to the extended pathway travelled by the tracer in a perpendicular direction to the particle's preferred orientation than the parallel one. The anisotropy in particles orientation was evidenced by either X-ray scattering (XRS; Wenk et al., 2008) or microscopy-imaging techniques; Sato, 2000; Suzuki et al., 2004. In addition, some models were proposed using molecular dynamics, random walk, or BD simulations to allow for the consideration of the specific role of the particles preferred orientation on the diffusion properties as in; Churakov and Gimmi, 2011; Tyagi et al., 2013; Bacle et al., 2016; Gimmi and Churakov, 2019; Underwood and Bourg, 2020.

Nevertheless, experimentally, none of these studies provided quantification of the degree of the anisotropy in the particles' preferred orientation, nor proposed an experimental method

to control the geometric organization of these media apart from increasing compaction degree. Although the latter increases the particles' preferred orientation, as discussed above, it decreases the total porosity. Therefore, it was impossible to discriminate the individual influence of each of these two parameters on the diffusion results. Anyway, in 2020, Dabat et al. succeeded to link (experimentally and by simulation) the anisotropy in particles' preferred orientation to the spatial anisotropy of water diffusion (i.e., De_z *vs.* $De_{x\text{-}y}$ in respect to sedimentation/compression plane) for Na-kaolinite samples (a non-charged/none swelling clay mineral). Their findings were possible because of the methodology they developed to prepare two samples of Na-kaolinite particles at the same total porosity but are different in their degree of anisotropy in particles' preferred orientation. Water diffusivity in these two samples were measured by *Pulsed Gradient Spin Echo attenuation by Nuclear Magnetic Resonance* (PGSE-NMR) technique.

Following the work of Dabat et al., (2020) on kaolinite, the first objective of this thesis was to expand their findings by investigating the influence of particle organization on the diffusion of water (HDO) and ions (Na^+ and Cl^-) in charged swelling/none-swelling clay minerals. This objective was based on the facts that (i) the geometry of porous media made from swelling clay minerals is affected by their expansion behaviors, and (ii) the structural charge in clay particles highly affect the dynamics of water and solutes in the vicinity of these particles. Hence, the first challenge in this study was to develop the protocol in Dabat et al., (2020) for kaolinite to: (i) prepare porous media at controlled porosity and variable degrees of anisotropy in particles preferred orientation from swelling/non-swelling clay minerals. (ii) allow for the prepared porous media to be directly mounted to the TD setup. Next, and with the developed protocol, it was possible to carry on with our first objective for two negatively charged clay minerals:

- A none-swelling Illite du Puy (IDP).
- A swelling Santa Olalla vermiculite (SO-vermiculite)

In water saturated conditions, a porous media made with vermiculite particles exhibits two types of porosities (i.e., interparticle vs. interlayer), while with illite particles it has only interparticle one. In addition, both minerals exhibit a substantial negative charge in their layers which allows them to adsorb cations and slow water mobility in the vicinity of their external surfaces. This charge also renders the whole interlayer porosity in vermiculite and a part of their interparticle inaccessible for anions.

Water mobility can be drastically reduced in the interlayer porosity and the vicinity of the charged external surfaces of clay particles, as revealed by molecular dynamic simulations (Titiloye and Skipper, 2001; Marry et al., 2002; Malikova et al., 2006; Michot et al., 2012) among others), and quasi-elastic neutron scattering studies (González Sánchez et al., 2008a; Bestel, 2014) performed on low charge swelling clays, e.g., montmorillonite. In addition, this charge makes the interlayer porosity non-accessible for anions (i.e., when the interlayer has 1W or 2W layers of water molecules), a well-known phenomenon is called *anionic exclusion* (e.g., Bourg et al., 2006; Glaus et al., 2007, 2010). Recently and during their work on water diffusion in Na-vermiculite samples, Tertre et al., (2018) reported experimental *D*e values close to those reported in the literature and obtained from Na-saturated kaolinite and illite samples. Interestingly, the total porosity of the kaolinite and illite (having only an interparticle porosity) was equal only to the interparticle porosity of Na-vermiculite. Such results suggested that the extra volume of interlayer porosity in vermiculite (which is accessible to water and cations) has a limited contribution to the total flux of water tracer diffusing through these samples. Their findings agreed with what was previously reported by Churakov and Gimmi, (2011) using random-walk simulation. However, there was no quantification of the degree of particles' preferred orientation in these studies, meaning that – and as discussed earlier- it is impossible to decouple the influence of porosity and particle organization on the diffusion results.

In this context, the second objective of this work is to quantitatively discuss the role of interlayer and interparticle porosities on the diffusion of chemical species in compacted samples made of swelling clay particles. To do so, the methodology relied on comparing diffusion results of water and ions (i.e., Na^+ and Cl^-) from samples that exhibit an interlayer porosity (i.e., Na-vermiculite) to the ones from samples with no interlayer porosity (i.e., Na-Illite and Na-Kaolinite) and for which their total porosity is equal or close to the interparticle porosity of one of vermiculite. Importantly, for better discrimination of the role played by the porosity type, the degree of particles' preferred orientation was quantified for all samples.

Finally, all experimental diffusion results on water tracer in this work were compared to those obtained by *Brownian Dynamics* (BD) simulations carried out by Eric Ferrage. The simulated results were obtained from 3D virtual porous media, generated to mimic the real ones in terms of mineralogy and porosity distribution, while also covering a large range of anisotropy degrees in particle orientations (details on simulation can be found in; Ferrage et al., 2015; Dabat et al., 2020).

This manuscript is divided into five chapters; the first two chapters are dedicated to this work's theoretical and methodological parts. The last three chapters corresponding to the objectives mentioned above in the form of published or draft publications:

- Chapter I includes theoretical concepts and definitions used further in this work: (i) clays and clay minerals' definition, structure, classification, and main physio-chemical properties. (ii) the main properties of a porous media constituted of clay particles. And (iii) the theory of water and ions diffusion in such media.
- Chapter II includes the methodology and main techniques used in this work: clay minerals used for experiments, building clay samples at different degrees in anisotropy of particles' preferred orientation, measurement of particles' organization, and techniques used to measure diffusion in these samples.
- Chapter III describes the detailed mineralogical and morphological study of different IDP size fractions. Such work was necessary to establish a baseline source for these materials used in this work and the *European Joint Programme on Radioactive Waste Management* (EURAD, 2019-2024). This project involves a large set of adsorption and diffusion studies of a large set of tracers. And since such work does not exist in the literature -to the extent of our knowledge- the included results can be used as key parameters in the diffusion and adsorption experiments in this work and the EURAD project.
- Chapter IV describes water tracer diffusion (i.e., HDO) results in SO-vermiculite and IDP samples at different degrees of anisotropy in particles' preferred orientation and for the same interparticle porosities.
- Chapter V describes the results on ions diffusion (i.e., Na^+ and Cl^-) in the same samples from Chapter IV under different salinity gradients.

Chapter I

Clay minerals and clay porous clay media

The essence of this work is the molecular diffusion of water and solutes in compressed samples built from clay minerals (i.e., clay porous media/clay samples). Therefore, the first section of this chapter summarizes the fundamental elements of clay minerals, including their definition, classification, basic blocks, general chemistry, and structural formula. The second section describes the main properties of the compressed samples and how molecular diffusion is mathematically expressed in such media.

I.1. Clay structure and classification

I.1.1. The definition of clay minerals

In this work, the term "clay" or "clay mineral" is used to describe minerals from the layered silicates group (phyllosilicate), which their layers are composed of tetrahedral and octahedral sheets (The clay minerals society glossary 2020). This term includes phyllosilicate of any size, such as macroscopic mica, vermiculite, and chlorite. Clay minerals are generally fine-grained with a high specific surface area, and some of their unique properties result from their small particle sizes. However, the term used here should not be confused with the term used in the granulometric sense, such as colloid science, pedology, and geology. In those domains, clays are generally considered as being the < 2 µm size fraction of the rocks (Bergaya and Lagaly, 2013). Hence, the clay fraction contains phyllosilicates but may also include other minerals, such as quartz, carbonates, or feldspars. More details on these definitions can be found on the clay minerals society website: https://www.clays.org/clay_glossary/ or/and in Bergaya and Lagaly, (2013).

I.1.2. The unit cell of clay minerals

As with every crystallized mineral, clay structures are described through their unit cell, the smallest part of the mineral's crystal with all its symmetry elements. Thus, the crystals can be reproduced by repeating the unit cell in the entire 3D space. Depending on the mineral type, the unit cell is formed from a single or several layers. Details on the crystallography and symmetry in clay minerals can be found elsewhere; Moore and Reynolds, (1997); Velde and Meunier, (2008); Waseda et al., (2011). Here, we focus on the general definitions in relation to this work.

The unit cell for clay minerals is defined by its three-axis (*a*, *b*, and *c*) and the angles between them (*α*, *β*, and *γ*) (Fig. I.1). The length of this three-axis can be calculated using atom to atom bonds length and basic geometry rules. However, since clay minerals have uniaxial symmetry (i.e., clay particles for which their c axis is the only symmetry axis (Wenk et al., 2010, and references therein), we are interested in the c-axis value. In this work, the c-axis value is denoted as the *basal spacing* (d_{001} or c*) in Å, this value corresponds to the layer-to-layer distance in one clay particle or the distance between 001 planes in the reciprocal space. The basal spacing is derived from the c-axis value in the real space by the relation c=c*/sin *β*.

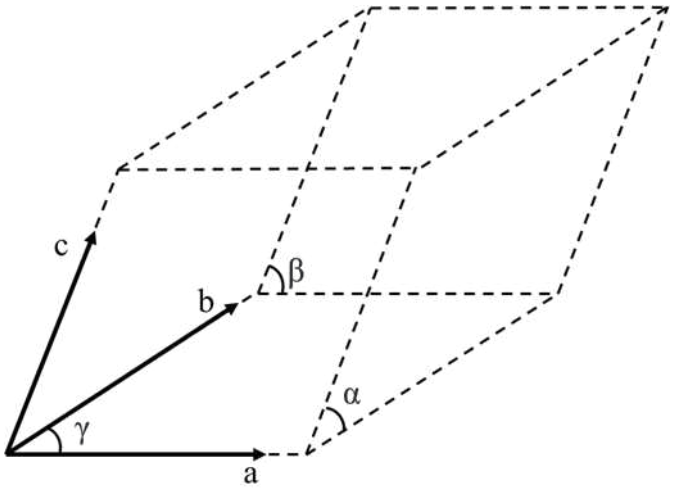


Fig. I.1. *The unit cell with it's a, b, and c dimensions and the angles α, β, and γ between them.*

I.1.3. The structure of the clay sheet

Clay particles are formed by stacking consecutive parallel layers. Each layer is composed of two sheets at a minimum: a tetrahedral and octahedral.

The tetrahedral sheet is created when a Si^{4+} or Al^{3+} atom is coordinated with 4 O^{2-} atoms in 4-fold coordination [(SiO_4^{4-}), (AlO_4^{5-})] forming a regular tetrahedron geometry with the Si (or Al) atom in the center as illustrated in Fig. I.2a. The Si-O bond length is estimated at 1.618 Å in Bergaya and Lagaly, (2013). Thus, all other dimensions can be calculated using basic geometry rules (Fig. I.2a). Noting that in Al^{3+} tetrahedron, the Al-O bond is greater than the Si-O bond: 1.77Å. Hence, all other dimensions will be more significant. The tetrahedron ring is formed when six tetrahedrons are linked together by sharing their three basal oxygens (Fig. I.2b). These rings are linked together to form the "tetrahedral sheet", with all their free apical

oxygens pointing in the same direction. The space between them defines the "hexagonal/siloxane cavity" (Fig. I.2c).

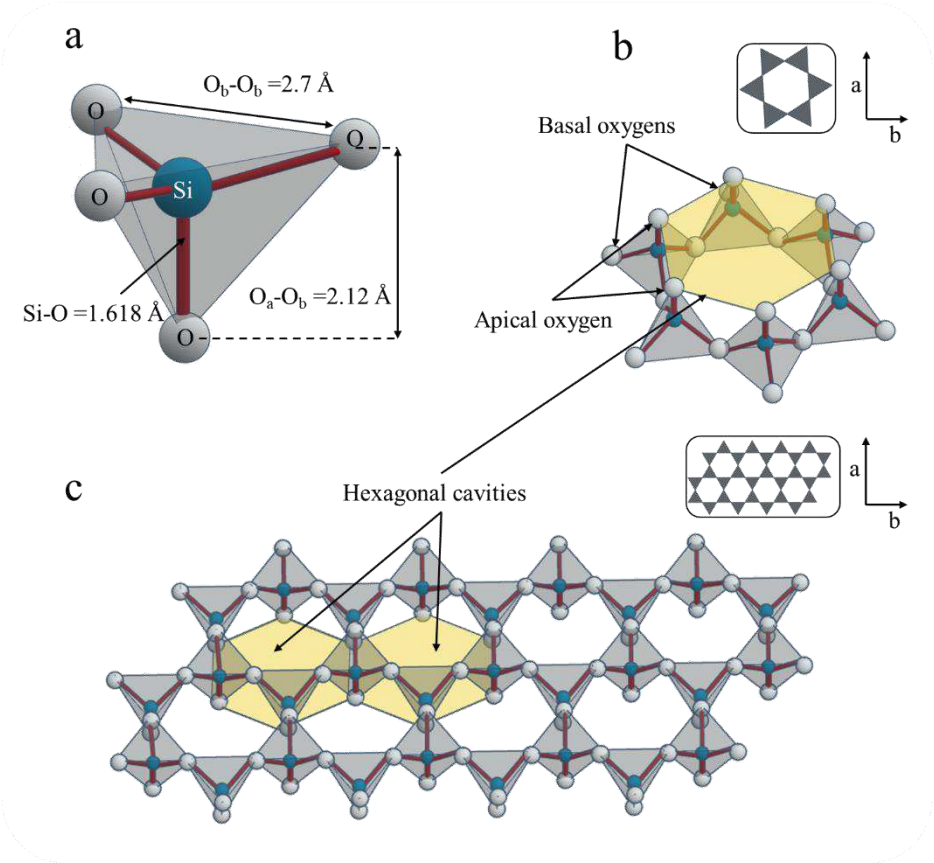


Fig. I.2. *Illustration of the structure of the tetrahedral sheet from the a-b plane. (a) single tetrahedron dimensions and atoms occupancies. (b) The tetrahedral ring formed from 6 tetrahedrons (c) the tetrahedral sheet and the hexagonal cavities. Si is silicon atom, O is oxygen atom, O_b is basal oxygen, and O_a is an apical oxygen.*

The octahedral sheet is formed when a divalent or trivalent cation (Al^{3+}, Fe^{3+}, Mg^{2+}, etc.) is coordinated with 6 O^{2-} or OH^- in 6-fold coordination (Fig. I.3a). From the ionic radii of the cation and the 6-folds coordination of O^{2-} (Meunier, 2005, and references therein), the edge length is 3.00 and 2.74 Å, and the thickness is 2.45 and 2.724 Å for the Mg and Al octahedrons, respectively (Fig. I.3a). The octahedral sheet is formed when the octahedrons rest on their triangular face and share their six vertices (Fig. I.3b). For trivalent cations such as Al^{3+}, the octahedrons will be arranged in a "gibbsite sheet" structure [$Al_2(OH)_6$], and only 2/3 of the central spaces are occupied by cation, leaving one vacant position to balance the total charge. Such arrangement is called a di-octahedral sheet (Fig. I.3b, left). For divalent cations (e.g., Mg^{2+}), the octahedrons are arranged in a "brucite sheet" [$Mg_3(OH)_6$] with no vacancies in the structure, leading to the formation of a tri-octahedral sheet (Fig. I.3b, right). Finally, the

unsatisfied coordination's of the oxygens on the edges of the octahedrons fix H^+ to form hydroxyl groups (OH groups).

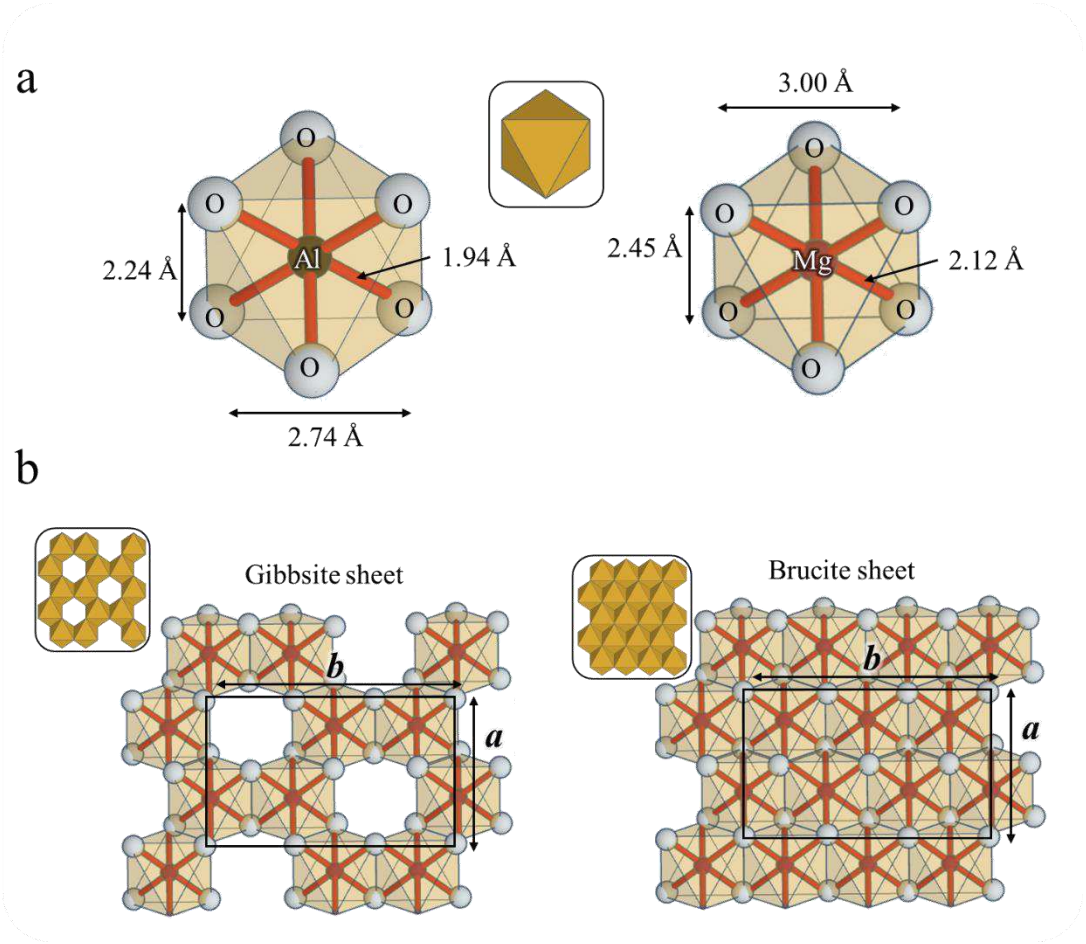


Fig. I.3. *Illustration of the structure of the octahedral sheet from the a-b plane. (a) single Al^{3+} octahedron dimension (left), single Mg^{2+} octahedron dimension (right). (b) View of di-octahedral sheet (left), View of tri-octahedral sheet (right). Al is aluminum atom, Mg is magnesium, and O is oxygen.*

I.1.4. Linkage and deformation of the tetrahedral and octahedral sheets

The tetrahedral sheet is linked to the octahedral through its apical oxygens. Yet, in one unit cell of clay mineral, the dimensions of the tetrahedra and octahedral sheets don't match. For instance, the calculated ***b*** value for the tetrahedral sheet is 9.27Å, and 8.99 and 8.19Å for the tri- and di-octahedral sheets, respectively. The same case for ***a*** parameter, which is calculated from the ***b*** value. To achieve the linkage between the two sheets, a deformation in their structure must occur. Hence, each tetrahedron in the tetrahedral ring will rotate by an angle "*a°*", as illustrated in Fig. I.4a.

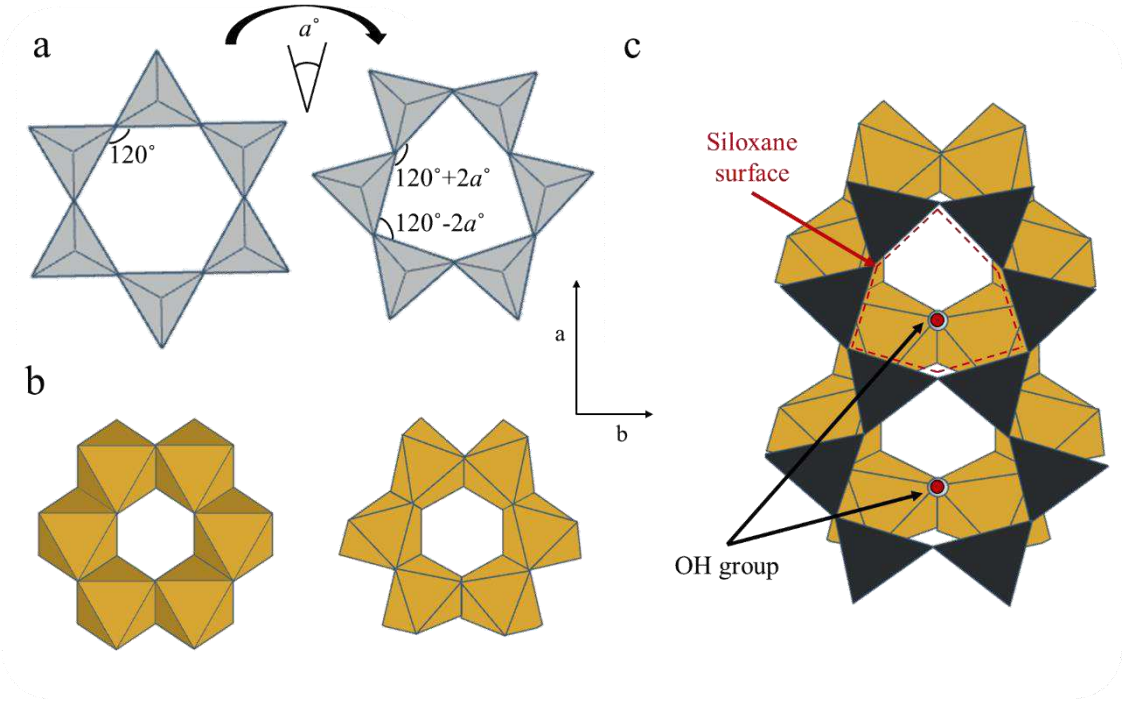


Fig. I.4. *Illustration of the deformation in the clay structure from hexagonal symmetry to ditrigonal symmetry. (a) Hexagonal tetrahedral sheet (left) compared to ditrigonal one (right). (b) Hexagonal di-octahedral sheet (left) compared to ditrigonal one (right). (c) The linkage between the deformed tetrahedral and octahedral sheets and the formation of the siloxane surfaces.*

Consequently, the tetrahedral sheet loses its hexagonal symmetry to a ditrigonal one. Because of the repulsion forces between basal oxygens of each adjacent tetrahedrons, a° will not exceed 30°. In addition, the occupied octahedrons become asymmetric in the di-octahedral sheet (Fig. I.4b). However, this is not the case for tri-octahedral sheets, which "theoretically" don't undergo any deformation. Furthermore, additional rotation and deformation may occur to achieve the linkage between the deformed sheets (Fig. I.4c).

I.1.5. The classification of the clay minerals

Based on their layer composition, the clay minerals are classified into three families (Table I.1):

I. The 1:1 family layer comprises one octahedral sheet and one tetrahedral sheet denoted as 1:1 or TO layer Fig. I.5a. Clay minerals from this family include kaolin and serpentine groups.

II. The 2:1 family layer comprises one octahedral sheet sandwiched between two tetrahedral sheets Fig. I.5b. Such arrangement is denoted as 2:1 or TOT layer. If no isomorphic substitutions in the TOT layer (e.g., Talc and Pyrophyllite),

Hydrogen bonds link every two consecutive layers together, and the space between the layers is the interlayer space/porosity. Suppose some isomorphic substitutions exist in the tetrahedral and/or octahedral sheets. In that case, a permanent charge is created in the layer, and cations are adsorbed in the interlayer space to neutralize the charge (more information is given below). In this family's swelling (expandable) clays, such as smectites and vermiculites, the interlayer space can be accessible for water, and cations are generally exchangeable. In the non-swelling clays such as illite and micas, the interlayer space is none-accessible for water, and the cations are theoretically none-exchangeable.

III. The 2:1:1 family: the clay layer has the same structure as the 2:1 family, but the interlayer cations are bonded with oxygen or hydroxyl to form a brucite or gibbsite-like octahedral sheet (Fig. I.5c).

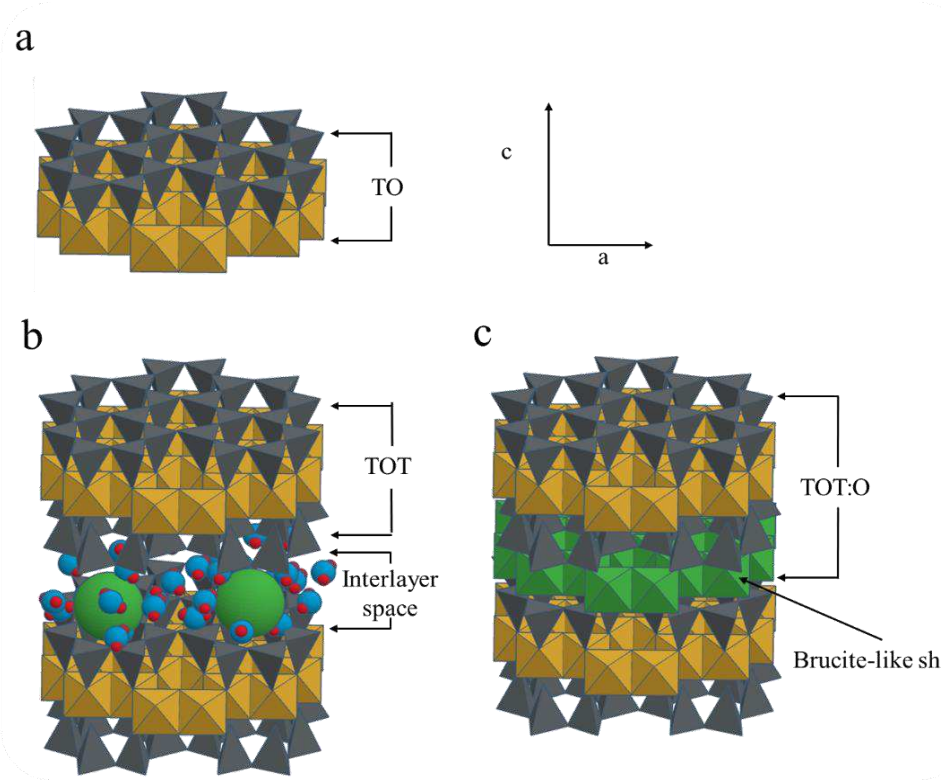


***Fig. I.5**. Illustration of clay minerals families based on their layer structure. (a) 1:1 or TO family: one layer is composed of one tetrahedral and one octahedral sheet. (b) 2:1 or TOT family: one layer is composed of two tetrahedral and one octahedral sheet. And for minerals with structural charge, the interlayer sheet is occupied by adsorbed cations (green balls) in the hexagonal cavities of the tetrahedral sheet, blue and red balls represent water molecules that may accompany the cations. (c) 2:1:1 or TOT-O family where one layer is composed of two tetrahedral and one octahedral sheet and the interlayer sheet is occupied by brucite or gibbsite-like sheet.*

This work uses three clay minerals: vermiculite and illite from the 2:1 family and kaolinite from the 1:1 (Table I.2). Hence, the following sections will focus only on the properties of these two families.

Table I.1. *Main families of clay minerals and their basic characteristics.*

Family	Mineral group	Example	Octahedral structure	Layer charge	Interlayer content	Basal spacing d_{001}
1:1	Kaolin	Kaolinite	Di	0	None	≈7.1 Å
		Halloysite	Di	0	Water	≈7.4 Å
	Serpentine	Berthierine	Tri	0	None	≈7.3 Å
2:1	Pyrophyllite /Talc	Pyrophyllite	Di	0	None	≈9.2 Å
		Talc	Tri	0	None	≈9.4 Å
	Mica	Illite	Di	1	K^+	≈10.0 Å
		Biotite	Tri	1	K^+	≈10.0 Å
	Smectite	Montmorillonite	Di	0.2-0.6	Exchangeable cations	Variable based on the hydration state
		Saponite	Tri	0.2-0.6	Exchangeable cations	
	Vermiculite	Vermiculite	Tri	>0.6-<1.0	Exchangeable cations	≈ 10 à 15 Å
		Vermiculite	Di	>0.6-<1.0	Exchangeable cations	≈ 10 à 15 Å
2:1:1	Chlorite	Clinochlore		Variable	$Mg(OH)_2$	≈14.2 Å
		Donbassite		Variable	$Al(OH)_3$	≈14.2 Å

I.1.6. The chemical formula of the clay minerals used in this work

The structural formulas give the chemical composition of a one-unit cell of the clay mineral. It shows the atoms occupancy of the octahedral, the tetrahedral, the quantity of O and OH groups, in addition to the content of interlayer cations if applicable. It includes the number of H_2O molecules adsorbed on the unit cell, measured from the weight loss at 900˚C for previously dehydrated samples at 110˚C. The structural formula for the 1:1 and 2:1 families can be written as follow:

a- For the 1:1 family: $(Si, Al)_4\ (Al, Mg, Fe, Ti)_4\ O_{10}\ (OH)_8.X\ H_2O$

b- For the 2:1 family: $(Si, Al)_8\ (Al, Mg, Fe, Ti)_4\ O_{20}\ (OH)_4.X\ H_2O$

In literature, and for simplicity purposes, the structural formula is commonly reported for half unit-cell. Hence, in this work, we report the structural formula for a half unit-cell that can be written:

a- For the 1:1 family: $(Si, Al)_2\ (Al, Mg, Fe, Ti)_2\ O_5\ (OH)_8.X\ H_2O$

b- For the 2:1 family: $(Si, Al)_4\ (Al, Mg, Fe, Ti)_2\ O_{10}\ (OH)_4.X\ H_2O$

Table I.2 *Morphological properties of the clay minerals used for through-diffusion experiments in this work*

	Size fraction	External surface area [a]	Aspect ratio [b]	Grain density	CEC	Layer charge
	µm	$m^2\ g^{-1}$		$g\ cm^{-3}$	(meq/100 g) at pH = 7	eq/h.u.c.[h]
SO-Vermiculite [c]	0.1-0.2	107.7[d]	0.08	2.72	220[e]	-0.84
Illite du Puy (IDP)	0.1-0.2	114.1	0.08	2.83	22.8[f]	-0.8
KGa-2 kaolinite [g]	~0.5 [c]	20.6	0.07[d]	2.62	3.3[g]	~0

[a] N_2 BET or low-pressure Ar adsorption
[b] The ratio between particle height to its basal diameter
[c] Reinholdt et al 2013
[d] Hassan et al. 2005
[e] replacing Mg^{2+} by Ca^{2+}
[f] replacing K^+ by Sr^{2+}
[g] Clay mineral society
[h] half unit cell

I.1.7. External surface properties and structural charge in clay minerals

The interaction between the clay particles and the ambient aqueous solution takes place throughout the external layer surfaces. Based on the layer type, we can distinguish between different reactive surfaces:

I. The external surfaces, including the basal and the lateral (edges) surfaces of the layer.

II. The internal surfaces, corresponding to the interlayer surface, are "reactive" only if the interlayer is accessible to water (i.e., swelling clay minerals such as smectite and vermiculite).

The external surfaces of the 2:1 clay layer (e.g., vermiculite and illite) include basal surfaces (Fig.I.5b), i.e., surfaces forming by the external siloxane cavities (Fig.I.4c). In an ideal clay layer with no permanent charge in its structure, the siloxane cavity becomes a weak electron donner (Lewis's base), and the surface is slightly hydrophobic. The charge in the 2:1 clay minerals arises from the isomorphous substitution in their layers. If a lower valence atom replaced one of higher valence, this would result in a positive charge deficiency (i.e., excess in the negative charge). For example, in the octahedral sheet, Al^{3+} atoms can be substituted by Mg^{2+} or vice-versa, creating a surplus in either positive or negative charge. In the tetrahedral sheet, the Si^{4+} atom can be replaced by Al^{3+}. Note that such substitution, according to Lowenstein's rule, cannot occur in two neighboring tetrahedrons. These types of substitutions create a "permanent charge" in the tetrahedral and octahedral sheets.

In some cases, the negative charge from the tetrahedral sheet can balance the octahedral sheet's positive one, resulting in a neutral layer. Otherwise, particularly in the 2:1 family, the clay layers will be negatively charged. Hence, the adsorbed cations will be in the hexagonal cavities on the interlayer surfaces to compensate for the charge. Charge compensating cations can either be dehydrated and non-exchangeable, such as K^+ in the interlayer of illite. Or they can be exchangeable such as Ca^{2+}, Na^+, and $Mg^{2+,}$ with full or partial hydration shells (hydrated complexes; Bergaya and Lagaly, 2013). Based on their size and hydration energy, cations can be adsorbed as two types of complexes (Fig. I.6): (1) outer-sphere complexes occur when water molecules surround the adsorbed cation, and the interaction with the clay surface occurs through its water ligands. And (2) inner-sphere complexes where the cation is directly adsorbed to the clay surface and connected to water molecules from the opposite side; the cations' adsorption occurs as inner-sphere complexes through ionic and partially covalent bonds. Hence, it is more stable than the outer-sphere one. Isomorphous substitution changes the hydrophobic nature of the hexagonal cavities to hydrophilic. Generally, substitution occurs randomly in the 2:1 clay layer resulting in a heterogeneous basal surface comprised of hydrophilic areas diffused between hydrophobic ones. Moreover, the generated charge in the tetrahedral sheet is closer to the hexagonal cavities, resulting in a stronger attraction of cations.

The 1:1 family (e.g., kaolinite) possesses a siloxane surface on the tetrahedral side and a hydroxyl surface on the octahedral one. The hydroxyl surface interacts with greater force than

the siloxane with the water molecules. The stronger interaction is mainly due to the shorter distance between the octahedral oxygen and the water molecules (which are hydrogen-bonded on the hydroxyl surface; Bergaya and Lagaly, 2013).

In addition to its permanent charge, the clay layer may exhibit a variable one on its edges. The variable charge can be either positive or negative and results from the interrupted bonds on the edges of the layer, such as Si–O M^{2+}/M^{3+}–OH bonds (M is an octahedral cation). These sites can fix either H^+ or OH^-, and their charge is pH-dependent in contrast to the permanent negative one in the layer structure.

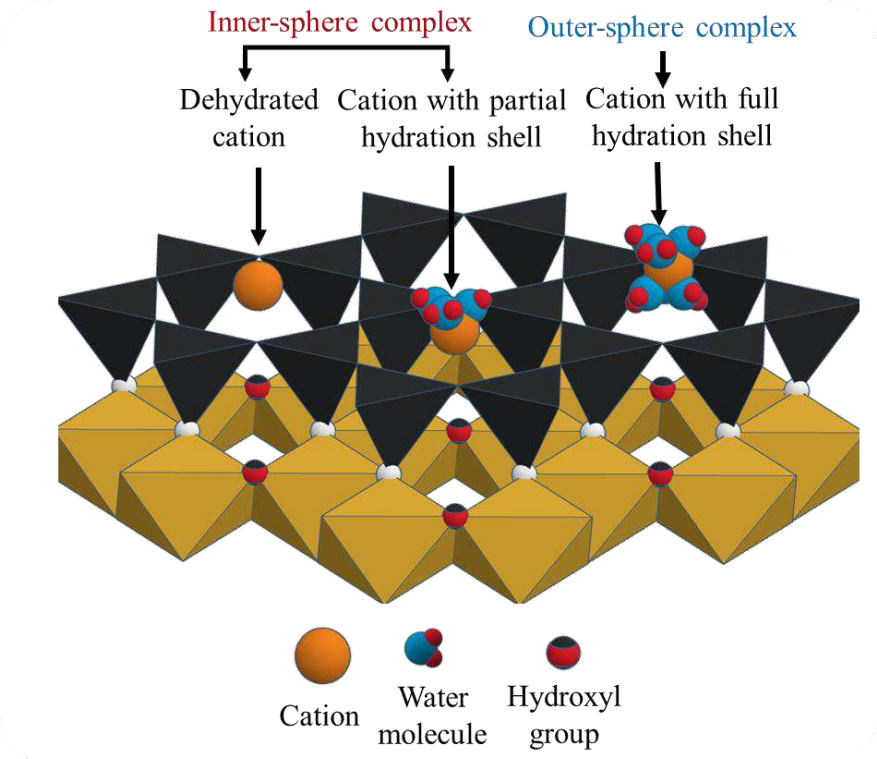


Fig. I.6. *The inner and outer spheres complexation and hydration shells of the cations on the external surfaces of clay layer.*

I.1.8. The Electrical Double Layer (EDL)

The ionic substitutions in the clay layers create a negative electrostatic potential field that decreases with the distance to the charged surface (Fig. I.7a). Thus, a layer of unevenly distributed ions with an overall positive charge, known as the electrical diffused double layer (EDL), is formed around its basal surfaces. The most used concept to describe the EDL is the Gouy-Chapman model modified by Stern in 1924; Stern, (1924). The Stern model divides the structure of the EDL into two elements; (1) the stern layer formed from the adsorbed cations on the siloxane surface either in outer or inner complexes (Fig. I.7b). and (2) the diffusive layer

(Fig. I.7b) formed from a semi-infinite layer of unequally distributed ions. Cations in the diffusive layer are not bonded to the clay surface, and their concentration increases with proximity to the charged clay surface while the concentration of anions decreases. This ions distribution leads to a gradual increase in the positive charge of the solution in the same direction to screen the countercharge of the basal surfaces. In this model, the solution becomes neutral at an infinite distance of the charged surfaces. The presence of the EDL renders a part of the porosity inaccessible for the anions, a phenomenon known as the *anionic exclusion* in the diffusion experiments (e.g., Jardat et al., 2009; Tournassat and Appelo, 2011; Tournassat and Steefel, 2015).

The thickness of the EDL depends mainly on the solution ionic strength, and to a lesser extent, on the charge of the clay mineral. It can be calculated as multiple of Debye lengths (κ^{-1}) from the Boltzmann distribution equation as:

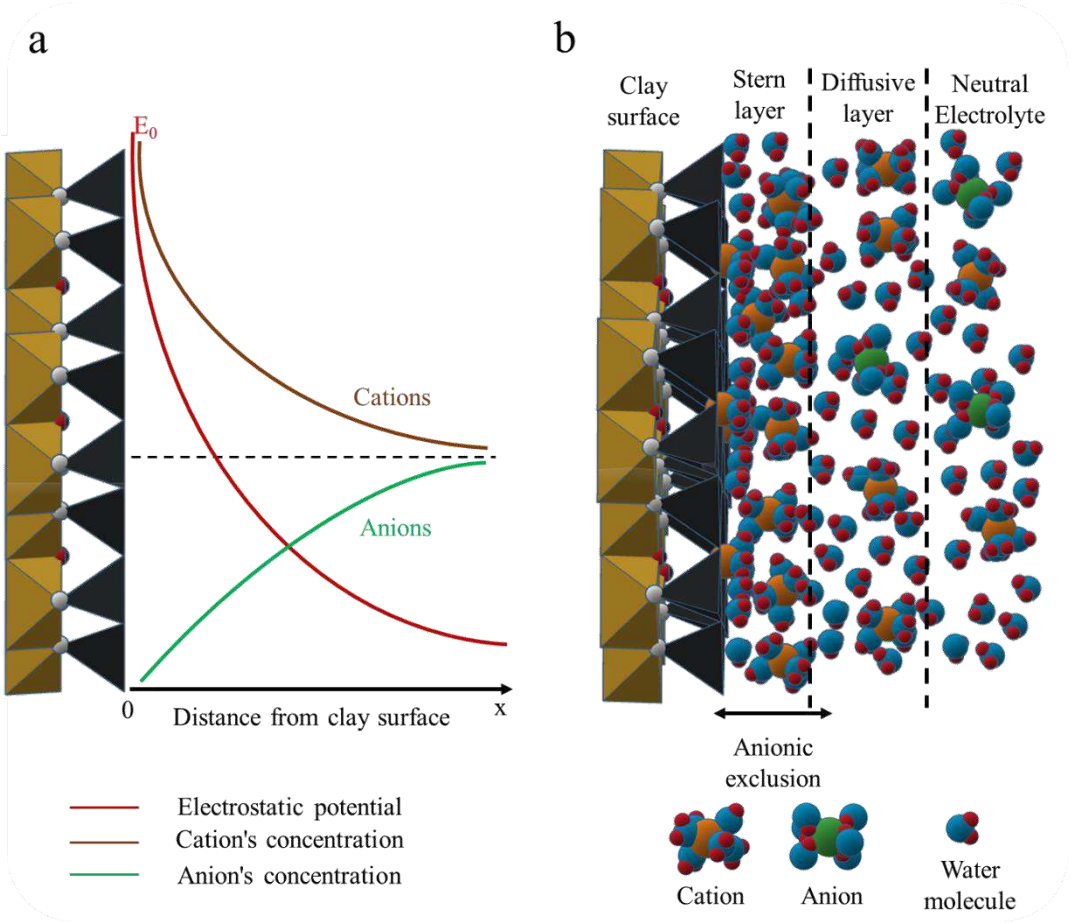


Fig. I.7. *Formation of the electrostatic diffuse double layer (EDL) on the clay basal surfaces. (a) Electrostatic potential and ions concentrations as function of the distance of the clay basal surface. (b) schematic presentation of the different domains inside the EDL.*

$$\kappa = \sqrt{\frac{2F^2 1000I}{\varepsilon RT}} \quad \text{(I.1)}$$

With F the Faraday constant, I is the ionic strength, ε is the water dielectric constant at T, R is the gas constant, and T is the temperature (K).

I.2. Clay porous media

I.2.1. Clay particles, aggregates, and porosity types

The stacking of clay layers leads to the formation of clay particles (Fig. I.8a). Particles size ranges from single sheets (≈1nm) to centimetric single crystals (i.e., Santa Olalla vermiculite). Different rotations and translations may occur during the stacking of the various layers to form a clay particle, resulting in the polytypes of the same mineral. On the one hand, the polytypes have the same chemical composition and layer structure but differ by their stacking mode. The stacking modes can be ordered, semi-ordered, or turbostratic (Fig. I.8b). Each corresponds to a polytype of the same mineral. The ordered and semi-ordered stacking are very common in micas, illite, and kaolinite. In contrast, turbostratic stacking is commonly found in the smectite family, particularly montmorillonite.

On the other hand, the stacking sequence of layers with different chemical compositions (interstratification) leads to mixed-layer minerals (MLM). MLMs are characterized by; the proportion of the various layers, layer compositions, and the ordering degree of the layers stacking sequence (Meunier, 2005; Moore and Reynolds, 1997). Examples of MLMs are smectite/ illite, kaolinite/smectite, and chlorite/saponite.

In a rock or an artificial porous medium, clay particles stack together to form "aggregates" (Bergaya and Lagaly, 2013), as illustrated in (Fig. I.8c). The spatial distribution of clay particles and their aggregates defines the interparticle porosity ($\boldsymbol{\varepsilon}_{\text{interp.}}$), the voids between clay particles (Fig. I.8c). If these particles belong to swelling clay minerals (section I.5), an additional volume of interlayer porosity ($\boldsymbol{\varepsilon}_{\text{interl.}}$) is present (Fig. I.8c).

In this work the terms clay porous media and clay sample are used interchangeably to refer to compressed sample made from clay particles.

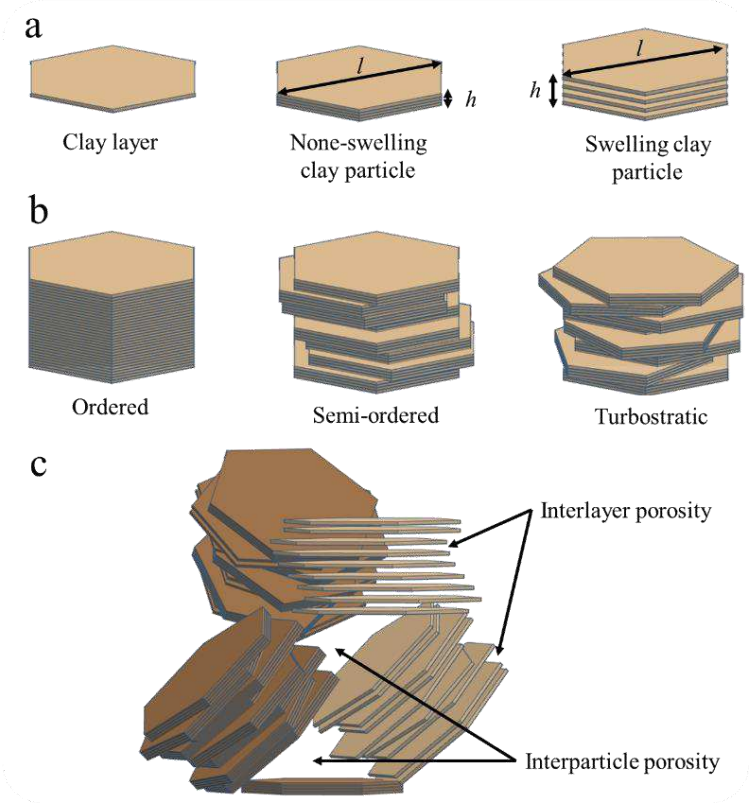


Fig. I.8. *Different stacking modes of the clay layers, and clay particles aggregates and the associated porosity types (interparticle and interlayer).*

I.2.2. Definition and main properties of a clayey medium

The terms clay sample or clayey medium are used here to describe a medium constituted from clay particles. These samples can be obtained at varying degrees in anisotropy in particles' preferred orientation, either by compressing dry clay powder or centrifugation of clay dispersion. For diffusion experiments, the samples are compressed to a specific height that corresponds to a certain porosity. We use a conditioned natural material and a particular size fraction of only one clay mineral in this work. The particle sizes range between 0.1 to 0.5 µm with a similar aspect ratio of < 0.1 (the ratio between the particle thickness *h* to its basal diameter *l*, Fig. I.8a), resulting in a large specific surface area of these particles (Table I.2).

Pores can be divided into three categories based on their diameter: (1) nanopores with diameter < 2nm, (2) mesopores with diameter between 2-50 nm, and (3) macropores with a diameter > 50 nm. Owing to their particles' morphology and size, porous clay media in this work are dominated by nano and mesopores. Moreover, because of their particles' important specific surface area, water and ions present in their nanopores are influenced by the proximity to these particles' surfaces. Because, most often, these surfaces have a very high adsorption

capacity and global negative charges (see section I.1.7). Consequently, the samples after compression have very low permeability, similar to that of the compacted clayey rocks considered for waste storage applications. Clayey rocks, such as the Callovian–Oxfordian formation, the permeability can be as low as 10^{-19} to 10^{-21} m^2 (Delay et al., 2006, 2014). Therefore, the advection flux is negligible, and diffusion is the primary conveying process of water/solutes. In such systems, the fluxes of water and solutes are estimated using classical Fick's second law for one-dimensional transport (details are in the next section) instead of Darcy's law generally used to measure advection flux.

In this text, the total porosity of the samples (ε) is expressed as a percentage ($0< \varepsilon <1$), representing the volume of the voids to that of the whole samples. A sample prepared from 1:1 or none swelling 2:1 clay particles will have only an interparticle porosity ($\varepsilon_{interp.}$). However, for a charged 2:1 clay mineral, a part of the interparticle porosity can be inaccessible for anions due to presence of the EDL. For samples made from swelling clays, two types of porosities exist: $\varepsilon_{interp.}$, and the interlayer porosity ($\varepsilon_{interl.}$) (See the definition in section I.1.5). ε_{interl} is generally only accessible for water and cations, as discussed in section I.1.8. To calculate the porosity of the clayey samples used in this work, please refer to section II.3.1.

I.2.3 Diffusion of water and solutes in a clayey medium

In the absence of advection flux, molecular diffusion of a chemical species in a water-saturated porous media is described by a diffusion coefficient (D, $m^2.s^{-1}$). Experimentally, different setups are used to obtain the D of a tracer (Bourg and Tournassat, 2015), and references therein). These setups yield different definitions of D, such as apparent, pore, and effective coefficients (Da, Dp, and De, respectively). And they can be derived from each other by the relation:

$$De = \alpha\, Da = \varepsilon_{eff.}\, Dp = \frac{\varepsilon_{eff}}{G} D_0 \qquad \text{(I.2)}$$

where α is the rock capacity factor (–), ε is the total porosity of the porous media, $\varepsilon_{eff.}$ is the accessible porosity for the chemical species (tracer), G is the geometrical factor, and D_0 is the self-diffusion coefficient of the chemical species in bulk water.

G can be defined as:

$$G = \frac{\tau^2}{\delta} \qquad \text{(I.3)}$$

Where δ (–) is the constrictivity factor describing the widening or narrowing of the pore (=1 for straight pore). τ (–) is the tortuosity factor ≥ 1 representing the longer path traveled by the diffusing species (more than straight lines) because of the pore-network geometry (pore shape, particle orientation, connectivity, and constrictivity (Appelo et al., 2010). δ and τ parameters are combined in the term G since they are coupled and cannot be measured separately (Van Loon and Mibus, 2015).

The rock capacity factor α is a term used to describe the adsorption capacity of the porous media for the chemical species of interest. α accounts for linear, reversible, and instantaneous adsorption. It represents the equilibrium ratio between the total concentration of the chemical species in the total volume of the porous media (C_t) and the concentration of the non-adsorbed species in the pore fluid (C_b).

$$\alpha = \frac{C_t}{C_b} = \varepsilon + \rho_d * K_d \tag{I.4}$$

where is K_d the distribution coefficient (m^3 kg^{-1}), and ρ_d is the dry bulk density (kg m^{-3}) (Shackelford and Moore, 2013). Generally, K_d is obtained either experimentally by batch sorption experiments or from the fitting of experimental data of *through diffusion* (TD) experiment using Eq. (I.5) for weak to moderate sorbing species (Van Loon et al., 2005).

Occasionally, the retardation factor R (–) is used instead of K_d. R can be expressed as a function of K_d by the equation:

$$R = 1 + \frac{\rho_d}{\varepsilon} K_d \tag{I.5}$$

For none-sorbing chemical species like water tracers (HDO, HTO) $K_d = 0$, $R_d = 1$, $\alpha = \varepsilon = \varepsilon_{eff}$, and from Eq. (I.2) $Da = Dp > De$. For non-sorbing anions, $K_d = 0$, $R_d = 1$, $\alpha = \varepsilon_{eff.} < \varepsilon$, and then $Da = Dp = De / \varepsilon_{eff}$ ($< De$). For sorbing cations and some anions in specific conditions, $K_d > 0$, $R_d > 1$ and $\alpha > \varepsilon$. Anions can be adsorbed in the porous media and, at the same time, are subject to an anionic exclusion (as from the interlayer porosity and possibly a part of the interparticle porosity) if the media is negatively charged. In this case, $K_d > 0$, $\varepsilon_{eff.} < \varepsilon$, and α is either higher or lower than ε, depending on the contribution of both anionic exclusion and adsorption.

The most common experimental setups to obtain macroscopic diffusion coefficients of a chemical tracer in compacted porous media are *closed-cell* (CC), *through-diffusion* (TD), and *in-diffusion* (ID) setups, details can be found in; Shackelford, (1991), Bourg and Tournassat,

(2015), and references therein). They can provide *Da* or *De* or both of them with timesteps of hours to several days. Other alternative experimental techniques used to obtain diffusion coefficients at shorter time scales (e.g., ms) include *electromigration* and *nuclear magnetic resonance* using *pulsed gradient spin echo* experiments (^{1}H PGSE-NMR).

All diffusion experiments in this work were performed using TD setup allows obtaining the *D*e in the direction perpendicular to the sedimentation plane of particles (i.e., De_z, perpendicular to the preferred orientation of clay particles). Note that, on one occasion, the diffusion of the water tracer was measured using ^{1}H PGSE-NMR technic in the Na-kaolinite sample. The motivation behind that was to assess the concordance of both methods, despite the significant difference in the probed timescales (i.e., ms and days for ^{1}H PGSE-NMR and TD experiments, respectively).

Chapter II

Material and Methods

Motivated by the need to quantitively investigate the contribution of some key parameters to the process of molecular diffusion of water and solutes in clayey porous media (i.e., compressed clay samples), this chapter describes the experimental methodologies used to investigate the influence on water and solutes diffusion of:

- Clay particles' preferred orientation (for a given interparticle porosity).
- Different porosities (i.e., interparticle and interlayer) in the samples made from swelling clay particles.

To the extent of our knowledge, these two fundamental parameters draw less attention in the world of diffusion-related studies compared to the porosity value (e.g., Shackelford and Moore, 2013; Xiang et al., 2013; Bestel et al., 2018) or ionic strength variation (e.g., Bourg et al., 2008; González Sánchez et al., 2008a; Glaus et al., 2010; Savoye et al., 2015). For these purposes, diffusion data of waters and ions (i.e., Na^+ and Cl^-) were obtained from compressed clay samples by a classical TD setup (Van Loon et al., 2003; Tertre et al., 2018). The samples were prepared with a new protocol developed in this work. This protocol allows preparing compacted porous media with controlled porosity and degree of particles' preferred orientation. In addition, the obtained samples can be directly mounted to TD setup without compromising their geometric organization. The total porosity values were chosen so that all samples have a similar interparticle porosity, whether made from swelling or non-swelling clays ((e.g., vermiculite and illite, respectively. By doing that, we evaluated the contribution to the diffusion process of the remaining interlayer porosity volume in the swelling clay samples. For a more constrained comparison, all samples were built from the same particle size fraction (i.e., 0.1-0.2µm) characterized by the same morphology (i.e., aspect ratio; the ratio between the particle thickness and its basal diameter). This particle size was chosen for two reasons: (i) the 0.1-0.2 µm size fraction it is not too prone to significant dissolution when immersed in pure water during the conditioning process. In addition, (ii) distinct size fraction minimizes the potential variation in the geometrical organization of the samples resulting from the variation in the particle size (i.e., particle organization, pore size distribution) as reported in; Hubert et al., (2013) and Ferrage et al., (2015).

The first section in Chapter II describes the nature and conditioning process of the clay minerals used to build the compressed samples. These minerals are Santa Olalla (SO) vermiculite, illite du Puy (IDP), and KGa-2 kaolinite.

SO-vermiculite is a charged, swelling clay mineral with interlayer and interparticle porosities. Although experimental diffusion data on swelling clay media were almost exclusively acquired with smectite particles or from natural clayey rock (e.g., Opalinus, Callovo-Oxfordian, and Boom clays), where smectite is the main swelling clay mineral (e.g., Appelo and Wersin, 2007; Bourg et al., 2007; Bourg and Tournassat, 2015; Tinnacher et al., 2016). However, in addition to the typical crystal swelling of smectite (Ferrage, 2016), this mineral exhibits an osmotic swelling in water-saturated conditions because of the low layers charge (e.g., Abend and Lagaly, 2000; Liu, 2013; Tertre et al., 2018). The latter allows for a non-defined volume of water molecules into their interlayer space, exfoliating the individual layers from the particles. The exfoliation distorts the particles' original organization in the porous media; the extent of this distortion depends on the particle's size and the nature of the interlayer cation (Michot et al., 2004). Consequently, the exfoliated layers (particularly in Na-saturated samples) may form a gel-like phase that induces significant variation in the diffusivity of chemical species in smectite, as reported by Melkior et al., (2009). In conclusion, osmotic swelling in smectites impedes clear discrimination between the volumes of interlayer and interparticle porosities. Such criteria are important to studying the effect of different types of porosities on the diffusion process. In this context, Saint Ollala (SO) vermiculite was the ideal candidate; it has a similar crystal structure to smectite but a considerably higher layer charge. The latter prevents the exfoliation of individual layers when immersed in water, preserving a well-defined interlayer volume when saturated with water (Faurel, 2012). In addition, the physicochemical properties of SO-vermiculite are well documented in literature (Gonzáles García and García Ramos, 1960; De La Calle et al., 1978; Marcos et al., 2003; Reinholdt et al., 2013).

IDP is a non-swelling clay mineral with a non-accessible interlayer porosity. This mineral has approximately the same negative charge as SO-vermiculite, making a more reasonable comparison of their diffusion results. This natural mineral has a relatively fine particle size (Rajec, 1999; Hassan et al., 2005), making it relatively easy to obtain the 0.1-0.2 µm size fraction with a very low content of mineralogical impurities. This size fraction has more or less the same basal to lateral surfaces ratio of vermiculite (0.18 *vs.* 0.21, respectively, as determined from Ar adsorption in this work and from Reinholdt et al., (2013). Furthermore, a large database

on IDP exists in the literature, providing an essential reference to compare with our results, since it was extensively used in diffusion experiments of water and various ions (González Sánchez et al., 2008b; Glaus et al., 2010; Altmann et al., 2015, and references therein).

KGa-2 kaolinite is also a none swelling mineral. In contrary to IDP, this mineral "theoretically" exhibits no structural charge, which provides a good reference for the diffusion of water and ions in the absence of adsorption and ionic exclusion (e.g., Glaus et al., 2007).

The second section of Chapter II details the conditioning, purification, and extraction processes of different size fractions of clay minerals in this work. The third section is the protocol used to build compacted samples to varying degrees of anisotropy in particles' preferred orientation. This protocol was developed from the methodology first proposed by Dabat et al. during his Ph.D. work (Dabat, 2019) on non-charged clays (i.e., kaolinite). Indeed, these authors established a method to prepare Na-kaolinite samples with the same total porosity (~0.5) but different in their degree of particles' preferred orientation. With these samples, these authors succeeded in connecting the spatial anisotropy of water diffusion to the degree of preferential orientation of the particles (Dabat et al., 2020). Their findings were based on experimental water diffusion analyses obtained from *Pulsed Gradient Spin Echo attenuation* by *Nuclear Magnetic Resonance* (PGSE- NMR) and numerical data from *Brownian dynamics* (BD) simulations using various *Virtual Porous Media* (VPMs). In our case, we developed this protocol to build samples from any clay type (swelling/none-swelling) that can be used for TD experiments. The fourth section describes the theoretical concepts and the experimental techniques used to quantify the degree of anisotropy in particles' preferred orientation in the compacted samples. The final fifth section includes the experimental methods to obtain diffusion coefficients of different tracers from these samples.

II.1. Materials

In this section, the structural charge of clays is reported for half unit cell in eq/formula half unit $(Si, Al)_4O_{10}$, and it ranges between 0 to 1 (Table I.1).

II.1.1. Santa Olalla vermiculite

The SO-vermiculite is a tri-octahedral 2:1 swelling clay mineral. The raw material were obtained from Santa Olalla (Huelva, Spain), and results from the alteration of a well - crystallized phlogopite (Gonzáles García and García Ramos, 1960; De La Calle et al., 1977). In its original form, the centimetric vermiculite crystals are Mg^{2+}-saturated, with substantial

negative charge deficiency mainly in the tetrahedral sheet. The structural formula was reported from the work of Marcos et al., (2003) and Arguelles et al., (2010):

$$[(Mg_{4.92}Fe_{0.44}Al_{0.60}Ti_{0.04})\ (Si_{5.66}Al_{2.34})\ O_{20}\ (OH)_4]\ (Mg_{0.76}Ca_{0.06}Na_{0.04}),\ 7.63\ H_2O]$$

The swelling and hydration properties of SO-vermiculite under different relative humidity conditions have been investigated in the work of Faurel, (2012). Briefly, in this work, we used a conditioned SO-vermiculite in Na^+ homo-ionic form (hereafter Na-vermiculite) for diffusion experiments in water-saturated conditions. In this form, this mineral exhibit one layer of water molecules (1W) at room humidity (~40-60%) and does not display osmotic swelling when saturated with water. Instead, it persists in two water-layers (2W) hydrates (Faurel, 2012; Lagaly and Dékány, 2013).

In this work, we used the 0.1-0.2 µm size fraction. This size fraction's morphological and crystal chemistry properties were determined by Reinholdt et al., (2013). These authors reported no important changes in the chemistry among the different size fractions; other parameters are included in Table I.2.

II.1.2. Illite du Puy

Three different raw IDP materials (samples) were used in this work, all originating from Oligocene lacustrine sediments in le Puy-en-Velay (Haute-Loire, France). Two samples were provided by The Argile du Velay company (www.argileduvelay.com), a clay ore mining company, and by the Commissariat à l'énergie atomique (CEA, Université Paris-Saclay, France). These two samples were only used in the characterization study in chapter III for comparison purposes.

The Raw IDP material used for TD experiments was provided by the Paul Scherrer Institute (PSI, Villigen, Switzerland) corresponded to the reference illite used in the Cat-Clay European project (Bradbury and Baeyens, 2009; Glaus et al., 2010, 2015; Altmann et al., 2015) and the ongoing European Join Project EURAD.

IDP is a naturally occurring material from an Oligocene sedimentary formation, and according to Gabis, (1963) who first described this series, the illite results from the illitization of detrital montmorillonite.

The most recent structural formula for Na-IDP was reported in Altmann et al., (2015) from *Electron Probe Micro Analyzer* (EPMA) and bulk analyses:

$$[(Si_{3.51}\ Al_{0.49})\ (Al_{1.2}\ Fe_{0.36}\ Mg_{0.39})\ O_{10}\ (OH)_2]\ (Ca_{0.06}\ Na_{0.08}\ K_{0.69})]$$

A detailed or brief characterization of the raw and the conditioned IDP is reported in many publications (e.g., Poinssot et al., 1999; Rajec, 1999; González Sánchez et al., 2008c; Bradbury and Baeyens, 2009; Glaus et al., 2010; Altmann et al., 2015) and the Ph.D. thesis of (Tessier, 1984; Bardot, 1998; Diaz, 2009; Rajyaguru, 2018). However, we found essential variations in the reported properties between these different studies, for example (i) the presence or absence of other clay minerals, such as kaolinite, smectite/illite MLMs, and (ii) differences in the nature and quantities of the associated accessory minerals, such as feldspars, quartz, and carbonates. And (iii) variation in structural formulas, layer charge, values of the specific surface area, and cationic exchange capacity. Because each of the properties above influences the diffusion process in these materials, we decided to make our own morphological and chemical characterization of different size fractions of IDP from this work, including the 0.1-0.2 µm used for diffusion experiments. The results are detailed in Chapter III.

II.1.3. KGa-2 kaolinite

The KGa-2 kaolinite is from the Source Clay Repository of the Clay Mineral Society, with an average size of the particles of approximately 0.5 µm (Hassan et al., 2005) and the structural formula from Mermut and Cano, (2001) is:

$$[(Al_{3.80}Ti_{0.13}Fe^{3+}_{0.07})\ (Si_{3.84}Al_{0.16})\ O_5(OH\ _4)]$$

II.2. Conditioning and preparation of the different size fractions

IDP raw material was washed with hydrochloric acid (pH 1, room temperature) to remove carbonate and sparingly soluble minerals. Carbonate dissolution was considered completed when the pH of the clay/acid suspension was between 5 to 5.5 after a few hours of contact (typically two hours). Carbonate removal was further confirmed by recording *X-Ray Diffraction* (XRD) pattern (not shown) from an oriented mount. Next, the materials were washed by centrifugation with distilled water, and the <50 µm of the was retrieved by wet sieving. For SO vermiculite, the centimetric mono-crystals were broken by sonication in wet conditions, as described in Reinholdt et al. (2013). Finally, pretreatment before saturation was made for KGa-2.

All three clay minerals were transformed into homoiconic form (e.g., Na-vermiculite, Na-IDP) through three cycles of saturation with high purity NaCl salt. In each cycle, the Na+ concentration was 100 times that of the cations released by the clay materials during the exchange process. The latter was estimated based on the mineral's cationic exchange capacity

(CEC) and solid mass. After the third cycle, the excess of salt was removed by dialysis, using a 6-8 KD membrane until the test with silver nitrate was negative.

From the dispersion of the conditioned clays, different size fractions were obtained using sequential separation by centrifugation protocol adapted from the one developed by Reinholdt et al. (2013). For IDP, the < 2 µm fraction was first separated by *Thermo Scientific legend XFR centrifuge from Fisher scientific*®. Then, 5g of < 2 µm material were divided between 6 centrifuging tubes (38.5mL polypropylene tubes) and dispersed in *Milli-Q*® (MQ) pure water by sonication, centrifuged using *Avanti J 301* centrifuge (swinging bucket rotor *JS-24.38*) from *Beckman Coulter*®. The extraction process for IDP started with the finest fraction (<0.05 µm) through 5 centrifugation cycles until the supernatant became clear. Followed by the coarser size fraction (0.05-0.1 µm), and then the 0.1-0.2 µm until the materials remained in the tubes are the 0.2-2 µm fraction. The extraction started with the <0.1 µm for SO-vermiculite, then the 0.1-0.2 µm fraction. Finally, three aliquots (1 mL each) from the dispersion of each fraction were dried at ambient humidity and weighted to calculate the conversion yields. Centrifugation parameters and mass contributions of each fraction are reported in Table II.1.

Table II.1. *Centrifuging parameters used for size fractioning of illite du Puy (IDP), and the relative mass contribution of each fraction.*

Fraction (µm)	Time (min)	Speed (rpm)	Acceleration (g)	E-IDP
<0.05	20	20000	72128	18.2
0.05-0.1	15	12500	28175	20.1
0.1-0.2	14	6500	7619	21.7
0.2-2	-	-	-	28.6
<2	3	1000	-	-
2-50	-	-	-	6.5
			Total Yield %	95.1

After size separation, the dispersion for each size fraction of IDP was divided into three portions: two were saturated with Ca^{2+} and K^{+} for XRD and CEC measurements, respectively.

The third portion was lyophilized for gas adsorption measurements. Note that for the 0.1-0.2 µm, a fourth portion of the dispersion was used in Na^+ form for diffusion experiments,

Finally, no size fractionation was performed on KGa-2 material; the reason was to keep the same sample composition as in Tertre et al., (2018) and Dabat et al., (2020), to which our results were compared.

II.3. Building the clay porous media

II.3.1 Building clay media with variable anisotropy in particles organization

Clay particles (particularly ones from in this work) have generally platelet shape with a low aspect ratio (i.e., thickness /diameter of the basal surface of < 0.1 (Fig. I.8)), as calculated from Ar adsorption measurements for kaolinite, vermiculite, and illite (Hassan et al., 2005; Reinholdt et al., 2013); Chapter III in this work, respectively). Such morphology dictates that particles tend to settle on their basal surfaces in an aqueous environment, a behavior known as the preferred orientation of clay particles. Therefore, two preparation methods were used to produce compressed cylindrical porous media (i.e., compressed samples), either isotropic or anisotropic, regarding particles' preferred orientation. Isotropic samples were prepared by uniaxial compression of dried clay powder. For that, the clay powder was directly placed inside *(poly)methyl methacrylate* (PMMA) tubes (diameter of 0.95 cm and a height of 7 cm) designed to be mounted directly to the TD setup. The samples were compressed with the aid of two metal pistons (one on each side) using a hydraulic press, as illustrated in Fig.II.1. For the Anisotropic samples, thanks to a protocol proposed for kaolinite by Dabat et al. (2020), we developed a methodology that allows to; (i) obtaining samples from either swelling or none-swelling clays having the same total porosity (ε) as the isotropic ones. Still, at a considerably higher degree of anisotropy in particles organization. (ii) to directly perform TD experiments. This protocol consists of the following steps, as illustrated in Fig.II.2:

1. Prepare a clay dispersion from the desired clay material at a known concentration. For that, the mass of the clay was decided based on the aimed porosity and final thickness of the sample (more details ahead). The volume of the dispersion corresponds to the required centrifugation runs (i.e., ten runs). For instance, samples for TD experiments are prepared in PMMA tubes with a diameter of 0.95 cm and a height of 7 cm. By subtracting the volume occupied by the (PTFE) cap (Fig. II.2) and the final sample volume at the end of the preparation. Hence, the remaining volume of the tube is ~ $3cm^3$ (Fig. II.2d). This volume can be filled

with ~3 mL of dispersion. Therefore, for ten centrifugation runs, we need ~30 mL of dispersion. For the solid /solution ratio in this work, we used clay dispersions at a concentration ranging from 20 to 40 g L^{-1}.

2. The second step starts with transferring 3 mL of the clay dispersion into the tube sealed from the bottom with a PTFE cap (II.2a). Then, the tube is placed into the centrifuging swinging bucket rotor (II.2b). Note that we used a special adapter to prevent tube rotation inside the containers (II.2a).
3. In the third step, horizontal centrifugation runs at ~23 850 g for 25 minutes were performed (Centrifuge *Avanti J 301*, rotor *JS-24.38* from *Beckman Coulter*®; Fig. II.2b). After each run, the clear supernatant was siphoned, and a new aliquot was added ((Fig. II.2c)). These steps were repeated ten times to obtain a sufficient mass in the tube (between 1-1.5 g) (II.2.d).
4. The fourth step, drying the sample: after centrifugation, the sample must be dried to determine the dry clay mass necessary for ε calculation (more details ahead). However, an unsuccessful attempt to dry one vermiculite sample (Fig.II.3a) at 60˚C proved to introduce significant shrinkage and distortion of its structure; a similar observation was reported in Loeber, (1992) and Durrieu et al., (1997). Therefore, we developed the protocol previously used for clay cakes preparation (Loeber, 1992; Pret, 2003) to dry the sample without compromising its geometry and particle organization. For this, the sample was first flash-frozen by immersion in *slush nitrogen* (SN_2) for 2-5 minutes (Fig.II.2e) and then dried by lyophilization at – 40°C for 2-3 hours (Fig.II.2f). Complete water removal was verified when the sample maintained a stable mass during the last hour of lyophilization. Finally, the sample was mounted to the TD cell and uniaxially compressed to the desired height (Fig.II.2g-i).

It is necessary to mention that SN_2 was used instead of *liquid nitrogen* (LN_2) because the latter introduced deformation in the sample, as shown in Fig.II.3b. Such deformation means that the internal organization of the particles is compromised, and the non-homogenous freezing of the sample causes it. Indeed, when the sample is immersed in LN_2, it raises its temperature to the boiling point (i.e., –196 °C). Hence, a layer of nitrogen vapor is formed around the sample that impedes heat transfer with the LN_2. This phenomenon is known as "gas film" (Goldstein et al., 1992; Pret, 2003).

To avoid the formation of the gas film, LN_2 is placed under a high vacuum for few minutes until its complete solidification. And by suddenly breaking the vacuum, a

"metastable paste" of solid and liquid nitrogen is formed with an average temperature of approximately –210°C (i.e., SN_2) (Goldstein et al., 1992; Pret, 2003). Thus, the sample temperature is no longer sufficient to raise nitrogen temperature to its boiling point at -196°C.

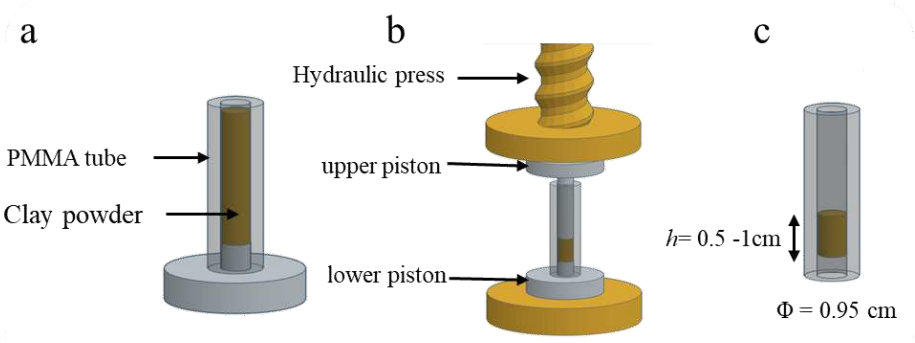


Fig. II.1. *Illustration of the method used to prepare clay samples at a low degree of particles preferred orientation (i.e., isotropic). (a) clay dried powder is placed in ploy methyl methacrylate (PMMA) tubes sealed from bottom with metal piston. (b) clay powder is compressed to a certain height by hydraulic press after installing an upper metal piston (c) the two pistons are removed after compression.*

Total porosity ε of all samples used in this work was calculated as the difference between the sample volume (considering the diameter of the tube and the sample's thickness after compression, *L*) and the volume occupied by the solid only (i.e., clay particles). The solid volume can be determined based on the sample dry mass and the clay grain density. The latter was calculated to be 2.62 g cm^{-3} for Na-kaolinite based on the structural formula and the crystal structure parameters refined by Sakharov et al., (2016) for KGa-2 kaolinite. For the 0.1-0.2 µm size fraction of Na-IDP used in diffusion experiments, the grain density was calculated to 2.83 g cm^{-3}, based on the structural formula, the (*a, b* parameters) and the c* parameter obtained during this work (Chapter III). Finally, for the 0.1-0.2 µm size fraction of Na-vermiculite, a grain density of 2.73 g cm^{-3} was used based on the (*a, b*) cell parameters and the chemical composition of the 2:1 layer reported by Arguelles et al., (2010) and the c* parameter value for dehydrated layers at 10 Å (Gieseking, 1975). However, Na-vermiculite displays a mono-hydrated state (1W) at room humidity and a bi-hydrated state (2W) in water-saturated conditions, respectively (Faurel, 2012). Thus, two hydrated densities of 2.49 and 2.24 g cm^{3} for 1W and 2W Na-vermiculite, respectively, were determined based on water content and c* parameters derived by Faurel. (2012) for 1W (4.13 $H_2O/O_{20}(OH)_4$, c* = 11.97 Å) and 2W layers (9.9 $H_2O/O_{20}(OH)_4$, c* = 14.86 Å). The value of hydrated density at 1W is essential to consider when preparing the sample from vermiculite powder (i.e., isotropic sample), it allows

for considering the quantity of adsorbed water at room humidity when measuring the powder mass.

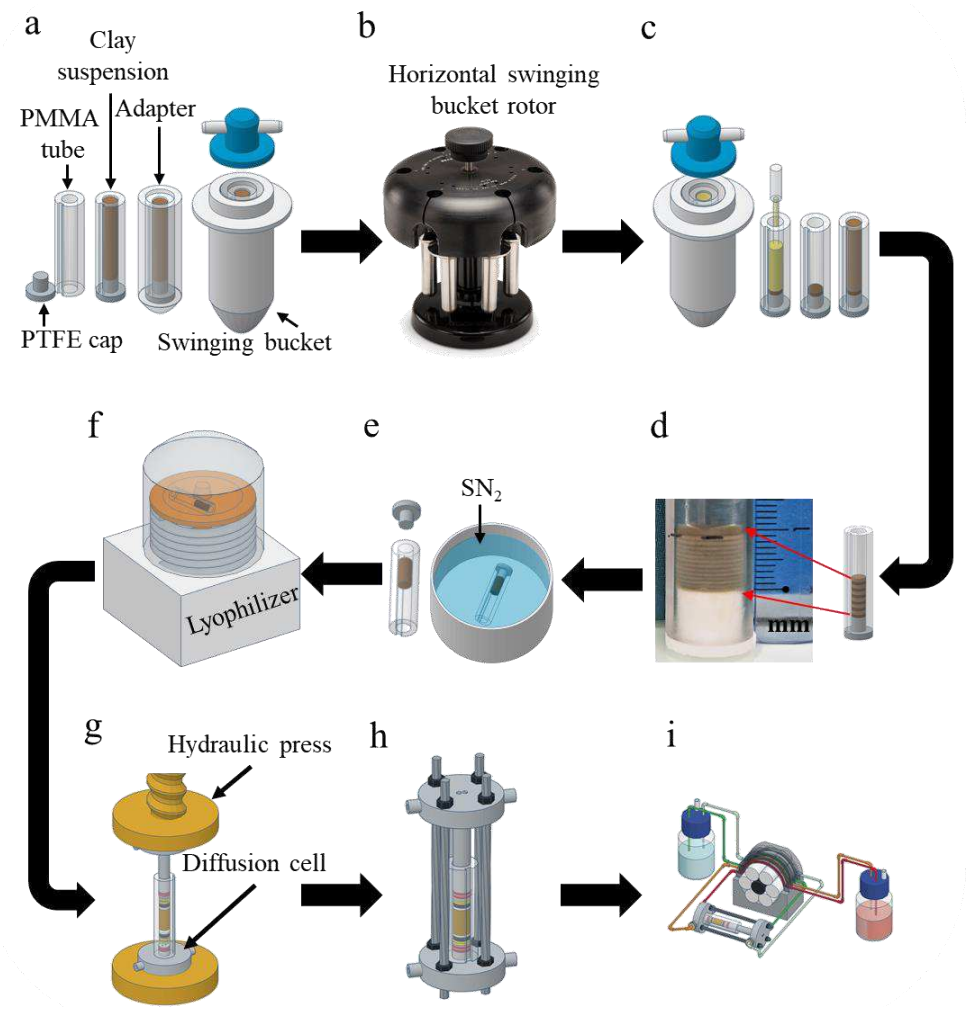


Fig. II.2. *Illustration of the protocol used to prepare clay samples at high degree of particles preferred orientation (i.e., anisotropic). (a) Clay dispersion is placed in ploy methyl methacrylate (PMMA) tubes sealed from bottom with poly tetrafluoroethylene (PTFE) caps placed in turn into swinging buckets. (b) PMMA tubes are centrifuged at ~23850 g for 25min in a horizontal swinging bucket rotor. (c) Supernatant is removed, and new clay dispersion is added. (d) 10 centrifugation cycles are performed to obtain enough mass in the tube. (e-f) The tube is immersed in slush nitrogen (SN_2) for few minutes to remove adhesion between the PTFE cap and the sample and immediately placed into a Lyophilizer to remove water by sublimation. (g) The sample is compressed to the desired height corresponds to the designed total porosity value. (h) Sample is mounted to the diffusion cell and the final height is maintained by threaded rods and nuts. (i) Diffusion cell is mounted into the Through-diffusion (TD) setup.*

Note that for Na-kaolinite and Na-IDP, only the *interparticle porosity* ($\varepsilon_{interp.}$) is accessible by the water tracer, resulting in $\varepsilon = \varepsilon_{interp.}$. By contrast, Na-vermiculite exhibits both

$\varepsilon_{interp.}$ and *interlayer porosity* ($\varepsilon_{interl.}$). By considering the difference in the c* parameter values between dehydrated layers at 10 Å (Gieseking, 1975) and fully water-saturated layers at 14.86 Å (Faurel, 2012), the interlayer volume corresponds approximately to 1/3 of the particle thickness in water-saturated conditions (i.e., during diffusion experiments). Consequently, the proportion of the $\varepsilon_{interp.}$ *vs.* $\varepsilon_{interl.}$ porosities for Na-vermiculite can be calculated for using the following relation:

$$\varepsilon = \varepsilon_{interp.} + \varepsilon_{interl.} = \varepsilon_{interp.} + \frac{1-\varepsilon_{interp.}}{3} \quad \text{(II.1)}$$

Finally, for each sample used in this work, a duplicate was prepared for particle organization measurements (more on this in the next section).

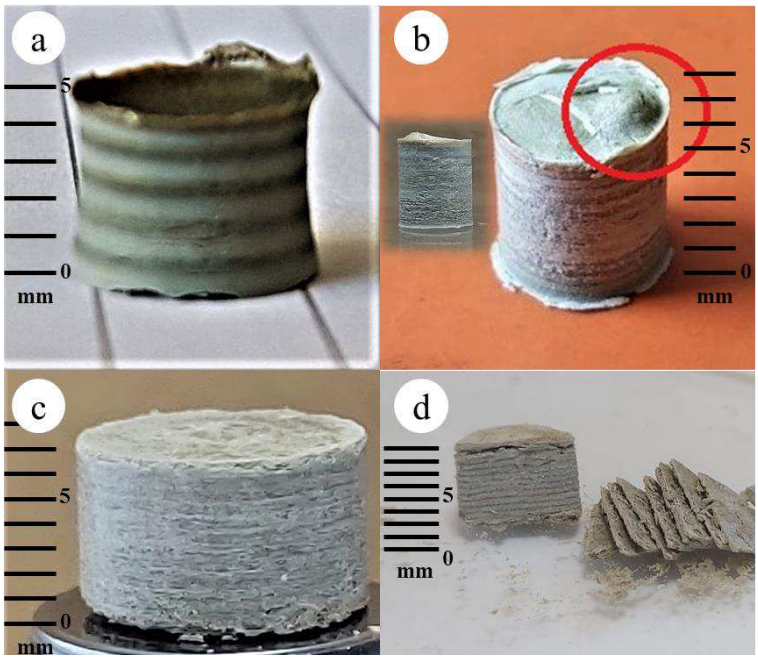


Fig. II.3. *Images of 0.1-0.2µm Na-vermiculite samples prepared by centrifugation to obtain high anisotropy in the particles preferred orientation. (a) Deformation in the geometry of the sample dried at 60˚C. (b) Deformation in the sample that was flash-frozen by plunging into liquid nitrogen (LN_2). (C) None-deformed sample that was flash-frozen by plunging into slush nitrogen (SN_2). (d) longitudinal section in one sample to show the successive beds of clay particles, each two beds (dark and light colored) correspond to one centrifugation cycles.*

II.3.2. Induration and slicing of the clay porous media

Induration of the duplicate samples was necessary to produce thin sections (i.e., lamellas) from which the *two-dimensional X-Ray Scattering* (2D-XRS) measurements were obtained (details are reported in the next section). The induration method relied on the thermal

impregnation with *methyl methacrylate* (MMA, $C_5H_8O_2$). This technique was developed by Sammaljärvi et al., (2012) and successfully applied to Na-kaolinite samples in Dabat et al., (2020). The duplicates samples were prepared in *polyetheretherketone* (PEEK) tubes (diameter of 0.64 cm and height of 7.5 cm) instead of PMMA because the latter can dissolve when in contact with MMA. Perforated PEEK caps and cellulose membranes with a pore size of 0.1 µm were set at each side to maintain the total porosity and particle organization during the induration process (Fig.II.4a). First, the tubes (containing the samples) were placed under a vacuum for 20 minutes in a hermetic cell to remove the residual water that may prevent MMA vapor from penetrating the sample pores. Next, liquid MMA mixed with thermal initiator *benzoyl peroxide* (BPO, at 0.5% of MMA mass) was introduced into the tubes without breaking the vacuum (Fig.II.4b). Sustaining the vacuum is necessary to maintain the pores in air-free condition, thus facilitating the access of MMA gas to the smallest pores. The tubes were kept in contact with liquid MMA for a few days up to two weeks (depending on the sample permeability) to promote the capillary saturation of the pores by the MMA+BPO mixture as much as possible. After saturation, the tubes were sealed with PTFE caps and placed in a water bath at 55°C for at least 24 hours (Fig.II.4c) for a complete polymerization of MMA into PMMA.

After induration, the samples were sliced with a circular saw longitudinally and transversely with respect to the tube axis (Fig.II.4d). The resulting slices were reduced on a polishing table to lamellas with a thickness of ~500 µm. This thickness is necessary to allow sufficient transmission of the X-ray beam during the 2D-XRS measurements (Dabat et al., 2020).

II.4. Analyzing the preferred orientation of clay particles

This work uses the $\langle P_2 \rangle$ order parameter to describe the degree of anisotropy in a particle's preferred orientation in the samples. Hence, we discuss in this section the theory behind the degree of anisotropy in particle's preferred orientation and how to obtain the *Orientation Distribution Function* (ODF) from the 2D-XRS measurements, from which the $\langle P_2 \rangle$ order parameter is calculated (Dabat et al., 2019, and references therein).

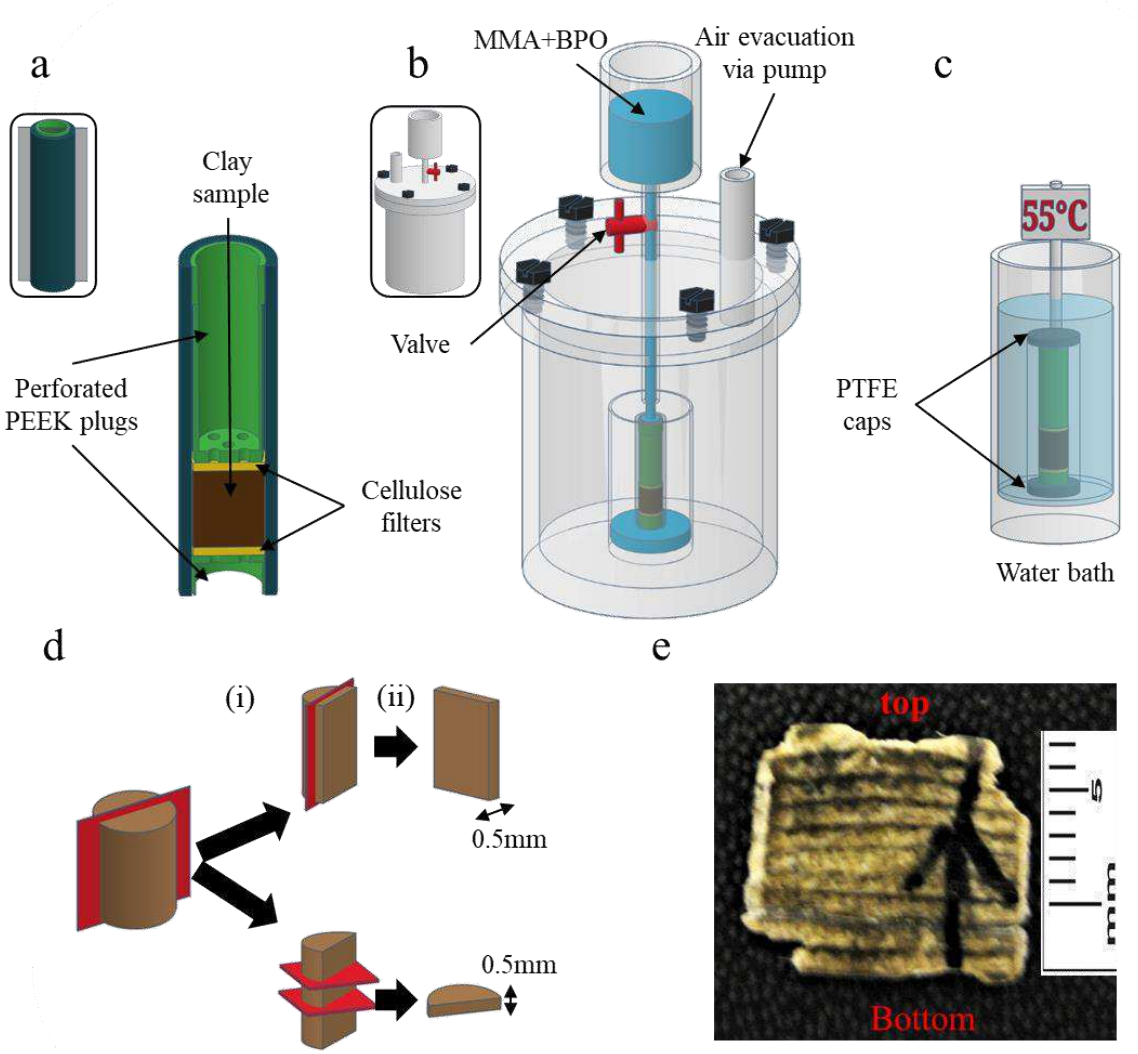


Fig. II.4. *Illustration of the method used to endure the clay samples. (a) cross-section in the sample tube. (b) hermetic cell used to put the sample under vacuum and to introduce the mixture of methyl methacrylate (MMA, $C_5H_8O_2$) and the thermal initiator benzoyl peroxide (BPO). (c) the sample is placed in a thermal bath at 55˚C. (d) After induration, the sample is cut into lamellas: (i) the sample is cut into two vertical halves, (ii) cutting the longitudinal and transversal lamellas (the cutting planes are shown in light color cuboid). The lamellas are reduced to a thickness of 500 µm by polishing. (e) longitudinal lamellas of Na-vermiculite.*

II.4.1. The Orientation Distribution Function (ODF)

The orientation of a platelet-shaped clay particle can be defined in an orthogonal framework as a function of the vector perpendicular to its basal surface z′ (Fig. II.5), the latter being defined in spherical coordinates as a function of two angles: θ, which is the azimuthal angle between z′ and the z-axis, and Φ, the polar angle in the (*xy*) plane (Fig. II.5). For clay particles with uniaxial symmetry whose z-axis is the only symmetry axis (Cebula, 1979; Wenk

et al., 2008; Hubert et al., 2013, and references therein), the probability for a particle orientation is equal over all possible Φ angle values. Therefore, the ODF can be described as a function of only its θ angle, i.e., $f(\theta)$, with the following constraints:

$$f(\theta) \geq 0 \tag{II.2}$$

$$f(\theta) = f(\pi - \theta) \tag{II.3}$$

$$\int_0^{\pi} f(\theta)\, sin(\theta) d\theta = 1 \tag{II.4}$$

Eqs. (II.2) and (II.3) indicate that the ODF is always positive, with the same probability of the particles pointing upward or downward. The term $f(\theta)\sin(\theta)$ in Eq. (II.4) corresponds to the normalization of all the particles in the sample which have an angle θ with the z-axis.

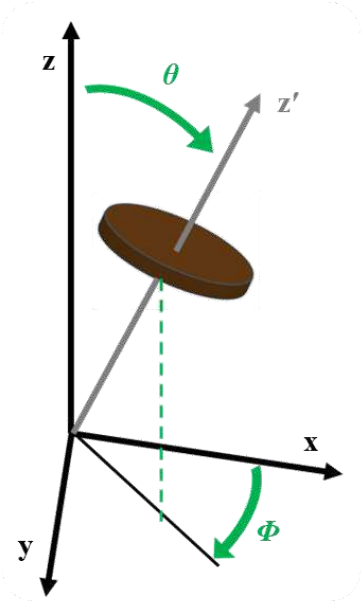


Fig. II.5. *The orientation of an individual clay particle in Spherical coordinates (ρ, θ, Φ) with respect to the sample tube (laboratory frame: (x,y,z)) and the angles (θ, Φ) describing the orientation of the*

II.4.2. Two-dimensional X-ray Scattering (2D-XRS) measurements

As discussed earlier, ODF can be extracted from 2D-XRS diffractograms. In this work, these measurements were performed at the *Laboratoire de Physique des Solides* (LPS) - Orsay, in collaboration with Erwan Paineau.

The experimental setup for 2D-XRS is illustrated in Fig.II.6. The X-ray beam is generated via a copper rotating anode generator (*RU H3R, Rigaku Corporation*, Japan) and equipped with a multilayer W/Si mirror (*Osmic*), which generates a monochromatic beam ($\lambda_{CuK\alpha}$ = 1.5418 Å) with a spot size of 1 mm^2 that passes through the slits to cover a 600 x 600 µm^2 surface of the sample. The X-ray beam is directed perpendicular to the studied sample by mounting it on a

goniometer head (Fig.II.6). The scattered signals (the diffraction cones) from the particles in the sample are collected on a 2D-detector (*MAR345, marXperts GmbH*®, Germany, 150-µm pixel size). The X-ray beam is blocked after the sample by a *beam stop* to avoid the detector's saturation. Increasing the sample-to-detector distance will increase the diffraction cones spreading and bring in focus the reflection rings at smaller θ_B values at the expense of the ones at larger values. For samples from this work, this distance was set to 250 mm; such configuration makes it possible to reach a scattering vector modulus down to $Q_{min} = 0.2$ Å^{-1} ($Q = 2\pi/d = 4\pi/\lambda \sin(\theta_B)$, where λ is the incident wavelength, and $2\theta_B$ is the scattering angle) corresponding to diffraction peaks range between 2 to 28 Å. The XRS patterns were acquired with a typical acquisition time of 900 s.

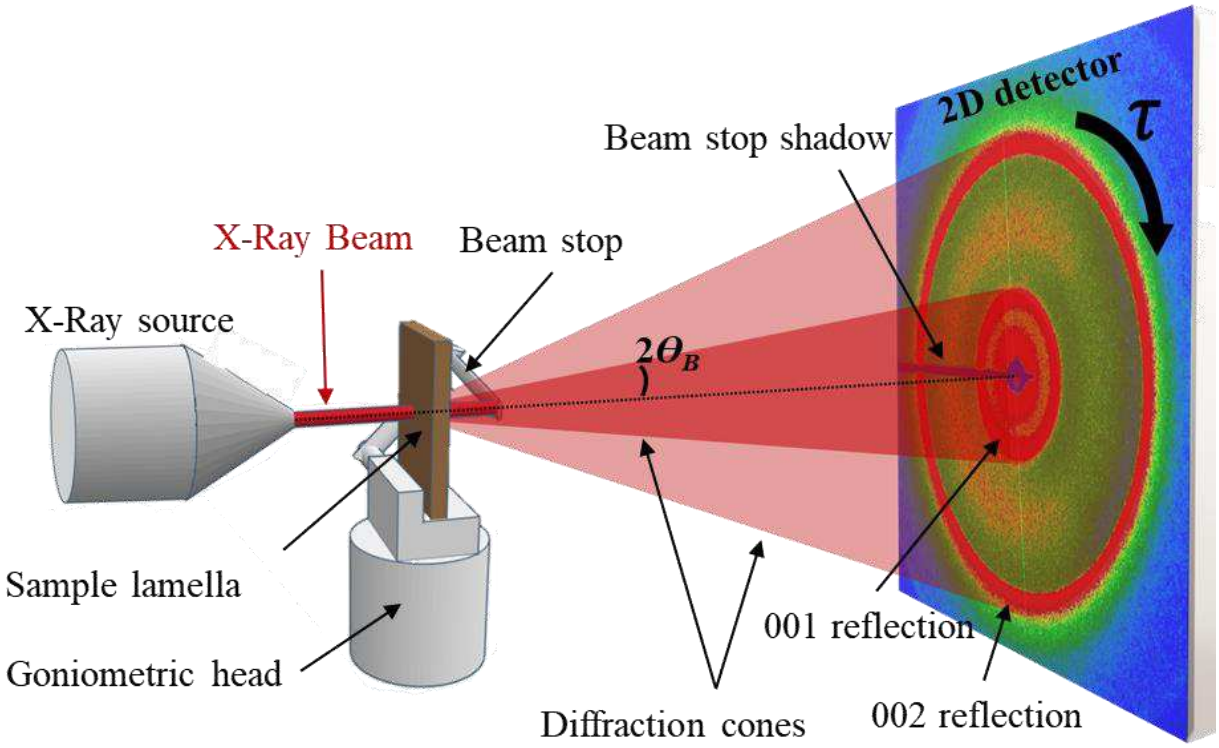


Fig. II.6. *How particles organization is measured from thin lamella of the clayey sample. Featuring an illustration of the X-ray scattering with a 2D-detector (2D-XRS) instrumental setup and the measurement of the particle orientation by azimuthal integration (along τ) of the scattered intensity.*

II.4.3. Treatment of 2D-XRS patterns

2D-XRS patterns are recorded from the longitudinal and transversal lamellas of the duplicated samples (see section II.3.1). The longitudinal lamellas were cut perpendicular to the sedimentation plane to allow the anisotropy in the particle's preferred orientation to appear in

the ODF. By contrast, the transversal lamellas were cut parallel to the sedimentation plane to verify the transverse isotropy of the sample (i.e., adequately prepared transversal lamella results in isotropic ODF).

Fig. II.7. shows 2D-XRS patterns recorded from longitudinal and transverse lamellas of one anisotropic vermiculite sample. The measured Bragg peaks scattered intensities (I) are displayed in color scale from white to black with increasing intensity. The black rings correspond to the *hkl* Bragg peaks of the clay in the sample. These patterns are processed by the software IMAGE developed at LPS. This software allows for full integration over the whole diffractogram to produce a 1D pattern of the Bragg peaks, as shown in Fig.II.8a. From the 001 Bragg peak in the 1D pattern, we can: (i) determine and remove the background, and (ii) from the width of this peak, we can define the radius for an azimuthal integration scan of I as a function of the angle τ (the angle between the normal of the incident beam and the surface of the 2D-detector, Fig.II.8b). Thus, the ODF results from this integration plotted as a function of the angle θ over the angular range [0; 2π]. This definition is valid by considering that $\tau = \theta$. And because of the position of the 001's reflection at low scattering angles ($2\theta_B$), the hypothesis $\tau = \theta$ is a rational approximation (see Dabat et al., (2019) for more details).

Before interpretation of the raw ODF, two corrections must be applied: (i) angle correction to obtain symmetric ODF function in respect to θ°, and (ii) background noise suppression. Details on these two corrections can be found in the thesis manuscript of Dabat, (2019).

The corrected ODF $f(\theta)$ can be expressed from the scattered intensity $I(\theta)$ evolution integrated from the 2D-XRS diffractograms as follows:

$$f(\theta) = \frac{I(\theta)}{\int_0^{\pi} I(\theta) sin(\theta) d\theta} \quad \text{(II.5)}$$

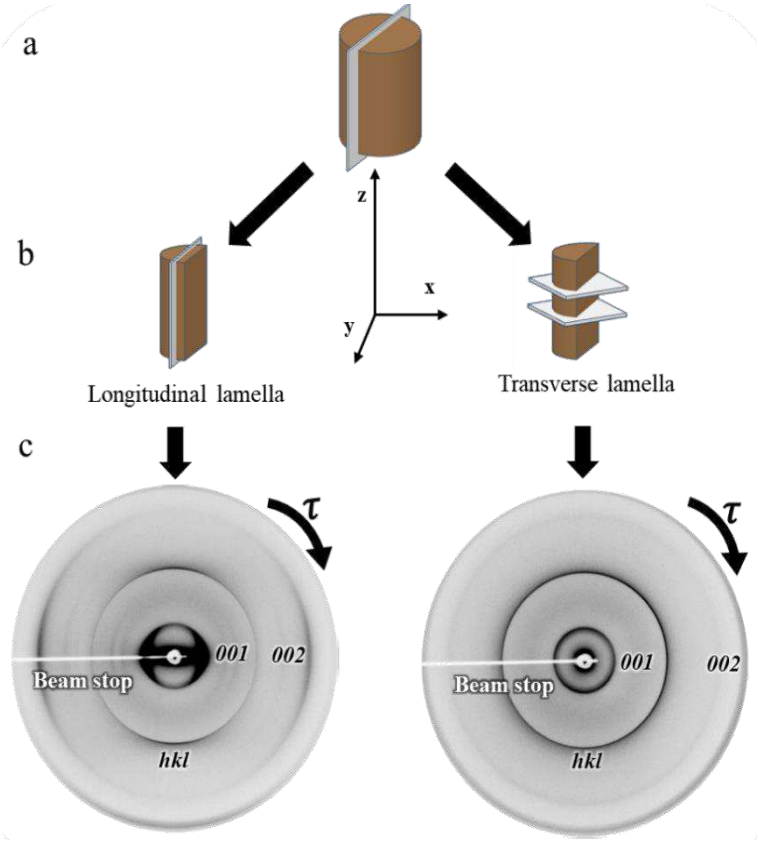


Fig. II.7. *Illustration of the longitudinal (a) and transversal (b) lamellas and their corresponding two-dimensional X-Ray Scattering (2D-XRS) diffractograms (c).*

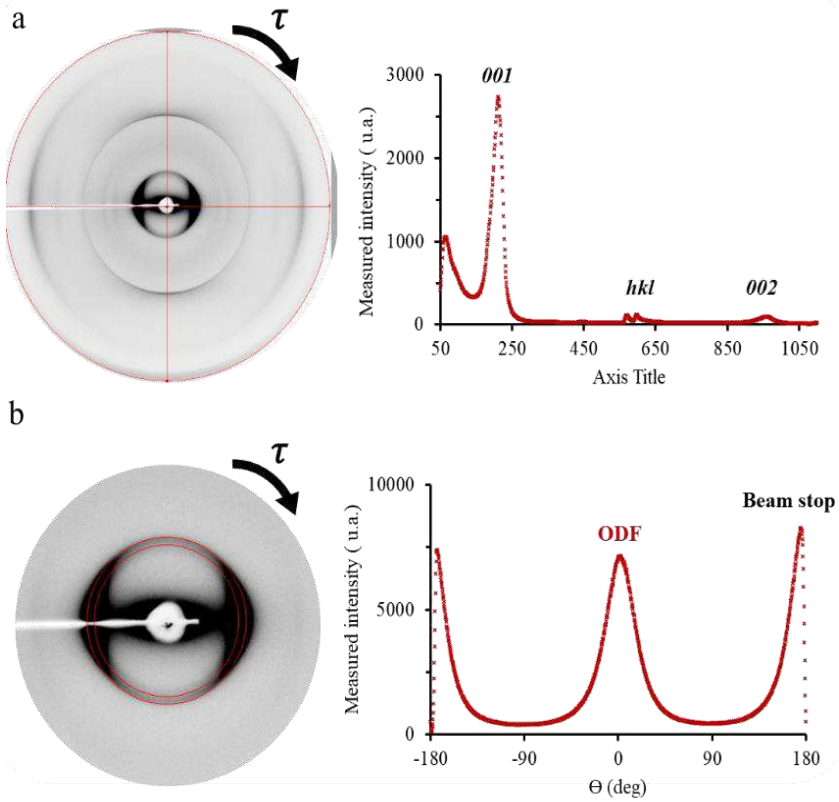


Fig. II.8. *Processing of the two-dimensional X-Ray Scattering (2D-XRS) diffractograms. (a) Full integration over the whole diffractogram to produce a 1D pattern of the Bragg peaks. (b) azimuthal integration scan of I as*

Fig. II.9a shows experimental 2D-XRS patterns for two vermiculite samples and their corresponding corrected ODFs in Fig. II.9b. In the pattern from the longitudinal lamella of the isotropic samples (Fig. II.9a, left), the *I* of the *00l* reflection in the form of a black ring indicates that the values of *I* are more or the same over all the angular range of the angle τ ($\tau = \theta$ for clay minerals). Similar *I* over the angular range of τ confirms that the particles inside the sample have no preferred orientation. Thus, the resulting ODF for this sample is approximately constant regardless of the θ angle (Fig. II.9b, left). By contrast, the pattern from the longitudinal lamella of the anisotropic sample (Fig. II.9a, right), the *I* of the *00l* reflection, has an ellipse shape. Such a shape reflects the anisotropy in the particle's preferred orientation in the sample, as most of the reflected *I* values come from specific τ angle values. So, the ODF for this sample displays a reversed bell-shaped curve in correspondence to this anisotropy (Fig. II.9b, right). For both samples, the ODFs of the transverse lamellas are isotropic, as expected for lamellas sliced in the direction parallel to the preferred orientation of the clay particles.

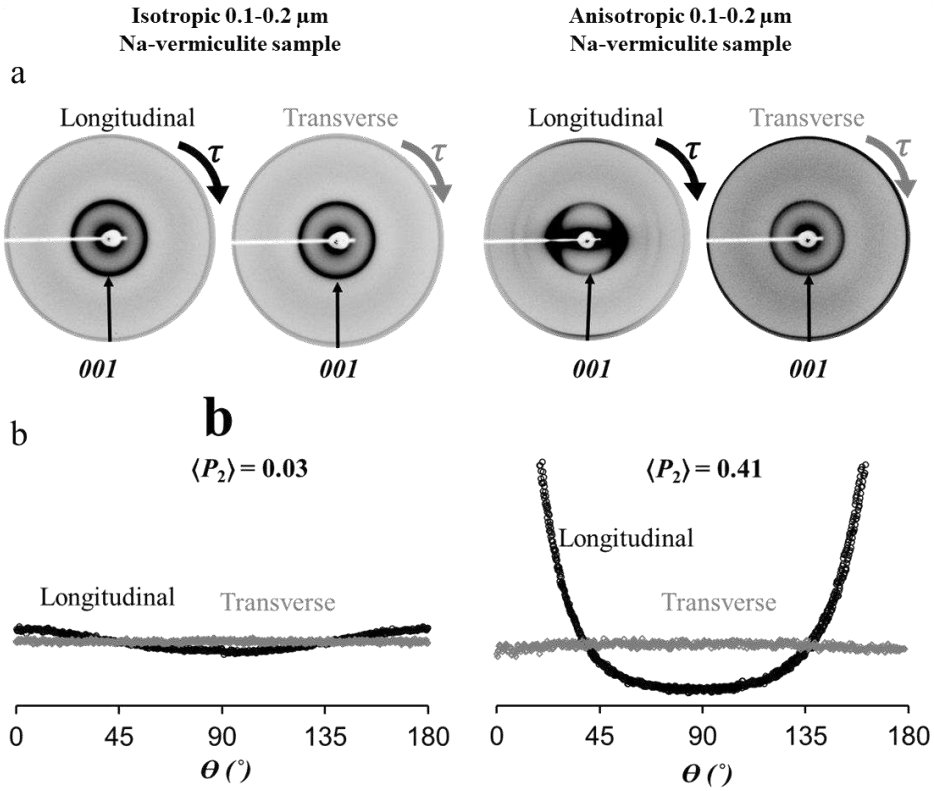


Fig. II.9. *Results from particle orientation measurements for Na-vermiculite samples. (a) 2D-patterns obtained by X-ray scattering technique from longitudinal and transverse lamellas (Fig.II.7b). Color scale ranges from light gray to black with increasing scattered intensity. (b) Orientation distribution functions (ODF) extracted from an azimuthal scan over 180° along the 001 reflection (Fig.II.8b) from longitudinal (black) and transverse (gray) lamellas. The intensities are normalized to the same value for comparison.*

II.4.4. Calculating the ⟨P2⟩ order parameter

The ODF $f(\theta)$ expressed in Eq. (II.5) can also be written with a second-order Legendre polynomial as follows:

$$\langle P_2 \rangle = \int_0^{\pi} \langle P_2 \rangle (cos\theta).f(\theta) sin(\theta) d\theta \quad \text{(II.6)}$$

From Eq. (II.6), the $\langle P_2 \rangle$ order parameter is defined; it is also referred to as the nematic order S (Dabat et al., 2018; Underwood and Bourg, 2020) or the Hermans parameter H (Hermans and Platzek, 1939). This parameter comprised 0 for an isotropic particle organization to 1 for a perfectly anisotropic organization when all particles had the same preferred orientation (i.e., bedding plane). For example, the $\langle P_2 \rangle$ value for the isotopic vermiculite sample is = 0.03 (Fig. II.9b, left), while a value of 0.41 is obtained for the anisotropic sample (Fig. II.9b, right). Finally, the reported $\langle P_2 \rangle$ values of the samples in this work are average values of several 2D-XRS patterns. Patterns were recorded from different spots in the same sample, to account for the possible heterogeneity in the particles' preferred orientation.

II.5. Experimental techniques used to measure diffusion in the clay porous media

II.5.1. Through-Diffusion (TD) experiment

TD experiments are widely used in literature to obtain the diffusion coefficient of a tracer in compacted porous media (i.e., Shackelford, 1991; Van Loon et al., 2003; Benning and Barnes, 2009; Savoye et al., 2012, see also the review of Bourg and Tournassat, (2015). The setup allows measuring the quantity (i.e., concentration) of a tracer/ species traversing a porous media in a direction parallel or perpendicular to the compression direction of the media. For the samples in this work, the setup was in the perpendicular configuration (i.e., perpendicular to the preferred orientation of the clay particles).

Our TD setup was used by Tertre et al., (2018) and Dabat, (2019) and was initially adopted from the one proposed by Van Loon et al., (2003). It consists of a diffusion cell (fig.II.10a) and a fluid circulation system (fig.II.10b). The diffusion cell contains two cover pistons and a sample tube (either in poly (methyl methacrylate, $C_5H_8O_2$) (PMMA), or in Polyether ether ketone (PEEK)). Inside the tube, the sample is sandwiched by a series of porous materials on each side to maintain its geometry and prevent fine particles from flowing into the aqueous circulation system. These porous materials are placed from the closest to the sample to the farther as follow: (i) cellulose membrane with a pore size of 0.1 µm, (ii) a stainless-steel filter

(pore diameter of 10 µm), and (iii) two PEEK grids (nominal spaces of 280 and 450 µm for mono filaments with diameters equal to 120 and 200 µm, respectively). The PEEK grids are used to homogenize the solution flow arriving at both sides of the sample, as suggested by Melkior, (2000). Before the TD experiment, the sample (in the diffusion cell) is saturated with *Milli-Q*® (MQ) water (~18.2 MΩ cm) by connecting the diffusion cell to the circulation system and maintain water circulation on each side of it for two weeks (Tertre et al., 2018).

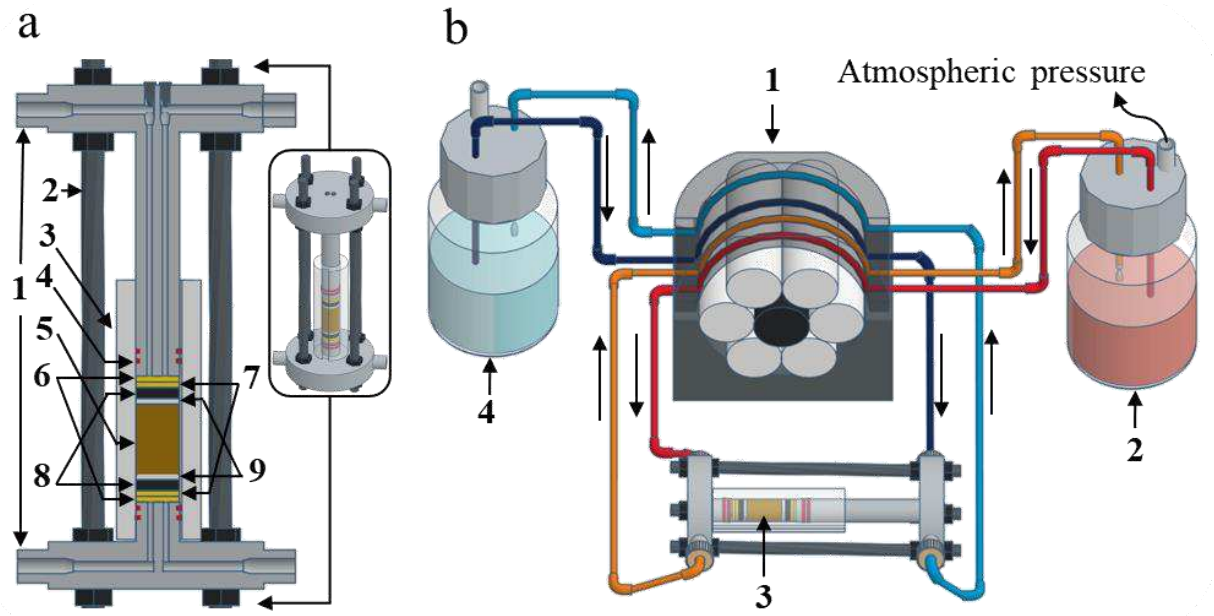


Fig. II.10. Illustration of the *through-diffusion* (TD) *setup.* ***(a)*** *Cross-section of the diffusion cell: (1) Cover pistons. (2) threaded rods and nuts. (3) Ploy methyl methacrylate (PMMA) tube. (4) sealing o rings. (5) clay sample. (6) Polyether ether ketone (PEEK) grid (nominal spaces of 450 µm for mono filaments with diameters equal to 200 µm). (7) PEEK grid (spaces of 280 µm for mono filaments with diameters equal to 120 µm). (8) stainless-steel filter (pore diameter of 10 µm). (9) cellulose membrane with a pore size of <0.1 µm.* ***(b)*** *TD setup: (1) peristaltic pump. (2) upstream reservoir. (3) clay sample. (4) downstream reservoir.*

The concept of our TD experiments is to create a salinity gradient of the chemical species between the upstream and the downstream reservoirs. This gradient results in a diffusion-driven transfer of these species from upstream to downstream through the porous medium. Understanding the effect of salinity gradient on the diffusion of water and solutes in porous clayey media is important because salinity gradient is frequently encountered in clay and clay-rich formations of interest for various applications. It occurs in glacier/ocean contact zones, coasts, and estuaries. And in the context of radioactive waste repositories, salinity gradient can

naturally exist as for the Bure site in the East Paris Basin -France, with salinities in some surrounding aquifer (Dogger) of 5 g L^{-1} compared to 1 g L^{-1} in the Callovo-Oxfordian formation considered for the burial of radioactive waste (Gonçalvès et al., 2004; Gueutin et al., 2007). Or it can (salinity gradient) be artificially induced when the nuclear waste packages are compromised, releasing large quantities of different salts, thus dramatically increasing the pore solutes salinity (Savoye et al., 2015). Thus, the upstream reservoir is filled with 50 mL of solution at a known species concentration using a high purity salt (i.e., Na^+ and Cl^- at 0.01 or 0.1 or 1M). In addition, to study water diffusion, the upstream reservoir is also spiked with deuterium oxide (HDO) at 0.55 M prepared by a dilution of Heavy-water (D_2O) solution (purity of 99.8 atom % D purchased from *Agros Organics*®). By contrast, the downstream reservoir contains ~ 50 mL of only MQ water.

After filling, the reservoirs are connected to the TD setup, and t=0 is set as the fluid circulation starts. Both reservoirs are regularly replaced with fresh ones (time step can vary between a few hours to a few days) to keep the gradient of tracer concentrations as constant as possible. Aliquots from the removed reservoirs are collected for ions/ HDO concentrations measurements.

Aqueous HDO, Na^+, and Cl^- concentrations were measured using water isotope analysis (LWIA DLT-100, *Los Gatos Research*), atomic absorption spectroscopy (*Varian AA240FS*), and liquid ion chromatography *(ICS 1000, Dionex)*, respectively. For HDO concentration measurement, water isotope analysis results are given as isotopic composition (δD) defined by the following relationship:

$$\delta D\ (‰) = 1000(\mathrm{R}/\mathrm{R_s} - 1) \qquad \text{(II.7)}$$

R and Rs are the isotopic ratios measured for the sample and a reference (VSMOW). R can be converted into an aqueous concentration of HDO (i.e., [HDO]) by the relationship:

$$[\mathrm{HDO}] = 111 \times \mathrm{R}/(1 - \mathrm{R}) \qquad \text{(II.8)}$$

With the assumptions that 1L of solution contains 111 moles of hydrogen atoms, and the density of the aqueous solution is 1 g cm^{-3}, considering the small amount of deuterium (<1 wt%) in solution. We considered the uncertainties on HDO measurements equal to 6% standard error as reported in Tertre et al., (2018). In addition, the existing natural concentrations of the tracers (i.e., HDO, Na^+, and Cl^-), potentially present in this saturation solution, were measured to correct the concentrations of the diffused tracer's traversing the samples.

The flux of the tracers can be derived from the measured concentrations in the downstream reservoirs by resolving the classical Fick's second law for one-dimensional transport:

$$\frac{\partial C}{\partial t} = \frac{D_e}{\alpha} \cdot \frac{\partial^2 C}{\partial x^2} = \frac{D_e}{\varepsilon + \rho_{\text{app}}\, K_{\text{d}}} \frac{\delta^2 C}{\partial x^2} \quad \text{(II.9)}$$

where C is the aqueous concentration (mol m^{-3}), t is the time (s), De is the effective diffusion coefficient (m^2 s^{-1}), K_d is the distribution coefficient (m^3 kg^{-1}), ρ_{app} is the bulk dry density (kg m^{-3}), and α the rock capacity factor (-). For water tracer, if no adsorption occurs, α it is equal to ε. Otherwise, α it could be greater (see section II.3 for details).

Eq. II.9 was resolved by considering the following boundary conditions:

$$C\,(x, t) = 0 \text{ for } t = 0 \quad \text{(II.10)}$$

$$C\,(x, t) = C_o \text{ at } x = 0 \text{ for } t > 0 \quad \text{(II.11)}$$

$$C\,(x, t) = 0 \text{ at } x = L \text{ for } t > 0 \quad \text{(II.12)}$$

With C_o is the HDO concentration in the upstream reservoir (mol m^{-3}) corrected from the natural concentration of HDO present in ultra-pure water, and L is the thickness of the clay sample (m).

As mentioned earlier, both upstream and downstream reservoirs are regularly replaced with fresh ones during TD experiments. By doing so, concentration measurements of the removed reservoirs showed that:

1. The decrease in tracers' concentrations in the upstream reservoirs was less than 3%.
2. The concentrations of the diffused tracers in the downstream reservoirs were always less than 1% of that of the upstream reservoirs.

Maintaining tracers' concentrations in both reservoirs within these limits is necessary to validate the hypothesis of a constant gradient of tracers during TD experiment. Such a hypothesis is essential for the above boundary conditions used to extract diffusion parameters.

Considering the above conditions, the flux of tracers diffused to the downstream reservoir (i.e., $J(x=L,t)$ in mol s^{-1}) can be calculated by the equation (II.13) from Crank, (1975) derived from Eq. (II.9):

$$J(x = L, t) = \frac{SC_0 D_e}{L}\left(1 + 2\sum_{n=1}^{\infty}(-1)^n \exp\left(\frac{-D_e n^2 \pi^2 t}{\alpha L^2}\right)\right) \quad \text{(II.13)}$$

with S is the cross-sectional area perpendicular to the diffusive direction (m^2). Hence, the cumulative tracer quantity in the downstream reservoir (i.e., n ($x=L$, t) in mol) can be described as follows:

$$n(x = L, t) = SC_O L\left(\frac{D_e}{L^2}t - \frac{\alpha}{6} - \frac{2\alpha}{\pi^2}\sum_{n=1}^{\infty}\frac{(-1)^n}{n^2}\exp\left(-\frac{D_e n^2 \pi^2}{L^2}t\right)\right) \quad \text{(II.14)}$$

The tracer diffusion through the metallic porous media must be taken into account not to underestimate the tracer' *De*, as indicated by Glaus et al., (2007); González Sánchez et al., (2008b). This correction is valid for the stationary state of the trace' flux and calculated by using the following formula from Melkior et al., (2009):

$$De = \frac{L\,F_{SS}}{C_0 - 2F_{SS}\frac{f}{\phi_F \varepsilon D_0}} \quad \text{(II.15)}$$

where F_{ss} is the value of the flux in the stationary state (mol s m^{-2}), f is the thickness of the porous media, and ϕ_F is the formation factor of the metallic porous media.

In addition, the D_0 values used here are corrected from salinity as in Mills and Lobo, (1989). Finally, TD experiments are performed in a climate-controlled room under temperatures ranging between 19-20 ˚C. For this, a temperature correction is applied to have *De* at 21˚C or 25˚C, as commonly reported in the literature. For example, the Stokes-Einstein relationship is used to calculate *De* at 21˚C as performed in Savoye et al., (2011):

$$D_e^{21^\circ C} = \frac{D_e^{initial}\,\eta_{initial}}{T_{initial}} \times \frac{T_{21^\circ C}}{\eta_{21^\circ C}} \quad \text{(II.16)}$$

With $\eta_{21^\circ C}$ the water viscosity at 21˚C (Pa s), and $\eta_{initial}$ is the water viscosity at the temperature at which the diffusion experiment was performed.

II.5.2. ^{1}H NMR pulsed Gradient Spin Echo experiments

On one occasion in this work, the Pulsed Gradient Spin Echo attenuation measurement by Nuclear Magnetic Resonance (PGSE-NMR) analyses was performed at the ICMN laboratory (Orléans, France) on a Na-kaolinite compacted sample. In volume-constrained PEEK tubes, the dried Na-kaolinite samples were first water-saturated by capillary imbibition; the bottom part of the sample was put in contact with deionized water. At the same time, the other side of the tube was connected to a primary vacuum pump to favor water migration and gentle evacuation of air from the pore network. The NMR measurements were performed using the same setup and experimental conditions as in Dabat et al., (2018); Porion et al., (2018) on a *Bruker® DSX100* spectrometer. This instrument operates with a static magnetic field of 2.35 T and is equipped with a saddle detection coil and a micro-imaging probe (*Micro5 Bruker*) with gradient coils to generate magnetic field gradients in three perpendicular directions. The macroscopic water mobility along any pre-selected direction within the sample was determined based on ^{1}H PGSE-NMR attenuation measurements (Stejskal and Tanner, 1965; Cotts et al.,

1989; Callaghan, 1993) by using the pulse sequence illustrated in Fig. II.11. The largest wave vector (q_{MAX}) associated with these attenuation measurements is defined as $q_{MAX} = \frac{\gamma.\delta.G_{MAX}}{\pi} =$ 6.81 10^4 m^{-1}, where γ is the proton gyromagnetic ratio (2.6752 10^8 read/s for ^1H), δ is the duration of each applied field gradient (i.e., 0.5 ms) (see Fig. II.11), and G_{MAX} is the largest applied field gradient (i.e., 1.6 Tesla m^{-1}). Accordingly, the spatial length over which the water dynamics are investigated is larger than 15 µm. For these experiments, the diffusion time (Δ) and the delay (τ) were set to 20 ms and 760 µs, respectively (Fig. II.11). The attenuation of the intensity of the NMR echo $I(q)/I(0)$ evolves according to a Gaussian relationship from which the components of the self-diffusion tensor are easily extracted (Cotts et al., 1989; Callaghan, 1993):

$$\frac{I(q)}{I(0)} = exp\left[-4\,\pi^2\,q^2\,\overrightarrow{e_g}^T\,\overleftrightarrow{Dp}\,\overrightarrow{e_g}\,(\Delta + 3\tau/2 - \delta/6)\right] \qquad \text{(II.17)}$$

where $\overrightarrow{e_g}$ is the direction of the applied field gradient, and $\overleftrightarrow{Dp}$ is the self-diffusion tensor. The pulsed gradients were applied along six non-collinear directions (Basser et al., 1994; Skare et al., 2000) noted $\overrightarrow{e_1} = \overrightarrow{e_x} = (1,0,0)$, $\overrightarrow{e_2} = \overrightarrow{e_y} = (0,1,0)$, $\overrightarrow{e_3} = \overrightarrow{e_z} = (0,0,1)$, $\overrightarrow{e_4} = \left(1/\sqrt{2}, 1/\sqrt{2}, 0\right)$, $\overrightarrow{e_5} = \left(0, 1/\sqrt{2}, 1/\sqrt{2}\right)$ and $\overrightarrow{e_6} = \left(1/\sqrt{2}, 0, 1/\sqrt{2}\right)$, respectively, with the direction $\overrightarrow{e_3}$ being parallel to the compaction/centrifugation axis of the clay sample.

From the six corresponding components of the water self-diffusion tensor, one can easily extract its three principal axes and the corresponding eigenvalues that describe the water mobility in the longitudinal or transverse direction of the tube axis. The PGSE-NMR attenuation measurements were performed at ~ 19°C (i.e., 292 K), and the associated experimental bulk water self-diffusion coefficient D_0 was measured at 2.0 ± 0.5.10^{-9} m^2 s^{-1} in these conditions

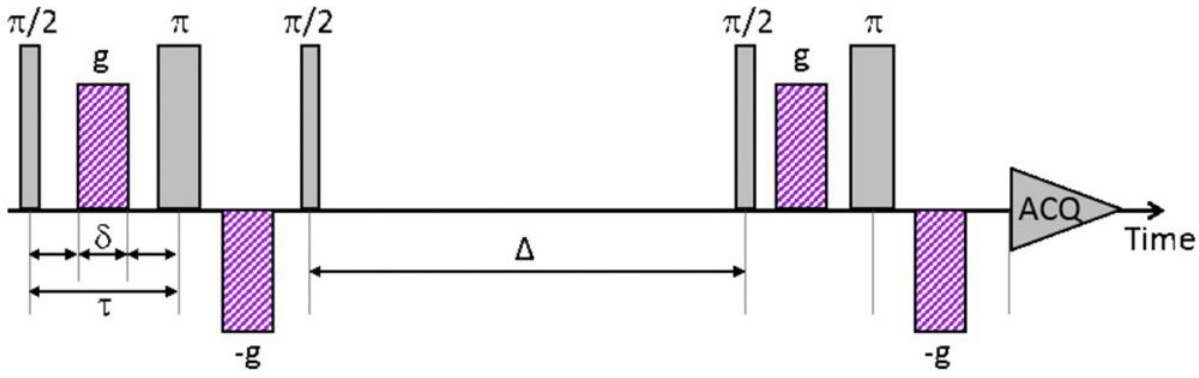


Fig. II.11. *Pulse sequence used to perform Pulsed Gradient Spin Echo (PGSE-NMR) attenuation measurements in Na-kaolinite samples.*

Chapter III

Mineralogical and morphological characterization of different size fractions of Illite du Puy

Illite du Puy (IDP) is a naturally occurring material used after purification and Na-saturation in several experiments of sorption/diffusion of cations/water tracers (Tessier, 1984; Bardot et al., 1998; Poinssot et al., 1999; Rajec, 1999; González Sánchez et al., 2008c; Bradbury and Baeyens, 2009; Diaz, 2009; Glaus et al., 2010; Altmann et al., 2015; Rajyaguru, 2018). These studies considered purified Na-IDP as an analogous clay model, where the analysis of solutes' transport properties is used to understand better this process in more complex natural systems (i.e., Argillite) used to host nuclear waste disposal facilities. However, the reported composition and Physio-chemical properties of bulk or purified Na-IDP vary between these different studies. Although purification procedures vary between different studies, this variation hints at a potential difference in the initial bulk material.

For these reasons, we decided to conduct a baseline study of IDP samples' mineralogical and morphological properties from three sources corresponding to different projects or publications in the literature. In addition, further analyses of morphological and Physio-chemical properties of the sample used for diffusion experiments in this work were performed.

This chapter includes the results of the analyses mentioned above in the form of a draft publication. This draft is under review by the co-authors. For this reason, their names are not included in this text until their approval.

A baseline study of mineralogical and morphological properties of different size fractions of illite du Puy

A. Asaad et al.

* E-mail addresses of the corresponding authors:

A. Asaad: ali.asaad@univ-poitiers.fr

Highlights

- Providing a baseline study of illite du Puy used in EURAD project.
- Geological setting responsible for mineralogical variability in the literature.
- Particles in the sub-fractions display similar crystal chemistry and aspect ratios.
- The grain density of illite du Puy particles was revisited and refined.

Abstract

The objective of this study is to revisit the mineralogical and Physio-chemical properties of illite du Puy material (Puy-en-Velay, France) envisaged as a model clay system in the European Joint Programme on Radioactive Waste Management (EURAD) project. This illite material is compared to the raw illitic one commonly extracted from the Velay ore site. Both materials were separated into different sub-fractions (i.e., <0.05, 0.05-0.1, 0.1-0.2, and 0.2-2 µm) to examine the mineralogical heterogeneity. The X-ray diffraction bulk analyses indicated that the observed variability in the literature in terms of the nature of accessory minerals and the presence of kaolinite was directly related to the geological sampling. At the same time, the conversion yields of different sub-fractions were similar for the two materials.

Further analyses were performed on the sub-fractions of illite used for the EURAD project utilizing a suite of different techniques. The clay mineralogy was refined into an illite-smectite mixed-layer mineral with a meagre amount (<5%) of smectite layers. No significant changes in crystal chemistry or particle lamellarity were observed between the different sub-fractions. However, the different sub-fractions display a wide range of specific surface areas, increasing by a factor 3 and ~5 of N_2 total surface area and cation exchange capacity values between the 0.2-2 µm and <0.05 µm size fractions, respectively. The EURAD illite and associated sub-fractions can be considered good material models to refine our understanding of solutes' adsorption and diffusion processes in porous media made from charged clay particles.

Introduction

For the past two decades, purified and conditioned illite du Puy (IDP) has been considered an analogous clay model of hosting clayey rocks (i.e., argillite) in nuclear waste disposal facilities. Numerous studies have focused on sorption/diffusion cations/water tracers in this material such as (Tessier, 1984; Bardot et al., 1998; Poinssot et al., 1999; Rajec, 1999; González Sánchez et al., 2008c; Bradbury and Baeyens, 2009; Diaz, 2009; Glaus et al., 2010; Altmann et al., 2015; Rajyaguru, 2018). In these works, physio-chemical properties of IDP, i.e., mineralogical composition, cation exchange capacities (CEC), specific surface area, and geometrical properties of IDP particles (the relative amount of lateral and basal surfaces) from (Bardot et al., 1998; Poinssot et al., 1999; Rajec, 1999; Hassan et al., 2005) represented key input parameters for interpretation of anionic exclusion and sorption reactions for solutes (e.g., (Bradbury and Baeyens, 2005, 2009; Rabung et al., 2005; González Sánchez et al., 2008c; Glaus et al., 2010, 2015; Altmann et al., 2015; Chagneau et al., 2015). Despite the large number of studies devoted to IDP, significant differences in the composition and thus reactive properties of this material can be pointed out in the literature. For example, Poinssot et al., (1999) reported the presence of kaolinite at ~5% and 7% in the raw and purified Na^+-saturated IDP, respectively, based on X-ray diffraction (XRD) and Fourier transform infrared spectrometry (FTIR). Contrastingly, Bradbury and Baeyens, (2009) and Altmann et al., (2015) reported a composition of the Na^+-saturated IDP of 88 wt.% illite and 12 wt.% sanidine (K-feldspar) also deduced from XRD measurements. Even though a part of the reported variations of CEC and specific surface area can be induced by the differences in the process used to purify the raw material (e.g., size separation and removal of accessory minerals), another origin may arise from contrasted mineralogical properties in the raw material, and it is linked to the geological setting and sampling strategy.

IDP originates from the Velay basin, Oligocene lacustrine sediments of about thirty kilometers in length located at le Puy-en-Velay (Haute-Loire) in the massif central region in France. The first mineralogical study of the Velay basin was carried out by Gabis, (1963) who divided the central area of the basin- rich in illite sediment- into three series: upper, lower, and medium series (30-80 m thick). According to Gabis, (1963), deposits from these series are predominately composed of ferruginous illite resulted from the illitization of detrital montmorillonite in alkaline lakes. In addition to illite, associated clay minerals may include (i) kaolinite in a proportion up to ~20% (Gabis, 1963), which decreases upward in the series and diminishes in the upper portion, (ii) illite/smectite mixed-layer minerals with a minor

smectite content (~20 to 30 %; Altmann et al., 2015), (iii) smectite which is mainly present in the upper portion. Other non-clay accessory minerals include potassic feldspars (mainly sanidine; Bradbury and Baeyens, 2009), carbonates, and quartz with varying proportions from 0 to 40%. In addition to their presence in the clayey levels, carbonates form banks of grey marl and calcite streaks intercalating with the clay-rich levels. Some of the clay-rich levels in the medium series exhibit remarkable mineralogy solely composed of illite. Although illite is still the dominant mineral through the stratigraphic profile, the other associated minerals in IDP material may significantly vary with the location and sampling strategy in the field.

In the context of nuclear waste disposal facilities, owing to the variability of the geological setting of IDP, particular attention has to be paid to the material sampling and the associated characterization before analysing the sorption and diffusion properties of water and pollutant tracers in this material. In the framework of the European Joint Programme on Radioactive Waste Management (EURAD, 2019-2024), a large set of studies involving adsorption and diffusion measurement of a large set of tracers using the same IDP raw material stresses for the need of a baseline analysis of IDP mineralogical and Physio-chemical properties. Hence, this study aims to (i) unravel the differences in mineralogy between IDP material used in EURAD and typical sampling in Velay ore used in previous works. And then (ii) to determine the mineralogy, crystal chemistry, and geometric characteristics of the IDP particles used in the current EURAD project as an analogous illite model. An initial quantitative mineralogical analysis of both IDP raw materials from the EURAD project and the Velay will be performed for these purposes. After the initial analysis, the materials will be purified and size-fractionated (i.e., <0.05, 0.05-0.1, 0.1-0.2, and 0.2-2 µm) to highlight the mineralogical heterogeneity in the different fractions. After a mineralogical comparison between the two IDP samples, a detailed characterization focusing on the different sub-fractions of the IDP sample used in the EURAD project will be provided, including (i) clay structure identification and smectite quantification by profile modelling of XRD 00ℓ reflections, (ii) structural formula and grain density calculations based on microchemical analysis by Scanning Electron Microscope (SEM) equipped with Energy Dispersive X-ray Spectrometer (EDX), (iii) specific surface area measurements and associated geometrical features of particles from low-pressure N_2/Ar adsorption at 77 K and (iv) CEC measurements from K^+-saturated samples. The results from this work will be compared to the literature data to establish a baseline source of Physio-chemical data of interest for using IDP as a model material to expand our understanding of the transport properties of solutes in the context of nuclear waste disposal facilities.

III.1. Materials and Methods

III.1.1. Illite du Puy materials

Three raw IDP samples were considered for this study, all originating from Oligocene lacustrine sediments in le Puy-en-Velay (Haute-Loire, France). The Argile du Velay company (www.argileduvelay.com) provided the first IDP sample collected from the clay ore during industrial sampling. The second IDP sample was provided by the Paul Scherrer Institute (PSI, Villigen, Switzerland) from its sampling campaign and corresponded to the reference illite used in the Cat-Clay European project (Bradbury and Baeyens, 2009; Glaus et al., 2010, 2015; Altmann et al., 2015) and the ongoing European Join Project EURAD. The third IDP material was provided by the Commissariat à l'énergie atomique (CEA, Université Paris-Saclay, France) from their sampling campaign, which was used in the previous works of Poinssot et al., (1999) and González Sánchez et al., (2008). However, different mineralogical analyses on the last sample revealed a similar composition to the Velay IDP (data not shown). Consequently, only Velay IDP will be presented here, and existing data on the CEA sample will be used for comparison.

For sample homogenization before bulk mineral quantification using X-ray diffraction (XRD) on randomly oriented powder, Velay and EURAD IDP samples (referred to as V-IDP and E-IDP materials, respectively) were gently crushed in an agate mortar and dry sieved at 50 µm.

The raw IDP samples were first washed with hydrochloric acid (pH=1, room temperature) to remove carbonate and sparingly soluble minerals for other analyses. Carbonate dissolution was considered finished when the pH of clay/acid suspension reached 5.5. Confirmation of complete removal of carbonates was obtained by recording XRD patterns (not shown) of the decarbonated material. The <50 µm of the decarbonated IDP was obtained by wet sieving, after several cycles of centrifugation with distilled water to remove the remaining acidic solution. Then, Na^+ saturation of IDP samples was achieved by three saturation cycles with a 1M NaCl solution, followed by removing excess salt by dialysis using a 6-8 KD membrane until the test with silver nitrate was negative.

Different size fractions were obtained from the dispersion of the Na+-saturated IDP samples by adapting the protocol of sequential fractionation developed by Reinholdt et al., (2013). The <2 µm fraction was first separated using a Thermo Scientific legend XFR centrifuge from Fisher scientific®. Then, 5 g of <2 µm IDP were divided between 6 centrifugation tubes (38.5 mL polypropylene tubes), dispersed in Milli-Q® pure water by

sonication, and centrifuged using Avanti J 301 centrifuge (swinging bucket rotor JS-24.38) from Beckman Coulter®. The sequential fractionation process started with the finest fraction (i.e., <0.05 µm), and five centrifugation cycles were performed until the supernatant became clear. Then, extractions of the coarser size fractions (0.05-0.1 and 0.1-0.2 µm) were performed using the same steps until the IDP material remaining in the tubes corresponds to the 0.2-2 µm fraction. Three aliquots of dispersion (1 mL) from each fraction were dried at ambient humidity and weighted to calculate the conversion yields. Centrifugation parameters and the yield of each fraction are reported in Table III.1.

After size separation, the resulting dispersion for each fraction was divided into three portions. Two were saturated with Ca^{2+} and K^{+} for XRD and CEC measurements, respectively, following the same procedure described above for saturation with Na^{+}. The Ca^{2+} and K^{+}-saturated IDP samples were stored in suspension at 4˚C. The last portion, corresponding to remaining Na^{+}-saturated dispersions, was lyophilized for gas adsorption measurements as described in section III.1.5.

Table III.1. Centrifuging parameters were used for size fractioning of the Velay and EURAD illite du Puy (V-IDP and E-IDP, respectively) with the relative mass contribution of each fraction.

Fraction (µm)	Time (min)	Speed (rpm)	Acceleration (g)	% Conversion	
				V-IDP	E-IDP
<0.05	20	20000	72128	19.5	18.2
0.05-0.1	15	12500	28175	23.8	20.1
0.1-0.2	14	6500	7619	22.1	21.7
0.2-2	-	-	-	22.0	28.6
<2	3	1000	-	-	-
2-50	-	-	-	6.0	6.5
			Total Yield %	93.4	95.1

III.1.2. Bulk mineral quantification using XRD refinement on randomly oriented powders

Considering the challenges of producing randomly oriented mounts of fine and homogenous particles, The XRD mounts for V-IDP and E-IDP bulk materials were prepared by filling the samples holder using the side-loading technique as in Kleeberg et al., (2008). Acquisition of XRD patterns of these samples was performed with a Bruker D8 advanced in Bragg-Brentano geometry using a copper source with CuKα_{1+2} wavelength and with an LYNXEYE detector for a step size of 0.02°2θ step over the 2−65 °2θ CuKα angular range. Analytical conditions were a voltage of 40 kV and an intensity of 40 mA. Crystalline phases quantification was carried out using the open-source Rietveld refinement program BGMN interfaced with Profex (Doebelin and Kleeberg, 2015). In both refinements, illite was modelled using a combination of both disordered and ordered 1M polytypes with a chemical composition matching the structural formula reported in the present study. The presence of K-feldspars was modelled considering a mixture of sanidine and microcline (Gabis, 1963; Bradbury and Baeyens, 2009). Other minerals included: Na-rich plagioclase (oligoclase; Gabis, 1963), calcite, trace amounts of quartz, anatase, and apatite. The R_{wp} goodness of fit parameter was used for the refinement (Howard and Preston, 1989).

III.1.3. Quantification of clay mineralogy using profile modelling of XRD 00ℓ reflections

The clay phases' characterization in the different E-IDP fractions was obtained from XRD analysis of oriented clay mounts. An aliquot of the Ca^{2+}-saturated clay dispersion was dropped onto a glass slide and dried at room temperature. The XRD patterns were recorded using a Panalytical X'Pert Pro MPD diffractometer equipped with an X'Celerator detector operating with an angular aperture of 1.021°. The scanning parameters included a step size of 0.033°2θ and 6 s for the counting time per step throughout the 2-50°2θ CuKα_{1+2} angular range. The divergence slit, the anti-scatter slit, and the two Soller slits were 0.125°, 0.25°, 2.3°, and 2.3°, respectively. For all samples, XRD patterns were recorded in air-dried (AD) conditions and after ethylene-glycol (EG) saturation by exposition of the clay mounts in EG atmosphere at 40°C for 24 h.

The algorithms developed initially by Sakharov and co-workers were used to model the 00ℓ reflections for the 2–50°2θ CuKα range using a trial-and-error approach (Sakharov et al., 1982a, 1982b, 1983). Instrumental and experimental factors, such as horizontal and vertical beam divergences, goniometer radius, and length and thickness of the oriented slides, were

measured and introduced without further adjustment. The mass absorption coefficient was set to 45 cm^2/g (Moore and Reynolds, 1997). For each XRD pattern, a single illite-smectite interstratified structure was used. Structural parameters, such as the proportion of illite layers, layer-to-layer (LLT) distance of illite layers, and the coherent scattering domain size (CSDS) along the c* axis, characterized by a lognormal distribution around a variable mean value (N) and a maximum CSDS value set to 80 layers (Drits, 1997), were adjusted to fit the experimental XRD patterns. The z-coordinates for all atoms within the 2:1 layer framework were set as proposed by Moore and Reynolds (Moore and Reynolds, 1997). The chemical composition was introduced according to the IDP structural formula reported in this work. The interlayer configuration of smectite was systematically constituted by 2 layers of water or EG molecules in AD (LLT=15 Å) and EG conditions (LLT=16.9 Å), respectively.

III.1.4. Microchemical analysis by electron microscopy

Microchemical analysis was performed on compressed pellets of clay powders from E-IDP sub-fractions using a JEOL JSM IT500 Scanning Electron Microscope (SEM) equipped with a Bruker Lynxeye Energy Dispersive X-ray Spectrometer (EDX) with an XFlash 4030 Silicon drift detector. The acquisition parameters for quantitative EDX analysis were as follows: acceleration voltage 15 kV, current beam 1 nA, counting time 50 s, working distance 11 mm, and analytical area of ~ 2 µm. The quality of the EDX quantitative analysis was confirmed by a series of standards, consisted of albite (Na, Al, Si), almandine (Mg, Fe), diopside (Ca), orthoclase (K), and spessartite (Mn). Matrix corrections were performed using the integrated program PhiRhoz correction. The reproducibility of the standard analyses was 1.5% for all chemical elements, except Na, for which the reproducibility was 3%.

III.1.5. Low-pressure nitrogen and argon adsorption at 77 K

Low pressure nitrogen (N_2) and argon (Ar) adsorption measurements on E-IDP fractions were performed at LIEC (Laboratoire Interdisciplinaire des Environnements Continentaux) Nancy-France. Adsorption isotherms were recorded with a customized quasi-equilibrium volumetric system using the continuous volumetry method at 77 K. A detailed description of the acquisition method, and experimental setup can be found in (Michot et al., 1990; Villieras et al., 1997; BARDOT, 1998).

Before adsorption measurements, E-IDP size fractions were flash-frozen by immersion in slush nitrogen (SN_2) for 2-5 minutes and dried by lyophilization at – 40°C. All samples were first outgassed at a 10-5 Pa residual pressure for at least 12 hours at 110°C to remove impurities

on the surfaces. Isotherms were recorded by slowly introducing adsorbate gaseous at a constant flow rate into the samples' cells. This method ensures quasi-equilibrium conditions for a wide range of pressures. The use of two probe molecules such as argon and nitrogen, and the capacity of the experimental setup to record around 3000 adsorption points (i) allows for cross-validation of the overall surface area of the particles while (ii) giving access to morphological properties of the clay particles such as the area of basal/lateral surfaces and the aspect ratio (the ratio between the particle's thickness and their diameter).

The experimental adsorption isotherms were analyzed by the Derivative Isotherm Summation (DIS) procedures introduced by Villieras et al., (1992) and later improved in Villieras et al., (1997) and Bardot et al., (1998). This procedure allows studying the energetic surface heterogeneity in highly heterogeneous materials such as clay particles. DIS is performed by fitting the experimental derivative isotherm with local theoretical ones corresponding to different adsorption energy domains (basal and lateral faces). Each local derivative isotherm is defined by three parameters (Bardot, 1998): the interaction energy between the solid and the adsorbed molecule (C) deduced from the peak position of ($\ln P/P_0$), the lateral interaction between two adjacent gas molecules (ω), and the monolayer capacity (V_m) of the domain which can be used to calculate the surface area by taking into account a cross-sectional area of 13.8 $Å^2$ and 16.2 $Å^2$ for the argon and nitrogen molecules, respectively.

Mean particles thickness (h) and basal diameter (l) reported in Table III.4 were calculated considering IDP particles as regular hexagonal plates using the equations reported in Hassan et al., (2005):

$$h = \frac{2}{\rho \times BSA} \quad \text{(III.1)}$$

$$l = \frac{8}{\sqrt{3} \times \rho \times LSA} \quad \text{(III.2)}$$

BSA and LSA are the basal and lateral surface areas from low-pressure Ar measurements, respectively. ρ is the grain density of E-IDP particles of Na^+-saturated E-IDP and calculated for the different sub-fractions using structural formulas and crystal structure parameters derived from XRD structural refinements.

III.1.6. Cation exchange capacity (CEC) measurements

The CEC measurements for E-IDP fractions were achieved by exchanging K^+-saturated E-IDP with Sr^{2+}. These cations were chosen after unsuccessful attempts using size fractions of Na^+-saturated forms of E-IDP exchanged by Ca^{2+} at neutral pH. Contrary to what was expected, the results showed a decrease in CEC with decreasing size fraction. Such behavior was attributed to the difficulty of saturating IDP particles' edges with Na^+ cation at neutral pH because of the high selectivity of H^+ over Na^+ for these types of sites (Tertre et al., 2011b, 2011a). Thus, and to ensure sufficient saturation of edge sites, variable air-dried masses of K^+-saturated samples (from 30 mg for the finest size fraction to ~100 mg for the coarsest one) were dispersed in 100 mL of 1 M $SrCl_2$ prepared with Milli-Q® pure water (18 MΩ·cm). The dispersions were placed in a mechanical agitator and allowed to react for one week. The clay slurry was then retrieved by centrifugation at 34000 g for 30 min (Centrifuge Avanti J 301, rotor JLA-16.250 from Beckman Coulter®) to ensure no fine particles were left in the supernatant. The excess of salt was removed from the clay slurry by dialysis in Milli-Q® pure water using a 6-8 KD membrane until the test with silver nitrate was negative, then it was dried at 60°C to determine the dry clay mass. The aqueous K^+ concentrations in the collected supernatants were measured by atomic absorption spectroscopy (AAS, Varian AA240FS). For analysis, the supernatants were diluted with 2% HNO_3, and Cs NO_3 at 2 g/L was added to account for possible interference during acquisitions. Measured K^+ concentrations ranged between 1-3 mg/L, which fall in the linear absorption range of K^+ in this device (between 0 to 5 mg/L).

The CEC was measured for all size fractions except the 2-50 µm because of insufficient materials. However, for this fraction, CEC is expected to be low in comparison to other size fractions as most of the accessory minerals (feldspars and quartz) are concentrated in this size fraction.

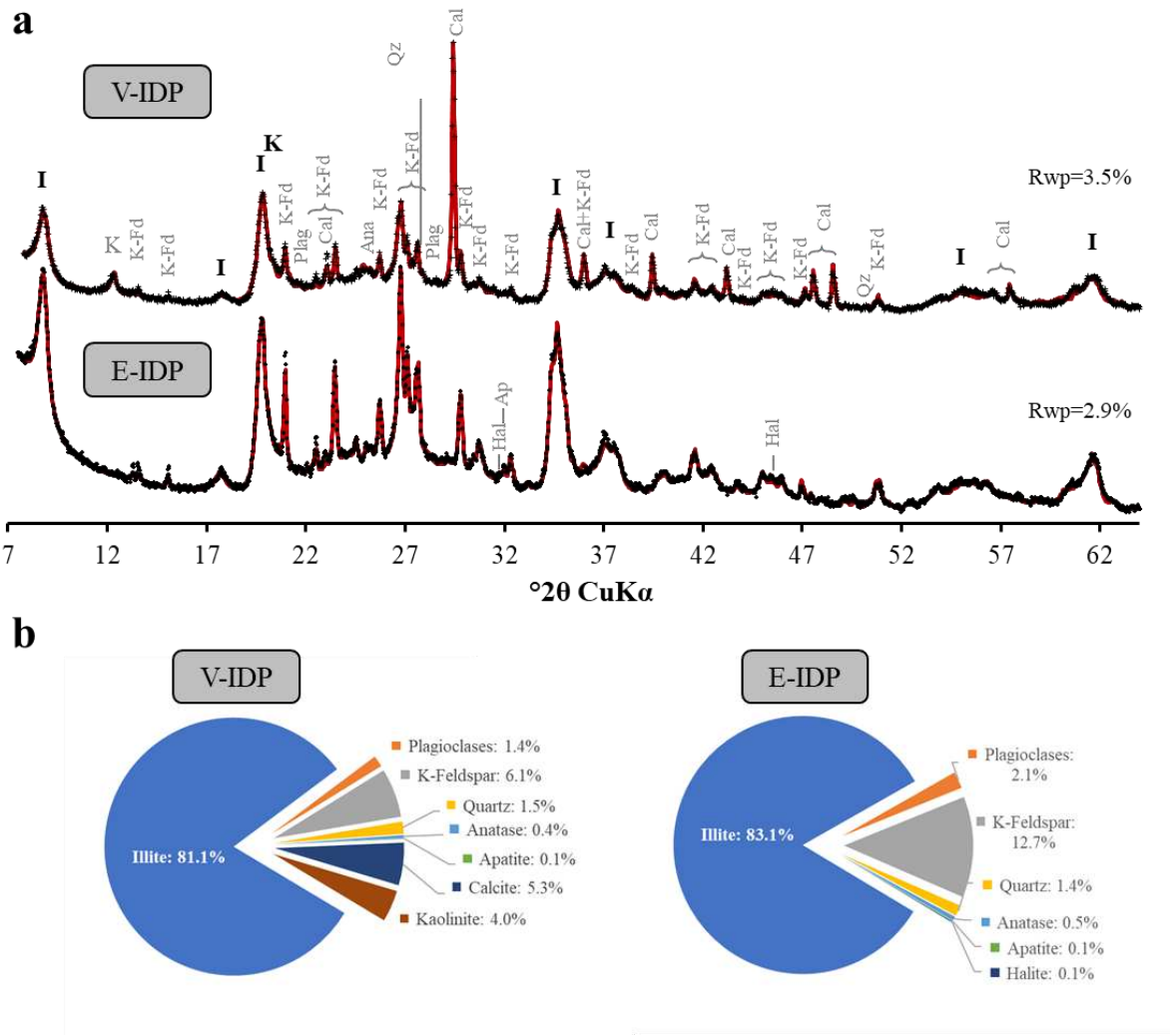


***Fig.III.1**. (a) Experimental X-ray diffraction patterns (black crosses) of randomly oriented Na^+-saturated bulk powders of Velay illite du Puy (V-IDP) and EURAD illite du Puy (E-IDP) together with calculated patterns obtained by BGMN Rietveld refinement (red solid lines). (b) Quantitative mineralogical composition (in wt. %) for the two types of samples as determined from Rietveld refinement with I: illite, K: kaolinite, K-Fd: potassium feldspar, Plag: plagioclase, Qz: quartz, Cal: calcite, Hal: halite, Ap: apatite, and Ana: anatase.*

III.2. Results and discussion

III.2.1. Mineralogy comparison between V-IDP and E-IDP raw materials

Fig.III.1a shows a comparison between XRD patterns from randomly oriented powders of raw V-IDP and E-IDP materials. Both XRD patterns exhibit typical reflections of illite and K-feldspars, while the V-IDP presents in addition reflections for kaolinite and calcite. Full pattern Rietveld refinement (Fig.III.1b) shows that the raw E-IDP sample is mainly composed

of 1M illite polytype (~83%), with ~15% of feldspars (plagioclase, sanidine, and microcline). The sample also contains small quantities of quartz with the addition of anatase, halite, and apatite of <1% each. The raw V-IDP samples are also dominated by 1M illite (~81%), with a small quantity of quartz, anatase, and apatite. The main differences with the raw E-IDP sample are a lower content of feldspars (7.5%) and significant contributions of calcite and kaolinite, with ~5 and 4%, respectively. Phase quantification, particularly the low amount of calcite and kaolinite in the E-IDP sample, allows us to consider this sample similar to the material used in (Tessier, 1984; Bardot, 1998; Bardot et al., 1998; Rajec, 1999; Hassan et al., 2005; Bradbury and Baeyens, 2009; Altmann et al., 2015). By comparison, the V-IDP mineralogical composition with large amounts of kaolinite agrees with the one used by (Poinssot et al., 1999; González Sánchez et al., 2008c; Diaz, 2009; Rajyaguru, 2018). By comparison with the XRD patterns in the work of Gabis, (1963), both IDP samples come from the middle series of the central zone of the Velay sedimentary basin (Fig.III.2). More precisely, the E-IDP sample likely belongs to the "green clay" level, alternating with marl banks in the middle of this series. In addition, according to Gabis, (1963), this level does not contain calcite minerals, unlike the beds just above or below it. The presence of kaolinite in the raw V-IDP sample suggests that it comes from the "versicolored clayey banks" below the "green clay" level, where illite and kaolinite form a mixture with 5-10% content of calcite (Fig.III.2).

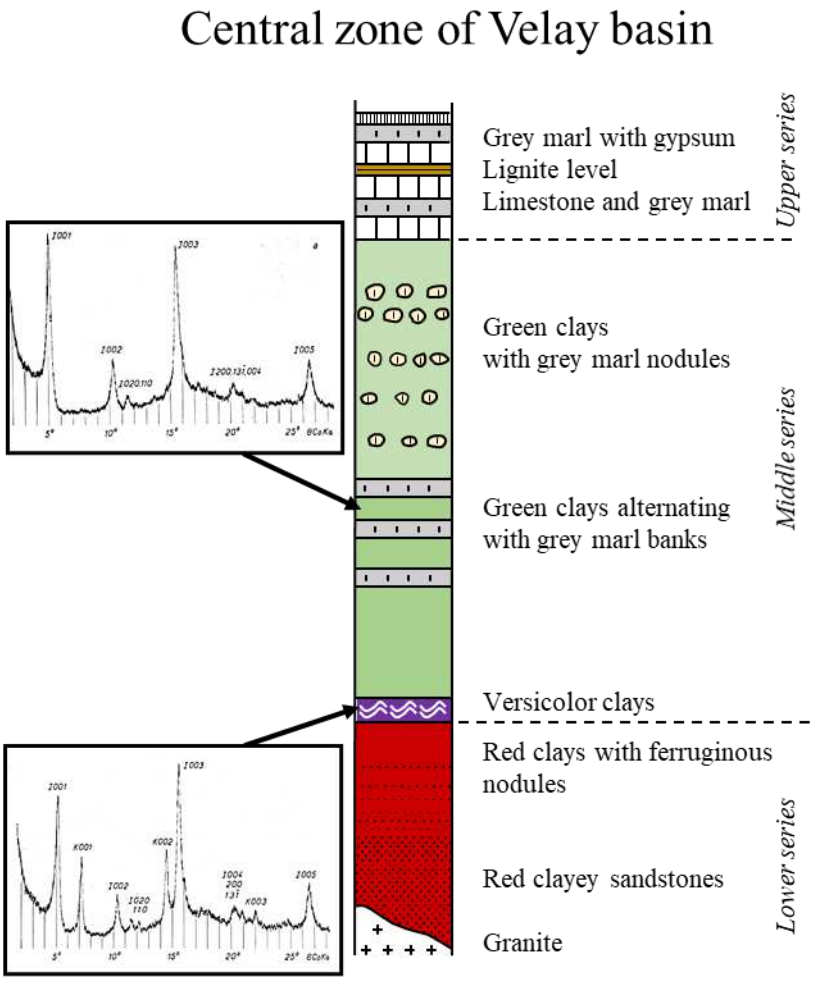


***Fig.III.2**. Lithological section of the central zone of the Velay basin (adapted from Gabis, (1963), illustrating the potential sampling locations of the two samples investigated in the present study. The experimental X-ray diffraction pattern from Gabis, (1963) obtained for green clays alternating with grey marl banks is similar to the EURAD illite du Puy (E-IDP; top) considering the absence of kaolinite and calcite. The XRD pattern collected for Versicolor clays at the bottom of the middle series by Gabis, (1963) with kaolinite and calcite as accessory minerals is similar to the pattern obtained for Velay illite du Puy (V-IDP; bottom).*

With more than 80% illite, both raw IDP samples are appropriate candidates for reference illite material. Naturally, removing the other none-illitic minerals is necessary; A simple and widely used method for purifying clay materials is size separation after dispersion and removal of soluble minerals (e.g., calcite). In this work, the results from sequential fractionation indicate that both IDP samples are widely dominated by <2 µm particles in similar contributions, 94 and 93% ((values are normalized to the total yield) for V-IDP and E-IDP samples, respectively (Table III.1), and all the <2 µm sub-fractions have a significant mass contribution of more than

18%. Yet, the 0.2-2 µm size fraction has a slightly higher contribution of ~5% in the E-IDP sample (Table III.1). As commonly observed in natural clay samples (Hubert et al., 2012; Viennet et al., 2015), the XRD patterns of the fine <0.2 µm sub-fractions (Fig.III.3) indicate that both IDP samples are almost entirely constituted from clay phases, and the accessory silicates remain concentrated in the 0.2-2 µm fraction. However, this method did not separate clay phases in the V-IDP sample, and kaolinite persists even in the finest fraction investigated (i.e., <0.05 µm). It worth noting that kaolinite traces remained even in <0.02 µm for the V-IDP sample (results not shown). By contrast, <0.2 µm sub-fractions of the E-IDP sample exhibit only 00ℓ reflections of illite, and a quasi-monomineralic sample of illite is thus obtained. Therefore, the minimal shifts of the 00ℓ reflections of illite after ethylene glycol solvation indicate that the illite phase of both IDP samples is most likely an illite-smectite mixed-layer mineral (MLM) mainly composed by illite layers with a marginal proportion of smectite layers (Fig.III.3). This illite-smectite mixed-layer mineral is present in all size fractions. The broadening of its 00ℓ reflections with the decrease of particle size is most likely because of the decrease in the coherent scattering domain size as previously observed for size fractionation of vermiculite (Reinholdt et al., 2013).

The mineralogical results show that a large amount of quasi mono-mineral illite sample can be obtained easily from the raw E-IDP by stopping the size fractionation at 0.2 µm (<0.2 µm fractions represent ~60% of raw E-IDP mass). With the assumption of accurate sampling because removing other clay minerals such as kaolinite is not achievable with this approach. The sub-fractions of E-IDP samples are further analyzed to establish baseline data of the materials used in the EURAD project. These analyses include the Physio-chemical properties, crystal structure, particle morphology, CEC, and crystal chemistry of these size fractions.

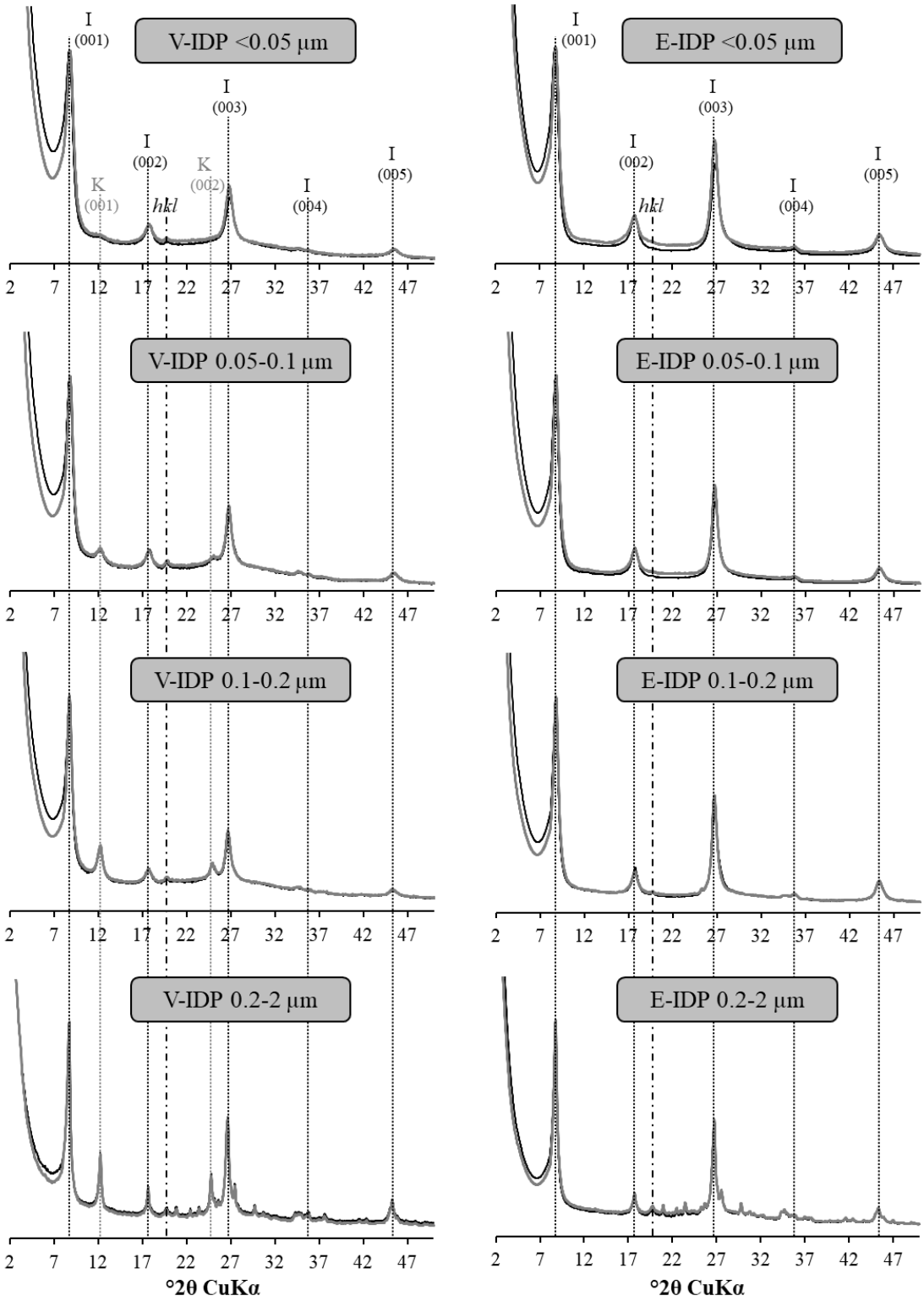


***Fig.III.3**. Experimental X-ray diffraction patterns of oriented Ca^{2+}-saturated preparations for the different sub-fractions of Velay illite du Puy (V-IDP, left) and EURAD illite du Puy (E-IDP, right). In black the patterns are recorded in air-dried condition, whereas the patterns after ethylene glycol solvation are shown in grey. I and K stand for illite and kaolinite reflections, respectively. Non-indexed reflections are associated with accessory minerals.*

III.2.2. Crystal-chemistry and geometrical characterization of sub-fractions from E-IDP sample

III.2.2.1. Crystal structure of illite-smectite MLM in E-IDP size fractions

The crystal structure of the illite phase in the different size fractions was determined by XRD profile modeling of 00ℓ reflections on AD and EG treatments (Fig.III.4). A single R0 illite-smectite MLM was sufficient to reproduce the experimental XRD profiles of 00ℓ reflections in the different sub-fractions and for both treatments. As reported in Table III.2, this illite-smectite MLM contains an overwhelming proportion of illite layers with a very low contribution of smectite layers, inferior to 5% irrespective of the size fraction. Except for the marginal increase of 1% of smectite layers, the main evolution of crystal structure with the decrease of particle size is the aforementioned gradual decrease of mean CSDS, from 14 layers (in EG state) for the coarsest 0.2-2 µm fraction to ~ 7 layers for the <0.05 µm size fraction. Note that the slight increase in the smectite layer content after EG saturation is consistent with the swelling in the EG state of initially collapsed smectitic layers in the AD state (Ferrage et al., 2011).

The different size fractions of the E-IDP sample are thus composed of a single type of clay mineral, an R0 illite-smectite MLM. Compared to previous studies that mention a proportion of smectite layers that can reach nearly 20 to 30% (Altmann et al., 2015), the illite-smectite MLM of the E-IDP sample is particularly rich in illite layers with less than 5% of smectite layers. Moreover, the crystal structure of the illite-smectite MLM is notably stable with the particle size. Indeed, only a decrease in CSDS with particle size decreases is noticed as generally previously observed (Hubert et al., 2012; Viennet et al., 2015; Bakker et al., 2019).

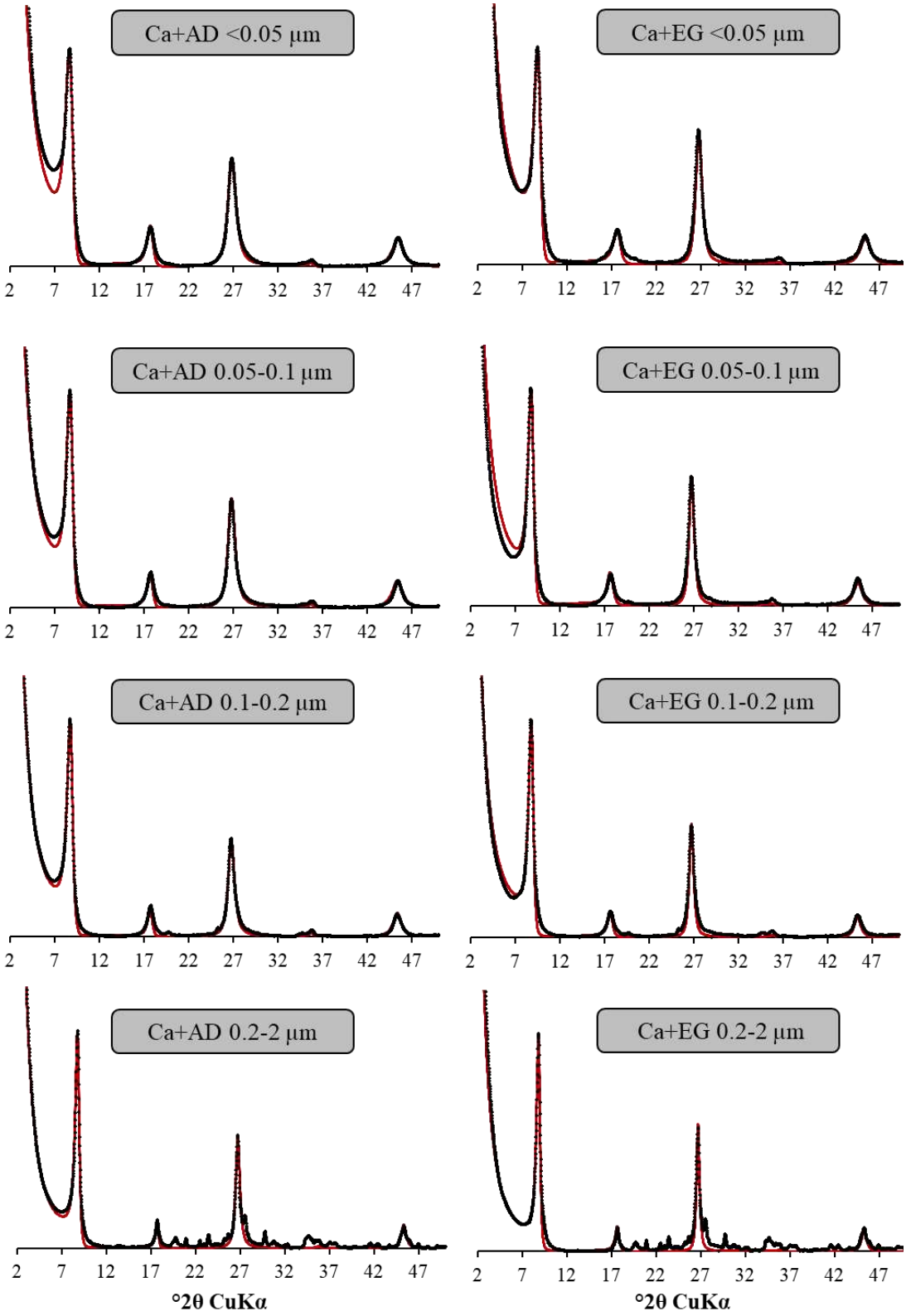


Fig.III.4. *Comparison between the experimental (crosses) and calculated (solid red lines) XRD patterns of oriented Ca^{2+}-saturated preparations recorded in air-dried (AD) and after ethylene-glycol (EG) saturation for the different sub-fractions of EURAD illite du Puy (E-IDP). The structural parameters of the illite-smectite mixed-layer minerals are reported in Table III.2.*

Table III.2. *Structural parameters for the modeling of experimental 00ℓ XRD reflections of the Ca^{2+}-saturated fractions of EURAD illite du Puy (E-IDP) in air-dried condition (AD) and after ethylene glycol solvation (EG).*

	AD			EG		
Fraction (µm)	% I/S [a]	N [b]	LLT Illite [c]	% I/S	N	LLT Illite
<0.05	97/3	7	9.97	96/4	7.6	9.97
0.05-0.1	97/3	8.2	9.98	96/4	9	9.98
0.1-0.2	97/3	9.3	9.99	97/3	10	9.99
0.2-2	98/2	12	10	97/3	14	10

[a] Relative proportion of illite and smectite layers. [b] Coherent scattering domain size value (in layers). [c] Layer-to-layer distance of illite layers (in Å).

III.2.2.2. Structural formulas and grain densities of E-IDP size fractions

Energy dispersive spectrometric (EDS) measurements by scanning electron microscopy were performed on the dry powder of the different fractions of the E-IDP sample compressed into pellets. All fractions were Na^{+}-saturated except for the <2 µm one, which was Ca^{2+}-saturated. The structural formula for each fraction is reported in Table III.3. During SEM observations of the compacted pellets, a dispersion of small grain of titanium oxides between clay particles was detected. Therefore, TiO_2 quantities were removed from the calculation of the structural formula. Moreover, as both the 0.2-2 and the <2 µm fractions contain feldspar impurities, the reported chemical composition does not correspond to pure illite mineral but more to a mixture of phases.

The deduced structural formulas are typical of ferruginous illitic material (Gabis, 1963; Tessier, 1984), with an increased Fe^{3+} occupation in the octahedral sheet at the expense of Al^{3+} content. There is a slight increase in Si^{4+} in the tetrahedral sheet compared to what is reported in the literature (Wilson, 2013). In addition, the octahedral occupancy is slightly higher than 4 and is attributed to the presence of small trioctahedral domains. Finally, for the three <0.2 µm fractions, which are more representative of a pure illitic phase, note that the charge of the interlayer decreases with decreasing the size fraction (Table 3). Such a decrease of layer charge for the finest illitic clay fraction was previously reported for soils environments (Robert et al.,

1991). This observation can be tentatively assigned to the formation conditions of the particles and the slight increase of smectite contribution in the finest fractions (Table 2). Another important observation is the remaining adsorbed Ca^{2+} in the interlayer space for finest size fractions (Table 3). This residual Ca^{2+} may be why the CEC measurements from Na^{+}-saturated samples give relatively low values in the case where Ca^{2+} concentration was not measured in the exchanged supernatant, as discussed in section 2.6. Overall, the structural formulas obtained for all sub-fractions are consistent with those reported in the literature and derived from different methods (Gabis, 1963; Tessier, 1984; Bardot, 1998; Poinssot et al., 1999; Altmann et al., 2015). Minor differences can be assigned to the choice of the size fractions and sampling region in the ore site.

Table III.3. *Structural formulas and grain densities for different fractions of EURAD illite du Puy (E-IDP).*

Size fraction (µm)	Structural formula [a]	Interlayer Charge (per $O_{20}(OH)_4$)	Calculated grain density (g cm^{-3})
<0.05	$[Al_{2.69}Mg_{0.78}Fe_{0.60}]_{\Sigma 4.08}(Si_{7.24}Al_{0.76})O_{20}(OH_4)(K_{1.19}Na_{0.08}Ca_{0.02})$	1.30	2.79
0.05-0.1	$[Al_{2.51}Mg_{0.80}Fe_{0.79}]_{\Sigma 4.10}(Si_{7.07}Al_{0.93})O_{20}(OH_4)(K_{1.16}Na_{0.08}Ca_{0.09})$	1.42	2.82
0.1-0.2	$[Al_{2.46}Mg_{0.79}Fe_{0.81}]_{\Sigma 4.06}(Si_{6.98}Al_{1.02})O_{20}(OH_4)(K_{1.31}Na_{0.19}Ca_{0.05})$	1.60	2.83
0.2-2	$[Al_{2.52}Mg_{0.74}Fe_{0.76}]_{\Sigma 4.02}(Si_{6.95}Al_{1.05})O_{20}(OH_4)(K_{1.55}Na_{0.06}Ca_{0.05})$	1.71	2.84
<2	$[Al_{2.50}Mg_{0.75}Fe_{0.80}]_{\Sigma 4.04}(Si_{7.02}Al_{0.98})O_{20}(OH_4)(K_{1.33}Na_{0.02}Ca_{0.11})$	1.57	2.83

[a] Fe is considered as Fe^{3+}

Grain densities for the different sub-fractions were calculated based on the structural formula (Table III.3) and cell parameters derived in this study. For *a* and *b* parameters, average values of disordered and ordered 1M illite polytypes obtained from bulk refinement were considered (i.e., a = 5.165 and b = 8.996 and a = 5.2269 and b = 9.049 for ordered and

disordered illite, respectively), with the layer-to-layer distances of illite for each sub-fraction in (Table III.2), corresponding to c* parameter, were used. The calculated grain densities show limited evolution with particle size (Table III.3). A mean grain density value of the <2 µm fraction of 2.83 g cm^{-3} can be calculated based on the relative proportion of the different sub-fractions. This value is slightly higher than the grain density of ~2.7-2.79 g cm^{-3} reported in the literature (Tessier, 1984; Bardot, 1998; Poinssot et al., 1999; Altmann et al., 2015) based on generic compositions and structural parameters.

III.2.2.3. Specific surface area and associated geometrical features of particles in E-IDP size fractions

The derivative isotherms of low-pressure argon adsorption at 77K and DIS decomposition for the different size fractions of Na^+-saturated E-IDP are shown in Fig.III.5. The parameters used for DIS modeling are reported in Table III.S1 (in the Supplementary Data (S.D.)). The lateral, basal, and total specific surface areas (LSA, BSA, and TSA, respectively) from DIS decomposition are reported in Table 4. This Table also includes the mean values for height (h) and basal length (l) of clay particles, calculated according to Eqs. III.1 and III.2, respectively, based on the grain densities reported in Table III.3.

The experimental derivative isotherms are similar for all size fractions and the decomposition procedure leads to the definition of 5 or 6 energy domains for the <0.1 µm and >0.1 µm fractions, respectively (Table III.S1). These different domains are either attributed to lateral (green dashed line; Fig.III.5) or basal (red dashed line; Fig.III.5) surfaces (Michot et al., 1990; Villieras et al., 1992, 1997; Bardot et al., 1998; Chemeda, 2021). The overall TSA values logically increase when decreasing fraction size and are consistent with N_2 adsorption results (Table III.4), considering the difference in acquisition method (continuous *vs*. point-by-point method for N_2 and Ar, respectively).

Mean particles lengths and heights derived from DIS decomposition are found to decrease when decreasing size fractions. The obtained mean particle dimensions are in fair agreement with those reported by Rajec, (1999) and Hassan et al., (2005) for the same material, although the size fraction was not controlled in these studies. The aspect ratio close to ~0.1 obtained here for <0.2 µm size fractions is also in good agreement with the results in Rajec, (1999) and Hassan et al., (2005). Note that the aspect ratio value is slightly higher for the 0.2-2 µm size fraction, which can be assigned to the presence of non-clay accessory minerals (Fig.III.1b). The aspect ratio for <0.2 µm size sub-fractions is interestingly similar to that obtained for Santa Olalla (SO) vermiculite by Reinholdt et al., (2013). These authors indeed reported an aspect ratio of

0.08 and a TSA value of ~108 $m^2.g^{-1}$ for the dried Na^+-saturated 0.1-0.2 µm size fraction of SO-vermiculite, in good agreement with results obtained for the same size fraction of E-IDP. This finding is of particular interest in the scope of investigating, for specific particle size and morphology, the influence of interlayer porosity on a given process (e.g., adsorption or diffusion of solutes species in porous clay media).

III.2.2.4. The cation exchange capacity of E-IDP size fractions

The measured CEC values of the different size fractions of E-IDP, reported in Table III.4, show a logical increasing trend with the decrease of particle size. In that regard, the CEC, mainly originating from the sorption sites on the particles' external surfaces, agrees with the evolution of N_2 or Ar TSA values. To further validate our results, the obtained CEC values for the <2 µm size fraction can be successfully compared to the calculated one (<2 $µm^{calc.}$) based on the relative proportion and associated CEC value of each sub-fraction (Table III.4). This excellent agreement between experimental and calculated CEC values is also obtained for N_2 TSA values between <2 µm and <2 $µm^{calc.}$ fractions, further confirming the consistency of the

Results derived for the different sub-fractions (Table III.4). Results from this study can be compared to ones from Altmann et al., (2015) on E-IDP. These authors reported a CEC value of 19 meq/100g and an N_2 TSA value of 110 $m^2\ g^{-1}$ for the Na^+-saturated sample. Both values are in good agreement with our results, despite that Altmann et al., (2015) reported contrasted mineralogy of the clay phase with a large amount of smectitic layers (20-30% vs. <5% in the present study). In contrast, the lower CEC and N_2 TSA values in Poinssot et al., (1999) for V-IDP (13.2 meq/100g and an N_2 TSA value of 97 $m^2\ g^{-1}$, respectively) can be tentatively assigned to the higher content of kaolinite in V-IDP material.

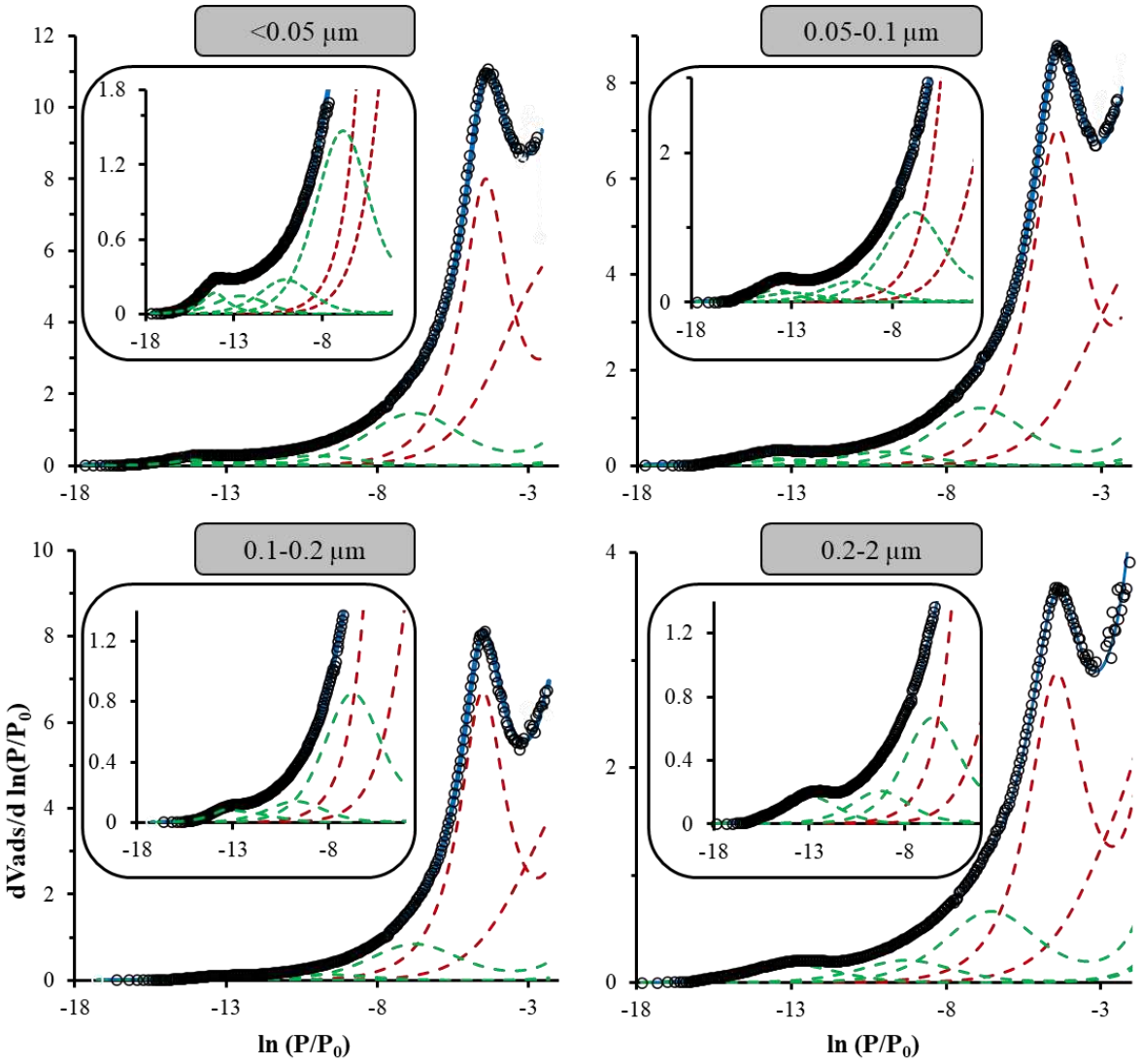


Fig. III.5. *Experimental low-pressure Ar derivative adsorption isotherms (open circles) were obtained at 77 K for the different Na^+-saturated sub-fractions of EURAD illite du Puy (E-IDP). Derivative isotherm summation (DIS) decompositions are reported as dashed lines (red and green for domains associated with Ar adsorption on basal and lateral surfaces, respectively). The sum of the different DIS contributions is shown as a solid blue line.*

***Table III.4**. Physio-chemical characterization of Na^+-saturated size fractions of EURAD illite du Puy (E-IDP) with a relative mass contribution to <2 µm, cationic exchange capacity, and surface properties. Surface measurements include the total specific surface area determined from both N_2 and Ar adsorption. Particle geometry analysis includes lateral and basal specific surface areas (LSA and BSA, respectively) and the height (h) and basal length (l) of clay particles obtained by low-pressure Ar adsorption and DIS decomposition.*

Sample		This study						Hassan et al. (2006) [c]	Rajec et al. (1999) [d]
		<0.05 µm	0.05-0.1 µm	0.1-0.2 µm	0.2-2 µm	<2 µm	<2 µm$^{calc.}$	IDP	IDP
Relative mass contribution to <2µm (%)		0.21	0.23	0.24	0.32	-	-	-	-
CEC (meq/100 g at pH = 7)		39.5	32.7	22.8	8.4	21.2	23.8	-	-
N_2 TSA ($m^2 g^{-1}$) [a]		184.6	153	114.1	60.8	123.6	120.2	-	-
Ar specific surface area ($m^2 g^{-1}$) [a]	Total (TSA)	158.2	133.2	109.2	60.7	-	-	171	233[c]
	Lateral (LSA)	30.4	27.3	16.7	15.6	-	-	38	29
	Basal (BSA)	127.8	105.9	92.5	45.1	-	-	133	
Geometrical parameters of particles from DIS decomposition	*h* (nm) [b]	5.5	6.5	7.4	16.4	-	-	5.7	3.6[d]
	l (nm) [b]	53.1	58.3	94.7	109.7	-	-	46.4	52.0
	aspect ratio (*h*/*l*)	0.10	0.11	0.08	0.15	-	-	0.12	0.07

[a] uncertainty on specific area values of ± 1 $m^2 g^{-1}$, [b] calculated using Eqs. 1 and 2. [c & d] calculated from fixed cations per $O_{10}(OH)_2$.

III.3. Concluding remarks and perspectives

The results obtained in this study confirm that illite du Puy is a model clay system almost solely constituted by illite clay minerals. Most of the variability in the characterization data found in literature originates from mineralogical variation resulting from geological sampling strategy. However, particles size distribution between the different sub-fractions is found similar irrespective of the sampling location.

A precise sampling in the sedimentary Velay clay-rich formation allows for the extraction of almost pure illite with a minor amount of non-clay phases. Using a suite of different techniques, different size fractions of this illitic material used in the ongoing EURAD project

was fully characterized. This sample was found to be an illite-smectite mixed-layer material but with an extremely low amount of smectite layers (<5%). No significant changes in crystal chemistry or particle aspect ratios were found between the different sub-fractions. These different sub-fractions display a large range of specific surface areas, increasing by a factor 3 and ~5 of N_2 TSA and CEC values between the 0.2-2 µm and <0.05 µm size fractions, respectively. The EURAD illite and associated sub-fractions can thus be considered as good models to understand better the adsorption and diffusion of solutes in clay-rich materials. The size fraction can be chosen to tune the surface area and thus enhance or reduce the anionic exclusion and adsorption effects of solutes in the case of diffusion studies of ionic tracers within compacted samples (Ochs et al., 2001; Sato and Suzuki, 2003; Van Loon et al., 2003, 2007; Appelo and Wersin, 2007; González Sánchez et al., 2008c; Melkior et al., 2009; Glaus et al., 2010, 2011; Mazurek et al., 2011; Savoye et al., 2012, 2015; Altmann et al., 2015; Bestel et al., 2018). Such a variation is also important to experimentally highlight the role played by the electrical double layers in the diffusion of cations and anions. Finally, the obtained similar aspect ratios and TSA for illite and vermiculite (Reinholdt et al., 2013) sub-fractions with comparable external CEC values represent a key asset for investigating, for a given particle size and morphology, the influence of interlayer porosity on solutes transport properties in porous media made of these two types of particles.

III.4. Acknowledgements

The results presented here are part of the Ph.D. thesis of A.A. granted by "Région Nouvelle-Aquitaine", University of Poitiers, France. The authors are grateful to the European Joint Program EURAD (WP "Future" - grant ID 847593), the CNRS interdisciplinary "défi Needs" program (Project DARIUS), the French government program "Investissements d'Avenir" (EUR INTREE, reference ANR-18-EURE-0010), and the European Union (ERDF) and "Région Nouvelle Aquitaine" for providing financial support for this study.

III.5. References

Altmann, S., Aertsens, M., Appelo, T., Bruggeman, C., Gaboreau, S., Glaus, M., Jacquier, P., Kupcik, T., Maes, N., Montoya, V., Rabung, T., Savoye, S., et al, 2015. Processes of cation migration in clayrocks: Final Scientific Report of the CatClay European Project. CEA.

Appelo, C.A.J., Wersin, P., 2007. Multicomponent Diffusion Modeling in Clay Systems with Application to the Diffusion of Tritium, Iodide, and Sodium in Opalinus Clay. Environ. Sci. Technol. 41, 5002–5007. https://doi.org/10.1021/es0629256

Bakker, E., Lanson, B., Findling, N., Wander, M.M., Hubert, F., 2019. Mineralogical differences in a temperate cultivated soil arising from different agronomic processes and plant K-uptake. Geoderma 347, 210–219. https://doi.org/10.1016/j.geoderma.2019.04.010

BARDOT, F., 1998. Les minéraux argileux et leur hétérogénéité superficielle : Influence de la nature des cations compensateurs de l'illite sur les mécanismes d'adsorption de gaz. Institut National Polytechnique de Lorraine, Lorraine -France.

Bardot, F., 1998. Les minéraux argileux et leur hétérogénéité superficielle : influence de la nature des cations compensateurs superficiels de l'illite sur les mécanismes d'adsorption de gaz.

Bardot, F., Villiéras, F., Michot, L.J., Francois, M., Gérard, G., Cases, J.M., 1998. High resolution gas adsorption study on illites permuted with various cations assessment of surface energetic properties. Journal of Dispersion Science and Technology 19, 739–759. https://doi.org/10.1080/01932699808913212

Bestel, M., Glaus, M.A., Frick, S., Gimmi, T., Juranyi, F., Van Loon, L.R., Diamond, L.W., 2018. Combined tracer through-diffusion of HTO and 22Na through Na-montmorillonite with different bulk dry densities. Applied Geochemistry 93, 158–166. https://doi.org/10.1016/j.apgeochem.2018.04.008

Bradbury, Baeyens, 2005. Experimental and Modelling Investigations on Na-Illite: Acid-Base Behaviour and the Sorption of Strontium, Nickel, Europium and Uranyl (TECHNICAL REPORT No. 04–02). Paul Scherrer Institut, Villigen.

Bradbury, M.H., Baeyens, B., 2009. Sorption modelling on illite Part I: Titration measurements and the sorption of Ni, Co, Eu and Sn. Geochimica et Cosmochimica Acta 73, 990–1003. https://doi.org/10.1016/j.gca.2008.11.017

Chagneau, A., Tournassat, C., Steefel, C.I., Bourg, I.C., Gaboreau, S., Esteve, I., Kupcik, T., Claret, F., Schäfer, T., 2015. Complete Restriction of 36 Cl – Diffusion by Celestite Precipitation in Densely Compacted Illite. Environ. Sci. Technol. Lett. 2, 139–143. https://doi.org/10.1021/acs.estlett.5b00080

Chemeda, Y.C., 2021. Assessment of surface heterogeneity of lime treated kaolinites: Probed by low-pressure argon and nitrogen gas adsorption. Applied Clay Science 8.

Diaz, N., 2009. Modélisation prédictive de la migration des anions par description de la microstructure de la roche : application à l'argilite du Callovo-Oxfordien. UNIVERSITE PARIS VI, Paris, France.

Doebelin, N., Kleeberg, R., 2015. Profex: a graphical user interface for the Rietveld refinement program BGMN. J Appl Crystallogr 48, 1573–1580. https://doi.org/10.1107/S1600576715014685

Drits, V., 1997. XRD Measurement of Mean Crystallite Thickness of Illite and Illite/Smectite: Reappraisal of the Kubler Index and the Scherrer Equation. Clays and Clay Minerals 45, 461–475. https://doi.org/10.1346/CCMN.1997.0450315

Ferrage, E., Vidal, O., Mosser-Ruck, R., Cathelineau, M., Cuadros, J., 2011. A reinvestigation of smectite illitization in experimental hydrothermal conditions: Results from X-ray diffraction and transmission electron microscopy. American Mineralogist 96, 207–223. https://doi.org/10.2138/am.2011.3587

Gabis, V., 1963. Étude minéralogique et géochimique de la série sédimentaire oligocène du Velay. Bulletin de la Société française de Minéralogie et de Cristallographie 86, 315–354. https://doi.org/10.3406/bulmi.1963.5663

Glaus, M.A., Aertsens, M., Maes, N., Van Laer, L., Van Loon, L.R., 2015. Treatment of boundary conditions in through-diffusion: A case study of 85Sr2+ diffusion in compacted illite. Journal of Contaminant Hydrology 177–178, 239–248. https://doi.org/10.1016/j.jconhyd.2015.03.010

Glaus, M.A., Frick, S., Rossé, R., Loon, L.R.V., 2010. Comparative study of tracer diffusion of HTO, 22Na+ and 36Cl− in compacted kaolinite, illite and montmorillonite. Geochimica et Cosmochimica Acta 74, 1999–2010. https://doi.org/10.1016/j.gca.2010.01.010

Glaus, M.A., Frick, S., Rossé, R., Van Loon, L.R., 2011. Consistent interpretation of the results of through-, out-diffusion and tracer profile analysis for trace anion diffusion in compacted montmorillonite. Journal of Contaminant Hydrology 123, 1–10. https://doi.org/10.1016/j.jconhyd.2010.11.009

González Sánchez, F., Van Loon, L.R., Gimmi, T., Jakob, A., Glaus, M.A., Diamond, L.W., 2008. Self-diffusion of water and its dependence on temperature and ionic strength in highly compacted montmorillonite, illite and kaolinite. Applied Geochemistry 23, 3840–3851. https://doi.org/10.1016/j.apgeochem.2008.08.008

Hassan, M.S., Villieras, F., Gaboriaud, F., Razafitianamaharavo, A., 2005. AFM and low-pressure argon adsorption analysis of geometrical properties of phyllosilicates. Journal of Colloid and Interface Science 296, 614–623. https://doi.org/10.1016/j.jcis.2005.09.028

Howard, S.A., Preston, K.D., 1989. Profile Fitting of Powder Diffraction Patterns, in: Modern Powder Diffraction; Bish, D. L., Post, J. E., Eds., Reviews in Mineralogy. Mineralogical Society of America, Washington, DC, pp. 217–275.

Hubert, F., Caner, L., Meunier, A., Ferrage, E., 2012. Unraveling complex <2 m clay mineralogy from soils using X-ray diffraction profile modeling on particle-size sub-fractions: Implications for soil pedogenesis and reactivity. American Mineralogist 97, 384–398. https://doi.org/10.2138/am.2012.3900

Kleeberg, R., Monecke, T., Hillier, S., 2008. Preferred Orientation of Mineral Grains in Sample Mounts for Quantitative XRD Measurements: How Random are Powder Samples? Clays Clay Miner. 56, 404–415. https://doi.org/10.1346/CCMN.2008.0560402

Mazurek, M., Alt-Epping, P., Bath, A., Gimmi, T., Niklaus Waber, H., Buschaert, S., Cannière, P.D., Craen, M.D., Gautschi, A., Savoye, S., Vinsot, A., Wemaere, I., Wouters, L., 2011. Natural tracer profiles across argillaceous formations. Applied Geochemistry 26, 1035–1064. https://doi.org/10.1016/j.apgeochem.2011.03.124

Melkior, T., Gaucher, E.C., Brouard, C., Yahiaoui, S., Thoby, D., Clinard, Ch., Ferrage, E., Guyonnet, D., Tournassat, C., Coelho, D., 2009. Na+ and HTO diffusion in compacted bentonite: Effect of surface chemistry and related texture. Journal of Hydrology 370, 9–20. https://doi.org/10.1016/j.jhydrol.2009.02.035

Michot, L., Francois, M., Cases, J.M., 1990. Surface heterogeneity studied by a quasi-equilibrium gas adsorption procedure. Langmuir 6, 677–681. https://doi.org/10.1021/la00093a025

Moore, D.M., Reynolds, R.C.J., 1997. X-ray Diffraction and the Identification and Analysis of Clay Minerals. Oxford University Press.

Ochs, M., Lothenbach, B., Wanner, H., Sato, H., Yui, M., 2001. An integrated sorption–diffusion model for the calculation of consistent distribution and diffusion coefficients in compacted bentonite. Journal of Contaminant Hydrology 47, 283–296. https://doi.org/10.1016/S0169-7722(00)00157-1

Poinssot, C., Baeyens, B., Bradbury, M.H., 1999. Experimental and modelling studies of caesium sorption on illite. Geochimica et Cosmochimica Acta 63, 3217–3227. https://doi.org/10.1016/S0016-7037(99)00246-X

Rabung, Th., Pierret, M.C., Bauer, A., Geckeis, H., Bradbury, M.H., Baeyens, B., 2005. Sorption of Eu(III)/Cm(III) on Ca-montmorillonite and Na-illite. Part 1: Batch sorption and time-resolved laser fluorescence spectroscopy experiments. Geochimica et Cosmochimica Acta 69, 5393–5402. https://doi.org/10.1016/j.gca.2005.06.030

Rajec, P., 1999. Effect of Illite Particle Shape on Cesium Sorption. Clays and Clay Minerals 47, 755–760. https://doi.org/10.1346/CCMN.1999.0470610

Rajyaguru, A., 2018. Impact of saline plume on containment properties of natural porous materials in geological disposal context: An experimental and REV simulation approach to go beyond Archie's law. PSL Research University, Paris, France.

Reinholdt, M.X., Hubert, F., Faurel, M., Tertre, E., Razafitianamaharavo, A., Francius, G., Prêt, D., Petit, S., Béré, E., Pelletier, M., Ferrage, E., 2013. Morphological properties of vermiculite particles in size-selected fractions obtained by sonication. Applied Clay Science 77–78, 18–32. https://doi.org/10.1016/j.clay.2013.03.013

Robert, M., Hardy, M., Elsass, F., 1991. Crystallochemistry, properties and organization of soil clays derived from major sedimentary rocks in France. Clay miner. 26, 409–420. https://doi.org/10.1180/claymin.1991.026.3.09

Sakharov, A., Naumov, A.S., Drits, V.A., 1983. X-ray scattering by defect layer structures. Kristallografia 28, 951–958.

Sakharov, A., Naumov, A.S., Drits, V.A., 1982a. X-ray diffraction by mixed-layer structures with random distribution of stacking faults. Dokl. Akad. Nauk 265, 339–343.

Sakharov, A., Naumov, A.S., Drits, V.A., 1982b. X-ray intensities scattered by layer structures with short-range ordering parameters S ≥ 1 and G ≥ 1. Dokl. Akad. Nauk 265, 871–874.

Sato, H., Suzuki, S., 2003. Fundamental study on the effect of an orientation of clay particles on diffusion pathway in compacted bentonite. Applied Clay Science 23, 51–60. https://doi.org/10.1016/S0169-1317(03)00086-3

Savoye, S., Beaucaire, C., Grenut, B., Fayette, A., 2015. Impact of the solution ionic strength on strontium diffusion through the Callovo-Oxfordian clayrocks: An experimental and modeling study. Applied Geochemistry 61, 41–52. https://doi.org/10.1016/j.apgeochem.2015.05.011

Savoye, S., Frasca, B., Grenut, B., Fayette, A., 2012. How mobile is iodide in the Callovo–Oxfordian claystones under experimental conditions close to the in situ ones? Journal of Contaminant Hydrology 142–143, 82–92. https://doi.org/10.1016/j.jconhyd.2012.10.003

Tertre, E., Ferrage, E., Bihannic, I., Michot, L.J., Prêt, D., 2011a. Influence of the ionic strength and solid/solution ratio on Ca(II)-for-Na+ exchange on montmorillonite. Part 2: Understanding the effect of the m/V ratio. Implications for pore water composition and element transport in natural media. Journal of Colloid and Interface Science 363, 334–347. https://doi.org/10.1016/j.jcis.2011.07.003

Tertre, E., Prêt, D., Ferrage, E., 2011b. Influence of the ionic strength and solid/solution ratio on Ca(II)-for-Na+ exchange on montmorillonite. Part 1: Chemical measurements, thermodynamic modeling and potential implications for trace elements geochemistry. Journal of Colloid and Interface Science 353, 248–256. https://doi.org/10.1016/j.jcis.2010.09.039

Tessier, M., 1984. Etude expe´rimentale de l'organisation des mate´riaux argileux : Hydratation, gonflement et structuration au cours de la dessiccation et de la re´humectation. INRA.

Van Loon, L.R., Glaus, M.A., Müller, W., 2007. Anion exclusion effects in compacted bentonites: Towards a better understanding of anion diffusion. Applied Geochemistry 22, 2536–2552. https://doi.org/10.1016/j.apgeochem.2007.07.008

Van Loon, L.R., Soler, J.M., Jakob, A., Bradbury, M.H., 2003. Effect of confining pressure on the diffusion of HTO, 36Cl− and 125I− in a layered argillaceous rock (Opalinus Clay): diffusion perpendicular to the fabric. Applied Geochemistry 18, 1653–1662. https://doi.org/10.1016/S0883-2927(03)00047-7

Viennet, J.-C., Hubert, F., Ferrage, E., Tertre, E., Legout, A., Turpault, M.-P., 2015. Investigation of clay mineralogy in a temperate acidic soil of a forest using X-ray diffraction profile modeling: Beyond the HIS and HIV description. Geoderma 241–242, 75–86. https://doi.org/10.1016/j.geoderma.2014.11.004

Villieras, F., Cases, J.M., Francois, M., Michot, L.J., Thomas, F., 1992. Texture and surface energetic heterogeneity of solids from modeling of low pressure gas adsorption isotherms. Langmuir 8, 1789–1795. https://doi.org/10.1021/la00043a018

Villieras, F., Michot, L.J., Bardot, F., Cases, J.M., François, M., Rudziński, W., 1997. An Improved Derivative Isotherm Summation Method To Study Surface Heterogeneity of Clay Minerals. Langmuir 13, 1104–1117. https://doi.org/10.1021/la9510083

Wilson, M.J., 2013. Rock-forming Minerals, Sheet Silicates: Clay Minerals, Second. ed. Geological Society of London, London.

III.6. Supplementary Data (S.D.)

A baseline study of mineralogical and morphological properties of different size fractions of illite du Puy

Table III.S1. *Main parameters obtained from the application of the DIS method to low-pressure Ar adsorption isotherms for the Na^+-saturated EURAD illite du Puy (Na-EIDP) size fractions.*

Energy domain	Parameters	Na-IDP size fraction (µm)					Hassan et al 2006[a]	Reinholdt et al 2013[b]	Adsorption surface attribution
		< 2	0.2-2	0.1-0.2	0.05-0.1	<0.05			
Domain 1	Ln(P/P$_0$)	-13.35	-13.01	-13.19	-13.48	-13.98	− 13.03	−13.0	
	V_m (cm^3 g^{-1})	0.21	0.70	0.20	0.82	0.43	0.21	0.31	
	w/kT	0.00	0.00	1.40	0.60	1.30	0.50	1.2	
	TSA (m^2 g^{-1})	0.78	2.59	0.72	3.06	1.61	0.70	1.2	Lateral
Domain 2	Ln(P/P$_0$)				-11.89	-13.13			
	V_m (cm^3 g^{-1})				0.24	0.42			
	w/kT				0.00	0			
	TSA (m^2 g^{-1})				0.90	1.54			Lateral
Domain 3	Ln(P/P$_0$)	-9.99	-9.29	-10.19	-9.49	-10.28	− 10.15	-9.2	
	V_m (cm^3 g^{-1})	0.60	0.84	0.60	1.30	1.16	2.03	1.92	
	w/kT	0.00	0.00	0.00	0.00	-0.20	0.00	-0.6	
	TSA (m^2 g^{-1})	2.22	3.12	2.22	4.81	4.29	7.50	7.1	Lateral
Domain 4	Ln(P/P$_0$)	-6.81	-6.55	-6.70	-6.62	-6.83	− 6.95	-6.4	
	V_m (cm^3 g^{-1})	3.37	2.66	3.72	4.99	6.20	8.00	3.07	
	w/kT	0.00	0.00	-0.10	0.00	-0.20	0.50	0	
	TSA (m^2 g^{-1})	12.51	9.86	13.79	18.51	22.99	29.70	11.4	Lateral
Domain 5	Ln(P/P$_0$)	-4.44	-4.43	-4.55	-4.46	-4.42	− 4.53	-4.2	
	V_m (cm^3 g^{-1})	18.11	7.38	14.28	13.65	18.60	19.19	9.84	
	w/kT	1.60	1.30	1.70	1.60	1.60	1.70	0	
	TSA (m^2 g^{-1})	67.17	27.38	52.97	50.64	69.00	71.20	36.5	Basal
Domain 6	Ln(P/P$_0$)	-2.34	-2.40	-2.50	-2.56	-2.57	− 2.66	-2.2	
	V_m (cm^3 g^{-1})	13.20	4.77	10.64	14.89	15.86	16.55	14.19	
	w/kT	0.00	0.00	0.00	0.00	0.00	0.00	0	
	TSA (m^2 g^{-1})	48.93	17.70	39.49	55.23	58.84	61.40	52.7	Basal

[a] for Illite du Puy, [b] for 0.1-0.2 µm Santa Olalla vermiculite

Chapter IV

Water diffusion in Na-vermiculite, illite and kaolinite

The protocol developed during this work (see Chapter II, section II.3) allowed us to compare diffusion results of different tracers in porous media having similar interparticle porosity, with or without accessible interlayer to water and cation (i.e., Na-vermiculite and IDP, respectively). Still, these porous media are different in their particle's organization (i.e., isotropic and anisotropic). Hence, this chapter is devoted to discussing results obtained for the diffusion of water tracer (HDO) in compacted clay samples made from Na-vermiculite, kaolinite, and illite particles. In contrast, the results obtained for ions diffusion (i.e., Na^+ and Cl^-) are reported and discussed in next chapter (V).

Section IV.1 is dedicated to HDO diffusion results in Na-IDP samples (only interparticle porosity). For this section, particle organization measurements from isotropic and anisotropic Na-IDP samples are first discussed, as well as the challenging procedure associated with building compressed samples from this mineral at given porosity and particle organization. After that, we discuss HDO diffusion results and their agreement with literature data. Next, in line with the first objective of this work, we compare results obtained with two isotropic samples (total porosity $\varepsilon = 0.28$ and 0.34, and $\langle P_2 \rangle = 0.11$), and one anisotropic sample (total porosity $\varepsilon = 0.38$ and $\langle P_2 \rangle = 0.54$). This contrast in the $\langle P_2 \rangle$ values permit us to examine the influence of particles organization on HDO mobility in IDP samples. Finally, experimental HDO diffusion data obtained with Na-IDP samples is compared to that obtained for Na-kaolinite, a non-charged clay mineral, and the results from BD simulation. The comparison with data obtained with Na-kaolinite allows assessing the influence of layer charge of IDP particles on the HDO diffusion process.

In section IV.2 is in the form of publication in *Applied Clay Science* in 2020. In this publication, and similar to Na-IDP samples, TD experiments of HDO through isotropic and anisotropic Na-vermiculite samples (i.e., $\langle P_2 \rangle = 0.03$ and 0.41 respectively) with the same total porosity were discussed. In addition, the results obtained with the dual-porosity isotropic Na-vermiculite sample were compared to that obtained with Na-kaolinite sample having only interparticle porosity, with this latter being equal to that of Na-vermiculite samples. This comparison provided experimental proof of the minor contribution of the interlayer porosity of the swelling clays in the flux of water diffusing through these porous media, in line with the

second objective of this work. It is worth noting that this observation was qualitatively described in Tertre et al., (2018) and by simulation as in Churakov and Gimmi, (2011), and it was quantified in this present study by controlling experimental particle organization parameters (i.e., $\langle P_2 \rangle$ values).

Section IV.3 discusses all HDO results obtained with porous media made with the three clay minerals used in this work (i.e., Na-vermiculite, IDP and kaolinite). We expand the discussion in section IV.2 on the role of different porosities in the water diffusion in clayey porous media by adding the results from Na-IDP samples. As far as we are concerned, comparing water diffusivity between Na-vermiculite and IDP is interesting because (i) these two minerals have a similar layer charge of ~0.85 eq for a half unit cell, (ii) the same particle size of 0.1-0.2 µm with particles having a similar aspect ratio of ~0.08 (Table I.2), and importantly (iii) comparable degrees of anisotropy in particles orientation.

Finally, all experimental HDO diffusion results are compared to those obtained by the BD simulation performed by Eric Ferrage. Simulated data was achieved from virtual porous media (VPMs) generated by a sequential deposition algorithm. VPMs were proven to stimulate well the geometrical properties of natural clay porous media (Ferrage et al., 2015). In addition, they are characterized by different degrees of anisotropy in particles' preferred orientation. Consequently, this tool (BD simulation on VPMs) was proven to provide quantitative information on the role played by the preferred orientation of the particles on water diffusion in compacted clayey media as in Dabat et al., (2020) and Asaad et al., (2021).

Table IV.1. Summary of all diffusion experiments carried out in this work. All *D*e values were corrected from possible temperature variations and are reported for 21˚C.

Clay mineral	Particles preferred orientation	Size fraction	L [d]	$\langle P_2 \rangle$ [a]	ε [b]	$\varepsilon_{interp.}$ [c]	Experimental technique	I [e]	De_z [f] HDO	De_z Na+	De_z Cl-
		(µm)	(mm)	-	%	%	-	(M)	($\times 10^{-10}$ m^2 s^{-1})	($\times 10^{-10}$ m^2 s^{-1})	($\times 10^{-10}$ m^2 s^{-1})
Na-KGa2	Isotropic	< 50	10	0.34	0.26	0.26	PGSE-NMR [g]	-	1.50 (1.35-1.65)	-	-
Ca-vermiculite	Isotropic	< 0.1	7.74	0.03	0.49	0.24	TD [h]	-	1.79 (1.34-2.33	-	-
Na-vermiculite	Isotropic	0.1-0.2	7.99	0.03	0.49	0.25	TD	0.01	1.80 (1.50-2.20)	0.34 (0.26-0.48)	0.18 (0.13-0.24)
								1	1.80 (1.60-2.10)	2.20 (1.90-2.60)	1.90 (1.60-2.20)
	Anisotropic	0.1-0.2	6.44	0.41	0.49	0.24	TD	0.01	0.89 (0.67-1.11)	0.20 (0.14-0.26)	0.13 (0.10-0.17)
								1	0.88 (0.75-1.05)	0.68 (0.48-0.88)	0.69 (0.55-0.82)
Na-IDP	Isotropic	0.1-0.2	8.11	0.11	0.28	0.28	TD	0.01	1.14 (0.91-1.37)	0.29 (0.22-0.41)	-
								0.1	0.92 (0.73-1.14)	0.50 (0.35-0.65)	0.61 (0.48-0.74)
								1	0.85 (0.76-1.00)	0.61 (0.55-0.90)	0.67 (0.52-0.81)
	Isotropic	0.1-0.2	9.51	0.11	0.34	0.34	TD	0.01	1.55 (1.28-1.89)	0.38 (0.18-0.52)	-
								0.1	1.55 (1.32-1.86)	1.13 (0.85-1.40)	1.15 (0.90-1.50)
								1	1.53 (1.22-1.90)	1.45 (1.16-1.74)	1.49 (1.01-1.85)
	Anisotropic	0.1-0.2	10.11	0.54	0.38	0.38	TD	0.1	0.96 (0.82-1.11)	0.78 (0.67-1.01)	0.82 (0.64-1.00)
	Anisotropic	0.1-0.2	7.9	0.54	0.37	0.37	TD	1	0.96 (0.83-1.15)	0.95 (0.76-1.14)	

[a] The order parameter (see text). [b] The total porosity. [c] The interparticle porosity. [d] Sample thickness. [e] Ionic strength of the upstream reservoir (salinity); downstream reservoir is always MQ water. [f] Effective diffusion coefficient in the direction perpendicular to the compression (i.e., the preferred orientation of the clay particles). [g] ^{1}H NMR pulsed gradient spin echo (PGSE-NMR) technique. [h] Through-diffusion technique.

IV.1. Water diffusion in Na-saturated illite du Puy (Na-IDP)

IV.1.1. Particle organization measurements in IDP

The 2D-XRS patterns for illite samples were recorded at the SOLEIL synchrotron site in Saclay-France, collaborating with Vincent Geoffroy (a Ph.D. student at the University of Poitiers) kindly recorded these samples during his work on particle organization in soil. For copyright reasons, information regarding acquisition parameters and data treatment software will be included in his forthcoming publication. Anyway, synchrotron measurement (2D-μDRX) and data treatment principles are the same as 2D-XRS in this Ms (Chapter II /Section II.4). However, compared to an average of 4 to 5 possible measurement points with a spot size of 1 mm^2 with the 2D-XRS method, synchrotron measurements allow a total scan of the clay lamella with a smaller X-ray spot size. Such higher resolution allows for a better examination of the variation in the orientation of the particles along the vertical cross-section of the sample (i.e., the longitudinal lamella). Hence, it allows for obtaining a higher spatial resolution of $\langle P_2 \rangle$ value along the z-direction of the experimental porous media.

Fig. IV.1 shows $\langle P_2 \rangle$ parameter values extracted from longitudinal lamellas from two Na-IDP samples. Results in Fig. IV.1a are from an isotropic sample prepared by compression of dry clay powder. To the left is a color scaled distribution map of the extracted $\langle P_2 \rangle$ values over the lamella surface, from which we can see that $\langle P_2 \rangle$ values are more or less close to 0.1. Note that for the upper and lower areas, these values slightly increased to ~0.2. Such local heterogeneity is mainly because these two areas contact the hydraulic press pistons while compressing the sample. Hence, a slight increase in the orientation of particles in these areas is expected.

Fig. IV.1a (right) is a chart of the number of particles with the same $\langle P_2 \rangle$ value. From these data, an average of $\langle P_2 \rangle$ value equal to ~0.11 was obtained. Such value implies that this sample is rather well isotropic in terms of particles' preferred orientation. Fig. IV.1b shows the same data as Fig. IV.1a but from an anisotropic Na-IDP sample prepared by centrifugation of clay dispersion. To the left, the distribution map is in from of successive areas of similar $\langle P2 \rangle$ values. Each area corresponds to one centrifugation cycle, consisting of one yellow and one blue stripe. Such distribution reflects the segregation of the particles during centrifugation. Considering that IDP samples are made from the 0.1-0.2 μm size fraction, the coarser particles (i.e., close to 0.2 μm) settle first to form the yellow stripe, while the finer one's sediment later

in the blue one above it. By examining the average ⟨P2⟩ values in each stripe, the coarser particles tend to be more oriented than the finer ones.

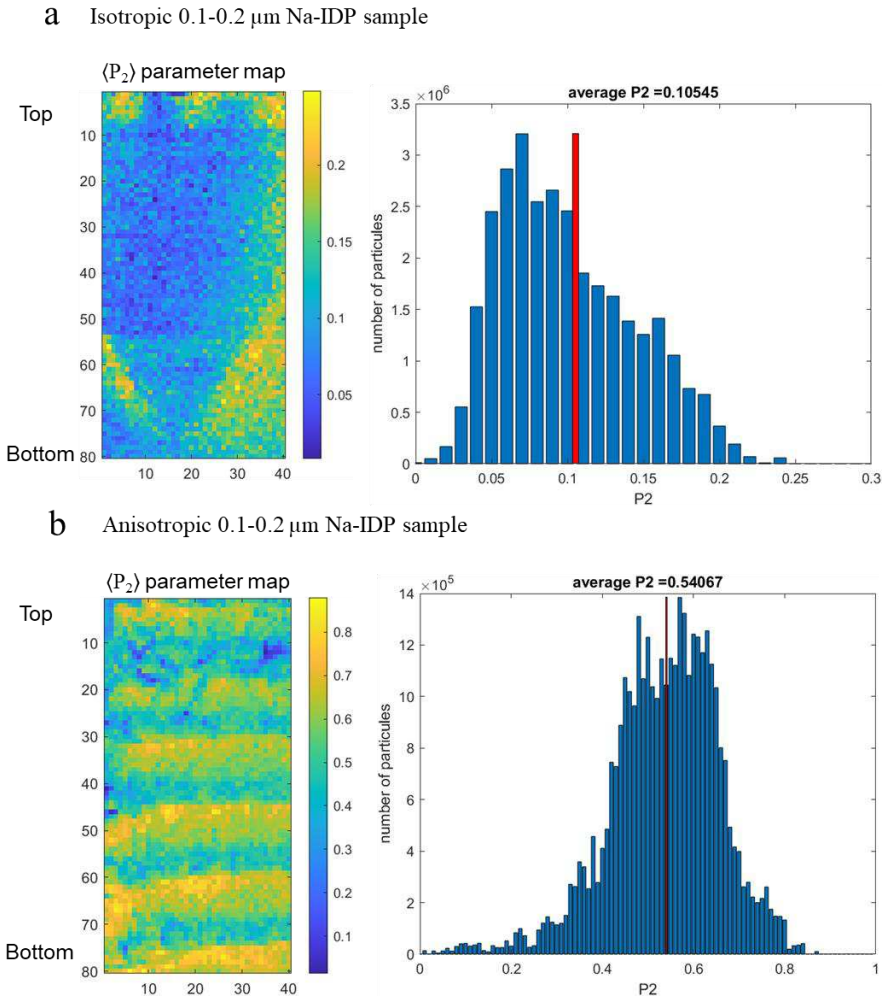


Fig. IV.1. *Measurement of the degree of anisotropy in particles preferred orientation in Na-illite du Puy (IDP) samples at total porosity value of ~0.3.*

The anisotropy is expressed by ⟨P_2⟩ parameters values (see text for details). Results were extracted from 2D µDRX in transmission mode patterns, recorded at the SOLEIL synchrotron site on the CRISTAL line in Paris-France. (a) Results from isotropic IDP sample prepared by compaction of dry powder. Left is a color scaled map of the extracted ⟨P_2⟩ parameters values from a longitudinal lamella (See Fig. II.4). Right is the ⟨P_2⟩ parameters values as function of the number of particles with the same ⟨P_2⟩ value. (b) Same graphs as (a) but obtained from anisotropic IDP sample prepared by centrifugation of clay dispersion.

In Fig. IV.1b (right), we see that the average ⟨P_2⟩ value is ~0.54 for the anisotropic sample, which is five times larger than the one of the isotropic samples at ~0.11. Such contrast

in $\langle P_2 \rangle$ values is sufficient to assess the influence of the anisotropy in particles' preferred orientation on the diffusion of water and solutes between these two samples.

IV.1.2. Experimental challenges and modification of the diffusion cell

TD experiments with IDP materials were the most challenging in this work because of the difficulties encountered in maintaining the sample's integrity (mechanical stability) inside the diffusion cell. Although the design of the TD cell (see Chapter II, section II.5.) was successfully used in Tertre et al., (2018) and Dabat, (2019), and in this work for Na-kaolinite and Na-vermiculite samples, a frequent release was encountered of Na IDP particles (0.1-0.2 µm size fraction) into the aqueous reservoirs, leading eventually to several failed experiments. The particles release was entirely random, either at the beginning of the experiment or several days later. To the extent of our knowledge, no similar observation was reported in the literature related to diffusion experiments with IDP, except for what was described by Altmann et al., (2015) as "a slight swelling of the Na-illite into the open cavities of the supporting PEEK plates was observed in the foregoing tests".

After dismantling the diffusion cells when the experiment failed, no damage was observed in the membrane filters, which -if present- may allow particles to travel through to the reservoirs. Another possible reason for the failed experiments could be the presence of small gaps between the membrane filter and the border of the tube. Such spaces may allow IDP particles to be in direct contact with the circulating solution and disperse into it. In contrast, no similar observation for Na-vermiculite particles because the latter tend to stay in aggregates. This behavior increases the overall coherency of the water-saturated Na-vermiculite samples. Eventually, diffusion experiments were carried out for IDP samples using a modified cell design, as illustrated in Fig. IV.2. The modified cell replaced the stainless-steel porous media and the cellulose filter with a membrane filter (MWCO 3.5 kD from Spectra/Por®). In addition, each piston′ end is bevelled to accommodate an O ring. The O ring acts as a seal to prevent particles migration through the borders of the tube when the sample is compressed.

With the new modified cell, a slight release of particles was observed in the aqueous reservoir only during the water saturation step (i.e., during the two first days of the whole experiment). No additional release was observed during the diffusion experiments (time 0 of the diffusion experiment generally starts at a minimum of one week after the beginning of the water saturation step). Note that the porosity of samples was recalculated by considering the mass of the particles released in the aqueous reservoirs during the water saturation step. For

this reason, Na-IDP samples have a higher interparticle porosity than Na-vermiculite (~0.3-0.35, 0.25, respectively). Contrary to the initial aim of building all the samples at the same

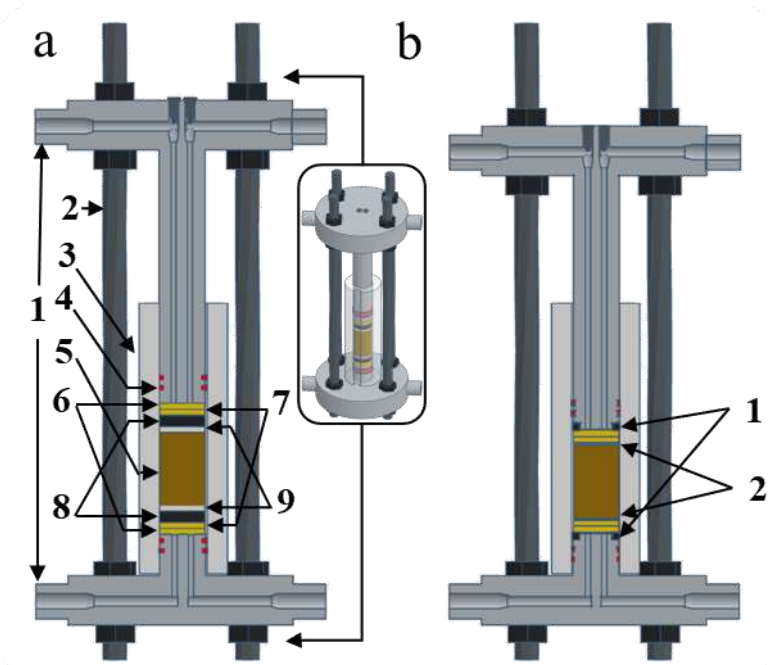


Fig. IV.2. *Cross-section of the different through-diffusion (TD) cells used in this work. (a) The original cell used for Na-vermiculite and kaolinite samples (description in Fig.II.10.). (b) The modified cell used for Na-IDP samples; (1) O rings. (2) membrane (MWCO 3.5 kD from Spectra/Por®).*

interparticle porosity values.

IV.1.3. Results and discussion

Water mobility (HDO) in Na-IDP samples was investigated perpendicular to the compression axis (*z*; normal to the preferred orientation of clay particles). The instantaneous flux and cumulative amounts of diffused water tracer (HDO) and the extracted effective diffusion coefficient (De_z) are shown in Fig. IV.3 for three IDP samples at different total porosities. The first two samples from the left are isotropic mediums (i.e., $\langle P_2 \rangle = 0.11$), while the third sample from the left is an anisotropic medium ((i.e., $\langle P_2 \rangle = 0.54$). De_z values of the isotropic samples were in good agreement with the values reported in (González Sánchez, 2007; Diaz, 2009; Glaus et al., 2010; Altmann et al., 2015), as shown in Fig. IV.4. This agreement was essential to validate the experimental setup, including the new modified cell and associated results.

The contrast in ⟨P_2⟩ values between the isotropic and the anisotropic samples is well reflected in their De_z values. For instance, De_z of the isotropic sample at $\varepsilon = 0.34$ is ~1.6 times higher than the one of the anisotropic at $\varepsilon = 0.38$ (Fig. IV.3; $De_z = 1.47\times 10^{-10}$ and 0.96×10^{-10} m^2s^{-1}, respectively), despite having ~ 4%. lower porosity. Moreover, the isotropic sample at ε = 0.28 yielded a De_z at 1.14×10^{-10}, higher than the anisotropic one with ~10% more porosity volume. Hence, in charged clayey media (e.g., IDP), and together with porosity, the preferred orientation of the particles is a first-order parameter controlling water diffusion. A similar conclusion was reported by Dabat et al., (2020) for porous media made with non-charged clayey particles (i.e., kaolinite).

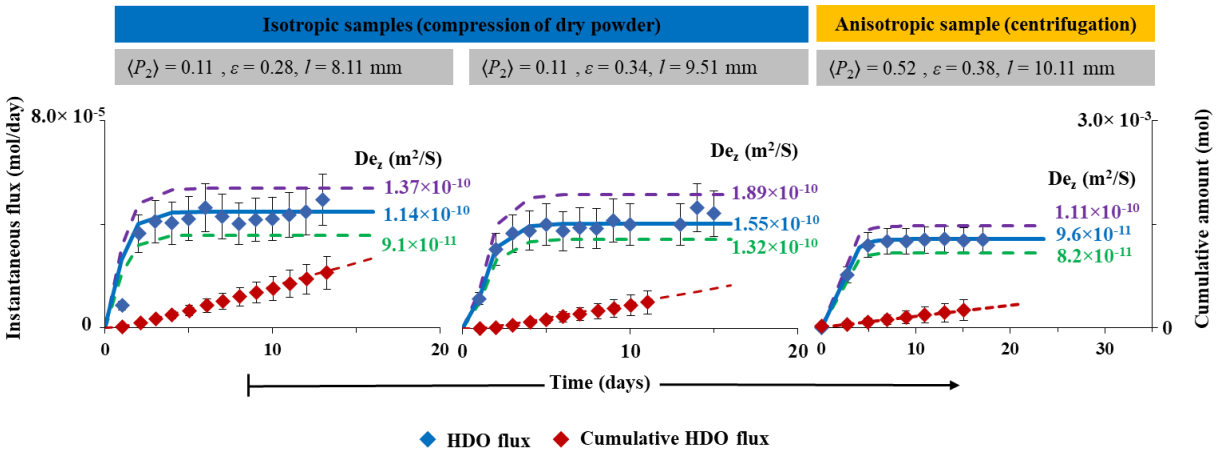


Fig. IV.3. *Experimental instantaneous flux (blue diamonds) and cumulative quantities (red diamonds) of HDO diffusing through IDP samples. The solid blue lines correspond to the fit of the experimental flux, Dashed lines correspond to simulated cumulative curves by considering the diffusion parameters interpreting the average experimental flux (Table IV.1). The scale for the vertical axes is the same for all the charts. ⟨P_2⟩ is the order parameter representing the degree of anisotropy in particles preferred orientation (see text for details). ε is the total porosity value (%).*

l is the sample thickness in mm. Cross-sectional area of the sample perpendicular to the diffusive direction = 7.09×10^{-5} m^2.

In Fig. IV.5, diffusion results of water obtained by BD simulation performed in VPMs at $\varepsilon = 0.27$ are compared to the experimental one obtained with porous media made of Na-IDP and Na-kaolinite particles (from this work ($\varepsilon = 0.26$) and from Glaus et al., (2010) $\varepsilon \approx 0.28$). Data obtained experimentally with both minerals agree with simulated data, and both follow the trend of diminishing De_z with increasing the anisotropy in particles orientation (i.e., increasing ⟨P_2⟩ value). Such agreement confirms that the different VPMs characterized by different porosity and particle organizations well represent the experimental samples, regardless

of differences in length and scales used (see Ferrage et al., (2015) for details). De_z obtained from Na-IDP particles are slightly lower than simulated De_z and experimental data from Na-kaolinite sample, despite being at higher porosity values (Table IV.1).

Although, some of these lower De_z values for Na-IDP samples originate from the difference in the particles size and thus pore geometry compared to Na-kaolinite samples (Table I.2). The main variation can be attributed to the negative structural charge in the IDP particles compared to the non-charged kaolinite particles. Indeed, the negative charge can drastically reduce the mobility of water molecules in the vicinity of external surfaces of the clay particles. Molecular dynamic simulations previously revealed such observation as in (Titiloye and Skipper, 2001; Marry et al., 2002; Malikova et al., 2006; Michot et al., 2012, among others), as well as data obtained by using quasi-elastic neutron scattering (González Sánchez et al., 2008a; Bestel, 2014) using low charge swelling clays, e.g., montmorillonite. In our case, BD simulation was carried out without considering this effect (more details in section IV.2.1), which explains the higher values for simulated data comparing to Na-IDP samples. Anyway, A new simulation package that considers this effect is planned to assess the sensitivity of the simulated data to this parameter; if time permits, the results will be included in the final version of this text. Another factor that can slightly offset the results obtained with IDP samples is the heterogeneity in the particles' preferred orientation within the Na-IDP samples. That is to say that the reported $\langle P_2 \rangle$ values for IDP samples are averaged ones, as illustrated in Fig. IV.1. However, some local heterogeneity may exist in areas with higher or lower $\langle P_2 \rangle$ values than the average ones. For instance, in the centrifuged sample, the average $\langle P_2 \rangle$ value is equal to 0.54, but $\langle P_2 \rangle$ values can reach 0.7/0.8 for some beds (Fig. IV.1b). Hence, areas with a higher $\langle P_2 \rangle$ value than the average one can further reduce water mobility in the porous media.

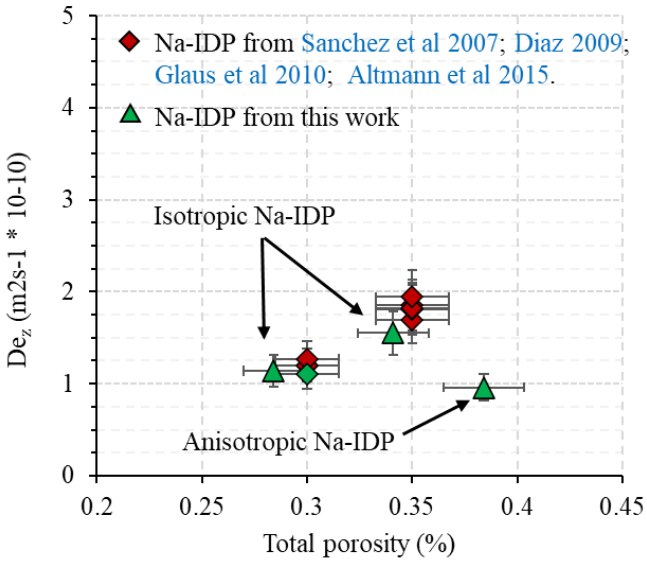


Fig.IV.4. *Comparison between effective diffusion coefficients (De_z) obtained from Na-illite du Puy (IDP) samples from this work and the published ones as function of the sample's total porosity. All De values are corrected from possible temperature variations and are reported for 21°C.*

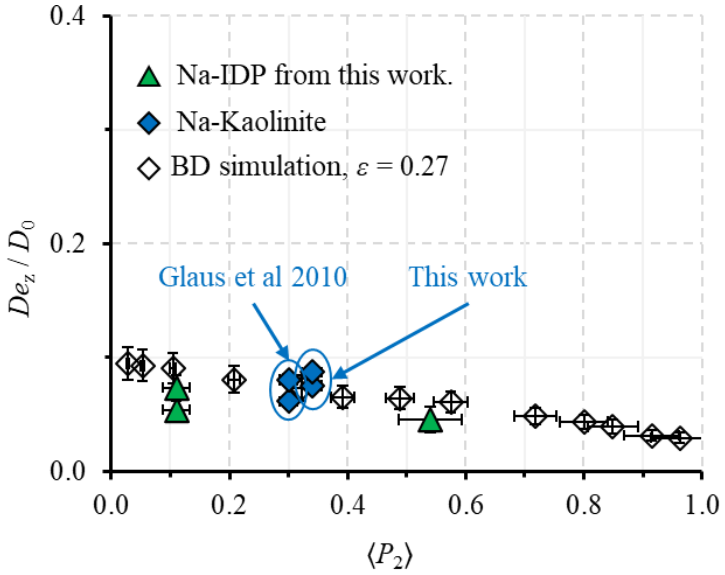


Fig. IV.5. *Comparison between effective diffusion coefficients (De_z) obtained from Brownian dynamics (BD) simulation (non-filled diamonds) performed on virtual porous media (VPMs) and data obtained from TD experiments performed with Na-illite du Puy (IDP) (filled diamonds) and Na-kaolinite (filled triangles) samples from this work and the published ones, as function of the sample's total porosity. All De values are corrected from possible temperature variations and are reported for 21˚C.*

IV.2. Water diffusion in Na-Santa Olalla (SO) vermiculite

IV.2.1. Article; Role of interlayer porosity and particle organization in the diffusion of water in swelling clays

Highlights

- Samples with the same interparticle porosity but different particle organizations.

- Reduction in the overall mobility of water in the presence of interlayer porosity.

- Minor role of interlayer porosity in flux traversing samples.

- Anisotropy in water diffusion is quantitatively related to the preferential orientation of the particles.

Applied Clay Science 207 (2021) 106089

Contents lists available at ScienceDirect

Applied Clay Science

journal homepage: www.elsevier.com/locate/clay

Research Paper

Role of interlayer porosity and particle organization in the diffusion of water in swelling clays

A. Asaad [a,*], F. Hubert [a], E. Ferrage [a], T. Dabat [a], E. Paineau [b], P. Porion [c], S. Savoye [d], B. Gregoire [a], B. Dazas [a], A. Delville [c], E. Tertre [a,*]

[a] IC2MP, Equipe HydrASA, UMR 7285 CNRS/Université de Poitiers, 86073 Poitiers, France [b] Université Paris-Saclay, CNRS, Laboratoire de Physique des Solides, 91405 Orsay, France [c] ICMN, UMR 7374 CNRS/Université d'Orléans, 45071 Orléans, France

[d] Université Paris-Saclay, CEA, Service d'Etude du Comportement de Radionucléides, 91191 Gif-sur-Yvette, France

ARTICLEINFO

Keywords:

Diffusion

Vermiculite

Dual porosity

Particle organization

Water tracer

Diffusion coefficient

ABSTRACT

This study focuses on the role played by the interparticle and interlayer porosities, and the preferred orientation of the particles on water diffusion in dual-porosity clayey media (i.e., swelling clay minerals). For this purpose, we use Na-vermiculite, a swelling clay that does not exhibit osmotic swelling and therefore allows a clear discrimination between the interparticle and interlayer porosities. Two samples were prepared with an equal proportion of interparticle and interlayer porosities (i.e., 0.25 each) but different degree of preferred particle orientation (i.e., isotropic vs anisotropic). Through-diffusion and pulsed gradient spin echo attenuation mea- surements by nuclear magnetic resonance of protons techniques were used to probe water mobility, while the orientation of the particles was quantified by X-ray scattering analysis. Experimental water diffusion results obtained with these two Na-vermiculite samples were compared to those with samples made of Na-kaolinite particles (non-swelling clay mineral) having only interparticle porosities equal to 0.25 and 0.5, corresponding respectively to the interparticle and the total porosity of the Na-vermiculite samples. In addition, these experi- mental results were compared to simulated data using Brownian dynamics with virtual porous media repre- sentative of the real samples. For the range of porosities investigated, a good agreement was observed between measured and simulated water mobilities. The obtained results confirmed the important role played by the preferential orientation of the particles on water dynamics in clayey media, through an important reduction of overall water mobility between the isotropic and anisotropic Na-vermiculite samples. These results also showed that for the same total porosity, the presence of interlayer porosity and associated nano-confinement led to a logical reduction in the pore diffusion coefficient of water in Na-vermiculite in comparison to Na-kaolinite. Moreover, in comparison with Na-kaolinite having the same interparticle porosity, results showed that the contribution of the interlayer volume on the traversing flux was small compared to the interparticle volume. Finally, the computed results revealed that the anisotropy in water diffusion can be directly predicted based on the degree of particles preferred orientation, irrespective of the total or the distribution of the different porosity types.

* Corresponding authors.

E-mail addresses: ali.asaad@univ-poitiers.fr (A. Asaad), emmanuel.tertre@univ-poitiers.fr (E. Tertre).

https://doi.org/10.1016/j.clay.2021.106089

Received 14 December 2020; Received in revised form 29 March 2021; Accepted 31 March 2021

0169-1317/© 2021 Elsevier B.V. All rights reserved.

Introduction

Diffusion is the main transport process in compacted clayey rocks owing to their low hydraulic conductivity (Pusch, 1979; Bourg et al., 2003; Bourg and Tournassat, 2015). This process has been extensively studied, especially in the context of the storage of nuclear waste and CO_2, and resulted in an abundance of experimental data obtained by various methods (such as through-diffusion (TD) experiments using tracers or quasi-elastic neutron scattering) and models describing the diffusion of different elements in clayey media (e.g., Sato and Suzuki, 2003; Van Loon et al., 2004; Andra, 2005; García-Gutiérrez et al., 2006; Landais, 2006; Bachu, 2008; González Sánchez et al., 2008a and b; Glaus et al., 2010; Gimmi and Kosakowski, 2011; Altmann et al., 2015; Savoye et al., 2015; Charlet et al., 2017; Bestel et al., 2018; Dagnelie et al., 2018). Note that these data were obtained for various media constitutive of mono- or multi-clayey phases and considering the presence or not of non-clayey minerals (Shackelford and Moore, 2013; Bourg and Tournassat, 2015; Charlet et al., 2017; Bestel et al., 2018 and references therein).

The organization and connectivity of the pore network are the main parameters that control diffusion of water in clayey media since water is usually inert from a chemical viewpoint (Bourg and Tournassat, 2015 and references therein). The influence of the total porosity value is the parameter that has been the subject of most extensive investigation. Thus, a logical decrease in the water diffusion coefficients with a diminution in the porosity is commonly reported (e.g., Tournassat and Steefel, 2019 and references therein). In contrast, less attention has been paid to the influence of other parameters, such as the preferential orientation of the clay particles, a typical property of these platelet materials in natural aqueous environments (Bennett et al., 1981), or to the distribution of different types of porosities (e.g., interlayer *vs.* interparticle porosity in swelling clay minerals). Nevertheless, by investigating the spatial anisotropy of the diffusion of water tracers in such media, either by TD experiments or by analyzing the 3D distribution of the tracer, several authors (Farver and Yund, 1999; Sato, 2000; Sato and Suzuki, 2003; Suzuki et al., 2004; García-Gutiérrez et al., 2006; Wenk et al., 2008; Wittebroodt et al., 2012; Xiang et al., 2013; Jacops et al., 2017; Dagnelie et al., 2017) have reported a significant diminution of the effective diffusion coefficients (*De*) of water in the direction perpendicular to the sedimentation beds with respect to the parallel direction. Such behavior was attributed to anisotropy in the shape and distribution of the pores between clay particles, resulting from their preferred orientation, as evidenced by either X-ray scattering (XRS, Wenk et al., 2008) or microscopy-imaging techniques (Sato, 2000; Suzuki et al., 2004).

The porosity and preferred orientation of the particles in clayey media are often coupled parameters (a decrease in the porosity leads to an increase in the particle orientation). Hence, it is complicated to discriminate the contribution of each parameter to the overall diffusion process. To overcome such limitation, Dabat et al., (2020) recently proposed a methodology that allow to prepare samples from Na-kaolinite particles (non-porous and non-charged particles) with similar porosity but different degrees of preferential orientation of the particles. These authors succeeded in connecting the anisotropy of the tensor diffusion of the water tracer to the preferential orientation of the particles in these samples for a porosity value of ~ 0.5 based on experimental water diffusion analyses obtained using pulsed gradient spin echo attenuation measurements by nuclear magnetic resonance (PGSE-NMR) and numerical data from Brownian dynamics (BD) simulations using various virtual porous media (VPMs). However, such a relationship remains to be investigated in the case of clay media made of swelling clay particles with two types of porosities (i.e., interlayer and interparticle) being accessible for the water. In such dual-porosity media with charged surfaces, water mobility in the interlayer space can be drastically reduced compared to that in the interparticle porosity, as revealed by molecular dynamic simulations (Titiloye and Skipper, 2001; Marry et al., 2002; Malikova et al., 2006; Michot et al., 2012 among others) and quasi-elastic neutron scattering studies (González Sánchez et al., 2008a; Bestel, 2014) performed on low charge swelling clays, e.g. montmorillonite. Note that this reduced mobility near the surface of the charged clayey particles is usually considered in reactive transport models (i.e., models that couple transport to chemical properties using continuum approaches (Ochs et al., 2001; Tournassat and Steefel, 2019 and references therein), which predict the diffusion of water in complex and heterogenous clayey media. The use of these numerical approaches allow for decoupling the diffusion that occurs in the different types of porosity (i.e., interlayer *vs.* interparticle porosities), while discrete models (e.g., molecular dynamics, random walk or BD simulations) also allow consideration of the specific role of the particles' preferred orientation on the diffusion properties (e.g., Churakov and Gimmi, 2011; Tyagi et al., 2013; Bacle et al., 2016; Gimmi and Churakov, 2019; Dabat et al., 2020; Underwood and Bourg, 2020). Beyond such numerical approaches, existing experimental water diffusion data in dual-porosity media were almost exclusively obtained with smectite particles (e.g., Bourg and Tournassat, 2015 and references therein). This mineral display, however, osmotic swelling in water-saturated conditions (i.e., incorporation of an ill-defined number of water molecules between the layers (Abend and Lagaly, 2000; Liu, 2013; Tertre et al., 2018 among others), which hampers the calculation of the respective interlayer and interparticle porosity volumes. In the scope of quantitatively discussing the role played by

interlayer and interparticle porosities on the diffusion of water, as well as by the preferred orientation of the clay particles, additional experimental data on dual-porosity clay media that are not sensitive to osmotic swelling are required. For this purpose, vermiculite clay mineral represents an ideal candidate. Vermiculite is a swelling clay mineral with a structure similar to smectite. However, owing to the higher layer charge, this mineral does not display osmotic swelling (Faurel, 2012) and exhibits well-defined interlayer volumes in water-saturated conditions, which allows for a better determination of the different interlayer and interparticle volumes in the samples. Tertre et al. (2018) used this mineral to perform water tracer diffusion experiments and highlighted the notable differences in the effective diffusion coefficients obtained in vermiculite compared to montmorillonite for similar total porosities. Moreover, by comparison with experimental data reported for kaolinite, these authors noticed that the experimental data were similar for the same interparticle porosity value. However, because the preferred orientation of the clay particles was not measured, it was not possible to deduce information on the contribution of different parameters (the porosity distribution or particles' orientation) to the overall water diffusion process.

The present study represents an extension of the work of Tertre et al. (2018) and the recent approach proposed by Dabat et al. (2020) for kaolinite clay mineral (at a porosity value of ~0.5), to the dual-porosity media made of Na-vermiculite particles. In this work, an experimental methodology was developed to obtain vermiculite samples with two degrees of preferential particle orientation, as measured by XRS analysis, for the same total porosity of 50% (the same total porosity used by Dabat et al. (2020) for Na-kaolinite samples). In such conditions, Na-vermiculite is composed of an equal proportion of interlayer and interparticle porosity proportions (i.e., ~ 0.25). Experimental diffusion data on water tracer (HDO) in these media were obtained using TD experiments that allow to determine the effective diffusion coefficients in the direction perpendicular to the sedimentation plane of the particles. To complete the experimental dataset on water diffusion, the sample set also included an additional clay medium of Na-kaolinite with a total porosity of ~ 0.25 (i.e., similar interparticle porosity as with Na-vermiculite). For this sample, both the TD and PGSE-NMR results on water diffusion were obtained to assess the concordance of the two methods on the analysis of water diffusion despite the significant difference in the timescales probed for water dynamics (i.e., ms and days for the PGSE-NMR and TD experiments, respectively). Following a coupled experimental-computational approach (Dabat et al., 2020), all these data were systematically compared to the results obtained by BD simulations, which were performed with 3D virtual porous media,

generated to mimic the real ones in terms of mineralogy and porosity distribution, while also covering a large range of anisotropy degrees in particle orientations.

2. Materials and Methods

2.1. Materials

The vermiculite used in this study is from Santa Olalla (Huelva, Spain; Gonzáles García and García Ramos, 1960; De La Calle et al., 1977). In its original form, the centimetric vermiculite crystals are Mg^{2+}-saturated with a structural formula (Marcos et al., 2003; Arguelles et al., 2010): $[(Mg_{4.92}Fe_{0.44}Al_{0.60}Ti_{0.04})\ (Si_{5.66}Al_{2.34})O_{20}(OH)_4](Mg_{0.76}Ca_{0.06}Na_{0.04}),\ 7.63H_2O]$. The 0.1-0.2 µm particle size fraction, used for this study, was obtained by sonication and centrifugation methods using the protocol established by Reinholdt et al., (2013). The kaolinite used is KGa-2 from the Source Clay Repository of the Clay Mineral Society, with an average size of the particles of approximately 0.5 µm (Hassan et al., 2005), and a structural formula (Mermut and Cano, 2001) of $[(Al_{3.80}Ti_{0.13}Fe^{3+}_{0.07})\ (Si_{3.84}Al_{0.16})O_5(OH_4)]$.

Both materials were exchanged into homoionic Na^+ form (i.e., Na-kaolinite and Na-vermiculite) using five saturation cycles with a 1-M NaCl solution, followed by removal of excess of salt by dialysis using a 6-8 KD membrane until test with silver nitrate was negative. Compacted samples were prepared from the dialyzed clay dispersion dried at 60°C and then sieved through a 50 µm mesh to remove the coarsest aggregates. A centrifuged sample made of Na-vermiculite particles was prepared directly from the dialyzed dispersion and was then stored at 4°C.

2.2. Preparation of samples with contrasted anisotropy in particle orientation

The methodology used to prepare compacted Na-kaolinite for PGSE-NMR experiments as well as experimental setup and acquisition conditions are detailed in section S1.1 in Supplementary Data (S. D.). For TD experiments, the isotropic samples were prepared by uniaxial compaction of dried clay powder in (poly)methyl methacrylate (PMMA) tubes (diameter of 0.95 cm and a height of 7 cm) as in Tertre et al. (2018). By contrast, a new protocol was developed in the present study to build an anisotropic Na-vermiculite medium with the same total porosity (ε) as the one obtained by compaction. This protocol is illustrated in Fig. 1 and was developed based on the centrifugation process used by Dabat et al., (2020) to prepare Na-kaolinite samples. It first consists of transferring 3 mL of Na-vermiculite dispersion (20 g/L) into PMMA tube designed to be mounted directly into the TD cell to avoid sample transfer and the associated potential damage (Fig. 1a). After a horizontal centrifugation run at

~23850 g for 25 minutes (Centrifuge Avanti J 301, rotor JS-24.38 from Beckman Coulter® (Fig. 1b)), the clear supernatant was removed, and a new aliquot was added (Fig. 1c). These steps were repeated ten times to obtain a sufficient mass in the tube (Fig. 1d). After centrifugation, it was necessary to dry the sample to determine its dried mass used in ε calculation (details in the next paragraph). However, because drying by heating can introduce an important shrinkage of samples and distortion of their structure (Loeber, 1992; Durrieu et al., 1997), a methodology previously developed for clay cakes (Loeber, 1992; Pret, 2003) was applied to preserve, as best as possible, the geometry and particle organization in the sample. Accordingly, the sample was first flash frozen by immersion in slush nitrogen (SN_2) for 2-5 minutes (Fig. 1e) and then dried by lyophilization at – 40°C for 2-3 hours. Complete water removal was insured when the sample maintained a stable mass during the last hour of lyophilization (Fig. 1f). Finally, the sample was mounted to the TD cell, uniaxially compressed to the desired height (Fig. 1g-h).

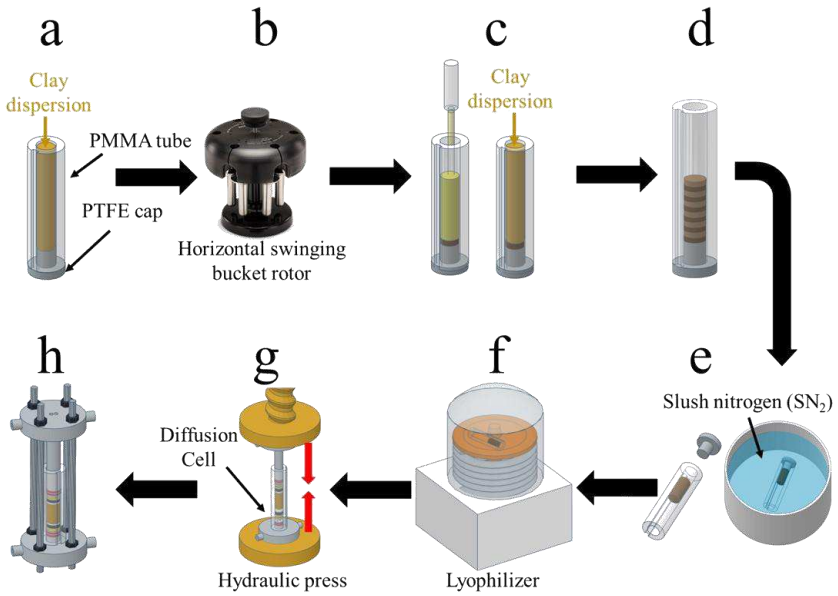


Fig. 1. *Illustration of the methodology used to prepare Na-vermiculite samples with a high degree of particles' preferred orientation. (a-d) Oriented sample is prepared by 10 runs of centrifugation of Na-vermiculite dispersion in (poly)methyl methacrylate (PMMA) tubes sealed from the bottom with (poly)tetrafluoroethylene (PTFE) caps and by removal of the supernatant after each centrifugation run. (e-f) Preparation of slush nitrogen and freezing of the sample followed by lyophilization. (g-h) Mounting the sample into the diffusion cell and compaction to a certain thickness to reach the desired total porosity value (see Section 2.2), the final thickness of the diffusion cell is maintained by threaded rods and nuts.*

The final thickness (L) of all samples prepared for this study are reported in Table 1. Total porosity ε was calculated as difference between the sample volume (considering the diameter of the tube and the sample's L), and the volume occupied by the solid only (i.e., clay particles), which was determined based on the sample dry mass (at the end of the lyophilization process) and clay grain density. The latter was calculated to be 2.62 g cm^{-3} for Na-kaolinite based on the structural formula and the crystal structure parameters refined for KGa-2 kaolinite by Sakharov et al. (2016) and 2.73 g cm^{-3} for Na-vermiculite using the (a,b) cell parameters and the chemical composition of the 2:1 layer reported by Arguelles et al. (2010) and the c* parameter (i.e., the basal spacing) value for dehydrated layers at 10 Å (Gieseking, 1975). However, Na-vermiculite displays a mono-hydrated state (1W) at room humidity and a bi-hydrated state (2W) in water-saturated conditions, respectively (Faurel, 2012). Consequently, two hydrated densities of 2.49 and 2.24 g cm^{3} for 1W and 2W Na-vermiculite, respectively were calculated based on water content and c* parameters derived by Faurel. (2012) for 1W (4.13 $H_2O/O_{20}(OH)_4$, c* = 11.97 Å) and 2W layers (9.9 $H_2O/O_{20}(OH)_4$, c* = 14.86 Å). Note that for Na-kaolinite, only the interparticle porosity ($\varepsilon_{interp.}$) is accessible by the water tracer, resulting in $\varepsilon = \varepsilon_{interp.}$, whereas Na-vermiculite exhibits both $\varepsilon_{interp.}$ and interlayer porosity ($\varepsilon_{interl.}$). By considering the difference in the c* parameter value between dehydrated layers at 10 Å (Gieseking, 1975) and fully water saturated layers at 14.86 Å (Faurel, 2012), the interlayer volume corresponds approximately to 1/3 of the particle thickness in water-saturated conditions. Consequently, the proportion of the $\varepsilon_{interp.}$ *vs.* $\varepsilon_{interl.}$ porosities for Na-vermiculite (Table 1) can be calculated for such conditions by using the following relation:

$$\varepsilon = \varepsilon_{interp.} + \varepsilon_{interl.} = \varepsilon_{interp.} + (1 - \varepsilon_{interp.})/3 \quad (1)$$

Finally, for each sample used in this study, a duplicate was prepared to be used for particle organization measurements.

***Table 1**. Experimental results for water tracer (HDO) in Na-kaolinite and Na-vermiculite from through-Diffusion (TD) and ^1H NMR pulsed gradient spin echo (PGSE-NMR) experiments, and the properties of the porous media used (material, thickness, porosity, degree in preferred orientation).*

	Na-kaolinite	Na-kaolinite	Na-vermiculite	Na-vermiculite
Preparation method	Compaction	Compaction	Compaction	Centrifugation
Experimental technique	PGSE-NMR	TD	TD	TD
Sample thick., L (mm)	10.00 ± 0.10	6.00 ± 0.10	7.99 ± 0.10	6.44 ± 0.10
Total porosity, ε	0.26 ± 0.02	0.26 ± 0.02	0.49 ± 0.02	0.49 ± 0.02
Interparticle poro., $\varepsilon_{interp.}$	0.26 ± 0.02	0.26 ± 0.02	0.24 ± 0.02	0.24 ± 0.02
Interlayer poro., $\varepsilon_{interl.}$	0.00 ± 0.02	0.00 ± 0.02	0.26 ± 0.02	0.26 ± 0.02
Order parameter, $\langle P_2 \rangle$	0.34 ± 0.02	0.34 ± 0.02	0.03 ± 0.02	0.41 ± 0.06
Dp_z [a] ($\times 10^{-10}$ m^2 s^{-1})	5.77 (5.19-6.35)	6.92 (5.38-9.23)	3.61 (3.06-4.49)	1.82 (1.37-2.27)
De_z [b] ($\times 10^{-10}$ m^2 s^{-1})	1.50 (1.35-1.65)	1.80 (1.40-2.40)	1.80 (1.50-2.20)	0.89 (0.67-1.11)
Dp_z/D_0 [c]	0.29 (0.26-0.32)	0.34 (0.26-0.45)	0.18 (0.15-0.22)	0.09 (0.07-0.11)
De_z/D_0 [d]	0.08 (0.07-0.08)	0.09 (0.07-0.12)	0.09 (0.07-0.11)	0.04 (0.03-0.05)
α [e]	-	0.30 (0.25-0.34)	0.49 (0.40-0.80)	0.49 (0.40-0.70)
K_d [f] (mL g^{-1})	-	0.02 (0.00-0.04)	0.00 (0.00-0.22)	0.00 (0.00-0.15)

[a] Pore diffusion coefficient of water in the direction perpendicular to the preferred orientation of the particles.

[b] Effective diffusion coefficient of water in the direction perpendicular to the preferred orientation of the particles.

[c] Pore diffusion coefficient of water normalized to the self-diffusion coefficient of HDO in bulk water.

[d] Effective diffusion coefficient of water normalized to the self-diffusion coefficient of HDO in bulk water.

[e] Rock capacity factor (see Eq. (S2) in S.D.).

[f] Distribution coefficient (see Eq. (S2) in S.D.).

2.3. Measurements of preferred orientation of clay particles through the $\langle P_2 \rangle$ order parameter

The degree of anisotropy in the orientation of clay particles in the samples used in this work was obtained from two-dimensional X-Ray Scattering (2D-XRS) patterns recorded from the duplicate samples. The measurements were performed at the Laboratoire de Physique des Solides (LPS) - Orsay, France. Sample preparation method (i.e., induration and slicing) and

2D-XRS acquisition parameters are detailed in S. D. (S.1.2). In this work, the degree of anisotropy in the orientation of clay platelets is reported in terms of $\langle P_2 \rangle$ order parameter values also referred to as the nematic order *S* (Dabat et al., 2018; Underwood and Bourg, 2020) or the Hermans parameter *H* (Hermans and Platzek, 1939). The $\langle P_2 \rangle$ order parameter can be derived from the orientation distribution functions (ODF) (Dabat et al., 2019, 2020 and references therein) obtained from 2D-XRS patterns. Briefly, in a spherical coordinate, the orientation of a platelet shape clay particle can be defined as a function of two angles: θ, which is the azimuthal angle between the normal of the particle (vector that is perpendicular to the basal surface of the particle) and the z axis, and Φ, the polar angle in the (*xy*) plane (Fig. 2a). For particles with uniaxial symmetry (i.e., clay particles for which their z axis is the only symmetry axis as in this study, Wenk et al. (2010) and references therein) the probability for a particle orientation over all possible Φ angle values is equal. Therefore, the orientation of a clay platelet (ODF) can be described as a function of only its θ angle, i.e., $f(\theta)$, with the following constraints:

$$f(\theta) \geq 0 \tag{2}$$

$$f(\theta) = f(\pi - \theta) \tag{3}$$

$$\int_0^{\pi} f(\theta)\, sin(\theta) d\theta = 1 \tag{4}$$

Eqs. (2) and (3) indicate that the ODF is always positive, with the same probability of the particles pointing upward or downward. The term $f(\theta)\sin(\theta)$ in Eq. (4) corresponds to the normalization over all the particles in the sample. From the 2D-XRS patterns, the scattered intensities (*I*) of the 001 Bragg peak modulated as a function of the angle τ (the angle between the normal of the incident beam and the surface of the 2D-detector), and the angle θ (Fig. 2b). Because of the position of the 001 reflection at low scattering angles ($2\theta_B$), the hypothesis $\theta = \tau$ is a valid approximation (Dabat et al., 2019). Hence, the ODF $f(\theta)$ can be expressed from the scattered intensity $I(\theta)$ evolution integrated from the 2D-XRS patterns as follows:

$$f(\theta) = \frac{I(\theta)}{\int_0^{\pi} I(\theta) sin(\theta) d\theta} \tag{5}$$

The ODF $f(\theta)$ can also be written with a second order Legendre polynomial as follows:

$$\langle P_2 \rangle = \int_0^{\pi} \langle P_2 \rangle (cos\theta).f(\theta) sin(\theta) d\theta \tag{6}$$

Finally, average value of $\langle P_2 \rangle$ calculated over the angular distribution using Eq. (6), is comprised between 0 for an isotropic particle organization and 1 for a perfectly anisotropic organization with all particles having the same preferred orientation (i.e., bedding plane).

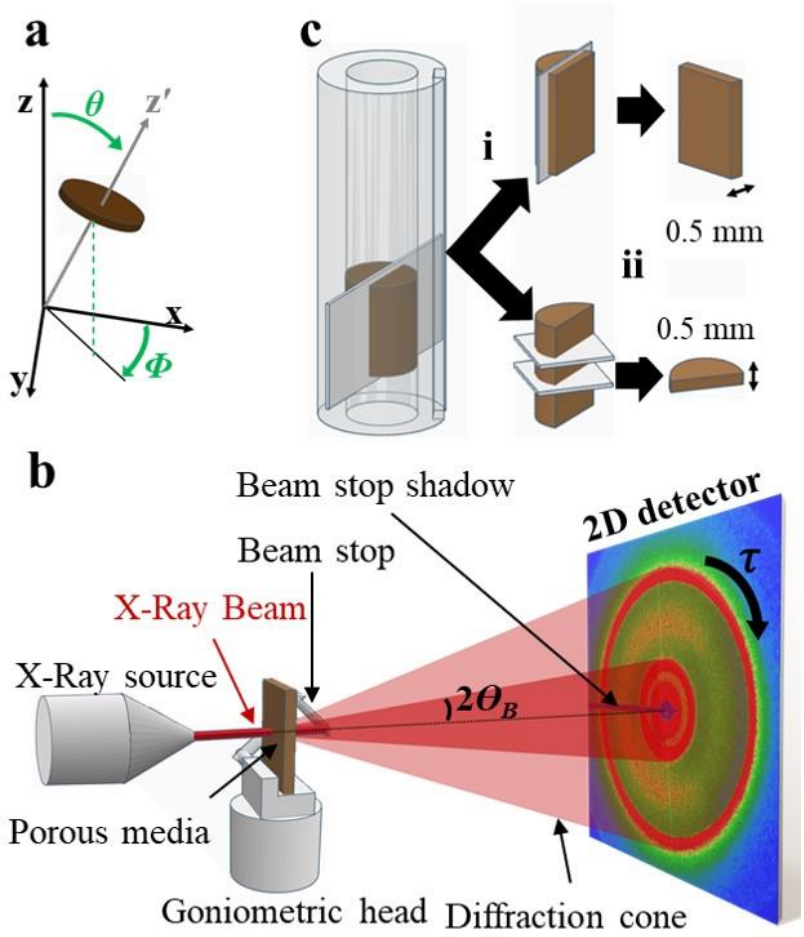


Fig. 2. *Experimental measurement of the particle orientation in clayey samples using an X-ray scattering technique with a 2D-detector (2D-XRS). (a) Spherical coordinates (ρ, θ, Φ) with respect to the sample tube (laboratory frame: (x,y,z)) and the angles (θ, Φ) describing the orientation of the normal (Oz') of an individual clay particle. (b) The 2D-XRS instrumental setup and measurement of the particle orientation by azimuthal integration (along τ) of the scattered intensity. (c) Illustration of the method to cut the indurated sample into lamellas: (i) the indurated sample is cut into two vertical halves, (ii) cutting the longitudinal and transversal lamellas (the cutting planes are shown in light color cuboid). The lamellas are reduced to a thickness of 500 µm by polishing.*

2.4. Water diffusion measurement in Na-vermiculite and kaolinite samples

Experimental water diffusion coefficients were obtained from Na-vermiculite and Na-kaolinite samples using PGSE-NMR and TD of the water tracer (HDO) experiments. Sample preparation, acquisition parameters, and data treatment are detailed in the S. D. (sections S.1.1 and S.1.3, respectively). It is important to note that the analysis of the TD results allow to obtain

the effective diffusion coefficient *De* of HDO in the *z*-direction of the tube (De_z), i.e., perpendicular to the compression direction/centrifugation plane of the sample, while the PGSE-NMR analysis allows to obtain the pore diffusion coefficients Dp_z and $Dp_{x,y}$.

De_z is defined from the self- diffusion coefficient of species in bulk water (D_0) by the following equation (Bear, 1972; Dykhuizen and Casey, 1989; Bourg et al., 2006):

$$De = \frac{\varepsilon}{G} D_0 \tag{7}$$

where ε is the accessible porosity for the tracer, and *G* the geometrical factor (tortuosity factor), which describes the impact of the pore-network geometry (pore shape, particle orientation, connectivity, and constrictively). The pore diffusion *Dp* can also be related to D_0 as follows:

$$Dp = \frac{1}{G} D_0 \tag{8}$$

Hence, in the case of water tracers for which the total porosity is accessible to diffusion and no adsorption occurs, the pore and effective diffusion coefficients are related to ε as follows:

$$De = \varepsilon\, Dp \tag{9}$$

2.5. Brownian dynamics simulations of water diffusion in virtual porous media

Mesoscale Brownian dynamics simulations of water diffusion in both Na-vermiculite and Na-kaolinite as a function of the anisotropy in the particles' orientation were performed on 3D virtual porous media (VPM). To cover a large range of anisotropy degrees in particle orientations, 13 particle packings were generated with $\langle P_2 \rangle$ values varied from 0.03 to 0.96 (Ferrage et al., 2018; Dabat et al., 2020); see Table. S1 in S. D., and Fig. 3a), mimicking the distribution of the shapes and sizes of the particles in these samples. The description of the generation of these VPM is detailed in S.1.4 of S. D.

Brownian dynamics simulations were performed according to the methodology detailed by Dabat et al. (2020). For the case where the time step δt is much larger than the velocity correlation time γ_i of probe i (i.e., $\gamma_i \delta t \gg 1$), and considering the probe's displacements as completely independent, the displacement of molecular probes in the framework of the general Langevin equation can be reduced as follows (Gunsteren et al., 1981):

$$\vec{x}_i(t + \delta t) = \vec{x}_i(t) + \vec{R}_i \tag{10}$$

with the random force $\vec{R}_i$ that satisfies a Gaussian distribution function with zero mean and standard deviation given by

$$\langle {R_i}^2 \rangle = 2 D_i \delta t \tag{11}$$

where D_i is the molecular self-diffusion of probe i. For diffusion within unrestricted isotropic media, the modulus of the random 3D displacements is quantified by the self-diffusion propagator, i.e., the density of the probability of the displacement distribution law (Callaghan, 1991; Bacle et al., 2016):

$$P(\vec{r},\Delta \mid \vec{r}_0\ ,0) = \{4\pi D\Delta\}^{-3/2} exp\left[-\frac{(\vec{r}-\vec{r}_0)^2}{4D\Delta}\right] \quad (12)$$

where Δ is the diffusion time. The self-diffusion propagator that quantifies the mobility along a single director is then defined by

$$P_\alpha(\overrightarrow{r_\alpha},\Delta \mid \overrightarrow{r_{\alpha_0}},0) = \{4\pi D_\alpha\Delta\}^{-1/2} exp\left[-\frac{(\overrightarrow{r_\alpha}-\overrightarrow{r_{\alpha_0}})^2}{4D_\alpha\Delta}\right] \quad (13)$$

where D_α is the component of the self-diffusion tensor that describes the mobility of the probe along the selected $\overrightarrow{e_\alpha}$ director (Callaghan, 1991).

For the BD simulations of water diffusion in Na-kaolinite with only interparticle porosity, the same methodology as used by Dabat et al. (2020) was applied. However, in contrast to simulations performed in this latter study, the size of the simulation box was not adapted to the size of the kaolinite particles. Indeed, in the absence of grain porosity and without consideration of specific interfacial effects on the probe dynamics, a mesoscopic simulation is independent of the particle size, given that the time step is correctly adapted to the modification of the length scale. Accordingly, the same simulation box as for Na-vermiculite (Table S1) was used to compute the water diffusion in the kaolinite samples. Such a consideration is also supported by the similar aspect ratios of particles for both types of minerals (0.08 and 0.07 for Na-vermiculite and kaolinite, respectively) (Hassan et al., 2005; Reinholdt et al., 2013). For interparticle diffusion in a kaolinite sample, a number N = 2000 of water probes with molecular self-diffusion D_0 set at $2.3.10^{-9}$ m^2 s^{-1} were introduced randomly into the interparticle porosity of the VPMs. A time step δt = 200 ps, over a total simulation time of 0.12 ms, was considered, and additional tests showed that smaller values did not provide a difference in the simulation results. During the simulations, the collision with the surface of the Na-kaolinite particles was treated as a Maxwell's A wall with the angular probability $f_A(\theta, f)$ of water probes rebounding from the surface given by

$$f_A(\theta,\phi)d\Omega = \cos\theta\ d\Omega/\pi \quad (14)$$

where θ and f are the usual polar and azimuthal angles (with respect to the normal of the surface of the particle), and $d\Omega$ is the element of the solid angle (Fig. 3b). That condition mimics the trajectory of a molecule by assuming a residence time at the solid surface that is long enough

to thermalize its velocity distribution function before being desorbed and returning to the fluid (Valleau et al., 1991).

For BD simulations of water diffusion in Na-vermiculite, the water probes were allowed to diffuse in both the $\varepsilon_{interp.}$ and $\varepsilon_{interl.}$ porosities. For the interparticle porosity values reported in Table S1, the total porosity of the VPM is calculated according to Eq. (1). The self-diffusion coefficients for the water molecules in the interlayer space $D_{interl.}$ were extracted from previous molecular dynamics simulations performed by Tertre et al. (2015) for Na-vermiculite. Although these authors only reported the self-diffusion coefficients for Na^+, the associated bi-dimensional self-diffusion coefficient for the water molecules was found to be at $D_{interl.} = 2.3.10^{-10}$ m^2 s^{-1}. Such a value is one order of magnitude lower than that of bulk water and is in agreement with numerical MD results and experimental quasi-elastic neutron scattering results obtained for tetrahedrally-charged trioctahedral saponite with different layer charges (Michot et al., 2012). Note that the obtained $D_{interl.}$ value is lower than commonly reported for montmorillonite (Swenson et al., 2000; Marry and Turq, 2003; Malikova et al., 2005, 2006; Skipper et al., 2006), related to the lower charge and location of the charge in the octahedral sheet of this mineral. For the initial configuration of the BD simulations, the 2000 water probes were randomly introduced in the simulation box with an acceptance probability of 1/3 when the probe was included in the solid. The same time step and simulation time as for water diffusion restricted to the interparticle porosity only was considered. During the simulation (Fig. 3c), the probes colliding with the basal surface of the particles were allowed to rebound according to Eq. (11), whereas a specific condition occurred in the case where the probe was in contact with a lateral surface. In such a condition, based on a system at equilibrium (Bacle et al., 2016), the probe was allowed to penetrate (or leave) the interlayer space of the particle according to the acceptance rule:

$$p_{acc}^{i\to j} = \min\left[1; \frac{p^j}{p^i} \times \frac{p_{gen}^{j\to i}}{p_{gen}^{i\to j}}\right] = \min\left[1; \frac{c_j}{c_i} \times \left(\frac{D_i}{D_j}\right)^{3/2} \times \exp\left(-\frac{\ell^2}{4D_j\delta t} + \frac{\ell^2}{4D_i\delta t}\right)\right] \quad (18)$$

where ℓ is the modulus of the displacement from Eq. (11), and c_i and c_j are the water probe concentrations in the environments i and j, respectively, with self-diffusion coefficients D_i and D_j. In the case of the probe that did not satisfy the acceptance rule to penetrate in the interlayer porosity, a rebound was then considered according to Eq. (14) (Fig. 3c).

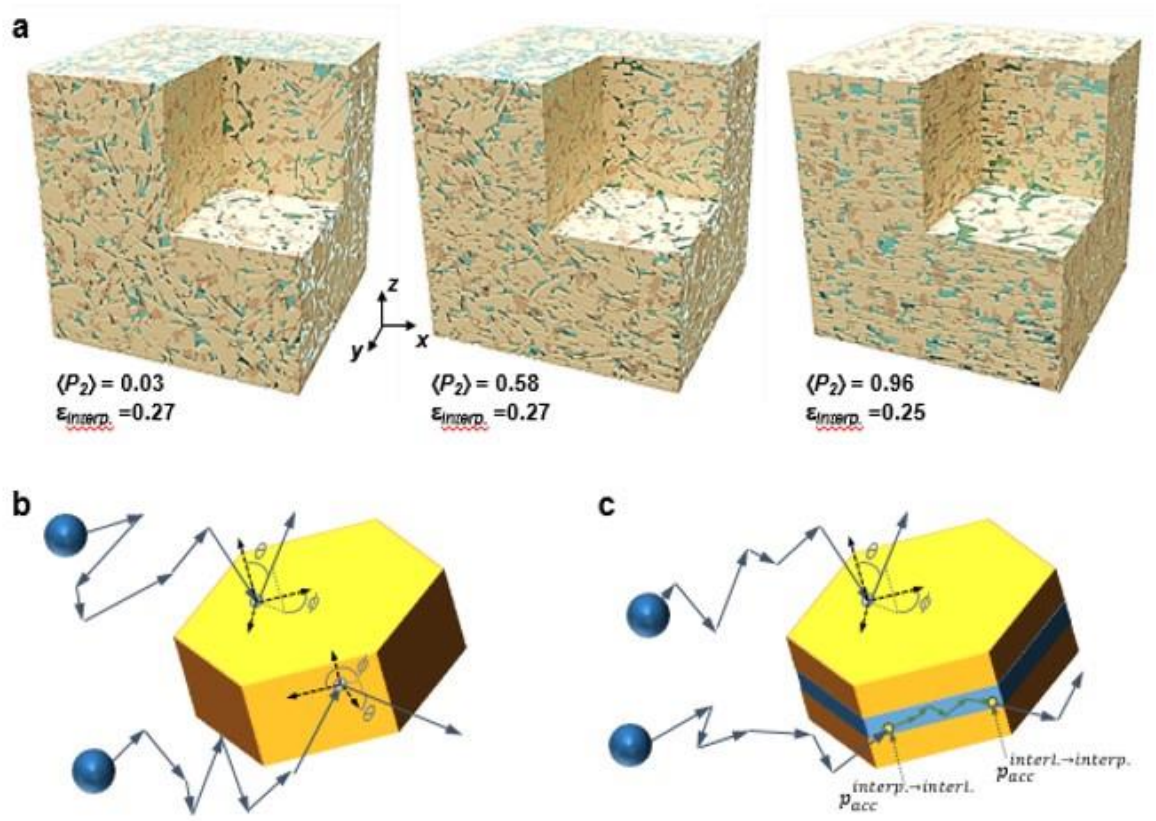


Fig. 3. *(a) Virtual porous media with similar interparticle porosity ($\varepsilon_{interp.}$) values but different anisotropy degrees in particle orientation (i.e., $\langle P_2 \rangle$ order parameter). (b) Illustration of Brownian dynamics displacements of water molecules in an Na-kaolinite sample. Water probes, with a self-diffusion coefficient D_0, diffuse in the interparticle porosity. A rebound of the water probe on a basal or lateral surface of the particle is treated according to Maxwell's A wall (see text for details). (c) Brownian dynamics of water diffusion in Na-vermiculite. The water probe, initially in the interparticle porosity and diffusing with D_0 as the self-diffusion coefficient, can either rebound on the basal surface or penetrate the interlayer space of the particle according to the acceptance rule $p_{acc}^{interp.\rightarrow interl.}$. If the acceptance rule is satisfied, the probe then diffuses in the interlayer space according to the self-diffusion coefficient $D_{interl.}$, which was extracted from molecular dynamics. Eventually, the water probe can leave the particle and go back to the interparticle porosity according to the acceptance rule $p_{acc}^{interl.\rightarrow interp.}$.*

For simulations of water diffusion in both Na-kaolinite and Na-vermiculite, the pore water diffusion coefficients Dp_α along a selected $\overrightarrow{e_\alpha}$ director were extracted from the asymptotic slope of the radial mean squared displacement, as follows:

$$Dp_\alpha = \lim_{\Delta \to \infty} \frac{\sum_{i=1}^{N} (x_{i,\alpha}(0) - x_{i,\alpha}(\Delta))^2}{2N\Delta} \quad (19)$$

where α refers to the single direction $\overrightarrow{e_\alpha}$ on which the mobility is extracted (other parameters were already defined above; uncertainty on the calculated Dp_α values were estimated at 10%).

3. Results and discussion

Measurement of preferred orientation of clay particles

For each sample, longitudinal and transverse 2D-XRS patterns were recorded (Fig. 2b, c) with respect to the sample tube axis (i.e., the direction of compaction/preferred orientation of clay particles) (Fig. 2a). These patterns are reported in Fig. 4a with their corresponding ODFs (Fig. 4b), whereas $\langle P_2 \rangle$ values extracted from these ODFs are reported in Table 1. For all samples, the transverse ODFs (in gray) remain approximately constant regardless of the θ angle (Fig. 4b), which indicates that the transverse lamellas are isotropic, as expected for lamellas sliced in the direction parallel to the preferred orientation of the clay particles. On the other hand, the longitudinal ODFs (in black) display symmetric profiles, which denotes a degree of anisotropy in the particles' orientation in this direction.

The longitudinal ODF of a Na-kaolinite sample prepared by compaction displays a reversed bell-shaped curve, which indicates a main preferred orientation for most of the clay particles in this sample. The corresponding $\langle P_2 \rangle$ value of 0.34 ± 0.025 was averaged from several measurement points. For Na-vermiculite samples, the corresponding longitudinal ODFs display different shapes, as reflected by their contrasted $\langle P_2 \rangle$ values of 0.03 ± 0.025 and 0.41 ± 0.06 for the compacted and centrifuged samples, respectively. For the purpose of this study, the contrast in the $\langle P_2 \rangle$ values between the two samples are sufficient for investigating the effect of the particles' organization on the diffusion of HDO. Uncertainties on the $\langle P_2 \rangle$ values were considered to be the standard deviation (STD) of a population of several measurement points from the same sample.

The relatively higher uncertainty for the $\langle P_2 \rangle$ values obtained from the centrifuged sample with respect to the compacted values (± 0.06 and ± 0.025, respectively) can be attributed to the influence of the preparation method (uniaxial compaction *vs* centrifuging). For example, in the case of a centrifuged sample, with a slight variation in the solid-solution ratio, hydrostatic or shear forces, and particles segregation between successive centrifuging cycles led to formation of successive beds with some heterogeneity in the particles' preferred orientation among them. Similarly, Dabat et al. (2020) also reported a slightly higher uncertainty for the $\langle P_2 \rangle$ value of

centrifuged Na-kaolinite samples (i.e., anisotropic) than for the more isotropic values obtained by compaction.

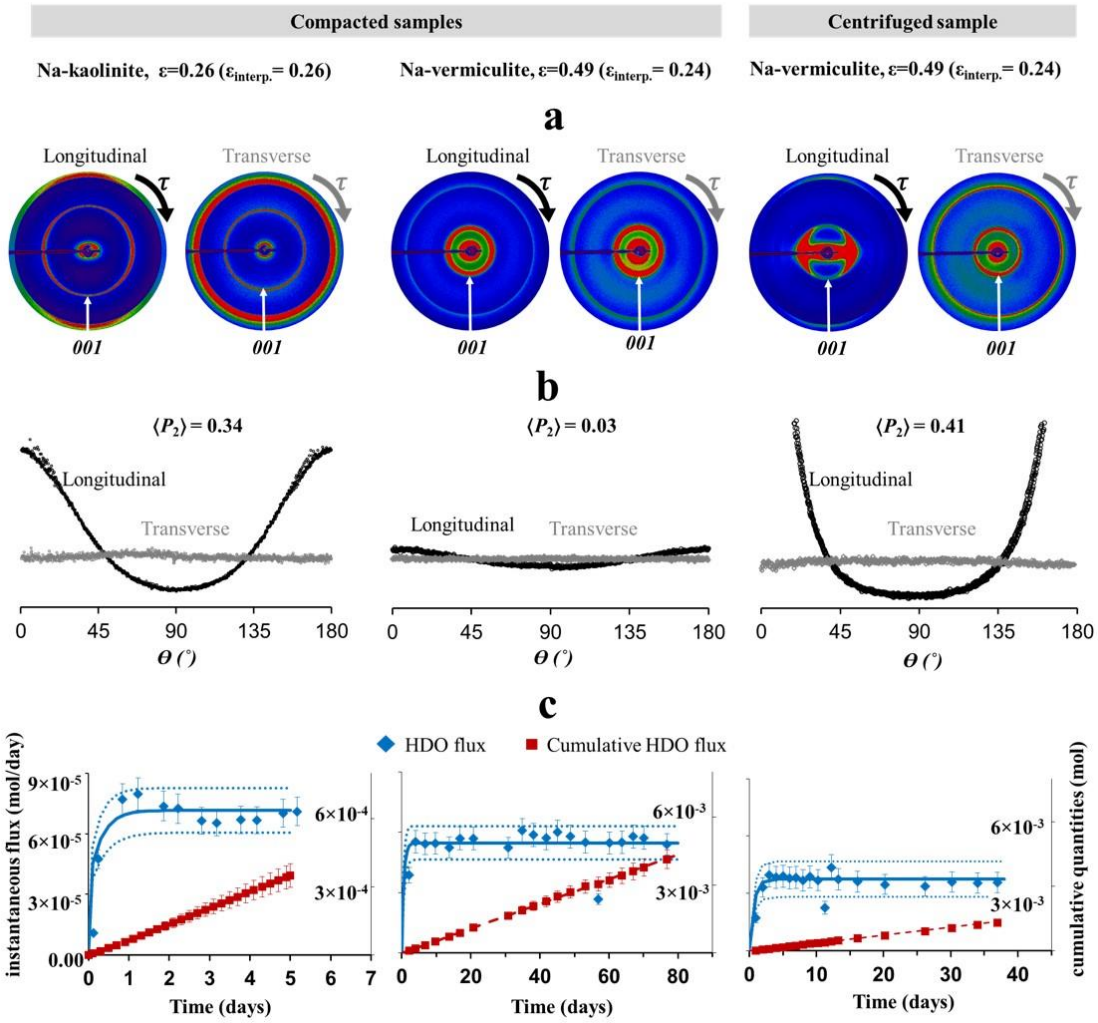


Fig. 4. *Results from particle orientation and water tracer (HDO) through–diffusion (TD) measurements for Na-kaolinite and Na-vermiculite samples. (a) 2D-patterns obtained by X-ray scattering technique from longitudinal and transverse lamellas (description in Fig. 2). Color scale ranges from light gray to black with increasing scattered intensity. (b) Orientation distribution functions (ODF) extracted from an azimuthal scan over 180° along the 001 reflection from longitudinal (black) and transverse (gray) lamellas. The intensities are normalized to the same value for comparison. (c) Experimental instantaneous flux (black diamonds) and cumulative quantities (gray squares) of HDO diffusing through the samples. The solid lines correspond to the fit of the experimental flux, whereas dotted lines are simulated flux curves calculated by considering the error range in the diffusion parameters (Table 1). Dashed lines correspond to simulated cumulative curves by considering the diffusion parameters interpreting the average experimental flux. The scale for the instantaneous flux axis is the same for all the charts.*

3.2. Water diffusion in Na-kaolinite

The HDO mobility in Na-Kaolinite samples ($\varepsilon = 0.26 \pm 0.025$, $\langle P_2 \rangle = 0.34 \pm 0.02$) was investigated in the direction of the compaction axis (normal to the preferred orientation of clay particles) with two analytical methods: PGSE-NMR and TD (see sections 2.4). The results from both experiments are reported in terms of the pore diffusion coefficient (Dp_z) and effective diffusion coefficient (De_z) (definitions in Section 2.4) in Table.1.

Data reported from Tertre et al. (2018) concerning the instantaneous flux of HDO measured in the downstream reservoir during TD experiments in this sample are shown in Fig. 4c. These data were interpreted with a De_z equal to 1.8 (1.4-2.4) $\times 10^{-10}$ m^2 s^{-1} and a rock capacity factor (α) value equal to ε ($\alpha = 0.30$ (0.25-0.34) *vs.* $\varepsilon = 0.26 \pm 0.02$), which allows us to confirm that HDO is an inert tracer for this sample (i.e., no significant HDO adsorption).

Considering the uncertainties associated for each type of measurement (~10 and ~15% for PGSE-NMR and TD, respectively), both techniques resulted in a similar Dp_z for HDO in Na-kaolinite samples (6.9 (5.4-9.2), and 5.8 (5.2-6.4) $\times 10^{-10}$ m^2 s^{-1}, respectively). This similarity indicates that both techniques, even though they probe very contrasted time scales (days for TD *vs* ms for PGSE-NMR), can be used interchangeably to investigate the dynamics of water tracer in samples composed of non-charged clayey particles irrespective of the differences in the spatial/temporal scales investigated. Accordingly, the PGSE-NMR method can be used for upscaling purposes, at least up to the centimeter scale investigated by the TD method. Moreover, similar Dp_z values mean that the two samples (the one prepared for PGSE-NMR analysis in this study and that used by Tertre et al. (2018) for TD experiments) have more or less the same porosity and degree of anisotropy in their particle orientations (considering the uncertainties on both parameters).

The Dp_z/D_0 values issued from the TD and PGSE-NMR experiments analysis are compared to those obtained from BD simulations using VPMs ($\varepsilon = \varepsilon_{interp.} = 0.25$-$0.27$; see Table S1), which are characterized by different $\langle P_2 \rangle$ parameter values (Figure 5a). Overall, the BD simulations show a decrease in Dp_z (measured in the direction normal to the preferred orientation) with the degree of anisotropy of the particles' orientation, in link with the increased tortuosity of the diffusion pathway. The good agreement between the experimental and simulated data obtained in this study for an interparticle porosity $\varepsilon_{interp.}$ close to 0.25 but also for a higher porosity value (i.e., 0.5; Dabat et al. (2020)) implies that the different VPMs generated and characterized by different porosity and particle organizations are well

representative of the real samples, despite the difference in length scales between the real samples and VPM's (Ferrage et al., 2015). BD simulations on VPMs can thus be considered a reliable tool to investigate water diffusion in clayey samples, especially in situations that are experimentally challenging to produce, such as samples that are characterized by different porosities and a high degree of anisotropy in the particle preferred orientation, since, most often, the two parameters are coupled (Dabat et al., 2018).

3.3. Water diffusion in Na-vermiculite

TD results obtained with Na-vermiculite samples were fitted with averaged α values equal to ε, resulting in $K_d = 0$ (Table 1), which indicates that HDO can be considered an inert tracer in Na-vermiculite samples, as also reported for kaolinite. However, slight HDO adsorption cannot be excluded, as suggested by the higher uncertainties obtained on the α values for Na-vermiculite samples compared to the kaolinite values. Such behavior was also reported by Tertre et al. (2018) for Na-vermiculite samples and can be attributed to slight HDO adsorption in the interlayer of Na-vermiculite in relation to its high layer charge. For the same ε value ($\varepsilon = 0.49 \pm 0.025$), the contrast in the particles' preferred orientation (Fig. 4b) between the compacted and centrifuged Na-vermiculite samples ($\langle P_2 \rangle = 0.03 \pm 0.02$, and 0.41 ± 0.06, respectively) is well reflected by the difference in their experimental Dp_z values (Table 1). Indeed, the HDO flux (Fig. 4c) through the compacted sample can be interpreted with a Dp_z value equal to 3.6 (3.0-4.5) $\times 10^{-10}$ m^2 s^{-1}, in comparison to almost two times lower Dp_z at 1.8 (1.4-2.3) $\times 10^{-10}$ m^2 s^{-1} obtained with the centrifuged sample. Such results indicate that the different Na-vermiculite samples were well-adapted for investigating, with similar total porosity, the influence of anisotropy in the particles' preferred orientation on the diffusion of water in a charged/dual porosity clayey media. Moreover, the data also infer that in a clayey media, and together with porosity, the preferred orientation of the particles acts as a first-order parameter in the control of the water diffusion. This behavior, previously reported by Dabat et al. (2020) for non-charged clayey samples (i.e., Na-kaolinite), therefore also extends to the case of charged clayey samples with a dual porosity. These findings decisively show that comprehensive data on the orientation of the particles in a clay-rich media is a prerequisite to correctly predict water diffusion within it. Finally, all the above stresses the need to develop diffusion models in which both the porosity and the degree of particle preferred orientation are explicitly included to increase the predictive capacity of such models.

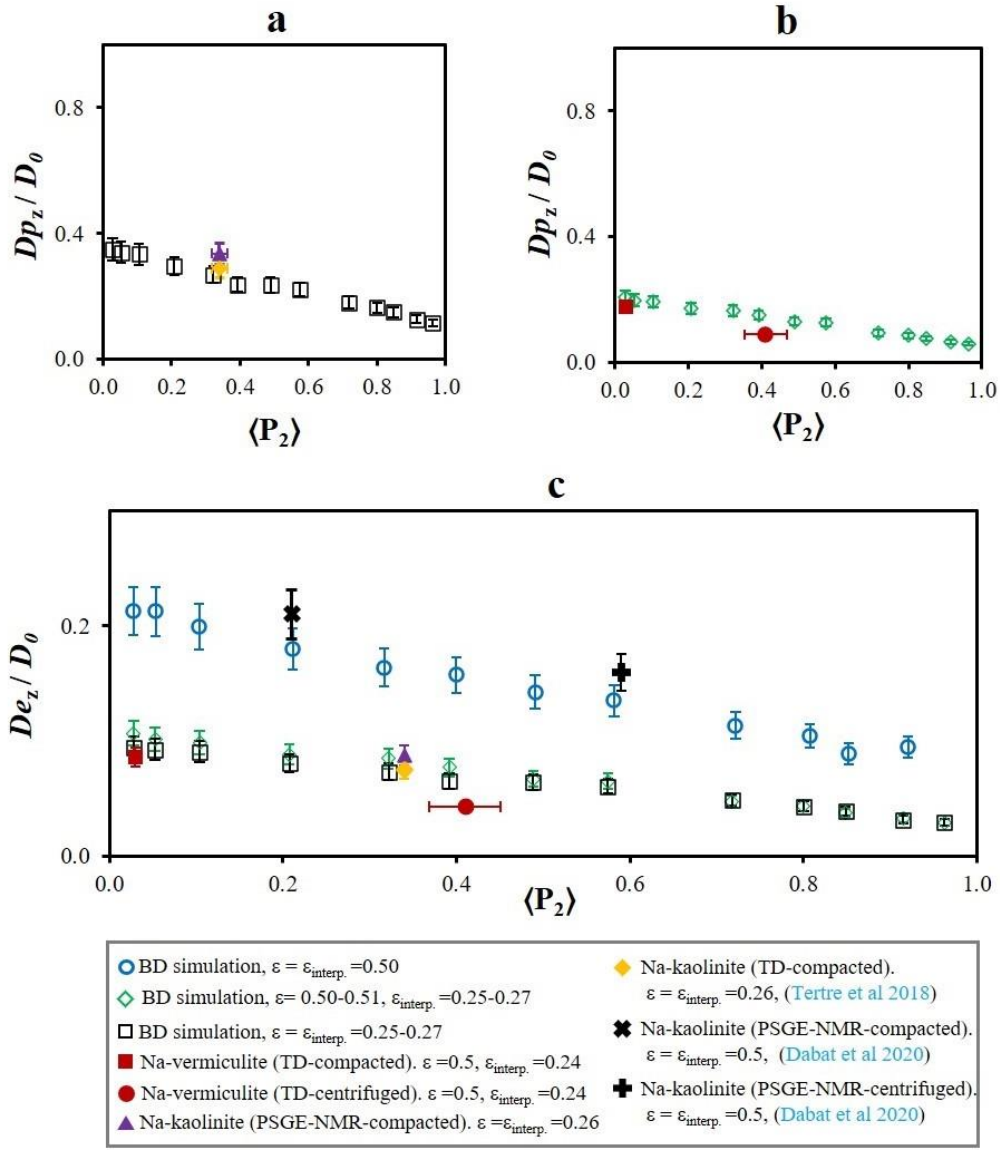


Figure 5. *Comparison between experimental and Brownian dynamics (BD) simulated water diffusion coefficients in the direction perpendicular to the preferred orientation of clay particles as a function of order parameter ⟨P_2⟩ values. All diffusion coefficients are normalized to the self-diffusion coefficient of HDO in bulk water (D_0). (a) Pore diffusion coefficients (Dp_z/D_0) of water in Na-kaolinite. Experimental data are shown in filled symbols (triangle and diamond for ^{1}H NMR Pulsed Gradient Spin Echo (PGSE-NMR) and through-diffusion (TD) methods, respectively), whereas simulated data are shown as none-filled squares. (b) Pore diffusion coefficients (Dp_z/D_0) of water in Na-vermiculite. Experimental data are shown in filled symbols (circle and square for the centrifuged and compacted samples, respectively), whereas simulated data are shown as none-filled diamonds. (c) Summary of (a) and (b) displayed as effective diffusion coefficients (De_z/D_0). Data are also compared to experimental (+ and × symbols) and simulated (none-filled circles) results from Dabat et al. (2020).*

In Fig. 5b and similar to Na-kaolinite samples, a good agreement is observed between experimental points from Na-vermiculite samples and simulated data ($\varepsilon = 0.50$-0.51 and $\varepsilon_{interp.} = 0.25$-$0.27$; Table S1). Moreover, despite the higher ε value for Na-vermiculite compared to Na-kaolinite, the lower Dp_z values obtained for Na-vermiculite clearly highlight the role played by the interlayer porosity on the overall reduced mobility of the water molecules in the vicinity of charged clay particles (Nakashima and Mitsumori, 2005; Michot et al., 2012; Porion et al., 2014). Note that in Fig. 5b, the point obtained for the centrifuged Na-vermiculite sample at $\langle P_2 \rangle = 0.41$ is somewhat lower than the corresponding simulated point. Such small aberration can be due to the slightly lower interparticle porosity in the case of the experimental Na-vermiculite sample ($\varepsilon_{interp.} = 0.24$) compared to that used for the BD simulation ($\varepsilon_{interp.} = 0.25$-$0.27$). In addition, one can consider that due to the increased heterogeneity for the centrifuged sample, which is characterized by the wider variation in $\langle P_2 \rangle$ values, water diffusion could be controlled by zones in the samples with higher $\langle P_2 \rangle$ values and not by the mean degree of preferred orientation. Despite this marginal difference, the good agreement between the experimental and calculated Dp_z values can be assigned to the lack of osmotic swelling in the Na-vermiculite sample, which allows a correct quantitative description of the different types of porosities volumes. In this respect, BD simulations on such granular virtual systems can be considered to be a useful tool for investigating the role played by different parameters (i.e., porosity, orientation of particles, and dual porosity volumes) on the overall diffusion process of water in Na-vermiculite dual porosity media.

3.4. The influence of interlayer vs. interparticle porosities on HDO diffusion in clayey samples

To assess the role played by the two porosities types (interlayer and interparticle), the HDO diffusivity is discussed below in terms of De_z since this parameter is commonly used over Dp_z in macroscopic models to describe the diffusing flux traversing a sample (Bourg and Tournassat, 2015; Tournassat and Steefel, 2019 and references therein). The obtained De_z values for water, normalized to self-diffusion in bulk D_0, measured for both materials (kaolinite and Na-vermiculite) using the two techniques (PSGE-NMR and TD), are plotted in Fig. 5c as a function of the $\langle P_2 \rangle$ parameter. These data are compared to the calculated ones obtained from BD simulations assuming that all porosity is accessible to diffusion (as confirmed by HDO alpha values previously discussed and reported in Table 1). Considering that experimental samples composed of Na-vermiculite and Na-kaolinite particles have approximatively the same interparticle porosity (i.e., 0.26 *vs.* 0.24 for kaolinite and vermiculite, respectively) and that all

of the porosity of the Na-vermiculite samples is accessible to water diffusion, one can expect that De_z obtained with Na-vermiculite samples are intermediate between those simulated for $\varepsilon_{interp.} = 0.25$ and $\varepsilon_{interp.} = 0.5$ (for similar $\langle P_2 \rangle$ values). In fact, experimental data obtained with Na-vermiculite ($\varepsilon = 0.49$) are drastically much closer to those simulated at $\varepsilon_{interp.} = 0.25$ than to those simulated at $\varepsilon_{interp.} = 0.5$ (Fig. 5c). Such behavior suggests that even though interlayer porosity is available for diffusion, the contribution of the flux of HDO diffusing in this interlayer volume is very marginal compared to that in the interparticle porosity, which results in De_z values that are almost independent of the interlayer porosity of the material. Interestingly, the evolution of the diffusion anisotropy ratios $\frac{De_{\overline{xy}}}{De_z}$ with the $\langle P_2 \rangle$ values reported in Fig. 6 indicates a significant increase in anisotropy with the increased degree of preferred orientation of particles. This behavior is the same for different values of the total porosity and different distributions between interparticle or interlayer volumes. This finding implies that the anisotropy of water diffusion can be, for the range of porosity investigated, directly linked to the $\langle P_2 \rangle$ parameter, irrespective of the porosity value or distribution. The limited contribution of interlayer porosity on the diffusive flux crossing a sample, reported in this study by coupling BD simulations with experimental results obtained with both Na-vermiculite and Na-kaolinite samples, is in agreement with the results reported by Churakov and Gimmi. (2011). Based on molecular dynamics and random walk simulations, these authors showed that the proportion of interlayer porosity (and associated diffusion) in the total porosity of virtual porous media has only a minor influence on the water diffusion. Note that the dominant role played by the interparticle porosity was already qualitatively addressed by Tertre et al. (2018) to explain the difference between experimental TD data obtained for Na-vermiculite and Na-kaolinite samples. However, although the porosity distribution (i.e., $\varepsilon_{interl.}$ and $\varepsilon_{interp.}$) was known in their Na-vermiculite samples, the particle organization in these samples was not quantified, rendering it impossible to decouple the role played by each one of these variables on the global diffusion process.

Furthermore, as previously discussed in the introduction, determination of the $\varepsilon_{interl.}/\varepsilon_{interp.}$ value is not easy for smectite due to osmotic swelling of this mineral, especially when the saturating cations are Na^+, which makes it difficult to discriminate the role played by interlayer and interparticle porosities on the global diffusivity of water tracer in this mineral. Such a phenomenon was, to some extent, indicated by Melkior et al. (2009), who reported that the effective diffusion coefficient of water tracer was significantly dependent on the nature of the compensating cations in samples made of smectitic particles (for the same total porosity), with De_z increasing from Na-smectite, Ca-smectite to Cs-smectite. These authors attributed this variation to the absence of gel formation for the Cs-samples compared to the Na-samples (and to a lesser extent in Ca-samples). This observation was most likely related to the difficulty of considering a defined interparticle porosity (i.e., pores not submitted to the particle charge) for Na-smectites compared to Cs ones, and consequently raises the question about the relevance of considering the De_z values obtained with Na-smectites as reference data for models describing dual porosity clayey system. In that regard, the experimental results obtained in this study with Na-vermiculite samples represent a new set of data for an extensive validation of dual-porosity reactive transport models.

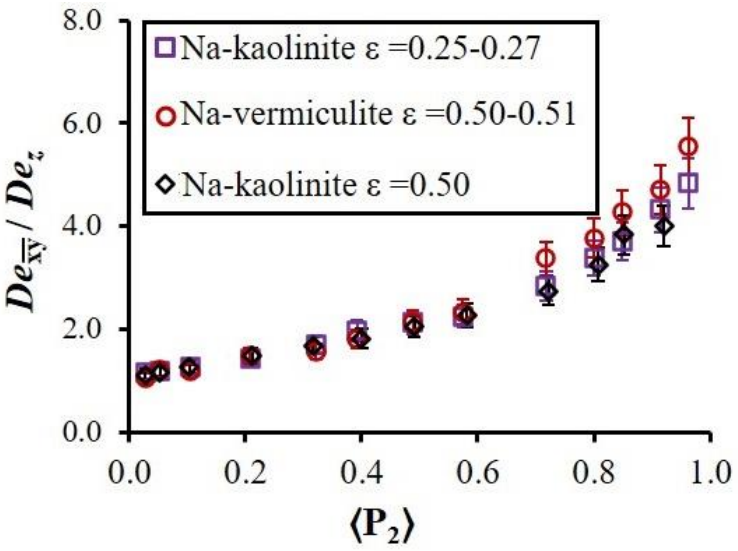


Fig. 6. *Influence of porosity and its distribution between interlayer and interparticle volumes on the evolution of the diffusion anisotropy ratio $De_{\overline{xy}}/De_z$ as a function of the order parameter (P_2). The anisotropy ratio is calculated based on the BD simulated mean effective water diffusion coefficients in the (x,y) plane ($De_{\overline{xy}}$) over the z direction (De_z) with respect to the direction of the preferred orientation of the clay particles. Data are shown for Na-kaolinite with ε = 0.25 (squares, this study) or ε = 0.50 (diamonds, Dabat et al. (2020)), and for Na-vermiculite with ε = 0.50-0.51 and $\varepsilon_{interp.}$ = 0.25-0.27 (circles, this study).*

4. Concluding remarks and perspectives

A methodology was developed in this study to prepare experimental clayey samples for which the porosity distribution (interlayer ($\varepsilon_{interl.}$)/interparticle ($\varepsilon_{interp.}$)) and particle organization can be controlled independently. These new procedures were successfully applied to prepare samples characterized by the same interparticle porosity but with the presence or not of interlayer porosity accessible to water diffusion (Na-kaolinite *vs* Na-vermiculite samples), used to investigate the role played by the two types of porosities and the particle organization on the global diffusion of water.

The similarity of the diffusion data obtained for Na-kaolinite by two independent experimental techniques (i.e., Pulsed Gradient Spin Echo attenuation measurements by Nuclear Magnetic Resonance (PGSE-NMR) and through-diffusion (TD)) probing different length and time scales (i.e., ms for PGSE-NMR *vs*. several days for TD), shows that a representative elementary volume for the analysis of water diffusion process in clayey materials was reached with PGSE-NMR method. Moreover, these two experimental techniques are found to be very complementary for the analysis of water diffusion in clayey media. On the one hand, PGSE-NMR allows obtaining the full tensor of the water diffusion on the same sample, whereas the TD experiments must be repeated when changing the probed direction of diffusion. On the other hand, PGSE-NMR cannot be used when the sample contains a very high quantity of paramagnetic elements, such as Fe in the Na-vermiculite used in this study, or when the probe confinement is high (the case of water molecule in the interlayer of Na-vermiculite as a result of its high structural charge). In that regard TD can be advantageously used irrespective of the chemical composition of the sample and interlayer probe confinement.

By accounting for the uncertainties in both the porosity and particle organization measurements, there were good agreements between the effective diffusion coefficients derived from the experimental measurements obtained for all samples and simulated data. This finding showed that, in a dual-porosity clayey media, even though the interlayer is accessible to water diffusion, interparticle porosity and preferential orientation of the particles act as first-order parameters in the global flux of water diffusing through these media, at least for the range of porosity investigated. These results were obtained irrespective of the directional diffusion probed, and they allowed us to conclude that the $\langle P_2 \rangle$ parameter (i.e., mathematical function derived from two-dimensional X-Ray Scattering measurements comprised between 0 for an isotropic particle organization and 1 for a perfectly anisotropic organization) is an excellent

descriptor of the anisotropy of the diffusion of water in materials made of swelling clay particles.

Due to osmotic swelling of montmorillonite clay minerals, especially when the charge compensating cation is Na^+, distribution of interparticle and interlayer porosities is extremely difficult to be determined. As logical continuation of this work, Na-vermiculite samples characterized by well-defined $\varepsilon_{interl.}/\varepsilon_{interp.}$ ratios and particle organization, can be used for further investigating the link between geometrical properties and the diffusion of charged (ionic) tracers in swelling clays. Such approach would likely provide key information for decoupling the role played by interfacial charges located on either basal or edge surfaces of Na-vermiculite from other parameters linked to the geometric organization of the particles, such as the preferential orientation of the clay particles or the different porosities accessible to diffusion.

Acknowledgments

The results presented are part of the Ph.D. thesis of A.A. granted by "Région Nouvelle-Aquitaine", University of Poitiers, France. Stephan Rouzière (LPS, Saclay, France) is acknowledged for technical assistance in the XRS measurements. Dr. Jerome Labanowski (IC2MP, Poitiers, France) is thanked for providing access to the lyophilizer used in this study. Claude Veit (IC2MP, Poitiers, France) is thanked for the design and conception of the compaction and centrifugation cells for the sample preparation. The authors are grateful to the CNRS interdisciplinary "défi Needs" through its "MiPor" program (Project DARIUS), the H2020 European program EURAD through its "Future" WP, the French government program "Investissements d'Avenir" (EUR INTREE, reference ANR-18-EURE-0010), and the European Union (ERDF) and "Région Nouvelle Aquitaine" for providing financial support for this study.

5. Supplementary data (S. D.)

S.1.1 reports method used to extract water mobility by ^1H NMR Pulsed Gradient Spin Echo (PGSE-NMR) experiments. S.1.2 reports information related to induration of the samples and two-dimensional X-Ray Scattering (2D-XRS) measurements. S.1.3 reports experimental conditions used for through-diffusion (TD) experiments as well as the method used to extract water mobility. S.1.4 reports the methodology used to generate the 13 virtual porous media used in this study to perform Brownian dynamic. Finally, table S1 contains the characteristics of these 13 virtual porous media.

6. References

Abend, S., Lagaly, G., 2000. Sol–gel transitions of sodium montmorillonite dispersions. Applied Clay Science 16, 201–227. https://doi.org/10.1016/S0169-1317(99)00040-X

Altmann, S., Aertsens, M., Appelo, T., Bruggeman, C., Gaboreau, S., Glaus, M., Jacquier, P., Kupcik, T., Maes, N., Montoya, V., Rabung, T., Savoye, S., et al, 2015. Processes of cation migration in clayrocks: Final Scientific Report of the CatClay European Project. CEA.

Andra, 2005. Argile : Évaluation de la Faisabilité du Stockage Géologique en Formation Argileuse. Document du Synthèse, Andra.

Arguelles, A., Leoni, M., Blanco, J.A., Marcos, C., 2010. Semi-ordered crystalline structure of the Santa Olalla vermiculite inferred from X-ray powder diffraction. American Mineralogist 95, 126–134. https://doi.org/10.2138/am.2010.3249

Bachu, S., 2008. CO2 storage in geological media: Role, means, status and barriers to deployment. Progress in Energy and Combustion Science 34, 254–273. https://doi.org/10.1016/j.pecs.2007.10.001

Bacle, P., Dufrêche, J.-F., Rotenberg, B., Bourg, I.C., Marry, V., 2016. Modeling the transport of water and ionic tracers in a micrometric clay sample. Applied Clay Science 123, 18–28. https://doi.org/10.1016/j.clay.2015.12.014

Bear, J., 1972. Dynamics of Fluids in Porous Media. Dover Publication, New York.

Bestel, M., 2014. Water–montmorillonite systems: Neutron scattering and tracer through-diffusion studies (Thesis). University of Bern, Bern-Switzerland.

Bestel, M., Glaus, M.A., Frick, S., Gimmi, T., Juranyi, F., Van Loon, L.R., Diamond, L.W., 2018. Combined tracer through-diffusion of HTO and 22Na through Na-montmorillonite with different bulk dry densities. Applied Geochemistry 93, 158–166. https://doi.org/10.1016/j.apgeochem.2018.04.008

Bennett, R.H., Brya, W.R., Keller, G.H., 1981. Clay fabric of selected submarine sediments; fundamental properties and models. Journal of Sedimentary Research 51, 217–232. https://doi.org/10.1306/212F7C52-2B24-11D7-8648000102C1865D

Bourg, I.C., Bourg, A.C.M., Sposito, G., 2003. Modeling diffusion and adsorption in compacted bentonite: a critical review. Journal of Contaminant Hydrology 61, 293–302. https://doi.org/10.1016/S0169-7722(02)00128-6

Bourg, I.C., Sposito, G., Bourg, A.C.M., 2006. Tracer diffusion in compacted, water-saturated bentonite. Clays Clay Miner. 54, 363–374. https://doi.org/10.1346/CCMN.2006.0540307

Bourg, I.C., Tournassat, C., 2015. Self-Diffusion of Water and Ions in Clay Barriers, in: Developments in Clay Science. Elsevier, pp. 189–226. https://doi.org/10.1016/B978-0-08-100027-4.00006-1

Callaghan, P.T., 1991. Principles of nuclear magnetic resonance microscopy. Clarendon Press.

Charlet, L., Alt-Epping, P., Wersin, P., Gilbert, B., 2017. Diffusive transport and reaction in clay rocks: A storage (nuclear waste, CO2, H2), energy (shale gas) and water quality issue. Advances in Water Resources 106, 39–59. https://doi.org/10.1016/j.advwatres.2017.03.019

Churakov, S.V., Gimmi, T., 2011. Up-Scaling of Molecular Diffusion Coefficients in Clays: A Two-Step Approach. J. Phys. Chem. C 115, 6703–6714. https://doi.org/10.1021/jp112325n

Dabat, T., Hubert, F., Paineau, E., Launois, P., Laforest, C., Grégoire, B., Dazas, B., Tertre, E., Delville, A., Ferrage, E., 2019. A general orientation distribution function for clay-rich media. Nat Commun 10, 5456. https://doi.org/10.1038/s41467-019-13401-0

Dabat, T., Mazurier, A., Hubert, F., Tertre, E., Grégoire, B., Dazas, B., Ferrage, E., 2018. Mesoscale Anisotropy in Porous Media Made of Clay Minerals. A Numerical Study Constrained by Experimental Data. Materials 11, 1972. https://doi.org/10.3390/ma11101972

Dabat, T., Porion, P., Hubert, F., Paineau, E., Dazas, B., Grégoire, B., Tertre, E., Delville, A., Ferrage, E., 2020. Influence of preferred orientation of clay particles on the diffusion of water in kaolinite porous media at constant porosity. Applied Clay Science 184, 105354. https://doi.org/10.1016/j.clay.2019.105354

Dagnelie, R.V.H., Arnoux, P., Enaux, J., Radwan, J., Ner, P., 2017. Perturbation induced by a nitrate plume on diffusion of solutes in a large-scale clay rock sample. Applied Clay Science 141. 219-226.

Dagnelie, R.V.H., Rasamimanana, S., Blin, V., Radwan, J., Thory, E., Robinet, J.-C., Lefèvre, G., 2018. Diffusion of organic anions in clay-rich media: Retardation and effect of anion exclusion. Chemosphere 213, 472–480. https://doi.org/10.1016/j.chemosphere.2018.09.064

De La Calle, C., Pezerat, H., Gasperin, M., 1977. Problemes d'ordre-désordre dans les vermiculites structure du minéral calcique hydraté a 2 couches. Journal de Physique 38, 128–133.

Durrieu, J., Argillier, J.F., Rosenberg, E., Li, Y., 1997. Static and Dynamic Filtration Properties of Aqueous Suspensions of Clays and Electrolytes. Rev. Inst. Fr. Pét. 52, 207–218. https://doi.org/10.2516/ogst:1997020

Dykhuizen, R.C., Casey, W.H., 1989. An analysis of solute diffusion in rocks. Geochimica et Cosmochimica Acta 53, 2797–2805. https://doi.org/10.1016/0016-7037(89)90157-9

Farver, J.R., Yund, R.A., 1999. Oxygen bulk diffusion measurements and TEM characterization of a natural ultramylonite: implications for fluid transport in mica-bearing rocks. J. Metamorph. Geol 17, 669–683.

Faurel, M., 2012. Conception et mise en place d'expériences de diffusion de l'eau et de solutés dans des milieux poreux modèles d'argiles gonflantes. Université de Poitiers, Poitiers, France.

Ferrage, E., Hubert, F., Baronnet, A., Grauby, O., Tertre, E., Delville, A., Bihannic, I., Prêt, D., Michot, L.J., Levitz, P., 2018. Influence of crystal structure defects on the small-angle neutron scattering/diffraction patterns of clay-rich porous media. J Appl Crystallogr 51, 1311–1322. https://doi.org/10.1107/S160057671801052X

Ferrage, E., Hubert, F., Tertre, E., Delville, A., Michot, L.J., Levitz, P., 2015. Modeling the arrangement of particles in natural swelling-clay porous media using three-dimensional packing of elliptic disks. Physical Review E 91, 062210. https://doi.org/10.1103/PhysRevE.91.062210

García-Gutiérrez, M., Cormenzana, J.L., Missana, T., Mingarro, M., Martín, P.L., 2006. Large-scale laboratory diffusion experiments in clay rocks. Physics and Chemistry of the Earth, Parts A/B/C 31, 523–530. https://doi.org/10.1016/j.pce.2006.04.004

Gieseking, J.E. (Ed.), 1975. Soil Components Vol. 2: Inorganic Components, 1st ed. Springer-Verlag Berlin Heidelberg.

Gimmi, T., Churakov, S.V., 2019. Water retention and diffusion in unsaturated clays: Connecting atomistic and pore scale simulations. Applied Clay Science 175, 169–183. https://doi.org/10.1016/j.clay.2019.03.035

Gimmi, T., Kosakowski, G., 2011. How Mobile Are Sorbed Cations in Clays and Clay Rocks? Environ. Sci. Technol. 45, 1443–1449. https://doi.org/10.1021/es1027794

Glaus, M.A., Frick, S., Rossé, R., Loon, L.R.V., 2010. Comparative study of tracer diffusion of HTO, 22Na+ and 36Cl− in compacted kaolinite, illite and montmorillonite. Geochimica et Cosmochimica Acta 74, 1999–2010. https://doi.org/10.1016/j.gca.2010.01.010

Gonzáles García, F., García Ramos, G., 1960. On the genesis and transformation of vermiculite. Presented at the Transactions 7th int. Congr. Soil Sci., Spain, pp. 482–491.

González Sánchez, F., Jurányi, F., Gimmi, T., Van Loon, L., Unruh, T., Diamond, L.W., 2008a. Translational diffusion of water and its dependence on temperature in charged and uncharged clays: A neutron scattering study. J. Chem. Phys. 129, 174706. https://doi.org/10.1063/1.3000638

González Sánchez, F., Van Loon, L.R., Gimmi, T., Jakob, A., Glaus, M.A., Diamond, L.W., 2008b. Self-diffusion of water and its dependence on temperature and ionic strength in highly compacted montmorillonite, illite and kaolinite. Applied Geochemistry 23, 3840–3851. https://doi.org/10.1016/j.apgeochem.2008.08.008

Gunsteren, W.F., Berendsen, H.J.C., Rullmann, J.A.C., 1981. Stochastic dynamics for molecules with constraints. Molecular Physics 44, 69–95. https://doi.org/10.1080/00268978100102291

Hassan, M.S., Villieras, F., Gaboriaud, F., Razafitianamaharavo, A., 2005. AFM and low-pressure argon adsorption analysis of geometrical properties of phyllosilicates. Journal of Colloid and Interface Science 296, 614–623. https://doi.org/10.1016/j.jcis.2005.09.028

Hermans, P.H., Platzek, P., 1939. Beiträge zur Kenntnis des Deformationsmechanismus und der Feinstruktur der Hydratzellulose. Kolloid-Z, Kolloid-Z 88, 68–72.

Jacops, E., Aertsens, M., Maes, N., Bruggeman, C., Swennen, R., Krooss, B., Amann-Hildenbrand, A., Littke, R., 2017. The Dependency of Diffusion Coefficients and Geometric Factor on the Size of the Diffusing Molecule: Observations for Different Clay-Based Materials. Geofluids 2017, 1–16. https://doi.org/10.1155/2017/8652560

Landais, P., 2006. Advances in geochemical research for the underground disposal of high-level, long-lived radioactive waste in a clay formation. Journal of Geochemical Exploration 88, 32–36. https://doi.org/10.1016/j.gexplo.2005.08.011

Liu, L., 2013. Prediction of swelling pressures of different types of bentonites in dilute solutions. Colloids and Surfaces A: Physicochemical and Engineering Aspects 434, 303–318. https://doi.org/10.1016/j.colsurfa.2013.05.068

Loeber, L., 1992. Etude de la structure des cakes d'argile formés sur la paroi des puits au cours du forage. Université d'Orléans, Orléans-France.

Malikova, N., Cadéne, A., Marry, V., Dubois, E., Turq, P., Zanotti, J.-M., Longeville, S., 2005. Diffusion of water in clays – microscopic simulation and neutron scattering. Chemical Physics 317, 226–235. https://doi.org/10.1016/j.chemphys.2005.04.035

Malikova, N., Cadène, A., Marry, V., Dubois, E., Turq, P., 2006. Diffusion of Water in Clays on the Microscopic Scale: Modeling and Experiment. J. Phys. Chem. B 110, 3206–3214. https://doi.org/10.1021/jp056954z

Marcos, C., Argüelles, A., Ruíz-Conde, A., P. J. Sánchez-Soto, Blanco, J.A., 2003. Study of the dehydration process of vermiculites by applying a vacuum pressure: formation of interstratified phases. Mineral. mag. 67, 1253–1268. https://doi.org/10.1180/0026461036760163

Marry, V., Turq, P., Cartailler, T., Levesque, D., 2002. Microscopic simulation of structure and dynamics of water and counterions in a monohydrated montmorillonite. The Journal of Chemical Physics 117, 3454–3463. https://doi.org/10.1063/1.1493186

Marry, V., Turq, P., 2003. Microscopic Simulations of Interlayer Structure and Dynamics in Bihydrated Heteroionic Montmorillonites. J. Phys. Chem. B 107, 1832–1839.

Melkior, T., Gaucher, E.C., Brouard, C., Yahiaoui, S., Thoby, D., Clinard, Ch., Ferrage, E., Guyonnet, D., Tournassat, C., Coelho, D., 2009. Na+ and HTO diffusion in compacted bentonite: Effect of surface chemistry and related texture. Journal of Hydrology 370, 9–20. https://doi.org/10.1016/j.jhydrol.2009.02.035

Mermut, A.R., Cano, A.F., 2001. Baseline Studies of the Clay Minerals Society Source Clays: Chemical Analyses of Major Elements. Clays and Clay Minerals 49, 381–386. https://doi.org/10.1346/CCMN.2001.0490504

Michot, L.J., Ferrage, E., Jiménez-Ruiz, M., Boehm, M., Delville, A., 2012. Anisotropic Features of Water and Ion Dynamics in Synthetic Na- and Ca-Smectites with Tetrahedral Layer Charge. A Combined Quasi-elastic Neutron-Scattering and Molecular Dynamics Simulations Study. J. Phys. Chem. C 116, 16619–16633. https://doi.org/10.1021/jp304715m

Nakashima, Y., Mitsumori, F., 2005. H2O self-diffusion restricted by clay platelets with immobilized bound H2O layers: PGSE NMR study of water-rich saponite gels. Applied Clay Science 28, 209–221. https://doi.org/10.1016/j.clay.2004.01.017

Ochs, M., Lothenbach, B., Wanner, H., Sato, H., Yui, M., 2001. An integrated sorption–diffusion model for the calculation of consistent distribution and diffusion coefficients in compacted bentonite. Journal of Contaminant Hydrology 47, 283–296. https://doi.org/10.1016/S0169-7722(00)00157-1

Porion, P., Faugère, A.M., Delville, A., 2014. Structural and Dynamical Properties of Water Molecules Confined within Clay Sediments Probed by Deuterium NMR Spectroscopy, Multiquanta Relaxometry, and Two-Time Stimulated Echo Attenuation. J. Phys. Chem. C 118, 20429–20444. https://doi.org/10.1021/jp506312q

Porion, P., Ferrage, E., Hubert, F., Tertre, E., Dabat, T., Faugère, A.M., Condé, F., Warmont, F., Delville, A., 2018. Water Mobility within Compacted Clay Samples: Multi-Scale Analysis Exploiting 1 H NMR Pulsed Gradient Spin Echo and Magnetic Resonance Imaging of Water Density Profiles. ACS Omega 3, 7399–7406. https://doi.org/10.1021/acsomega.8b01083

Pret, D., 2003. Nouvelles méthodes quantitatives de cartographie de la minéralogie et de la porosité dans les matériaux argileux : application aux bentonites compactées des barrières ouvragées. Université de Poitiers, Poitiers-France.

Pusch, R., 1979. Highly Compacted Sodium Bentonite for Isolating Rock-Deposited Radioactive Waste Products. Journal Nuclear Technology 45, 153–157. https://doi.org/10.13182/NT79-A32305

Reinholdt, M.X., Hubert, F., Faurel, M., Tertre, E., Razafitianamaharavo, A., Francius, G., Prêt, D., Petit, S., Béré, E., Pelletier, M., Ferrage, E., 2013. Morphological properties of vermiculite particles in size-selected fractions obtained by sonication. Applied Clay Science 77–78, 18–32. https://doi.org/10.1016/j.clay.2013.03.013

Sakharov, B.A., Drits, V.A., McCarty, D.K., Walker, G.M., 2016. Modeling Powder X-Ray Diffraction Patterns of the Clay Minerals Society Kaolinite Standards: Kga-1, Kga-1b, and Kga-2. Clays Clay Miner. 64, 314–333. https://doi.org/10.1346/CCMN.2016.0640307

Sato, H., 2000. The Effect of Pore Structural Factors on Diffusion in Compacted Sodium Bentonite. MRS Proc. 663, 605. https://doi.org/10.1557/PROC-663-605

Sato, H., Suzuki, S., 2003. Fundamental study on the effect of an orientation of clay particles on diffusion pathway in compacted bentonite. Applied Clay Science 23, 51–60. https://doi.org/10.1016/S0169-1317(03)00086-3

Savoye, S., Beaucaire, C., Grenut, B., Fayette, A., 2015. Impact of the solution ionic strength on strontium diffusion through the Callovo-Oxfordian clayrocks: An experimental and modeling study. Applied Geochemistry 61, 41–52. https://doi.org/10.1016/j.apgeochem.2015.05.011

Shackelford, C.D., Moore, S.M., 2013. Fickian diffusion of radionuclides for engineered containment barriers: Diffusion coefficients, porosities, and complicating issues. Engineering Geology 152, 133–147. https://doi.org/10.1016/j.enggeo.2012.10.014

Skipper, N.T., Lock, P.A., Titiloye, J.O., Swenson, J., Mirza, Z.A., Howells, W.S., Fernandez-Alonso, F., 2006. The structure and dynamics of 2-dimensional fluids in swelling clays. Chemical Geology 230, 182–196. https://doi.org/10.1016/j.chemgeo.2006.02.023

Suzuki, S., Sato, H., Ishidera, T., Fujii, N., 2004. Study on anisotropy of effective diffusion coefficient and activation energy for deuterated water in compacted sodium bentonite. Journal of Contaminant Hydrology 68, 23–37. https://doi.org/10.1016/S0169-7722(03)00139-6

Swenson, J., Bergman, R., Howells, W.S., 2000. Quasielastic neutron scattering of two-dimensional water in a vermiculite clay. J. Chem. Phys. 113, 2873–2879. https://doi.org/10.1063/1.1305870

Tertre, E., Delville, A., Prêt, D., Hubert, F., Ferrage, E., 2015. Cation diffusion in the interlayer space of swelling clay minerals – A combined macroscopic and microscopic study. Geochimica et Cosmochimica Acta 149, 251–267. https://doi.org/10.1016/j.gca.2014.10.011

Tertre, E., Savoye, S., Hubert, F., Prêt, D., Dabat, T., Ferrage, E., 2018. Diffusion of Water through the Dual-Porosity Swelling Clay Mineral Vermiculite. Environ. Sci. Technol. 52, 1899–1907. https://doi.org/10.1021/acs.est.7b05343

Titiloye, J.O., Skipper, N.T., 2001. Molecular dynamics simulation of methane in sodium montmorillonite clay hydrates at elevated pressures and temperatures. Molecular Physics 99, 899–906. https://doi.org/10.1080/00268970010028863

Tournassat, C., Steefel, C.I., 2019. Reactive Transport Modeling of Coupled Processes in Nanoporous Media. Reviews in Mineralogy and Geochemistry 85, 75–109. https://doi.org/10.2138/rmg.2019.85.4

Tyagi, M., Gimmi, T., Churakov, S.V., 2013. Multi-scale micro-structure generation strategy for up-scaling transport in clays. Advances in Water Resources 59, 181–195. https://doi.org/10.1016/j.advwatres.2013.06.002

Underwood, T.R., Bourg, I.C., 2020. Large-Scale Molecular Dynamics Simulation of the Dehydration of a Suspension of Smectite Clay Nanoparticles. J. Phys. Chem. C 124, 3702–3714. https://doi.org/10.1021/acs.jpcc.9b11197

Valleau, J., Diestler, D., Cushman, J., Schoen, M., Hertzner, A., Riley, M., 1991. Comment on: Adsorption and diffusion at rough surfaces. A comparison of statistical mechanics, molecular dynamics, and kinetic theory. The Journal of Chemical Physics 95, 6194–6195.

Van Loon, L.R., Soler, J.M., Jakob, A., Bradbury, M.H., 2003. Effect of confining pressure on the diffusion of HTO, 36Cl− and 125I− in a layered argillaceous rock (Opalinus Clay): diffusion perpendicular to the fabric. Applied Geochemistry 18, 1653–1662. https://doi.org/10.1016/S0883-2927(03)00047-7

Van Loon, L.R., Soler, J.M., Müller, W., Bradbury, M.H., 2004. Anisotropic Diffusion in Layered Argillaceous Rocks: A Case Study with Opalinus Clay. Environ. Sci. Technol. 38, 5721–5728.

Wenk, H.-R., Kanitpanyacharoen, W., Voltolini, M., 2010. Preferred orientation of phyllosilicates: Comparison of fault gouge, shale and schist. Journal of Structural Geology 12, 478-489.

Wenk, Voltolini, Mazurek, Loon, V.L.R., Vinsot, 2008. Preferred Orientations and Anisotropy in Shales: Callovo-Oxfordian Shale (France) and Opalinus Clay (Switzerland). Clays Clay Miner. 56, 285–306. https://doi.org/10.1346/CCMN.2008.0560301

Wittebroodt, C., Savoye, S., Frasca, B., Gouze, P., 2012. Diffusion of HTO, 36Cl- and 125I- in Upper Toarcian argillite samples from Tournemire: Effects of initial iodide concentration and ionic strength. Applied Geochemistry 27, 1432-1441.

Xiang, Y., Al, T., Scott, L., Loomer, D., 2013. Diffusive anisotropy in low-permeability Ordovician sedimentary rocks from the Michigan Basin in southwest Ontario. Journal of Contaminant Hydrology 155, 31-45.

IV.2.1. Supplementary data for "Role of interlayer porosity and particle organization in the diffusion of water in swelling clays"

Supplementary Data for

Role of interlayer porosity and particle organization in the diffusion of water in swelling clays

A. Asaad[1,*], F. Hubert[1], E. Ferrage[1], T. Dabat[1], E. Paineau[2], P. Porion[3], S. Savoye[4], B. Gregoire[1], B. Dazas[1], A. Delville[3], E. Tertre[1,*]

[1] IC2MP, Equipe HydrASA, UMR 7285 CNRS/Université de Poitiers, 86073 Poitiers, France.

[2] Université Paris-Saclay, CNRS, Laboratoire de Physique des Solides, 91405 Orsay, France

[3] ICMN, UMR 7374 CNRS/Université d'Orléans, 45071 Orléans, France

[4] Université Paris-Saclay, CEA. Service d'Etudes du Comportement de Radionucléides, 91191 Gif-sur-Yvette, France

* E-mail addresses of the corresponding authors:

A. Asaad: ali. asaad@univ-poitiers.fr

E. Tertre : emmanuel.tertre@univ-poitiers.fr

S.1. Materials and methods

S.1.1. ^1H NMR Pulsed Gradient Spin Echo experiments

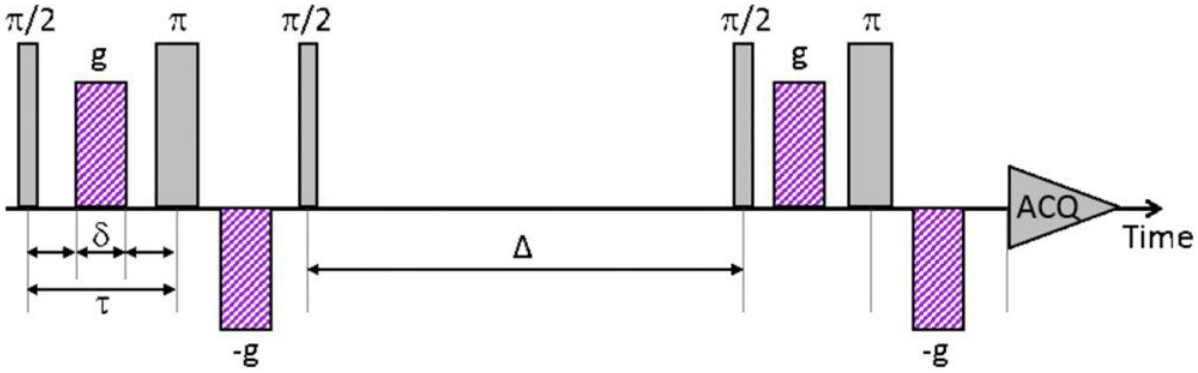
The Pulsed Gradient Spin Echo attenuation measurements by Nuclear Magnetic Resonance (PGSE-NMR) analyses were performed at the ICMN laboratory (Orléans, France) on the Na-kaolinite compacted sample. The dried Na-kaolinite samples, in volume-constrained Polyether ether ketone (PEEK) tubes (see Section S.1.1), were first water-saturated by capillary imbibition. To do so, the bottom part of the sample was put in contact with deionized water, while the other side of the tube was connected to a primary vacuum pump to favor water migration and gentle evacuation of air from the pore network. The NMR measurements were performed using the same setup and experimental conditions as in (Porion et al., 2018; Dabat et al., 2020) on a Bruker® DSX100 spectrometer. This instrument operates with a static magnetic field of 2.35 T and is equipped with a saddle detection coil and a micro-imaging probe (Micro5 Bruker) with gradient coils to generate magnetic field gradients in three perpendicular directions. The macroscopic water mobility along any pre-selected direction within the sample was determined based on ^{1}H PGSE-NMR attenuation measurements (Stejskal and Tanner, 1965; Cotts et al., 1989; Callaghan, 1991) by using the pulse sequence illustrated in Fig. S1. The largest wave vector (q_{MAX}) associated with these attenuation measurements is defined as $q_{MAX} = \frac{\gamma.\delta.G_{MAX}}{\pi}$ = 6.81 10^4 m^{-1}, where γ is the proton gyromagnetic ratio (2.6752 10^8 read/s for ^{1}H), δ is the duration of each applied field gradient (i.e., 0.5 ms) (see Fig. S1) and G_{MAX} is the largest applied field gradient (i.e., 1.6 Tesla m^{-1}). Accordingly, the spatial length over which the dynamics of the water is investigated is larger than 15 µm. For these experiments, the diffusion time (Δ) and the delay (τ) were set to 20 ms and 760 µs, respectively (Fig. S1). The attenuation of the intensity of the NMR echo $I(q)/I(0)$ evolves according to a Gaussian relationship from which the components of the self-diffusion tensor are easily extracted (Cotts et al., 1989; Callaghan, 1991):

$$\frac{I(q)}{I(0)} = exp\left[-4\,\pi^2\,q^2\,\overrightarrow{e_g}^T\,\overleftrightarrow{Dp}\,\overrightarrow{e_g}\,(\Delta + 3\tau/2 - \delta/6)\right] \quad \text{(S1)}$$

where $\overrightarrow{e_g}$ is the direction of the applied field gradient, and $\overleftrightarrow{Dp}$ is the self-diffusion tensor. The pulsed gradients were applied along six non-collinear directions (Basser et al., 1994; Skare et al., 2000) noted $\overrightarrow{e_1} = \overrightarrow{e_x} = (1,0,0)$, $\overrightarrow{e_2} = \overrightarrow{e_y} = (0,1,0)$, $\overrightarrow{e_3} = \overrightarrow{e_z} = (0,0,1)$, $\overrightarrow{e_4} = \left(1/\sqrt{2}, 1/\sqrt{2}, 0\right)$, $\overrightarrow{e_5} = \left(0, 1/\sqrt{2}, 1/\sqrt{2}\right)$ and $\overrightarrow{e_6} = \left(1/\sqrt{2}, 0, 1/\sqrt{2}\right)$, respectively, with the direction $\overrightarrow{e_3}$ being parallel to the compaction/centrifugation axis of the clay sample. From the six corresponding components of the water self-diffusion tensor, one can easily extract its three

principal axes and the corresponding eigenvalues that describe the water mobility in the longitudinal or transverse direction of the tube axis. The PGSE-NMR attenuation measurements were performed at ~ 19°C (i.e., 292 K), and the associated experimental bulk water self-diffusion coefficient D_0 was measured at $2.0 \pm 0.5.10^{-9}$ m^2 s^{-1} in these conditions.

Fig. S1. *Pulse sequence used to perform Pulsed Gradient Spin Echo (PGSE-NMR) attenuation measurements in Na-kaolinite samples.*



S.1.2. Induration of the samples and two-dimensional X-Ray Scattering measurements

For each sample used in this study, a duplicate was prepared to be used for particle organization measurements. Induration of the duplicate samples was performed to produce thin sections for two-dimensional X-Ray Scattering (2D-XRS) measurements. The induration method used here was based on the thermal impregnation technique with methyl methacrylate (MMA, $C_5H_8O_2$), which was developed by Sammaljärvi et al. (2012) and successfully applied for Na-kaolinite samples (Dabat et al., 2020). The duplicates for 2D-XRS were prepared in PEEK tubes (diameter of 0.64 cm and height of 7.5 cm) instead of PMMA because the latter can dissolve when in contact with MMA. Perforated PEEK caps and cellulose membrane with a pore size of 0.1 µm were placed at each side to maintain both the total porosity and particle organization of the sample during the induration process. The duplicates were first placed under a vacuum for 20 minutes to remove the residual water that could interfere with the polymerization of MMA. Then, liquid MMA mixed with thermal initiator benzoyl peroxide (BPO, at 5% of MMA mass) was introduced into the tubes without breaking the vacuum to facilitate the access of MMA gas to the smallest pores. The samples were kept in contact with liquid MMA for a few days up to two weeks (in the case of centrifuged Na-vermiculite) to promote as much as possible the capillary saturation of the pores by the MMA+BPO mixture. After saturation, the PEEK tubes that contained clayey samples were sealed with PTFE caps

and placed in a water bath at 55°C for at least 24 hours to complete the polymerization of MMA into PMMA.

Following the induration process, the obtained samples were cut longitudinally and transversely with respect to the tube axis (Fig. 2a) using a circular saw (Fig. 2b). The resulting lamellas were reduced by a polishing table to 500 µm thickness to allow sufficient transmission for the XRS measurements (Dabat et al., 2020). Acquisition of two-dimensional XRS (2D-XRS) patterns for anisotropy in particle orientation measurements was performed at the Laboratoire de Physique des Solides (LPS) - Orsay, France. The X-ray beam is generated via a copper rotating anode generator (RU H3R, Rigaku Corporation, Japan), equipped with a multilayer W/Si mirror (Osmic), which generates a monochromatic beam ($\lambda_{CuK\alpha}$ = 1.5418 Å) with a spot size of 1 mm^2 that passes through the slits to cover a 600 x 600 μm^2 surface of the sample. The scattering signals (Fig. 2c) from the sample were collected on a 2D-detector (MAR345, marXperts GmbH®, Germany, 150-µm pixel size). The sample-to-detector distance was set to 250 mm. This configuration makes it possible to reach a scattering vector modulus down to Q_{min} = 0.2 $Å^{-1}$ ($Q = 2\pi/d = 4\pi/\lambda \sin(\theta_B)$, where λ is the incident wavelength, and $2\theta_B$ is the scattering angle). The sample lamellas were aligned perpendicular to the incident X-ray beam by mounting them on a goniometer head, and the XRS were acquired with a typical acquisition time of 900 s.

S.1.3. Through-diffusion experiments on the HDO tracer

The experimental setup for the Through-Diffusion (TD) experiments on the water tracer (HDO) was previously used by Tertre et al. (2018) and originally adapted from the one proposed by Van Loon et al. (2003). The configurations of this setup allow for measuring HDO diffusion along the *z*-direction, i.e., perpendicular to the compaction plane and the preferred orientation of the clay particles. It consists of a fluid circulation system and a PMMA tube that contains the clay sample compacted at the desired ε value (see section 2.2 in the original text). The sample is retained in the tube via a series of components on each side, listed from the closest to the sample to the farthest, as follows: (i) cellulose membrane with a pore size of 0.1 µm, (ii) a stainless-steel filter (pore diameter of 10 µm), and (iii) two PEEK grids (nominal spaces of 280 and 450 µm for mono filaments with diameters equal to 120 and 200 µm, respectively). The PEEK grids are used to homogenize the flow of the solution that arrives at each side of the sample (Melkior, 2000). The fluid circulation system consists of two 50-mL reservoirs (i.e., upstream, and downstream reservoirs) and a peristaltic pump used to ensure the constant circulation of the solutions. Prior to the TD experiment, the sample was saturated with Milli-

Q® water (~18.2 MΩ cm) by maintaining circulation of the water on each side of it for two weeks (Tertre et al., 2018).

For the TD experiments, the upstream reservoir was filled with 50 mL of a 0.01-M NaCl solution, spiked with HDO at 0.55 M and prepared by a dilution of initial D_2O solution (purity of 99.8 atom % D purchased from Agros Organics®), and the downstream reservoir was filled with 50 mL of Milli-Q water. The 0.01-M NaCl solution was used in the upstream reservoir to to measure the in addition to HDO the diffusion of ions (i.e., Na^+, Cl^-) as performed previously in Tertre et al. (2018); data which are not reported in this present study. The two reservoirs were then connected to the TD setup, and t=0 was set as the fluid circulation started. To keep the HDO concentration gradient as constant as possible between the two reservoirs, both reservoirs were regularly replaced with fresh ones (the time step can vary between a few hours to 1 day depending on the experiments), and 1 mL aliquot from the reservoirs were collected for the HDO concentration measurements. The results from the upstream reservoirs (not shown) confirmed that the decrease in the HDO concentration did not exceed 3%, which validated the hypothesis of a constant gradient of HDO during the experiment (see below for the boundary conditions).

All of the TD experiments were performed in a climate-controlled room under a temperature of 20 ± 1 ˚C. The HDO concentrations were determined by water isotope analysis (LWIA DLT-100, Los Gatos Research), and the amount of HDO diffusing in the downstream reservoir was calculated by accounting for the HDO concentration that was naturally present in ultrapure water (i.e., 1.6529×10^{-2} M), as performed in Tertre et al. (2018).

The results from the TD experiments were analyzed by resolving the classical Fick's second law for one-dimensional transport:

$$\frac{\partial C}{\partial t} = \frac{D_e}{\alpha} \cdot \frac{\partial^2 C}{\partial x^2} = \frac{D_e}{\varepsilon + \rho_{app}\, K_d} \frac{\delta^2 C}{\partial x^2} \quad \text{(S2)}$$

where C is the aqueous concentration (mol m^{-3}), t is the time (s), De is the effective diffusion coefficient (m^2 s^{-1}), K_d is the distribution coefficient (m^3 kg^{-1}), ρ_{app} is the bulk dry density (kg m^{-3}), and α is the rock capacity factor. For the water tracer (-), if no adsorption occurs, then α is equal to ε, while if adsorption occurs, α could be greater than ε. Eq. (S2) was resolved by using the following initial and boundary conditions:

$$C\,(x, t) = 0 \text{ for } t = 0 \quad \text{(S3)}$$

$$C\,(x, t) = C_o \text{ at } x = 0 \text{ for } t > 0 \quad \text{(S4)}$$

$$C\,(x, t) = 0 \text{ at } x = L \text{ for } t > 0 \quad \text{(S5)}$$

where C_o is the HDO concentration in the upstream reservoir (mol m^{-3}) corrected from the natural concentration of HDO present in ultra-pure water, and L is the thickness of the sample (m). By considering these equations, the diffusive flux (i.e., $J(x=L,t)$ in mol s^{-1}) in the downstream reservoir can be described according to Eq. (S6), as reported by Crank (1975):

$$J(x = L, t) = \frac{SC_0D_e}{L}\left(1 + 2\sum_{n=1}^{\infty}(-1)^n \exp\left(\frac{-D_e n^2\pi^2 t}{\alpha L^2}\right)\right) \quad \text{(S6)}$$

where S is the cross-sectional area perpendicular to the diffusive direction (m^2). The corresponding total amount of cumulative tracer in the downstream reservoir (i.e., n ($x=L$, t) in mol) is as follows:

$$n(x = L, t) = SC_OL\left(\frac{D_e}{L^2}t - \frac{\alpha}{6} - \frac{2\alpha}{\pi^2}\sum_{n=1}^{\infty}\frac{(-1)^n}{n^2}\exp\left(-\frac{D_e n^2\pi^2}{L^2}t\right)\right) \quad \text{(S7)}$$

As done in Tertre et al. (2018), the diffusion parameters (i.e., *De* and α) were obtained by least-square fitting of the experimental results of the diffusive flux incoming in the downstream reservoir. To accomplish that step, fully analytical solutions were obtained in Laplace space and were then subsequently numerically inverted to provide the solution in time (more details in Savoye et al., 2015). Fitting procedures were performed by accounting for diffusion in stainless-steel filters, as performed in Tertre et al. (2018). Uncertainties in both D_e and α were calculated by considering the uncertainties in the measured tracer fluxes (corresponding to the uncertainty in the concentration measurements; see Table 1).

S.1.4. Generation of virtual porous media for Brownian dynamics simulation

Mesoscale Brownian dynamics simulations of water diffusion in both Na-vermiculite and Na-kaolinite as a function of the anisotropy in the particles' orientation were performed on 3D virtual porous media (VPM; see Table S1), mimicking the distribution of the shapes and sizes of the particles in these samples. The description of the generation of these VPM has been extensively described elsewhere (Ferrage et al., 2015; Dabat et al., 2018, 2020). Briefly, the particles are allowed to settle in a square simulation box with periodic conditions along the *x* and *y* axes (*z* axis pointing upward; Fig. 2a), according to a steepest descent algorithm to reduce the barycenter altitude. A log normal distribution in the dimensions (i.e., basal surface, particle diameter, ratio between thickness and diameter, and ellipticity degree) of the individual particles was obtained from the work of Ferrage et al. (2015) and based on the experimental morphological study of Reinholdt et al. (2013) for the 0.1–0.2 µm size fraction of vermiculite from Santa Olalla, Spain, investigated here. During the settling process, the particles are allowed to slide, swivel or rotate with a random amplitude that ranges from zero to a maximum value. A wide range of degree of anisotropy in the particles' orientation is then obtained by

tuning the amplitudes of the movements, leading to a variation in the degree of freedom in the particle motions (Ferrage et al., 2015). This degree of anisotropy of the particles' orientation was extracted by calculating the average of the second-order Legendre polynomial on the angular distribution of the particle orientations, as follows:

$$\langle P_2 \rangle = \langle P_2(cos\theta) \rangle = \langle 3cos^2\theta - 1 \rangle / 2 \quad \text{(S8)}$$

where θ is the angle between the normal unit vector of the particle and the z axis of the simulation box (Fig. 4a). This $\langle P_2 \rangle$ order parameter, also referred to as the nematic order S (Dabat et al., 2018; Underwood and Bourg, 2020) or the Hermans parameter H (Hermans and Platzek, 1939), takes the value of 0 for an isotropic organization and 1 when all of the particles are perfectly oriented in the bedding (all normal to the particles aligned with the z axis of the simulation box).

To cover over a large range of anisotropy degrees in particle orientations, 13 particle packings with $\langle P_2 \rangle$ values that varied from 0.03 to 0.96 were generated according to this algorithm ((Ferrage et al., 2018; Dabat et al., 2020); see Table S1 and Fig. 4a). This methodology leads, however, to different interparticle porosity values as a function of $\langle P_2 \rangle$ and does not allow obtaining periodic conditions in the z direction. To overcome these drawbacks for the BD simulations, additional treatments, as detailed by Dabat et al. (2020), were applied to the different obtained VPM. Briefly, a cubic sub-volume of ~2000 particles was first extracted, and particles were then polygonized considering 12 in-plane vectors plus 2 vectors passing along the normal of the particles. Periodic conditions with the minimum-image convention were applied along the three directors, $\overrightarrow{e_x}$, $\overrightarrow{e_y}$, and $\overrightarrow{e_z}$, of the simulation box. Based on the obtained sub-volumes, two subsequent treatments were applied to reduce the interparticle porosity of the packings and to reach an interparticle porosity value that is close to that of the water-saturated samples analyzed in this study by PGSE-NMR and through-diffusion experiments, i.e., $\varepsilon_{interp.}$~0.25 (Dabat et al., 2020). The first treatment consists of allowing each particle to grow along its 14 vectors, with detection and rejection of particle overlapping. The second treatment implies the injection of a new particle on the surface of an existing particle and the subsequent particle growth to fill the porosity. The two processes led to final interparticle porosity values of approximately 0.27 for packings with $0.03 \leq \langle P_2 \rangle \leq 0.85$ and approximately 0.25 for packings with $\langle P_2 \rangle = 0.92$ and 0.96 (Table S1; Fig. 4a). Because these treatments lead to a decrease in the particle sizes and thus an increase in the overall specific surface areas (SSA) of the sample, a last treatment involved the dilatation of the simulation box (and thus particle) dimensions. For vermiculite, the final cubic lengths of the VPM are ~1 µm

(i.e., between 1.12 and 0.99 for the order parameter $\langle P_2 \rangle$ ranging from 0.03 to 0.96, respectively; see Table S1) and of the SSA values are ~95 $m^2 g^{-1}$, which is in agreement with the experimental results from Reinholdt et al. (2013). The total number of particles ranges between ~11000 and ~7400, for the more isotropic and anisotropic organizations, respectively (Table S1).

Table S.1. *Characteristics of the 13 virtual porous media used for the Brownian dynamics simulations. The* $\langle \boldsymbol{P_2} \rangle$ *and* $\varepsilon_{interp.}$ *values stand for the order parameter and the interparticle porosity, respectively. The* $N_{part.}$ *and* ℓ_{box} *parameters stand for the total number of particles and the cubic length of the simulation box (in µm), respectively.*

Pack. #	$\langle P_2 \rangle$	$\varepsilon_{interp.}$	$N_{part.}$	ℓ_{box}
1	0.028	0.272	10639	1.12
2	0.053	0.274	10932	1.12
3	0.104	0.271	11039	1.13
4	0.208	0.272	11139	1.13
5	0.322	0.272	11307	1.12
6	0.392	0.275	11092	1.12
7	0.489	0.273	11139	1.15
8	0.575	0.275	11404	1.15
9	0.718	0.269	11446	1.16
10	0.800	0.264	11693	1.16
11	0.849	0.264	11863	1.18
12	0.915	0.249	11526	1.18
13	0.963	0.253	7403	0.99

References for S.D.

Basser, P.J., Mattiello, J., Lebihan, D., 1994. Estimation of the Effective Self-Diffusion Tensor from the NMR Spin Echo. Journal of Magnetic Resonance, Series B 103, 247–254. https://doi.org/10.1006/jmrb.1994.1037

Callaghan, P.T., 1991. Principles of nuclear magnetic resonance microscopy. Clarendon Press.

Cotts, R.M., Hoch, M.J.R., Sun, T., Markert, J.T., 1989. Pulsed field gradient stimulated echo methods for improved NMR diffusion measurements in heterogeneous systems. Journal of Magnetic Resonance (1989) 83, 252–266. https://doi.org/10.1016/0022-2364(89)90189-3

Crank, J., 1975. The Mathematics of Diffusion, 2nd ed. Oxford University Press: London.

Dabat, T., Porion, P., Hubert, F., Paineau, E., Dazas, B., Grégoire, B., Tertre, E., Delville, A., Ferrage, E., 2020. Influence of preferred orientation of clay particles on the diffusion of water in

kaolinite porous media at constant porosity. Applied Clay Science 184, 105354. https://doi.org/10.1016/j.clay.2019.105354

Dabat, T., Mazurier, A., Hubert, F., Tertre, E., Grégoire, B., Dazas, B., Ferrage, E., 2018. Mesoscale Anisotropy in Porous Media Made of Clay Minerals. A Numerical Study Constrained by Experimental Data. Materials 11, 1972. https://doi.org/10.3390/ma11101972

Ferrage, E., Hubert, F., Tertre, E., Delville, A., Michot, L.J., Levitz, P., 2015. Modeling the arrangement of particles in natural swelling-clay porous media using three-dimensional packing of elliptic disks. Physical Review E 91, 062210. https://doi.org/10.1103/PhysRevE.91.062210

Ferrage, E., Hubert, F., Baronnet, A., Grauby, O., Tertre, E., Delville, A., Bihannic, I., Prêt, D., Michot, L.J., Levitz, P., 2018. Influence of crystal structure defects on the small-angle neutron scattering/diffraction patterns of clay-rich porous media. J Appl Crystallogr 51, 1311–1322. https://doi.org/10.1107/S160057671801052X

Melkior, T., 2000. Etude méthodologique de la diffusion de cations interagissant dans des argiles : application : mise en œuvre expérimentale et modélisation du couplage chimie-diffusion d'alcalins dans une bentonite synthétique (Ph.D. Thesis). Ecole Centrale Paris, Paris, France.

Hermans, P.H., Platzek, P., 1939. Beiträge zur Kenntnis des Deformationsmechanismus und der Feinstruktur der Hydratzellulose. Kolloid-Z, Kolloid-Z 88, 68–72.

Porion, P., Ferrage, E., Hubert, F., Tertre, E., Dabat, T., Faugère, A.M., Condé, F., Warmont, F., Delville, A., 2018. Water Mobility within Compacted Clay Samples: Multi-Scale Analysis Exploiting 1 H NMR Pulsed Gradient Spin Echo and Magnetic Resonance Imaging of Water Density Profiles. ACS Omega 3, 7399–7406. https://doi.org/10.1021/acsomega.8b01083

Reinholdt, M.X., Hubert, F., Faurel, M., Tertre, E., Razafitianamaharavo, A., Francius, G., Prêt, D., Petit, S., Béré, E., Pelletier, M., Ferrage, E., 2013. Morphological properties of vermiculite particles in size-selected fractions obtained by sonication. Applied Clay Science 77–78, 18–32. https://doi.org/10.1016/j.clay.2013.03.013

Sammaljärvi, J., Jokelainen, L., Ikonen, J., Siitari-Kauppi, M., 2012. Free radical polymerisation of MMA with thermal initiator in brick and Grimsel granodiorite. Engineering Geology 135–136, 52–59. https://doi.org/10.1016/j.enggeo.2012.03.005

Savoye, S., Beaucaire, C., Grenut, B., Fayette, A., 2015. Impact of the solution ionic strength on strontium diffusion through the Callovo-Oxfordian clayrocks: An experimental and modeling study. Applied Geochemistry 61, 41–52. https://doi.org/10.1016/j.apgeochem.2015.05.011

Skare, S., Hedehus, M., Moseley, M.E., Li, T.-Q., 2000. Condition Number as a Measure of Noise Performance of Diffusion Tensor Data Acquisition Schemes with MRI. Journal of Magnetic Resonance 147, 340–352. https://doi.org/10.1006/jmre.2000.2209

Stejskal, E.O., Tanner, J.E., 1965. Spin Diffusion Measurements: Spin Echoes in the Presence of a Time-Dependent Field Gradient. The Journal of Chemical Physics 42, 288–292.

IV.3. A comparison of HDO diffusion in Na-IDP, Na-vermiculite, and Na-kaolinite

This work's unique dataset on water diffusivity was obtained from compressed samples built from swelling/none-swelling, charged/none charged clay minerals. In the previous sections, we discussed for each used clay mineral individually: (i) the role played by the two types of porosity (interlayer and interparticle), and (ii) the influence of structural charge of the clay particles on HDO diffusion. Here, we expand these discussions by comparing HDO experimental results for all clay minerals obtained experimentally or by BD simulation in this work, and from the literature.

Fig. IV.6 shows the diffusion coefficient obtained from this work and published data using Na- saturated IDP, vermiculite, montmorillonite, and kaolinite samples. In Fig. IV.6a and b, De_z and Dp_z values, respectively, are plotted as a function of the total porosity. Data in this figure summarize the main findings of the previous sections:

i. The influence of particles' preferred orientation is evident for both Na-IDP and vermiculite samples. Evidently, De_z (or Dp_z) obtained with these samples are considerably lower than values obtained for isotropic ones, even though they have the same mineralogy and particles size and similar (or even lower) total porosity.
ii. The impact of the osmotic swelling in Na-montmorillonite samples is clear. Indeed, De_z (or Dp_z) reported from literature for Na-montmorillonite are significantly lower than those obtained for samples made from other minerals; that do not exhibit osmotic swelling.
iii. HDO mobilities obtained with samples made of none-swelling clay minerals (i.e., Na-IDP and Na-KGa2) whose porosity is only an interparticle, yielded a higher De_z (or Dp_z) than the samples made from swelling clay minerals (i.e., Na-vermiculite and Na-montmorillonite). Indeed, De_z (or Dp_z) of Na-kaolinite samples at $\varepsilon \approx 0.25$ are similar to those of Na-vermiculite $\varepsilon \approx 0.5$ with $\varepsilon_{intrp.} \approx 0.24$. This resemblance in D values highlights the marginal contribution of the interlayer porosity to HDO flux in the Na-vermiculite samples.

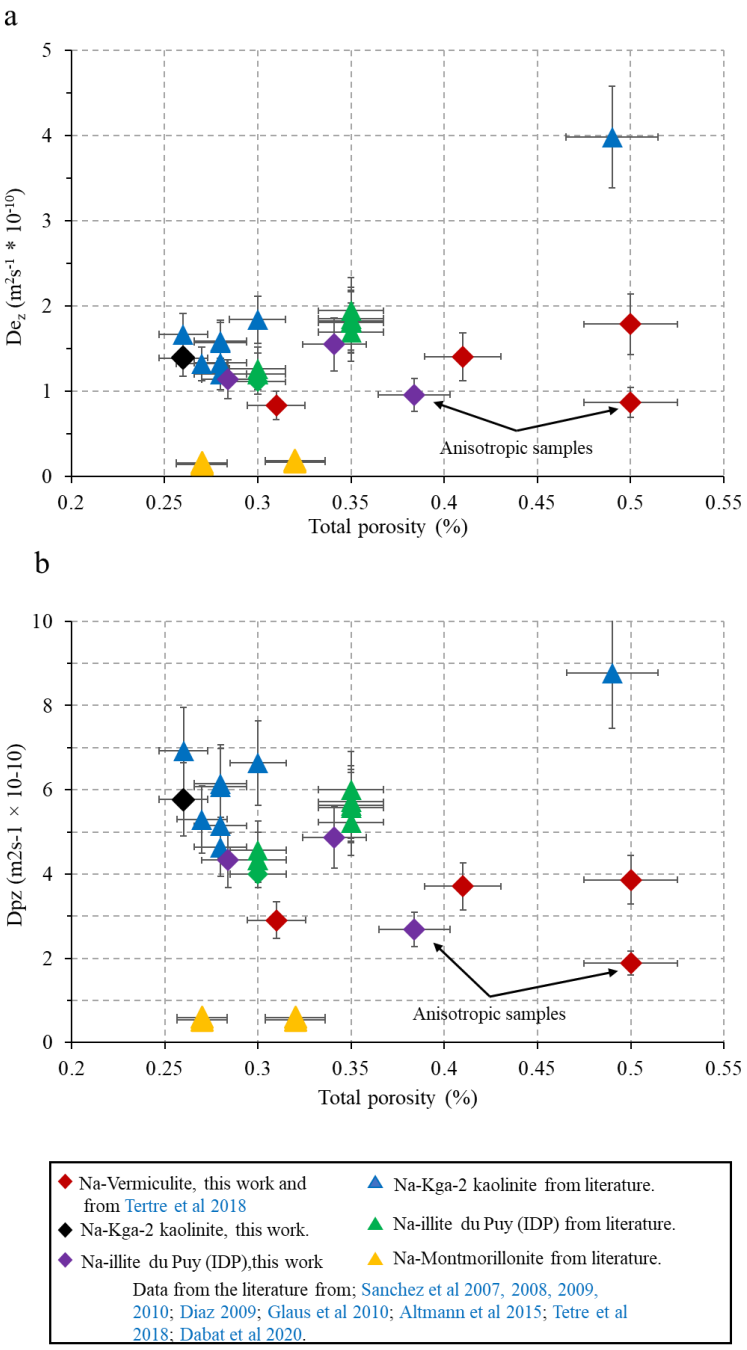


Fig.IV.6. *Comparison between diffusion coefficients of water tracers (HDO/HTO) from this work and published data obtained from compressed samples of different clay minerals.*

(a) Comparison based on effective diffusion coefficients in the direction perpendicular to sedimentation planes (De_z).

(b) Comparison based on pore diffusion coefficients in the direction perpendicular to sedimentation planes (Dp_z).

Anisotropic samples are samples from this work prepared by centrifugation of clay dispersion to have high degree of anisotropy in particles preferred orientation.

It is worth noting that, even though Na-IDP samples still yielded higher De_z (or Dp_z) values than Na-vermiculite one (for a comparable interparticle porosity and a degree in anisotropy in particle preferred orientation), the difference is less pronounced than the one existing between Na-kaolinite and vermiculite samples. This observation can be attributed to several factors: (i) the substantial layer charge in IDP particles that slow water mobility in the vicinity of their external basal surfaces, as discussed in section IV.1.3. (ii) the uncertainty associated with porosity calculation in Na-vermiculite samples. Indeed, as detailed in section

II.3.1 from Chapter II, the volumes of interlayer and interparticle porosities are calculated assuming that the interlayer of particles is filled with two layers (2W) of water molecules (2W) when saturated with water. This assumption is valid in the case of clay dispersion, as reported in Faurel, (2012). However, with the very high solid/solution ratio in compacted Na-vermiculite samples, some particles may be in a 2W/1W mixed layer configuration, leading to a slightly underestimating the interparticle porosity volume (See Eq. II.1). Finally, (iii) as previously discussed, the differences in pore network sizes and morphology between Na-IDP and Na-kaolinite samples may also contribute to IDP samples' lower HDO mobility than kaolinite ones; kaolinite particles are of a larger average size (≈ 0.5 µm *vs* 0.1-0.2 µm for kaolinite and IDP, respectively). In addition, kaolinite particles used have a more platelet morphology than the more barrel shaped IDP particles (Rajec, 1999; Hassan et al., 2005). Such differences in size and morphology are reflected in their pore size distribution (centered to 50 nm for compacted Na-kaolinite samples (Vasseur et al., 1995) versus 80 % of the pores of Na-IDP which are 10 nm pores, as reported in Altmann et al., (2015).

Finally, for Vermiculite, we performed another TD experiment in porous media made from < 0.1 µm size fraction Ca-vermiculite (Fig. A1 in the annexes; in connection to the work of Tertre et al., (2021) resulted in similar De_z of HDO of the ones obtained with 0.1-0.2 µm Na-vermiculite (Table IV.1). This finding agrees with what was reported by Tertre et al., (2018) of no effect of particle size on the diffusion of the water tracer in 0.1-0.2 and 1-2 µm size fractions of Na-vermiculite samples. Hence, this agreement permits us to conclude that, for the size fractions investigated (i.e., < 2 µm) of SO-vermiculite, there is no apparent effect of particle size nor the nature of interlayer cations (i.e., Na^+ and Ca^{2+}) on the diffusion of water tracer in compacted porous media made from SO-vermiculite particles.

IV.4. Summary of Chapter IV

By comparison with data reported in the literature, the novelty of this work was to quantify (experimentally and to a lesser extent by simulation) the effect of some parameters governing the diffusion of water in porous clayey media, such as distribution of porosity between the interlayer and interparticle, particles' preferred orientation, and layer charge of the particles. Our experimental approach relied on: (i) careful choice of clay material representing charge/non-charged and swelling/non-swelling minerals, (ii) prepare compressed samples from these materials at the same porosity but different degrees of anisotropy in particles' preferred

orientation (i.e., isotropic and anisotropic), (iii) the used samples have comparable interparticle porosity volume, with an extra interlayer porosity volume in Na-vermiculite samples is accessible to water. With such a configuration, the contribution of each type of porosity to the diffusion process occurring through diffusion experiments can be assessed.

The main results obtained in Chapter IV can be summarized as follow:

i. The preferred orientation of clay particles, as the porosity, is a first-order parameter in controlling the water mobility in clayey porous media regardless of clay mineral type. Indeed, for water tracer (HDO), anisotropic Na-IDP and vermiculite samples (samples having a high degree in anisotropy in particles preferred orientation) yielded almost two times lower diffusion coefficient than the isotropic samples, despite having similar or a slightly higher total porosity.

ii. For similar interparticle porosity and particles preferred orientation, the mobility of HDO in compacted porous media made of charged and none-swelling clay minerals is further reduced compared to mobility measured for ones made of non-charged clay particles. This finding was based on comparing experimental water diffusion data obtained with Na-IDP (charged and none-swelling) and Na-kaolinite (none-charged and none-swelling) from this work and what is published in the literature.

iii. In a dual-porosity clayey medium, interparticle porosity is the primary conveyor of water flux diffusing through this medium. This finding was based on a comparison of HDO diffusion coefficients obtained for (a) media made from Na-kaolinite and Na-IDP particles characterized by only interparticle porosity to (b) media made with Na-vermiculite samples having similar interparticle porosity but higher total porosity volume (the extra porosity volume is a water accessible interlayer porosity).

iv. Two experimental techniques (i.e., Through Diffusion (TD) and Pulsed Gradient Spin Echo attenuation measurements by Nuclear Magnetic Resonance (PGSE-NMR)) lead to similar diffusion coefficients for HDO diffusing in Na-kaolinite samples characterized by the same porosity and preferential particle orientation. Then, even though the two technics probe very contrasted time scales (days for TD *vs* ms for PGSE-NMR), both methods can be used interchangeably to investigate water dynamics in samples composed of non-charged clayey particles.

v. All experimental data obtained in this study for samples made with different clay minerals were either in good or fair agreement with the calculated ones by Brownian Dynamics (BD) simulation, as shown in Fig. IV.7. Simulated data was extracted from

virtual porous media (VPMs). These VPMs were designed to mimic the samples' mineralogy and porosity distribution (interparticle *vs* interlayer). The simulation also allowed to cover a wide range of degrees in anisotropy of particles' preferred orientation. Hence, the agreement between simulated and experimental data implies that (i) the VPMs characterized by different porosity and particle organizations are well representative of the experimental samples, despite the difference in length scales (Ferrage et al., 2015), and (ii) BD simulations on VPMs are very interesting to explore situations challenging to produce experimentally, such as samples characterized by a very high degree of anisotropy in the particle preferred orientation.

vi. No evident effect was observed of particle size or nature of the interlayer cations on the diffusion of water in compacted SO-vermiculite samples. This observation was based on TD results from different size fractions representing the < 2 µm fraction of SO-vermiculite and for Na^{+} and Ca^{2+} as interlayer cations.

Chapter V:

Na^+ and Cl^- diffusion in Na-vermiculite and Na-illite

V.I. Generalities

The previous chapter discussed the diffusion of water tracer (HDO) in compressed samples made of Na-IDP, vermiculite and kaolinite particles. The results showed the influence of particles' preferred orientation, porosity type, and layer charge on HDO diffusion in these porous media. Here, we continue to investigate the impact of these parameters on the diffusion of Na^+ and Cl^- in the Na-IDP and vermiculite samples.

On the one hand, HDO has access to the total porosity of the porous media and can be considered as a non-sorbing tracer. However, slight adsorption may occur, as in vermiculite (Tertre et al., 2018); this work (see chapter IV)), and in Na-IDP (Glaus et al., 2010; Altmann et al., 2015) porous media (based on the reported α values which were equal (or slightly higher) to the total porosity of the samples). This slight adsorption of HDO can be tentatively assigned to the high layer charge of these minerals. In addition to being a non-sorbing tracer, results showed that HDO/HTO diffusion is independent of the salinity (i.e., ionic strength) regardless of the nature of the porous media chosen, as commonly reported in literature (Van Loon et al., 2007; González Sánchez et al., 2008; Melkior et al., 2009; Glaus et al., 2010; Altmann et al., 2015; Bourg and Tournassat, 2015) and for Na-vermiculite and IDP in this work.

On the other hand, ionic diffusion in negatively charged porous media is highly dependent on the ionic strength of the pore water (salinity), and on the presence or not of a salinity gradient through these media (Dabat, 2019 among others). As a result, the accessible porosity for anions can be smaller than the total porosity because of repulsion from external surfaces of negatively charged clay particles (i.e., anionic exclusion). Indeed, part of the interparticle porosity is partly or wholly inaccessible to anions because of the EDL formation around the external surfaces of negatively charged clay particles (see section I.1.8) (Jardat et al., 2009; Churakov and Gimmi, 2011; Glaus et al., 2011; Tournassat and Appelo, 2011; Tournassat and Steefel, 2015). In addition, the interlayer porosity, which is accessible to water and cations in swelling clay minerals (e.g., Na-vermiculite), is entirely inaccessible for anions (e.g., Cl^-), except for some specific conditions (e.g., see discussion in Tournassat et al. (2016).

The diffusion of ions in clay and clay-rich porous media has been extensively studied in the literature. Indeed, diffusion of various ions (e.g., Na^+, Sr^{2+}, K^+, Cs^+, Rb^+, I^-, Cl^-, Br^-) has

been investigated in porous media made of a single clay phase (i.e., IDP, kaolinite, montmorillonite) and in natural complex rocks including multi clay phases (Opalinus clay, Callovo-Oxfordian clay and Boom clay; Van Loon et al., 2004; Descostes et al., 2008; Appelo et al., 2010; Glaus et al., 2010; Savoye et al., 2010, 2012; Churakov and Gimmi, 2011; Maes et al., 2012; Altmann et al., 2015; Yang et al., 2015; Bacle et al., 2016; Tinnacher et al., 2016; Bestel et al., 2018), see also the reviews of Tournassat and Steefel (2015) and Charlet et al. (2017). Most of these diffusion experiments in these studies were performed under constant salinity (i.e., constant ionic strength) of the background electrolytes in the upstream and downstream reservoirs. In addition, radioactive isotopes (e.g., $^{22}Na^{+}$, $^{36}Cl^{-}$) of the investigated species were used at trace concentration compared to the background electrolytes.

At constant ionic strength (i.e., no salinity gradient), and because the concentration of the tracers is negligible to that of the background electrolytes, tracers diffuse separately, without affecting the electroneutrality of the solution (i.e., independent diffusion). For this reason, accelerated cations diffusion in the EDL (surface diffusion) and in the interlayer porosity are generally reported due to cation adsorption in the charged porous media (i.e., in IDP and vermiculite porous media; Glaus et al., 2010; Altmann et al., 2015; Dabat, 2019: Dabat et al., in preparation). Hence, the independent diffusion generally results in considerably higher mobility of cations comparing to anions because of the reasons above (e.g., Glaus et al., 2010; Altmann et al., 2015).

In this work, and as mentioned in Chapter II/section II.5.2, we study the diffusion of non-radioactive Na^{+} and Cl^{-} by using different concentrations gradients between the two aqueous reservoirs (i.e., 0.01, 0.1 and 1 M in the upstream reservoir, and only MQ water in the downstream one). In this case, ions should co-diffuse to respect the electroneutrality of the solution in both reservoirs. Under such conditions, and because anions can be subject to anionic exclusion in clayey porous media made of negatively charged particles (Na-vermiculite and IDP), cations diffusion is controlled by that of anions (Dabat, 2019). Hence, Na^{+} and Cl^{-} in our experiments should yield similar mobilities since they have the same absolute valency number. In addition, their mobility can be compared to those generally obtained for $^{36}Cl^{-}$ in literature by considering no salinity gradient (for similar porous media).

V.2 Summary of the TD experiments

Through-diffusion (TD) of Na^{+} and Cl^{-} was investigated in compressed samples from two Na-saturated clay minerals: Santa Olalla vermiculite (Na-vermiculite) and illite du Puy (Na-

IDP). The 0.1-0.2 µm size fraction was used for both minerals. The Na-vermiculite samples have a total porosity of $\boldsymbol{\varepsilon} = 0.49$, including ~0.24 of interparticle porosity ($\boldsymbol{\varepsilon}_{interp.}$) and 0.25 of interlayer one ($\varepsilon_{interl.}$). Vermiculite particles have a negative layer charge of approximately 0.84 eq/h.u.c (Arguelles et al., 2010). In water-saturated conditions (i.e., during TD experiments), the interlayer of Na-vermiculite particles contains two layers of water molecules; then $\boldsymbol{\varepsilon}_{interl.}$ is bi-hydrated (Faurel, 2012). In this configuration, most probably, Cl^- cannot access to the interlayer of Na-vermiculite because of the repulsion forces from the negatively charged layers (see discussion in Tournassat et al., (2016)). Moreover, depending on the ionic strength of the pore water (i.e., salinity), a part of the interparticle porosity may also be inaccessible to Cl^-, as discussed above. Na-vermiculite sample in this work has a high degree of anisotropy in particles' preferred orientation (i.e., anisotropic; $\langle P_2 \rangle$ order parameter = 0.41). Na^+ and Cl^- diffusion results from this sample are compared to those obtained by Dabat (2019) for an isotropic one at the same total porosity ($\langle P_2 \rangle$ order parameter = 0.03) using 0.01 and 1 M salinity gradients.

As far as they are concerned, porous media made with Na-IDP particles have only interparticle porosity ($\boldsymbol{\varepsilon} = \boldsymbol{\varepsilon}_{interp.}$), with 0.1-0.2 µm IDP particles having a negative layer charge of around 0.80 eq/h.u.c (more details in Chapter III). The interlayer of IDP is inaccessible for the different tracers (including HDO). In this work, we compare results obtained for both Na^+ and Cl^- ions diffusing through three different IDP samples: two isotropic ($\langle P_2 \rangle$ order parameter = 0.11; $\varepsilon = 0.28$ and 0.34) and two anisotropic samples ($\langle P_2 \rangle$ order parameter = 0.54; $\varepsilon = 0.38$ and 0.37) using 0.01, 0.1 and 1 M of salinity gradients.

The lowest salinity gradient used in this work is 0.01 M and the highest one is 1 M for experiments carried out with both Na-IDP and Na-vermiculite samples. These gradient conditions were chosen to have comparable results to those obtained by Thomas Dabat (Dabat, 2019), who studied diffusion of Na^+ and Cl^- in isotropic Na-vermiculite porous media. As far as we are concerned, such comparison allows to investigate the diffusion behavior of these ions in a swelling clay mineral (Na-vermiculite) and non-swelling clay (Na-IDP) having similar $\boldsymbol{\varepsilon}_{interp.}$.

When using a 0.01 M salinity gradient, and irrespective of the clay porous medium used, the De_z of Na^+ is consistently higher than that of Cl^-, sometimes by a factor 2 (Table IV.1). For example, in both isotropic and anisotropic Na-vermiculite samples (Table IV.1), Na^+ returned in a higher De_z of Cl^- by ~1.9 and 1.5 times, respectively. This difference can be attributed to

CO_2 dissolved in the reservoirs from the ambient air (reservoirs are open to the ambient air during the TD experiment to avoid overpressure in the fluids' circulation system caused by trapped air; Fig. II.10). Hence, the formed aqueous carbonates and bicarbonates (CO_3^{2-}, HCO_3^-) ions can co-diffuse with Na^+ leading to an increase in Na^+ flux. Indeed, the DIC (total dissolved inorganic C content) can be up to a concentration of 10^{-4} M in freshwater (Cole and Prairie, 2014), which is ~ 5× 10^{-6} mole in the 50 mL reservoir used in our TD experiments. By comparing this value with the diffused flux of Cl^- at 0.01 M salinity, which is between 2 to 3 × 10^{-7} mole day^{-1} (see Fig. V.4a), the contribution of carbonates ions is probably not negligible. For this reason, and since cations co-diffuse with anions as mentioned above, we can consider that the De_z of Na^+ represents the effective diffusion coefficient of the sum of total diffused anions (i.e., Cl^- and carbonates). Note that at higher salinity gradients (i.e., 1 M), this effect diminishes drastically because carbonates and bicarbonates concentrations become negligible compared to that of Cl^-. Another factor that contributes to the higher uncertainties on De_z of Na^+ and Cl^- at 0.01M salinity gradient is the short timestep that we used (1 day), and as a result, the concentrations of ions in the downstream reservoirs which were sometimes low and close to the detection limits of the atomic absorption spectroscopy and ion chromatography devices (~ 0.12 and 0.15 ppm for Na^+ and Cl^-, respectively). Hence, we could not obtain reliable effective diffusion coefficients for Cl^- diffusing through Na-IDP samples at 0.01 M, and those measured for Na^+ diffusing through Na-IDP and Na-vermiculite samples have higher uncertainties by approximately 30% compared to ones obtained for higher salinity gradients.

Note that membrane effect was previously reported in the literature for diffusion experiments performed with low porosity porous media made of smectites (e.g., Heister et al., 2005), leading to a flux of water (by osmose) from the low salinity reservoir (downstream in our case) to the high salinity reservoir (upstream in our case). However, this process was not observed during the different TD experiments performed in this work, because no increase in mass was detected in the upstream reservoirs; such behavior indicates that, for the range of porosities and ionic strengths investigated, no "membrane effect" within the used porous media of Na-IDP and vermiculite.

Importantly, when comparing the mobility of HDO to the ones of Na^+ and Cl^-, De_z are normalized to the D_0 of the species in bulk water at 21˚C. For TD experiments from this work, and because of the co-diffusion phenomena discussed earlier, the De_z of Na^+ and Cl^- are normalized to D_0 of the NaCl salt reported in Mills and Lobo (1989). For $^{36}Cl^-$ data from the literature, De_z were normalized to the D0 of $^{36}Cl^-$ at 21˚C as in Savoye et al. (2011).

V.3. Na^+ and Cl^- diffusion in Na-saturated Illite du Puy (Na-IDP)

Considering the difficulties encountered with TD experiments with IDP material discussed in the previous chapter (See IV.1.2), the robustness of our results was verified by the good agreement of the De_z/D_0 (as explained in the above) of Na^+ and Cl^- obtained in this work with those reported from literature for $^{36}Cl^-$ obtained from compacted Na-IDP porous media, as shown in Fig. V.1.

Interestingly, this agreement suggests no, or a minor effect of the salinity gradient used in TD experiments in this work. A similar observation was previously reported in Dabat (2019) for experiments carried out with compacted porous media (isotropic) made of Na-vermiculite particles and using 0.01 M salinity gradients.

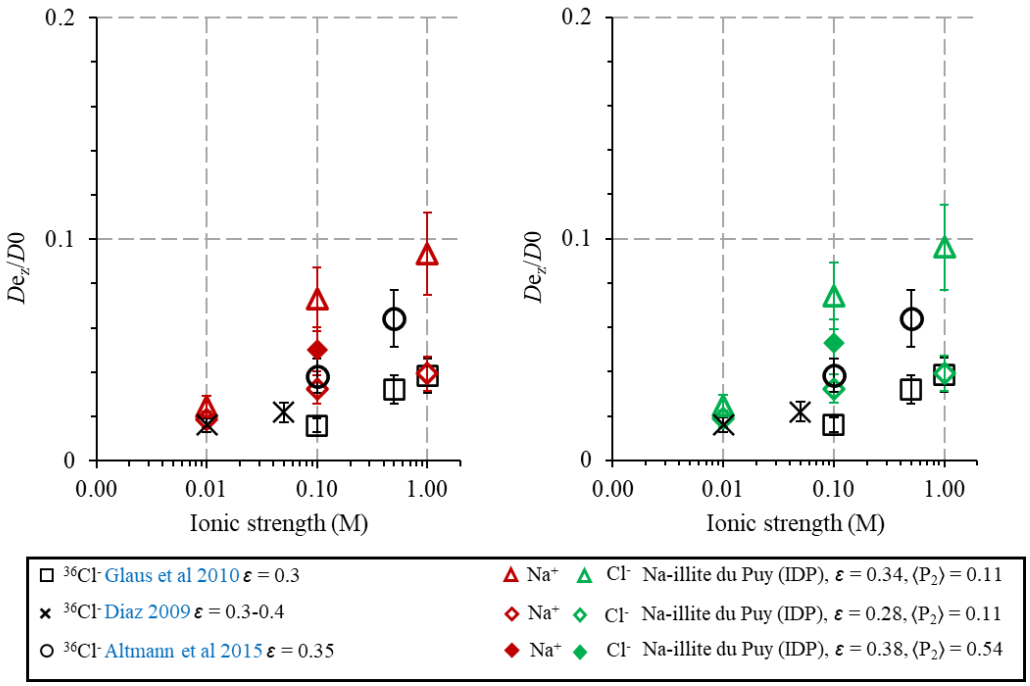


Fig. V.1. *Comparison between effective diffusion coefficients (De_z/D_0) of Na^+ and Cl^- obtained from Na-illite du Puy (IDP) samples from this work (red and green symbols, respectively) and the ones from published $^{36}Cl^-$ (black symbols) as a function of the sample's total porosity. For normalization, D_0 of NaCl was used for Cl^- and Na^+ from this work, while D_0 of $^{36}Cl^-$ was used for $^{36}Cl^-$ from the literature.*

The results of TD experiments and the analytical solutions for the diffusion of Na^+ and Cl^- in Na-IDP samples using a 0.1 and 1 M salinity gradient are reported in Fig.V.2, for two isotropic (ε = 0.28 and 0.34) and two anisotropic (ε = 0.38 and 0.37) samples.

Using a 1 M salinity gradient (Fig. V.2a), De_z of Na^+ and Cl^- in both samples are equal or slightly lower than the one of HDO (Table IV.1). This similarity indicates no or marginal anionic exclusion within these samples using this very high salinity gradient, in line with the diminishing of the EDL due to the high concentration of ions in pore water (at least for a significant fraction of the sample). However, it seems that a slight anionic exclusion persists in the lower porosity sample ($\boldsymbol{\varepsilon}$ = 0.28; Table IV.1), probably due to higher compaction in this sample that may lead to more pore throats (pores are very small and inaccessible to anions due to overlapping of the EDL).

Anionic exclusion is more significant by using a 0.1 M salinity gradient (Fig. V.2b) compared to 1 M, in agreement with the increase in the EDL thickness with the decrease of the salinity. Indeed, $\frac{De_z\ HDO/D_0HDO}{De_z\ Ion/D_0Ion}$ ratio is between 1.5-2 for all three samples used by considering a salinity gradient of 0.1 M compared to ~1 for 1 M (Table IV.1).

At 0.1 and 1 M salinity gradients, the strong effect of increased anisotropy in the particles' preferred orientation (i.e., increasing $\langle P_2 \rangle$ value) is evident by the decrease of the De_z of both Na^+ and Cl^- in the two anisotropic samples (ε = 0.38 and 0.37; $\langle P_2 \rangle$ = 0.54) by factor ~1.5 (i.e., $\frac{De_{z\ Iso}}{De_{z\ Aniso}}$) compared to those of the isotropic sample (ε = 0.34; $\langle P_2 \rangle$ = 0.11), even though the isotropic samples has 4% less porosity volume (Fig. V.2b; Table IV.1). Moreover, the ratios $\frac{De_{z\ Iso}}{De_{z\ Aniso}}$ for ions and HDO are similar in Na-IDP samples (i.e., 1.4 and 1.6, respectively).

Fig. V.3 shows the best-fit solution of the diffused Na^+ flux using a 0.01 M salinity gradient, obtained from the two isotropic Na-IDP samples ($\boldsymbol{\varepsilon}$ = 0.28 and 0.34; no data from the anisotropic samples for this salinity gradient). Fluxes can be interpreted with De_z values = 0.29 (0.22-0.41) $\times 10^{-10}$ and 0.38 (0.18-0.52) $\times 10^{-10}$ $m^2\ s^{-1}$ for the isotropic samples at $\boldsymbol{\varepsilon}$ = 0.28 and 0.34, respectively. These values are ~4 times lower than De_z of HDO reported for these samples (Table IV.1), reflecting the important anionic exclusion using this salinity condition (i.e., 0.01 M). It worth mentioning that, by considering the uncertainties in Na^+ measurements at this salinity, this ratio is not far from the 5.8 obtained by Diaz, (2009) using a porous media made with Na-IDP particles at ($\boldsymbol{\varepsilon}$ = 0.42; I= 0.01 M).

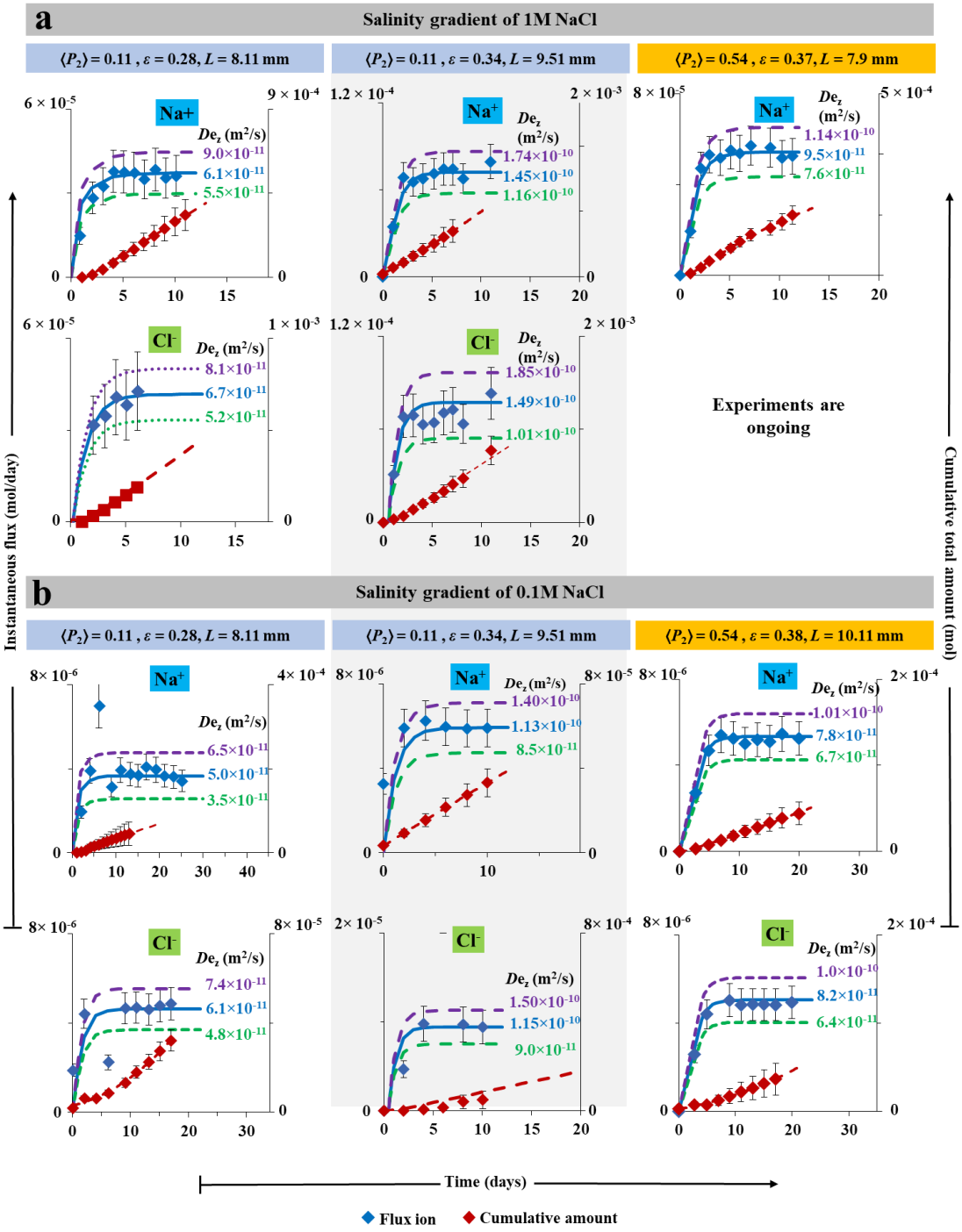


Fig. V.2. *Experimental instantaneous flux (blue diamonds) and cumulative quantities (red diamonds) of* Na^+ *and* Cl^- *diffusing through IDP samples. The solid blue lines correspond to the fit of the experimental flux, whereas dotted lines are simulated flux curves calculated by considering the error range in the diffusion parameters (Table IV.1). Dashed lines correspond to simulated cumulative curves by considering the diffusion parameters interpreting the average experimental flux.*

$\langle P_2 \rangle$ *is the order parameter representing the degree of anisotropy in particles preferred orientation (see text for details).* ε *is the total porosity value (%). L is the sample thickness in mm.*

All De values are corrected from possible temperature variations and are reported for 21°C. Cross-sectional area of the sample perpendicular to the diffusive direction = 7.09×10^{-5} m^2.

Finally, by using a 0.01 M salinity gradient, De_z values for Na^+ in the isotropic Na-IDP samples are similar to those obtained with the isotropic Na-vermiculite sample having a comparable interparticle porosity (De_z = 3.4 (2.6 - 4.8)) × 10^{-11} m^2 s^{-1}; $\varepsilon_{interp.}$ = 0.25; Table IV.1). This similarity indicates that the main flux of Na^+ indeed diffuses in the interparticle porosity of Na-vermiculite, and that Cl^-, as well as Na^+, are excluded from the interlayer porosity of the vermiculite particles. This exclusion of both ions agrees with the hypothesis of co-diffusion of ions under salinity gradient discussed in the beginning of this chapter. Moreover, these values are similar to De_z of $^{36}Cl^-$ in Diaz, (2009) obtained under 0.01 M NaCl salinity (De_z = 2.9 (2.6-3.2)) ×10^{-11} m^2 s^{-1}; ε = 0.42), indicating no effect of the presence or not of low salinity gradient of 0.01 M on the diffusion of anions in Na-IDP samples, as discussed earlier.

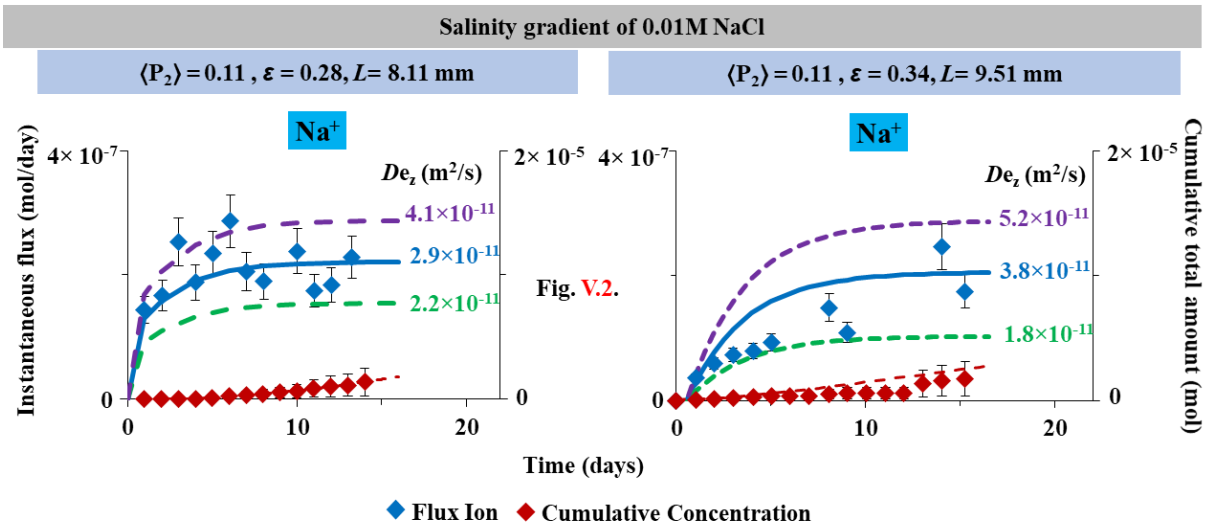


Fig. V.2.

Fig. V.3. *Experimental instantaneous flux (blue diamonds) and cumulative quantities (red diamonds) of* Na^+ *diffusing through IDP samples. The solid blue lines correspond to the fit of the experimental flux, whereas dotted lines are simulated flux curves calculated by considering the error range in the diffusion parameters (Table IV.1). Dashed lines correspond to simulated cumulative curves by considering the diffusion parameters interpreting the average experimental flux.*

$\langle P_2 \rangle$ *is the order parameter representing the degree of anisotropy in particles preferred orientation (see text for details).* ε *is the total porosity value (%). L is the sample thickness in mm*

All De values are corrected from possible temperature variations and are reported for 21°C. Cross-sectional area of the sample perpendicular to the diffusive direction = 7.09×10^{-5} m^2.

V.4. Na^+ and Cl^- diffusion in Na-Santa Olalla (SO) vermiculite

The experimental instantaneous flux and cumulative quantities of diffused Na^+ and Cl^- in Na-vermiculite samples are shown in Fig. V.4 in addition to the analytical fit and extracted De_z values using salinity gradients of 1 (Fig. V.4a) and 0.01 M (Fig. V.4b).

With 1 M salinity gradient, the ratio $\frac{De_z\,HDO/D_0HDO}{De_z\,Na^+/D_0\,Na^+}$ is slightly inferior to 1 in the isotropic sample, in line with the EDL's diminishing and thus the anionic exclusion (Table IV.1). However, for the anisotropic sample, this ratio is around 1.3 for both Na^+ and Cl^-, suggesting the remaining of slight anionic exclusion even at such high ionic strength. This can tentatively be attributed to the difference in pore space geometry in this sample resulting from particles' preferred orientation. Considering that the anisotropic sample was prepared by centrifugation of clay dispersion, in such conditions, segregation of the particles occurs, where coarser particles tend to settle before the finer ones, leading to increased heterogeneity in pores' shape and sizes between areas with different particle sizes. Then, probably, the more oriented particles in the anisotropic sample can increase the pore throat, at least in the z-direction. By contrast, the isotropic sample was obtained by compressing dry clay powder, where the random distribution and orientation of the particles led to more homogeneous pores in terms of geometry.

Under 0.01 M salinity gradient (Fig. V.3b), the ratio $\frac{De_z\,HDO/D_0HDO}{De_z\,Na^+/D_0\,Na^+}$ in Na-vermiculite sample (Table IV.1) indicates that Na^+ diffused ~ 5.5 and 4.5 times slower than HDO in the isotropic and the anisotropic samples, respectively. This ratio is considerably larger for Cl^- which diffuses 10 and 7 times slower than HDO in the isotropic and anisotropic samples (after normalization to D_0). As discussed above, this difference between Na^+ and Cl^- is probably because of dissolved carbonates anions co-diffusing with Na^+ cations. Anyway, the low De_z of ions reflects the important anionic exclusion within the Na-vermiculite media under such low salinity gradient (i.e., 0.01 M).

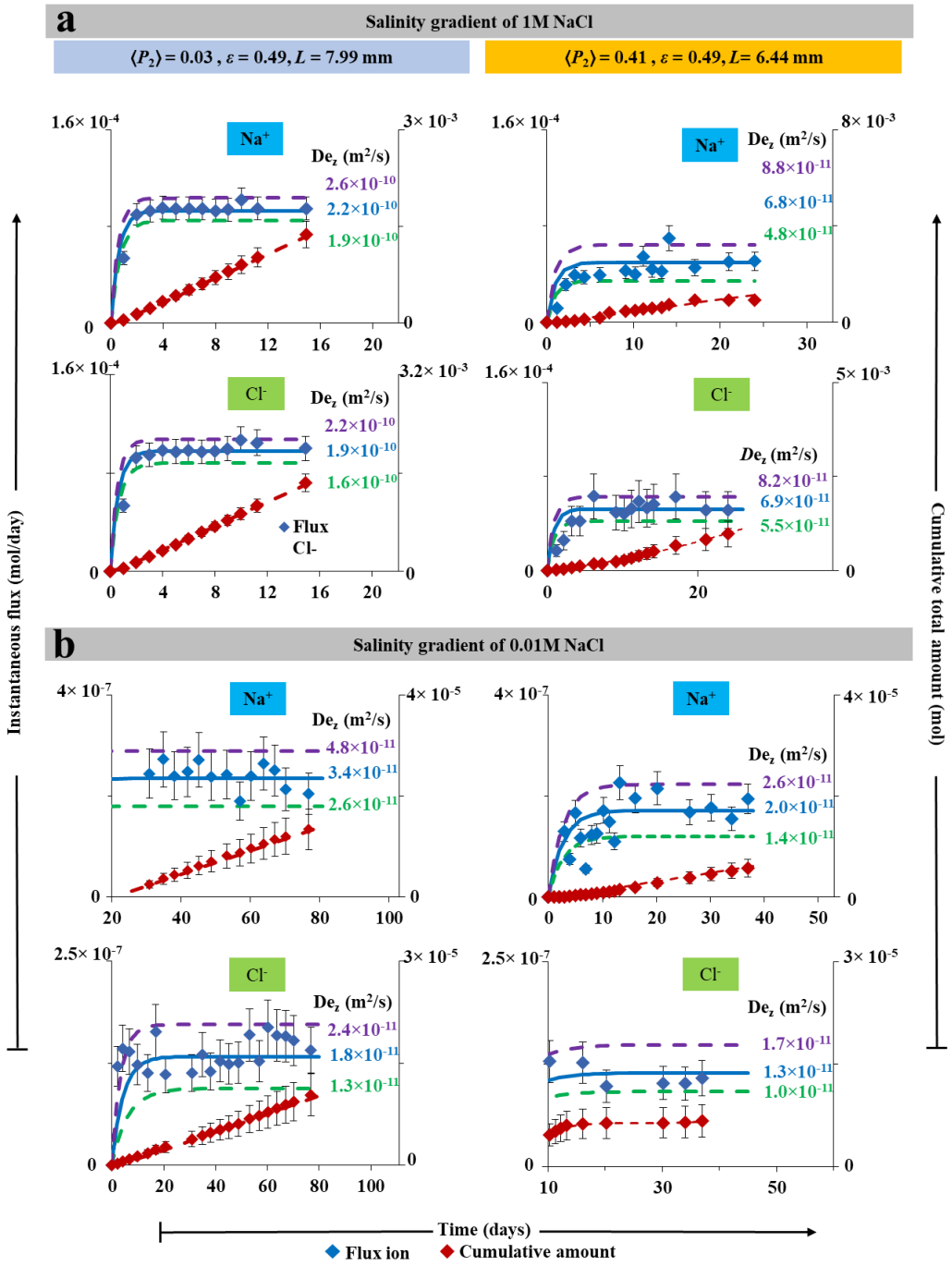


Fig. V.4. *Experimental instantaneous flux (blue diamonds) and cumulative quantities (red diamonds) of Na^+ and Cl^- diffusing through Na-vermiculite samples. The solid blue lines correspond to the fit of the experimental flux, whereas dotted lines are simulated flux curves calculated by considering the error range in the diffusion parameters (Table IV.1). Dashed lines correspond to simulated cumulative curves by considering the diffusion parameters interpreting the average experimental flux.* $\langle P_2 \rangle$ *is the order parameter representing the degree of anisotropy in particles preferred orientation (see text for details).* ε *is the total porosity value (%). L is the sample thickness in mm. All De values are corrected from possible temperature variations and are reported for 21°C. Cross-sectional area of the sample perpendicular to the diffusive direction = 7.09×10⁻⁵ m².*

V.5. Summary and conclusions

This chapter discussed the results obtained from TD experiments of Na^+ and Cl^- in compacted porous media made of Na-vermiculite and Na-IDP particles under different salinity gradient conditions. The sample-set included isotropic and anisotropic samples in terms of particles' preferred orientation. All samples used in this work were built to have similar or comparable volumes of interparticle porosity ($\varepsilon_{interp.}$). The latter is the only porosity type in Na-IDP samples, while ones made from Na-vermiculite particles exhibited an extra volume of interlayer porosity ($\varepsilon_{inerl.}$) potentially accessible for water and cations.

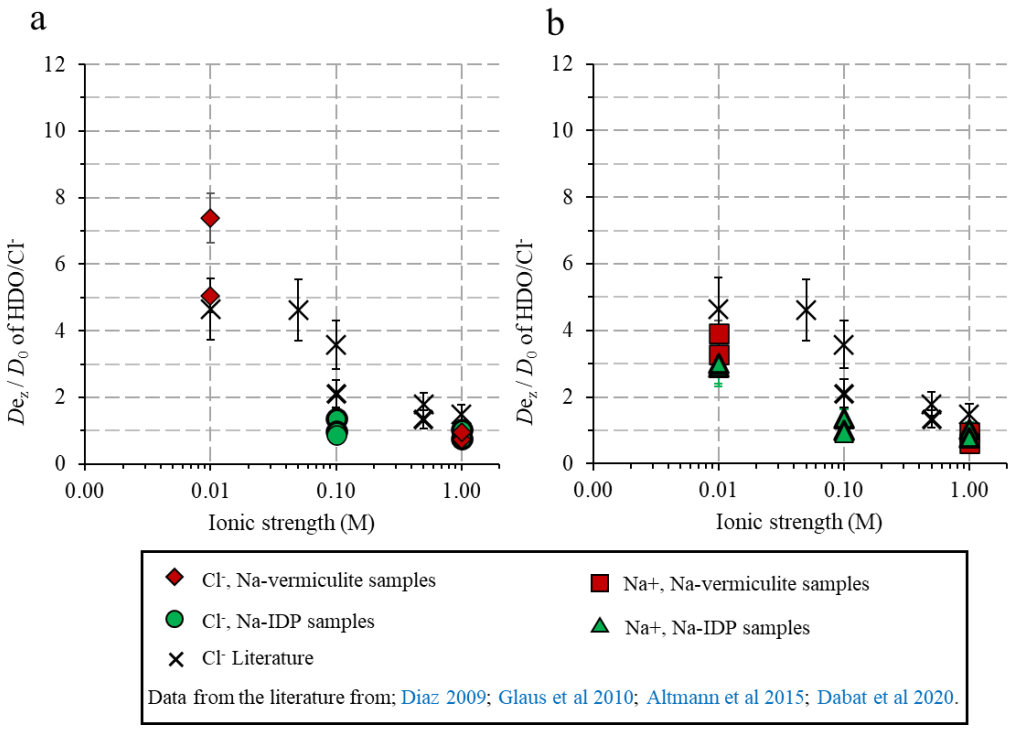


Fig. V.5. *Comparison of the ratio* $\frac{De_z/D_0HDO}{De_z/D_0Ion}$ *obtained for* Na^+ *and* Cl^- *diffusing through Na-illite du Puy (IDP) and Na-vermiculite samples in this work using different salinity gradients, and data reported from the literature and obtained for* $^{36}Cl^-$ *under constant salinity. Salinity indicated on the horizontal axis is that of the upstream reservoir in case of salinity gradient conditions.* D_0 *of NaCl was used for* Cl^- *and* Na^+ *from this work, while* D_0 *of* $^{36}Cl^-$ *was used for* $^{36}Cl^-$ *from the literature. All De values are corrected from possible temperature variations and are reported for 21 °C.*

Fig. V.5 compares the ratios $\frac{De_zHDO/D_0HDO}{De_zion/D_0ion}$ measured for ions at different salinity gradients for Na-IDP, Na-vermiculite samples from this work, and those from literature for $^{36}Cl^-$ from (Diaz, 2009; Glaus et al., 2010; Altmann et al., 2015) obtained from Na-IDP samples at constant salinity. Data from this work and the literature follow the logical trend of decreasing

$\frac{De_zHDO/D_0HDO}{De_zanion/D_0anion}$ of anions (or salt) with increasing the salinity due to the enhanced electrostatic shielding of the negative charge of the clay particles (i.e., decreasing the thickness of the EDL), as discussed earlier.

The trend obtained in this work of the $\frac{De_zHDO/D_0HDO}{De_zion/D_0ion}$ values is similar for Na-IDP and Na-vermiculite samples, and it is logical with the evolution of salinity (with or without salinity gradients); starting with strong anionic exclusion at 0.01 M salinity gradient, which practically disappears at 1 M with a ratio $\frac{De_zHDO/D_0HDO}{De_zion/D_0ion}$ close to ≈ 1. For Na-IDP samples used this work, the value of $\frac{De_zHDO/D_0HDO}{De_zion/D_0ion}$ reduces significantly between 0.01 M (~4) and 0.1 M (~1.5) salinity for both Na^+ and Cl^- (i.e., NaCl salt), indicating that most of the negative charge in IDP particles external surfaces is screened when using a 0.1 M salinity gradient condition.

Results obtained in this work with Na-IDP and Na-vermiculite samples for ionic diffusion are in good agreement with those obtained for $^{36}Cl^-$ in literature and obtained with compacted Na-IDP samples (Fig. V.5). However, the diminishing of the anionic exclusion with increasing the ionic strength is lower in Na-IDP samples from the literature (no salinity gradient) than those from this work (with salinity gradient). Indeed, the ratio $\frac{De_zHDO/D_0HDO}{De_zCl-/D_0Cl-}$ for Na-IDP samples from the literature is constantly higher, particularly when compared to one obtained in this work (Fig. V.5b). However, even by using a salinity gradient of 1 M, this ratio is 1.3-1.5 for Na-IDP samples from the literature compared to ~1 in Na-IDP and Na-vermiculite from this work, suggesting slight residual anionic exclusion in these samples. This observation can be tentatively assigned to higher heterogeneity in the pore size and shapes related to more heterogeneous particle size for the sample used in the literature. Indeed, these samples are prepared of non-specified size fraction or by using the < 0.5 µm fraction following the methodology given in Baeyens and Bradbury, (1997). However, IDP particle size distribution is heterogeneous in both cases, since ~ 40% of the particles are < 0.1 µm, including that ~20% of the particles are < 0.05 µm regardless of the source material (Table III.1). Such fine and heterogeneous particle size will lead to heterogeneity in the pore size and shapes, with an essential portion of the pores so small that the EDL will overlap even at a 1 M salinity rendering the pore inaccessible to Cl^-. On the contrary, Na-vermiculite and Na-IDP samples used in the present work are built from more homogenous particle sizes (i.e., 0.1-0.2 µm), leading probably to more homogenous and larger pore sizes.

Finally, the main findings of this chapter at the time of the writing can be summarized as follows:

i. For the isotropic samples, the diffusion of Na^+ and Cl^- is similar between Na-IDP and Na-vermiculite for comparable interparticle porosity. This conclusion was based on similarities in De_z values of Na^+ and Cl^- obtained in this work using different salinity gradients, and data obtained in literature for $^{36}Cl^-$ without a salinity gradient (after normalization of the results to (i) D_0 of the NaCl salt for data obtained with salinity gradient vs (ii) D_0 of $^{36}Cl^-$ for data from literature obtained without salinity gradients). This comparison allows also to confirm that the diffusion of anions is independent of the presence or not of a salinity gradient, when the salinity used for data reported in literature is equal to that used for the upstream reservoir in this work.

ii. Similar to HDO diffusion, the preferred orientation of clay particles and the interparticle porosity are first-order parameters in controlling the Na^+ and Cl^- mobilities in clayey porous media made from a "real dual-porosity" clay mineral (i.e., Na-vermiculite) or a mono porosity (Na-IDP) clay mineral. The words "real dual-porosity" refer to clay minerals that allow to maintain a well-defined interlayer volume in water-saturated conditions.

iii. Anionic exclusion is also a first-order parameter controlling the diffusion of both Na^+ and Cl^- in charged clayey porous media (i.e., Na-IDP, Na-vermiculite) using salinity gradients. In such media, the anionic exclusion is a function of the nature of the diffused species, ionic strength, and the amount of negative structural charge in the clay particles. However, particles size distribution is also a controlling factor because it defines the geometry of the pore network. As seen earlier, the anionic exclusion probably persists by using a 1 M salinity in Na-IDP samples by considering literature data (no salinity gradient), with approximately 40% of their particles being < 0.1 μm, contrary to what is measured in this work using porous media built with particles having more homogenous size fraction (i.e., 0.1-0.2 μm).

General conclusions and perspectives

The molecular diffusion of water and solutes through compacted porous clay media has been longstanding subject in the literature. Mainly because this process is the primary transporter of chemical species through such media. Molecular diffusion in clay media comprises several complex phenomena resulting from the physio-chemical properties of the clay particles. For example, the negative charge in clay particles is the reason for adsorption-desorption, ionic exclusion, slowed and enhanced diffusion (compared to diffusion in bulk solution) of chemical species, in addition to the difference in the species' dynamics as function of the different types of porosities (i.e., interparticle and interlayer). Moreover, diffusion of species through clay porous media is expected to be strongly anisotropic due to the lamellar morphology of clay particles.

Understanding the factors that control molecular diffusion in compacted clay media is very important, because they are used or considered for the storage and confinement of radioactive wastes and the capture of CO_2 in subsurface geological repositories. In addition, swelling clays are the main constituent of *Geosynthetic Clay Liners* (GCL) and *Compacted Clay Liners* (CCL) used as barriers in the landfills of domestic and chemical wastes. Moreover, clay minerals (particularly swelling ones) control several properties of soils, as their contents and mobilities of nutritive cations (as Ca^{2+}, K^{+}), permeabilities, and their contaminant retention capabilities.

In this context, the present thesis dealt quantitively with two important parameters that control the diffusion of species in compacted porous media. This was achieved through an experimental methodology developed from the one in Dabat (2019). The two parameters investigated in this work were (i) the anisotropy in the preferred orientation of clay particles, and (ii) the role of dual porosities (interlayer *vs.* interparticle). Compacted porous media in this work were made from a single clay mineral (i.e., model system). As well, the careful choice of the clay minerals in this work allowed to qualitatively discuss the influence of their structural charge on the diffusion of water and solutes in these media. Additionally, the obtained results for water diffusion from these media were used to validate ones obtained from *Brownian dynamics* (BD) simulation using *virtual porous media* (VPMs) designed to simulate the experimental ones' mineralogy and internal organization. Consequently, the good agreement found in this work between simulated and experimental results demonstrated the good

prediction capacity of BD simulation. Also, this agreement indicated that BD simulation can be used with good confidence to simulate conditions that are difficult to produce experimentally.

The objectives of this thesis were achieved by building different compacted porous media from single clay phase. These media can be either at low anisotropy (i.e., isotropic) or having high anisotropy (i.e., anisotropic) in terms of the preferred orientation of clay particles, but always having a similar total porosity volume (ε). By using *through diffusion* (TD) setup and different salinity gradients, these media allowed to obtain quantitative information on the influence of particles preferred orientation on the diffusion of water, Na^+ and Cl^-. In addition, the porous media used in this work were either built from non-swelling clay minerals (i.e., having only interparticle porosity, $\varepsilon_{interp.}$) or from swelling clays exhibiting both $\varepsilon_{interp.}$ and interlayer porosity ($\varepsilon_{interl.}$). The latter (i.e., $\varepsilon_{interl.}$) is theoretically accessible for water and cations. All these media had similar $\varepsilon_{interp.}$ with or without extra volume of $\varepsilon_{interl.}$. Consequently, the comparison between TD results from these media (i.e., swelling, and non-swelling) provided quantitative data on the contribution of each type of porosity to the diffusion of water, Na^+ and Cl^-. Finally, the $\langle P_2 \rangle$-order parameter extracted from *2-dimensional X-ray scattering* measurement (2D-XRS) was used as a quantitative descriptor of the anisotropy in particle orientation for porous clay media, based on the methodology reported in Dabat et al (2020) and Dabat (2019).

The clay minerals used in this work were (i) Santa-Olalla (SO) vermiculite, a swelling clay mineral that maintains both $\varepsilon_{interp.}$ and $\varepsilon_{interl.}$ when compacted into porous media. The coexistence of these porosities is due to the substantial layers' negative charge in SO-vermiculite which prevents osmotic swelling in water saturated conditions (i.e., during TD experiments). Different size fractions can be obtained from SO-vermiculite with variable properties by following the protocol described in Reinholdt et al. (2013). In addition, the work of Dabat (2019) already provided TD results for water, Na^+ and Cl^- from an isotropic sample built from this mineral. In the present work, data from Dabat (2019) were compared to one from anisotropic sample built during this thesis having the same total porosity. (ii) Illite du Puy (IDP) is a none swelling clay mineral with only $\varepsilon_{interp.}$ and has similar negative structural charge to SO-vermiculite. This mineral (IDP) has been extensively used in studies published in the literature devoted to diffusion and adsorption of various tracers, which provided a solid database to validate the results of this work from the same mineral. (iii) KGa-2 kaolinite, which is a non-charged and non-swelling clay mineral. Hence, it can be used as reference for diffusion of tracers under no effects of structural charge or the dual porosity of clay minerals. For this

mineral, Dabat et al (2020) had developed a methodology to prepare isotropic and anisotropic samples having similar total porosity. These authors (Dabat et al., 2020) used this methodology to obtain quantitative information on the anisotropy of water diffusion in Na-kaolinite samples as a function of particles preferred orientation using *Pulsed Gradient Spin Echo attenuation by Nuclear Magnetic Resonance* (PGSE-NMR) technique.

It is worth mentioning that, for TD experiments performed in this study, a distinct size fraction (0.1-0.2 µm) of IDP and SO-vermiculite was used. This size fraction from both minerals had similar properties (external surface area, structural charge, and aspect ratio; the ratio between the particle thickness *h* to its basal diameter *l*) which permitted to:

i. Having sufficient external specific surface area to study the anionic exclusion in these minerals (Reinholdt et al., (2013); results from the present work).
ii. Qualitatively discuss the influence of negative structural charge on TD results.
iii. Minimize the potential influence of the variation in pore geometry with heterogenous particles sizes, and thus the influence on diffusion results.

The first achievement of this work was extending the methodology proposed by Dabat et al (2020) for kaolinite. The developed protocol was adapted for swelling clay minerals that - unlike kaolinite- their geometry and particles organization are affected by their swelling/un-swelling behaviors. Consequently, this protocol allowed to prepare porous media from any clay type (swelling or none swelling) with controlled porosity volume and distribution ($\varepsilon_{interp.}$ *vs.* $\varepsilon_{interl.}$), and with variable degrees of anisotropy in particles preferred orientation (i.e., isotropic *vs.* anisotropic). Moreover, the prepared porous media could be directly mounted to the TD setup to avoid compromising their geometry.

The first part devoted to results in this Ms. (chapter III) included detailed mineralogical and morphological characterizations of IDP material used for TD experiments in this work. This step was necessary for the interpretation of our TD results because the reported mineralogical and physio-chemical properties of IDP materials vary between different studies published in the literature. In conclusion, this study (chapter III) showed that IDP is a model clay system almost solely constituted by illite clay layers in the 0.1-0.2 µm used for TD experiments. It also indicated that most of the variability in the characterization data found in literature originates from mineralogical variation resulting from geological sampling strategy. However, particles size distribution between the different sub-fractions was found similar irrespective of the sampling location. It also provided a baseline for the material used in this

work and in the ongoing *European Joint Programme on Radioactive Waste Management* (EURAD) project.

Following our methodology described above, the second part dedicated for results in this Ms (chapter IV) included and discussed TD results on water diffusion in porous media made with IDP, vermiculite, and kaolinite particles. The third part (chapter V) reported and discussed TD results for Na^+ and Cl^- in porous media made with Na-IDP and vermiculite. The results (for Na^+ and Cl^-) were obtained with different salinity gradients (i.e., 0.01, 0.1, and 1M of NaCl in the upstream reservoir, and only pure water in the downstream). In the light of the results obtained for water and ions, the following conclusions can be reached:

I. The preferred orientation of clay particles is a first-order parameter in controlling water, Na^+, and Cl^- mobilities in clayey porous media regardless of the clay mineral type. For both IDP and vermiculite, the ratio $\frac{De_{z\,Iso}}{De_{z\,Aniso}}$ for HDO, Na^+ and Cl^- was between 1.5-2 for the similar total porosity values.
II. In the presence of salinity gradient, the diffusion of cations is controlled by that of anions (co-diffusion). Under such conditions, anionic exclusion is also a first-order parameter controlling the diffusion of Na^+ and Cl^- under salinity gradients in charged clayey porous media (i.e., Na-IDP, Na-vermiculite). In such media, the anionic exclusion is a function of the nature of the diffused species, ionic strength, and the amount of negative structural charge in the clay particles. However, particles size distribution is also a controlling factor because it defines the geometry of the pore network.
III. In a dual-porosity clayey medium (i.e., Na-vermiculite), interparticle porosity is the primary conveyor of water, Na^+, and Cl^- fluxes diffusing through this medium. This conclusion is valid for ions in the presence of salinity gradient; when the diffusion of cations is controlled by that of anions (co-diffusion), which was the case for TD experiments performed in this work.
IV. For similar interparticle porosity and anisotropy in particles preferred orientation, the mobility of HDO, Na^+, and Cl^- in compacted porous media made of charged and none-swelling clay minerals (i.e., Na-IDP) is further reduced compared to mobility measured for ones made of non-charged clay particles (i.e., Na-kaolinite).
V. Two experimental techniques (i.e., TD and PGSE-NMR) lead to similar diffusion coefficients for HDO diffusing in Na-kaolinite samples having the same porosity and preferential particle orientation. Hence, even though the two technics probe very contrasted time scales (days for TD *vs* ms for PGSE-NMR), both methods can be used

interchangeably to investigate water dynamics in samples composed of non-charged clayey particles.

VI. All TD data obtained for water were either in good or fair agreement with calculated ones by BD simulation, irrespective of the clay mineral used. This agreement proved that the size of VPMs is sufficient to reproduce the dynamics of water measured at the centimeter scale (i.e., TD).

VII. No evident effect was observed of particle size nor the nature of interlayer cations on the diffusion of water in compacted SO-vermiculite samples. This observation was based on similar TD results obtained at the same total porosity from different size fractions of SO-vermiculite, and for Na^+ and Ca^{2+} as interlayer cations.

Finally, by taking into consideration the results and findings of this thesis, the following future perspectives can be pursued:

I. IDP materials display a wide range of particles sizes in the < 2 µm fraction, with an important mass contribution of each sub-fraction (< 0.05; 0.05-0.1; 0.1-0.2; 0.2-2 µm). These sub-fractions provide a large range of specific external surface areas. Thus, it can be interesting to use these sub-fractions to tune the surface area, and thus enhance or reduce the anionic exclusion and adsorption effects of solutes in diffusion studies of ionic tracers within compacted samples of IDP particles. In addition, one may build isotropic and anisotropic samples from different size fractions of IDP and SO-vermiculite. Such approach can provide insights on how the influence of particles orientation on tracers' dynamics will vary with the different size fractions.

II. It is possible to introduce accessory minerals (e.g., quartz or feldspars) at known quantities and morphology to the porous media build from a single clay mineral. Hence, their influence on the internal organization of the medium can be assisted, and thus on the diffusion of different tracers in such medium.

III. For ions diffusion, it is possible to perform TD experiments with Na-vermiculite porous media using 0.1 and 0.5 M salinity gradients. Results from such experiments can be compared to the results obtained in this work using 0.01 and 1 M salinity gradients. For instance, TD results from Na-IDP samples in this work showed that most of the structural charge in the Na-IDP sample was screened by cations at a 0.1 M salinity gradient. Hence, it could be interesting to see if a similar tendency can be observed for Na-vermiculite.

IV. The reactive transport of ions (by considering ion-exchange reaction) is also an interesting subject to investigate in porous media made with IDP or SO-vermiculite

particles. In this work, we performed one TD experiment for the diffusion of Sr^{2+} in Ca^{2+}-saturated < 0.1 μm of SO-vermiculite (the same experiment from which HDO data were discussed in chapter IV; results for ions are included in the annexes but were not discussed in the Ms.). It can be interesting to extend this work for porous media built with different size fractions and also for isotropic and anisotropic samples from the same mineral.

V. The good agreement between experimental and those obtained from BD simulation for water diffusion in this work is a motivation to expand the simulation to the case of anions (e.g., Cl^-). Such work will shed light on how anionic exclusion behaves at very high degrees of anisotropy in particles ' preferred orientation.

The end

References

Abend, S., Lagaly, G., 2000. Sol–gel transitions of sodium montmorillonite dispersions. Applied Clay Science 16, 201–227. https://doi.org/10.1016/S0169-1317(99)00040-X

Abu-Jdayil, B., 2011. Rheology of sodium and calcium bentonite–water dispersions: Effect of electrolytes and aging time. International Journal of Mineral Processing 98, 208–213. https://doi.org/10.1016/j.minpro.2011.01.001

Altmann, S., Aertsens, M., Appelo, T., Bruggeman, C., Gaboreau, S., Glaus, M., Jacquier, P., Kupcik, T., Maes, N., Montoya, V., Rabung, T., Savoye, S., et al, 2015. Processes of cation migration in clayrocks: Final Scientific Report of the CatClay European Project. CEA.

Altmann, S., Tournassat, C., Goutelard, F., Parneix, J.-C., Gimmi, T., Maes, N., 2012. Diffusion-driven transport in clayrock formations. Applied Geochemistry 27, 463–478. https://doi.org/10.1016/j.apgeochem.2011.09.015

Amundson, R., Berhe, A.A., Hopmans, J.W., Olson, C., Sztein, A.E., Sparks, D.L., 2015. Soil and human security in the 21st century. Science 348, 1261071–1261071. https://doi.org/10.1126/science.1261071

Andra, D., 2005. Argile: évaluation de la faisabilité du stockage géologique en formation argileuse. Document du Synthèse, Andra.

Appelo, C.A.J., Van Loon, L.R., Wersin, P., 2010. Multicomponent diffusion of a suite of tracers (HTO, Cl, Br, I, Na, Sr, Cs) in a single sample of Opalinus Clay. Geochimica et Cosmochimica Acta 74, 1201–1219. https://doi.org/10.1016/j.gca.2009.11.013

Appelo, C.A.J., Wersin, P., 2007. Multicomponent Diffusion Modeling in Clay Systems with Application to the Diffusion of Tritium, Iodide, and Sodium in Opalinus Clay. Environ. Sci. Technol. 41, 5002–5007. https://doi.org/10.1021/es0629256

Arguelles, A., Leoni, M., Blanco, J.A., Marcos, C., 2010. Semi-ordered crystalline structure of the Santa Olalla vermiculite inferred from X-ray powder diffraction. American Mineralogist 95, 126–134. https://doi.org/10.2138/am.2010.3249

Asaad, A., Hubert, F., Ferrage, E., Dabat, T., Painaeu, E., Porion, P., Savoye, S., Gregoire, B., Dazas, B., Delville, A., Tertre, E., 2021. Role of interlayer porosity and particle organization in the diffusion of water in swelling clays. Applied Clay Science 12.

Bachu, S., 2008. CO2 storage in geological media: Role, means, status and barriers to deployment. Progress in Energy and Combustion Science 34, 254–273. https://doi.org/10.1016/j.pecs.2007.10.001

Bacle, P., Dufrêche, J.-F., Rotenberg, B., Bourg, I.C., Marry, V., 2016. Modeling the transport of water and ionic tracers in a micrometric clay sample. Applied Clay Science 123, 18–28. https://doi.org/10.1016/j.clay.2015.12.014

Baeyens, B., Bradbury, M.H., 1997. A mechanistic description of Ni and Zn sorption on Na-montmorillonite Part I: Titration and sorption measurements. Journal of Contaminant Hydrology 27, 199–222. https://doi.org/10.1016/S0169-7722(97)00008-9

Bailey, L., Lekkerkerker, H.N.W., Maitland, G.C., 2015. Smectite clay – inorganic nanoparticle mixed suspensions: phase behaviour and rheology. Soft Matter 11, 222–236. https://doi.org/10.1039/C4SM01717J

Bakker, E., Lanson, B., Findling, N., Wander, M.M., Hubert, F., 2019. Mineralogical differences in a temperate cultivated soil arising from different agronomic processes and plant K-uptake. Geoderma 347, 210–219. https://doi.org/10.1016/j.geoderma.2019.04.010

Bardot, F., 1998. Les minéraux argileux et leur hétérogénéité superficielle : influence de la nature des cations compensateurs superficiels de l'illite sur les mécanismes d'adsorption de gaz.

Bardot, F., 1998. Les minéraux argileux et leur hétérogénéité superficielle : Influence de la nature des cations compensateurs de l'illite sur les mécanismes d'adsorption de gaz. Institut National Polytechnique de Lorraine, Lorraine -France.

Bardot, F., Villiéras, F., Michot, L.J., Francois, M., Gérard, G., Cases, J.M., 1998. High resolution gas adsorption study on illites permuted with various cations assessment of surface energetic properties. Journal of Dispersion Science and Technology 19, 739–759. https://doi.org/10.1080/01932699808913212

Beall, G., 2003. The use of organo-clays in water treatment. Applied Clay Science 24, 11–20. https://doi.org/10.1016/j.clay.2003.07.006

Bennett, R.H., Brya, W.R., Keller, G.H., 1981. Clay fabric of selected submarine sediments; fundamental properties and models. Journal of Sedimentary Research 51, 217–232. https://doi.org/10.1306/212F7C52-2B24-11D7-8648000102C1865D

Benning, J.L., Barnes, D.L., 2009. Comparison of modeling methods for the determination of effective porosities and diffusion coefficients in through-diffusion tests: DETERMINING EFFECTIVE POROSITIES. Water Resour. Res. 45. https://doi.org/10.1029/2008WR007236

Bergaya, F., Lagaly, G. (Eds.), 2013. Handbook of clay science. Pt. A: Fundamentals, 2. ed. ed, Developments in clay science. Elsevier, Amsterdam.

Bergaya, Lagaly, G., 2013. General Introduction, in: Developments in Clay Science. Elsevier, pp. 1–19. https://doi.org/10.1016/B978-0-08-098258-8.00001-8

Bestel, M., 2014. Water–montmorillonite systems: Neutron scattering and tracer through-diffusion studies (Thesis). University of Bern-Bern, Bern-Switzerland.

Bestel, M., Glaus, M.A., Frick, S., Gimmi, T., Juranyi, F., Van Loon, L.R., Diamond, L.W., 2018. Combined tracer through-diffusion of HTO and 22Na through Na-montmorillonite with different bulk dry densities. Applied Geochemistry 93, 158–166. https://doi.org/10.1016/j.apgeochem.2018.04.008

Bleam, W.F., 1990. The Nature of Cation-Substitution Sites in Phyllosilicates. Clays and Clay Minerals 38, 527–536. https://doi.org/10.1346/CCMN.1990.0380510

Bolton, A.J., Maltman, A.J., Fisher, Q., 2000. Anisotropic permeability and bimodal pore-size distributions of fine-grained marine sediments. Marine and Petroleum Geology 16.

Bourg, I.C., Bourg, A.C.M., Sposito, G., 2003. Modeling diffusion and adsorption in compacted bentonite: a critical review. Journal of Contaminant Hydrology 61, 293–302. https://doi.org/10.1016/S0169-7722(02)00128-6

Bourg, I.C., Sposito, G., Bourg, A.C.M., 2008. Modeling the diffusion of Na+ in compacted water-saturated Na-bentonite as a function of pore water ionic strength. Applied Geochemistry 23, 3635–3641. https://doi.org/10.1016/j.apgeochem.2008.09.004

Bourg, I.C., Sposito, G., Bourg, A.C.M., 2007. Modeling Cation Diffusion in Compacted Water-Saturated Sodium Bentonite at Low Ionic Strength. Environ. Sci. Technol. 41, 8118–8122. https://doi.org/10.1021/es0717212

Bourg, I.C., Sposito, G., Bourg, A.C.M., 2006. Tracer diffusion in compacted, water-saturated bentonite. Clays Clay Miner. 54, 363–374. https://doi.org/10.1346/CCMN.2006.0540307

Bourg, I.C., Tournassat, C., 2015. Self-Diffusion of Water and Ions in Clay Barriers, in: Developments in Clay Science. Elsevier, pp. 189–226. https://doi.org/10.1016/B978-0-08-100027-4.00006-1

Bradbury, Baeyens, 2005. Experimental and Modelling Investigations on Na-Illite: Acid-Base Behaviour and the Sorption of Strontium, Nickel, Europium and Uranyl (TECHNICAL REPORT No. 04–02). Paul Scherrer Institut, Villigen.

Bradbury, M.H., Baeyens, B., 2009. Sorption modelling on illite Part I: Titration measurements and the sorption of Ni, Co, Eu and Sn. Geochimica et Cosmochimica Acta 73, 990–1003. https://doi.org/10.1016/j.gca.2008.11.017

Brigatti, M.F., Galán, E., Theng, B.K.G., 2013. Structure and Mineralogy of Clay Minerals, in: Developments in Clay Science. Elsevier, pp. 21–81. https://doi.org/10.1016/B978-0-08-098258-8.00002-X

Bruggeman, C., Maes, N., Aertsens, M., Cannière, P.D., 2009. Tritiated water retention and migration behaviour in Boom Clay 61.

Callaghan, P.T., 1993. Principles of nuclear magnetic resonance microscopy, illustrated, reprint, revised ed. Clarendon Press.

Carretero, M.I., Pozo, M., 2009. Clay and non-clay minerals in the pharmaceutical industry. Applied Clay Science 46, 73–80. https://doi.org/10.1016/j.clay.2009.07.017

Cebula, D.J., 1979. Neutron Diffraction from Clay-Water Systems. Clays and Clay Minerals 27, 39–52. https://doi.org/10.1346/CCMN.1979.0270105

Chagneau, A., Tournassat, C., Steefel, C.I., Bourg, I.C., Gaboreau, S., Esteve, I., Kupcik, T., Claret, F., Schäfer, T., 2015. Complete Restriction of $^{36}Cl^-$ Diffusion by Celestite Precipitation in Densely Compacted Illite. Environ. Sci. Technol. Lett. 2, 139–143. https://doi.org/10.1021/acs.estlett.5b00080

Charlet, L., Alt-Epping, P., Wersin, P., Gilbert, B., 2017. Diffusive transport and reaction in clay rocks: A storage (nuclear waste, CO2, H2), energy (shale gas) and water quality issue. Advances in Water Resources 106, 39–59. https://doi.org/10.1016/j.advwatres.2017.03.019

Chemeda, Y.C., 2021. Assessment of surface heterogeneity of lime treated kaolinites: Probed by low-pressure argon and nitrogen gas adsorption. Applied Clay Science 8.

Christidis, G.E., 2013. Assessment of Industrial Clays, in: Developments in Clay Science. Elsevier, pp. 425–449. https://doi.org/10.1016/B978-0-08-098259-5.00017-2

Christidis, G.E., Blum, A.E., Eberl, D.D., 2006. Influence of layer charge and charge distribution of smectites on the flow behaviour and swelling of bentonites. Applied Clay Science 34, 125–138. https://doi.org/10.1016/j.clay.2006.05.008

Churakov, S.V., Gimmi, T., 2011. Up-Scaling of Molecular Diffusion Coefficients in Clays: A Two-Step Approach. J. Phys. Chem. C 115, 6703–6714. https://doi.org/10.1021/jp112325n

Cole, J.J., Prairie, Y.T., 2014. Dissolved CO2 in Freshwater Systems☆, in: Reference Module in Earth Systems and Environmental Sciences. Elsevier, p. B9780124095489094000. https://doi.org/10.1016/B978-0-12-409548-9.09399-4

Cotts, R.M., Hoch, M.J.R., Sun, T., Markert, J.T., 1989. Pulsed field gradient stimulated echo methods for improved NMR diffusion measurements in heterogeneous systems. Journal of Magnetic Resonance (1969) 83, 252–266. https://doi.org/10.1016/0022-2364(89)90189-3

Crank, J., 1975. The Mathematics of Diffusion, 2nd ed. Oxford University Press: London.

Dabat, T., 2019. Anisotropie d'orientation des particules des milieux poreux argileux et implication sur la diffusion de l'eau. Université de Poitiers.

Dabat, T., Hubert, F., Paineau, E., Launois, P., Laforest, C., Grégoire, B., Dazas, B., Tertre, E., Delville, A., Ferrage, E., 2019. A general orientation distribution function for clay-rich media. Nat Commun 10, 5456. https://doi.org/10.1038/s41467-019-13401-0

Dabat, T., Mazurier, A., Hubert, F., Tertre, E., Grégoire, B., Dazas, B., Ferrage, E., 2018. Mesoscale Anisotropy in Porous Media Made of Clay Minerals. A Numerical Study Constrained by Experimental Data. Materials 11, 1972. https://doi.org/10.3390/ma11101972

Dabat, T., Porion, P., Hubert, F., Paineau, E., Dazas, B., Grégoire, B., Tertre, E., Delville, A., Ferrage, E., 2020. Influence of preferred orientation of clay particles on the diffusion of water in kaolinite porous media at constant porosity. Applied Clay Science 184, 105354. https://doi.org/10.1016/j.clay.2019.105354

Dagnelie, R.V.H., Arnoux, P., Enaux, J., Radwan, J., Ner, P., 2017. Perturbation induced by a nitrate plume on diffusion of solutes in a large-scale clay rock sample. Applied Clay Science 141, 2019–226.

Day, D.T., Gilpin, J.E., 1909. The Changes in Crude Petroleum Effected by Diffusion through Clay. Industrial & Engineering Chemistry 1, 449–455.

De La Calle, C., Pezerat, H., Gasperin, M., 1977. Problemes d'ordre-désordre dqns les ver,iculites structure du minéral calcique hydraté a 2 couches. Journal de Physique 38, 128–133.

De La Calle, C., Suquet, H., Dubernat, J., Pezerat, H., 1978. Mode d'empilement des feuillets dans les vermiculites hydratées à 'deux couches.' Clay Minerals 13, 275–297. https://doi.org/10.1180/claymin.1978.013.3.04

Delay, J., Bossart, P., Ling, L.X., Blechschmidt, I., Ohlsson, M., Vinsot, A., Nussbaum, C., Maes, N., 2014. Three decades of underground research laboratories: what have we learned? Geological Society, London, Special Publications 400, 7–32. https://doi.org/10.1144/SP400.1

Delay, J., Trouiller, A., Lavanchy, J.-M., 2006. Propriétés hydrodynamiques du Callovo-Oxfordien dans l'Est du bassin de Paris : comparaison des résultats obtenus selon différentes approches. Comptes Rendus Geoscience 338, 892–907. https://doi.org/10.1016/j.crte.2006.07.009

Descostes, M., Blin, V., Bazer-Bachi, F., Meier, P., Grenut, B., Radwan, J., Schlegel, M.L., Buschaert, S., Coelho, D., Tevissen, E., 2008. Diffusion of anionic species in Callovo-Oxfordian argillites and Oxfordian limestones (Meuse/Haute–Marne, France). Applied Geochemistry 23, 655–677. https://doi.org/10.1016/j.apgeochem.2007.11.003

Diaz, N., 2009. Modélisation prédictive de la migration des anions par description de la microstructure de la roche : application à l'argilite du Callovo-Oxfordien. UNIVERSITE PARIS VI, Paris, France.

Dill, H.G., 2020. A geological and mineralogical review of clay mineral deposits and phyllosilicate ore guides in Central Europe – A function of geodynamics and climate change. Ore Geology Reviews 119, 103304. https://doi.org/10.1016/j.oregeorev.2019.103304

Doebelin, N., Kleeberg, R., 2015. Profex: a graphical user interface for the Rietveld refinement program BGMN. J Appl Crystallogr 48, 1573–1580. https://doi.org/10.1107/S1600576715014685

Drits, V., 1997. XRD Measurement of Mean Crystallite Thickness of Illite and Illite/Smectite: Reappraisal of the Kubler Index and the Scherrer Equation. Clays and Clay Minerals 45, 461–475. https://doi.org/10.1346/CCMN.1997.0450315

Durrieu, J., Argillier, J.F., Rosenberg, E., Li, Y., 1997. Static and Dynamic Filtration Properties of Aqueous Suspensions of Clays and Electrolytes. Rev. Inst. Fr. Pét. 52, 207–218. https://doi.org/10.2516/ogst:1997020

Dzene, L., Ferrage, E., Hubert, F., Delville, A., Tertre, E., 2016. Experimental evidence of the contrasting reactivity of external vs. interlayer adsorption sites on swelling clay minerals: The case of Sr2+-for-Ca2+ exchange in vermiculite. Applied Clay Science 132–133, 205–215. https://doi.org/10.1016/j.clay.2016.06.007

Evangelou, V.P., 1998. Environmental Soil and Water Chemistry: Principles and Applications, Environmental Chemistry. JOHN WILEY & SONS, INC., New York.

Farver, J.R., Yund, R.A., 1999. Oxygen bulk diffusion measurements and TEM characterization of a natural ultramylonite: implications for fluid transport in mica-bearing rocks. J. Metamorph. Geol 17, 669–683.

Faurel, M., 2012. Conception et mise en place d'expériences de diffusion de l'eau et de solutés dans des milieux poreux modèles d'argiles gonflantes. Université de Poitiers, Poitiers, France.

Ferrage, E., 2016. Investigation of the Interlayer Organization of Water and Ions In Smectite from the Combined Use of Diffraction Experiments And Molecular Simulations. a Review of Methodology, Applications, And Perspectives. clays clay miner 64, 348–373. https://doi.org/10.1346/CCMN.2016.0640401

Ferrage, E., Hubert, F., Baronnet, A., Grauby, O., Tertre, E., Delville, A., Bihannic, I., Prêt, D., Michot, L.J., Levitz, P., 2018. Influence of crystal structure defects on the small-angle neutron scattering/diffraction patterns of clay-rich porous media. J Appl Crystallogr 51, 1311–1322. https://doi.org/10.1107/S160057671801052X

Ferrage, E., Hubert, F., Tertre, E., Delville, A., Michot, L.J., Levitz, P., 2015. Modeling the arrangement of particles in natural swelling-clay porous media using three-dimensional packing of elliptic disks. Physical Review E 91. https://doi.org/10.1103/PhysRevE.91.062210

Ferrage, E., Lanson, B., Michot, L.J., Robert, J.-L., 2010. Hydration Properties and Interlayer Organization of Water and Ions in Synthetic Na-Smectite with Tetrahedral Layer Charge. Part 2. Toward a Precise Coupling between Molecular Simulations and Diffraction Data. J. Phys. Chem. C 114, 4515–4526. https://doi.org/10.1021/jp909860p

Ferrage, E., Sakharov, B.A., Michot, L.J., Delville, A., Bauer, A., Lanson, B., Grangeon, S., Frapper, G., Jiménez-Ruiz, M., Cuello, G.J., 2011. Hydration Properties and Interlayer Organization of Water and Ions in Synthetic Na-Smectite with Tetrahedral Layer Charge. Part 2. Toward a Precise Coupling between Molecular Simulations and Diffraction Data. J. Phys. Chem. C 115, 1867–1881. https://doi.org/10.1021/jp105128r

Fischer, H., 2003. Polymer nanocomposites: from fundamental research to specific applications. Materials Science and Engineering: C 23, 763–772. https://doi.org/10.1016/j.msec.2003.09.148

Fripiat, J., Cases, J., Francois, M., Letellier, M., 1982. Thermodynamic and microdynamic behavior of water in clay suspensions and gels. Journal of Colloid and Interface Science 89, 378–400. https://doi.org/10.1016/0021-9797(82)90191-6

Gabis, V., 1963. Étude minéralogique et géochimique de la série sédimentaire oligocène du Velay. Bulletin de la Société française de Minéralogie et de Cristallographie 86, 315–354. https://doi.org/10.3406/bulmi.1963.5663

García-Gutiérrez, M., Cormenzana, J.L., Missana, T., Mingarro, M., Martín, P.L., 2006. Large-scale laboratory diffusion experiments in clay rocks. Physics and Chemistry of the Earth, Parts A/B/C 31, 523–530. https://doi.org/10.1016/j.pce.2006.04.004

Gherardi, F., Xu, T., Pruess, K., 2007. Numerical modeling of self-limiting and self-enhancing caprock alteration induced by CO2 storage in a depleted gas reservoir. Chemical Geology 244, 103–129. https://doi.org/10.1016/j.chemgeo.2007.06.009

Gieseking, J.E. (Ed.), 1975. Soil Components Vol. 2: Inorganic Components, 1st ed. Springer-Verlag Berlin Heidelberg.

Glaus, M.A., Aertsens, M., Maes, N., Van Laer, L., Van Loon, L.R., 2015. Treatment of boundary conditions in through-diffusion: A case study of 85Sr2+ diffusion in compacted illite. Journal of Contaminant Hydrology 177–178, 239–248. https://doi.org/10.1016/j.jconhyd.2015.03.010

Glaus, M.A., Baeyens, B., Bradbury, M.H., Jakob, A., Van Loon, L.R., Yaroshchuk, A., 2007. Diffusion of ^{22} Na and ^{85} Sr in Montmorillonite: Evidence of Interlayer Diffusion Being the Dominant Pathway at High Compaction. Environ. Sci. Technol. 41, 478–485. https://doi.org/10.1021/es061908d

Glaus, M.A., Frick, S., Rossé, R., Loon, L.R.V., 2010. Comparative study of tracer diffusion of HTO, 22Na+ and 36Cl− in compacted kaolinite, illite and montmorillonite. Geochimica et Cosmochimica Acta 74, 1999–2010. https://doi.org/10.1016/j.gca.2010.01.010

Glaus, M.A., Frick, S., Rossé, R., Van Loon, L.R., 2011. Consistent interpretation of the results of through-, out-diffusion and tracer profile analysis for trace anion diffusion in compacted montmorillonite. Journal of Contaminant Hydrology 123, 1–10. https://doi.org/10.1016/j.jconhyd.2010.11.009

Goldstein, J., Newbury, D.E., Echlin, P., Joy, D., D. Romig Jr., A., Lyman, Charles.E., Fiori, C., Lifshin, E., 1992. Scanning Electron Microscopy and X-Ray Microanalysis, Earth Sciences & Geography. Springer US, New York.

Gonçalvès, J., Violette, S., Wendling, J., 2004. Analytical and numerical solutions for alternative overpressuring processes: Application to the Callovo-Oxfordian sedimentary sequence in the Paris basin, France: PROCESSES LIKELY TO EXPLAIN OVERPRESSURES IN SHALES. J. Geophys. Res. 109. https://doi.org/10.1029/2002JB002278

Gonzáles García, F., García Ramos, G., 1960. On the genesis and transformation of vermiculite. Presented at the Transactions 7th int. Congr. Soil Sci., Vol. 4, pp. 482–491.

Gonzáles García, F, García Ramos, G., 1960. On the genesis and transformation of vermiculite. Presented at the Transactions 7th int. Congr. Soil Sci., Spain, pp. 482–491.

González Sánchez, F., 2007. Water diffusion through compacted clays analyzed by neutron scattering and tracer experiments. University of Bern.

González Sánchez, F., Jurányi, F., Gimmi, T., Van Loon, L., Unruh, T., Diamond, L.W., 2008a. Translational diffusion of water and its dependence on temperature in charged and uncharged clays: A neutron scattering study. J. Chem. Phys. 129, 174706. https://doi.org/10.1063/1.3000638

González Sánchez, F., Van Loon, L.R., Gimmi, T., Jakob, A., Glaus, M.A., Diamond, L.W., 2008b. Self-diffusion of water and its dependence on temperature and ionic strength in highly compacted montmorillonite, illite and kaolinite. Applied Geochemistry 23, 3840–3851. https://doi.org/10.1016/j.apgeochem.2008.08.008

González Sánchez, F., Van Loon, L.R., Gimmi, T., Jakob, A., Glaus, M.A., Diamond, L.W., 2008c. Self-diffusion of water and its dependence on temperature and ionic strength in highly compacted montmorillonite, illite and kaolinite. Applied Geochemistry 23, 3840–3851. https://doi.org/10.1016/j.apgeochem.2008.08.008

Gueutin, P., Altmann, S., Goncalves, J., Cosenza, P., Violette, S., 2007. Osmotic interpretation of overpressures from monovalent based triple layer model, in the Callovo-Oxfordian at the Bure site. Physics and Chemistry of the Earth 7.

Harvey, C.C., Murray, H.H., 1997. Industrial clays in the 21st century: A perspective of exploration, technology, and utilization. Applied Clay Science 11, 285–310. https://doi.org/10.1016/S0169-1317(96)00028-2

Hassan, M.S., Villieras, F., Gaboriaud, F., Razafitianamaharavo, A., 2005. AFM and low-pressure argon adsorption analysis of geometrical properties of phyllosilicates. Journal of Colloid and Interface Science 296, 614–623. https://doi.org/10.1016/j.jcis.2005.09.028

Heister, K., Kleingeld, P.J., Gustav Loch, J.P., 2005. Quantifying the effect of membrane potential in chemical osmosis across bentonite membranes by virtual short-circuiting. Journal of Colloid and Interface Science 286, 294–302. https://doi.org/10.1016/j.jcis.2005.01.044

Hermans, P.H., Platzek, P., 1939. Beiträge zur Kenntnis des Deformationsmechanismus und der Feinstruktur der Hydratzellulose. Kolloid-Z, Kolloid-Z 88, 68–72.

Howard, S.A., Preston, K.D., 1989. Profile Fitting of Powder Diffraction Patterns, in: Modern Powder Diffraction; Bish, D. L., Post, J. E., Eds., Reviews in Mineralogy. Mineralogical Society of America, Washington, DC, pp. 217–275.

Hubert, F., Bihannic, I., Prêt, D., Tertre, E., Nauleau, B., Pelletier, M., Demé, B., Ferrage, E., 2013. Investigating the Anisotropic Features of Particle Orientation in Synthetic Swelling Clay Porous Media. Clays Clay Miner. 61, 397–415. https://doi.org/10.1346/CCMN.2013.0610501

Hubert, F., Caner, L., Meunier, A., Ferrage, E., 2012. Unraveling complex <2 m clay mineralogy from soils using X-ray diffraction profile modeling on particle-size sub-fractions: Implications for soil pedogenesis and reactivity. American Mineralogist 97, 384–398. https://doi.org/10.2138/am.2012.3900

Ito, A., Wagai, R., 2017. Global distribution of clay-size minerals on land surface for biogeochemical and climatological studies. Sci Data 4, 170103. https://doi.org/10.1038/sdata.2017.103

Jacops, E., Aertsens, M., Maes, N., Bruggeman, C., Swennen, R., Krooss, B., Amann-Hildenbrand, A., Littke, R., 2017. The Dependency of Diffusion Coefficients and Geometric Factor on the Size of the Diffusing Molecule: Observations for Different Clay-Based Materials. Geofluids 2017, 1–16. https://doi.org/10.1155/2017/8652560

Jardat, M., Dufrêche, J.-F., Marry, V., Rotenberg, B., Turq, P., 2009. Salt exclusion in charged porous media: a coarse-graining strategy in the case of montmorillonite clays. Phys. Chem. Chem. Phys. 11, 2023. https://doi.org/10.1039/b818055e

Jiang, S., 2012. Clay Minerals from the Perspective of Oil and Gas Exploration, in: Valaskova, M. (Ed.), Clay Minerals in Nature - Their Characterization, Modification and Application. InTech. https://doi.org/10.5772/47790

Johnston, C.T., 2018. Clay mineral–water interactions, in: Developments in Clay Science. Elsevier, pp. 89–124. https://doi.org/10.1016/B978-0-08-102432-4.00004-4

Kasthurba, A.K., Santhanam, M., Mathews, M.S., 2007. Investigation of laterite stones for building purpose from Malabar region, Kerala state, SW India – Part 1: Field studies and profile characterisation. Construction and Building Materials 21, 73–82. https://doi.org/10.1016/j.conbuildmat.2005.07.006

Ketzer, J.M., Carpentier, B., Le Gallo, Y., Le Thiez, P., 2005. Geological Sequestration of CO_2 in Mature Hydrocarbon Fields. Basin and Reservoir Numerical Modelling of the Forties Field, North Sea. Oil & Gas Science and Technology - Rev. IFP 60, 259–273. https://doi.org/10.2516/ogst:2005016

Kleeberg, R., Monecke, T., Hillier, S., 2008. Preferred Orientation of Mineral Grains in Sample Mounts for Quantitative XRD Measurements: How Random are Powder Samples? Clays Clay Miner. 56, 404–415. https://doi.org/10.1346/CCMN.2008.0560402

Komine, H., Ogata, N., 2004. Predicting Swelling Characteristics of Bentonites. J. Geotech. Geoenviron. Eng. 130, 818–829. https://doi.org/10.1061/(ASCE)1090-0241(2004)130:8(818)

Kouakou, C.H., Morel, J.C., 2009. Strength and elasto-plastic properties of non-industrial building materials manufactured with clay as a natural binder. Applied Clay Science 44, 27–34. https://doi.org/10.1016/j.clay.2008.12.019

Lagaly, G., Dékány, I., 2013. Colloid Clay Science, in: Developments in Clay Science. Elsevier, pp. 243–345. https://doi.org/10.1016/B978-0-08-098258-8.00010-9

Landais, P., 2006. Advances in geochemical research for the underground disposal of high-level, long-lived radioactive waste in a clay formation. Journal of Geochemical Exploration 88, 32–36. https://doi.org/10.1016/j.gexplo.2005.08.011

Liu, L., 2013. Prediction of swelling pressures of different types of bentonites in dilute solutions. Colloids and Surfaces A: Physicochemical and Engineering Aspects 434, 303–318. https://doi.org/10.1016/j.colsurfa.2013.05.068

Loeber, L., 1992. Etude de la structure des cakes d'argile formés sur la paroi des puits au cours du forage. Université d'Orléans, Orléans-France.

Maes, N., Salah, S., Bruggeman, C., Aertsens, M., Martens, E., Laer, L.V., 2012. Strontium retention and migration behaviour in Boom Clay (Scientific Report SCK). SCK•CEN, Mol, Belgium.

Mahato, N., Banerjee, A., Gupta, A., Omar, S., Balani, K., 2015. Progress in material selection for solid oxide fuel cell technology: A review. Progress in Materials Science 72, 141–337. https://doi.org/10.1016/j.pmatsci.2015.01.001

Malikova, N., Cadène, A., Marry, V., Dubois, E., Turq, P., 2006. Diffusion of Water in Clays on the Microscopic Scale: Modeling and Experiment. J. Phys. Chem. B 110, 3206–3214. https://doi.org/10.1021/jp056954z

Marcos, C., Argüelles, A., Ruíz-Conde, A., P. J. Sánchez-Soto, Blanco, J.A., 2003. Study of the dehydration process of vermiculites by applying a vacuum pressure: formation of

interstratified phases. Mineral. mag. 67, 1253–1268. https://doi.org/10.1180/0026461036760163

Marry, V., Turq, P., Cartailler, T., Levesque, D., 2002. Microscopic simulation of structure and dynamics of water and counterions in a monohydrated montmorillonite. The Journal of Chemical Physics 117, 3454–3463. https://doi.org/10.1063/1.1493186

Mazurek, M., Alt-Epping, P., Bath, A., Gimmi, T., Niklaus Waber, H., Buschaert, S., Cannière, P.D., Craen, M.D., Gautschi, A., Savoye, S., Vinsot, A., Wemaere, I., Wouters, L., 2011. Natural tracer profiles across argillaceous formations. Applied Geochemistry 26, 1035–1064. https://doi.org/10.1016/j.apgeochem.2011.03.124

Melkior, T., Gaucher, E.C., Brouard, C., Yahiaoui, S., Thoby, D., Clinard, Ch., Ferrage, E., Guyonnet, D., Tournassat, C., Coelho, D., 2009a. Na+ and HTO diffusion in compacted bentonite: Effect of surface chemistry and related texture. Journal of Hydrology 370, 9–20. https://doi.org/10.1016/j.jhydrol.2009.02.035

Melkior, T., Gaucher, E.C., Brouard, C., Yahiaoui, S., Thoby, D., Clinard, Ch., Ferrage, E., Guyonnet, D., Tournassat, C., Coelho, D., 2009b. Na+ and HTO diffusion in compacted bentonite: Effect of surface chemistry and related texture. Journal of Hydrology 370, 9–20. https://doi.org/10.1016/j.jhydrol.2009.02.035

Mermut, A.R., Cano, A.F., 2001. Baseline Studies of the Clay Minerals Society Source Clays: Chemical Analyses of Major Elements. Clays and Clay Minerals 49, 381–386. https://doi.org/10.1346/CCMN.2001.0490504

Meunier, A., 2005. Clays. Springer, Berlin; New York.

Michot, L., Francois, M., Cases, J.M., 1990. Surface heterogeneity studied by a quasi-equilibrium gas adsorption procedure. Langmuir 6, 677–681. https://doi.org/10.1021/la00093a025

Michot, L.J., Bihannic, I., Porsch, K., Maddi, S., Baravian, C., Mougel, J., Levitz, P., 2004. Phase Diagrams of Wyoming Na-Montmorillonite Clay. Influence of Particle Anisotropy. Langmuir 20, 10829–10837. https://doi.org/10.1021/la0489108

Michot, L.J., Ferrage, E., Jiménez-Ruiz, M., Boehm, M., Delville, A., 2012. Anisotropic Features of Water and Ion Dynamics in Synthetic Na- and Ca-Smectites with Tetrahedral Layer Charge. A Combined Quasi-Elastic Neutron-Scattering and Molecular Dynamics Simulations Study. J. Phys. Chem. C 116, 16619–16633. https://doi.org/10.1021/jp304715m

Mills, R., Lobo, V.M.M., 1989. Self-diffusion in Electrolyte Solutions: A Critical Examination of Data Compiled from the Literature. Elsevier Science Publisher B.V.

Moore, D.M., Reynolds, R.C.J., 1997. X-ray Diffraction and the Identification and Analysis of Clay Minerals. Oxford University Press.

Muhammed, N.S., Olayiwola, T., Elkatatny, S., 2021. A review on clay chemistry, characterization and shale inhibitors for water-based drilling fluids. Journal of Petroleum Science and Engineering 206, 109043. https://doi.org/10.1016/j.petrol.2021.109043

Mukai, H., Motai, S., Yaita, T., Kogure, T., 2016. Identification of the actual cesium-adsorbing materials in the contaminated Fukushima soil. Applied Clay Science 121–122, 188–193. https://doi.org/10.1016/j.clay.2015.12.030

Mukhopadhyay, R., Bhaduri, D., Sarkar, B., Rusmin, R., Hou, D., Khanam, R., Sarkar, S., Kumar Biswas, J., Vithanage, M., Bhatnagar, A., Ok, Y.S., 2020. Clay–polymer nanocomposites: Progress and challenges for use in sustainable water treatment. Journal of Hazardous Materials 383, 121125. https://doi.org/10.1016/j.jhazmat.2019.121125

Murray, H., 2002. Industrial Clays Case Study 9.

Nuntiya, A., Prasanphan, S., 2006. The Rheological Behavior of Kaolin Suspensions. Chiang Mai J. Sci. 33, 271–281.

Ochs, M., Boonekamp, M., Wanner, H., Sato, H., Yui, M., 1998. A Quantitative Model for Ion Diffusion in Compacted Bentonite. Radiochimica Acta 82. https://doi.org/10.1524/ract.1998.82.special-issue.437

Ochs, M., Lothenbach, B., Wanner, H., Sato, H., Yui, M., 2001. An integrated sorption–diffusion model for the calculation of consistent distribution and diffusion coefficients in compacted bentonite. Journal of Contaminant Hydrology 47, 283–296. https://doi.org/10.1016/S0169-7722(00)00157-1

Pan, X.-F., Gao, H.-L., Lu, Y., Wu, C.-Y., Wu, Y.-D., Wang, X.-Y., Pan, Z.-Q., Dong, L., Song, Y.-H., Cong, H.-P., Yu, S.-H., 2018. Transforming ground mica into high-performance biomimetic polymeric mica film. Nat Commun 9, 2974. https://doi.org/10.1038/s41467-018-05355-6

Poinssot, C., Baeyens, B., Bradbury, M.H., 1999. Experimental and modelling studies of caesium sorption on illite. Geochimica et Cosmochimica Acta 63, 3217–3227. https://doi.org/10.1016/S0016-7037(99)00246-X

Porion, P., Ferrage, E., Hubert, F., Tertre, E., Dabat, T., Faugère, A.M., Condé, F., Warmont, F., Delville, A., 2018. Water Mobility within Compacted Clay Samples: Multi-Scale Analysis Exploiting ^{1}H NMR Pulsed Gradient Spin Echo and Magnetic Resonance Imaging of Water Density Profiles. ACS Omega 3, 7399–7406. https://doi.org/10.1021/acsomega.8b01083

Pret, D., 2003. Nouvelles méthodes quantitatives de cartographie de la minéralogie et de la porosité dans les matériaux argileux : application aux bentonites compactées des barrières ouvragées. Université de Poitiers, Poitiers-France.

Pusch, R., 1979. Highly Compacted Sodium Bentonite for Isolating Rock-Deposited Radioactive Waste Products. Journal Nuclear Technology 45, 153–157. https://doi.org/10.13182/NT79-A32305

Rabung, Th., Pierret, M.C., Bauer, A., Geckeis, H., Bradbury, M.H., Baeyens, B., 2005. Sorption of $Eu^{(III)}/Cm^{(III)}$ on Ca-montmorillonite and Na-illite. Part 1: Batch sorption and time-resolved laser fluorescence spectroscopy experiments. Geochimica et Cosmochimica Acta 69, 5393–5402. https://doi.org/10.1016/j.gca.2005.06.030

Rajec, P., 1999. Effect of Illite Particle Shape on Cesium Sorption. Clays and Clay Minerals 47, 755–760. https://doi.org/10.1346/CCMN.1999.0470610

Rajyaguru, A., 2018. Impact of saline plume on containment properties of natural porous materials in geological disposal context: An experimental and REV simulation approach to go beyond Archie's law. PSL Research University, Paris, France.

Razakamanantsoa, A.R., Barast, G., Djeran-maigre, I., 2012. Hydraulic performance of activated calcium bentonite treated by polyionic charged polymer. Applied Clay Science 59–60, 103–114. https://doi.org/10.1016/j.clay.2012.01.022

Reinholdt, M.X., Hubert, F., Faurel, M., Tertre, E., Razafitianamaharavo, A., Francius, G., Prêt, D., Petit, S., Béré, E., Pelletier, M., Ferrage, E., 2013. Morphological properties of vermiculite particles in size-selected fractions obtained by sonication. Applied Clay Science 77–78, 18–32. https://doi.org/10.1016/j.clay.2013.03.013

Robert, M., Hardy, M., Elsass, F., 1991. Crystallochemistry, properties and organization of soil clays derived from major sedimentary rocks in France. Clay miner. 26, 409–420. https://doi.org/10.1180/claymin.1991.026.3.09

Robin, V., Tertre, E., Beaufort, D., Regnault, O., Sardini, P., Descostes, M., 2015. Ion exchange reactions of major inorganic cations (H+, Na+, Ca2+, Mg2+ and K+) on beidellite: Experimental results and new thermodynamic database. Toward a better prediction of contaminant mobility in natural environments. Applied Geochemistry 59, 74–84. https://doi.org/10.1016/j.apgeochem.2015.03.016

Sakharov, A., Naumov, A.S., Drits, V.A., 1983. X-ray scattering by defect layer structures. Kristallografia 28, 951–958.

Sakharov, A., Naumov, A.S., Drits, V.A., 1982a. X-ray diffraction by mixed-layer structures with random distribution of stacking faults. Dokl. Akad. Nauk 265, 339–343.

Sakharov, A., Naumov, A.S., Drits, V.A., 1982b. X-ray intensities scattered by layer structures with short-range ordering parameters $S \geq 1$ and $G \geq 1$. Dokl. Akad. Nauk 265, 871–874.

Sakharov, B.A., Drits, V.A., McCarty, D.K., Walker, G.M., 2016. Modeling Powder X-Ray Diffraction Patterns of the Clay Minerals Society Kaolinite Standards: Kga-1, Kga-1b, and Kga-2. Clays Clay Miner. 64, 314–333. https://doi.org/10.1346/CCMN.2016.0640307

Sammaljärvi, J., Jokelainen, L., Ikonen, J., Siitari-Kauppi, M., 2012. Free radical polymerisation of MMA with thermal initiator in brick and Grimsel granodiorite. Engineering Geology 135–136, 52–59. https://doi.org/10.1016/j.enggeo.2012.03.005

Sato, H., 2000. The Effect of Pore Structural Factors on Diffusion in Compacted Sodium Bentonite. MRS Proc. 663, 605. https://doi.org/10.1557/PROC-663-605

Sato, H., Ashida, T., Kohara, Y., Yui, M., Sasaki, N., 1992. Effect of Dry Density on Diffusion of Some Radionuclides in Compacted Sodium Bentonite. Journal of Nuclear Science and Technology 29, 873–882. https://doi.org/10.1080/18811248.1992.9731607

Sato, H., Suzuki, S., 2003. Fundamental study on the effect of an orientation of clay particles on diffusion pathway in compacted bentonite. Applied Clay Science 23, 51–60. https://doi.org/10.1016/S0169-1317(03)00086-3

Savoye, S., Beaucaire, C., Grenut, B., Fayette, A., 2015. Impact of the solution ionic strength on strontium diffusion through the Callovo-Oxfordian clayrocks: An experimental and modeling study. Applied Geochemistry 61, 41–52. https://doi.org/10.1016/j.apgeochem.2015.05.011

Savoye, S., Frasca, B., Grenut, B., Fayette, A., 2012. How mobile is iodide in the Callovo–Oxfordian claystones under experimental conditions close to the in-situ ones? Journal of Contaminant Hydrology 142–143, 82–92. https://doi.org/10.1016/j.jconhyd.2012.10.003

Savoye, S., Goutelard, F., Beaucaire, C., Charles, Y., Fayette, A., Herbette, M., Larabi, Y., Coelho, D., 2011. Effect of temperature on the containment properties of argillaceous rocks: The case study of Callovo–Oxfordian claystones. Journal of Contaminant Hydrology 125, 102–112. https://doi.org/10.1016/j.jconhyd.2011.05.004

Savoye, S., Page, J., Puente, C., Imbert, C., Coelho, D., 2010. New Experimental Approach for Studying Diffusion through an Intact and Unsaturated Medium: A Case Study with Callovo-Oxfordian Argillite. Environ. Sci. Technol. 44, 3698–3704. https://doi.org/10.1021/es903738t

Shackelford, C.D., 1991. Laboratory diffusion testing for waste disposal — A review. Journal of Contaminant Hydrology 7, 177–217. https://doi.org/10.1016/0169-7722(91)90028-Y

Shackelford, C.D., Moore, S.M., 2013. Fickian diffusion of radionuclides for engineered containment barriers: Diffusion coefficients, porosities, and complicating issues. Engineering Geology 152, 133–147. https://doi.org/10.1016/j.enggeo.2012.10.014

Stejskal, E.O., Tanner, J.E., 1965. Spin Diffusion Measurements: Spin Echoes in the Presence of a Time-Dependent Field Gradient. The Journal of Chemical Physics 42, 288–292. https://doi.org/10.1063/1.1695690

Stern, O., 1924. Zur Theorie der Elektrolytischen Doppelschicht. Zeitschrift für Elektrochemie 30, 508–516. https://doi.org/10.1002/bbpc.192400182

Suzuki, S., Sato, H., Ishidera, T., Fujii, N., 2004. Study on anisotropy of effective diffusion coefficient and activation energy for deuterated water in compacted sodium bentonite. Journal of Contaminant Hydrology 68, 23–37. https://doi.org/10.1016/S0169-7722(03)00139-6

Tertre, E., Ferrage, E., Bihannic, I., Michot, L.J., Prêt, D., 2011a. Influence of the ionic strength and solid/solution ratio on Ca $^{(II)}$-for-Na^{+} exchange on montmorillonite. Part 2: Understanding the effect of the m/V ratio. Implications for pore water composition and element transport in natural media. Journal of Colloid and Interface Science 363, 334–347. https://doi.org/10.1016/j.jcis.2011.07.003

Tertre, E., Prêt, D., Ferrage, E., 2011b. Influence of the ionic strength and solid/solution ratio on $Ca^{(II)}$-for-Na^{+} exchange on montmorillonite. Part 1: Chemical measurements, thermodynamic modelling and potential implications for trace elements geochemistry.

Journal of Colloid and Interface Science 353, 248–256. https://doi.org/10.1016/j.jcis.2010.09.039

Tertre, E., Savoye, S., Hubert, F., Prêt, D., Dabat, T., Ferrage, E., 2018a. Diffusion of Water through the Dual-Porosity Swelling Clay Mineral Vermiculite. Environ. Sci. Technol. 52, 1899–1907. https://doi.org/10.1021/acs.est.7b05343

Tessier, M., 1984. Etude experimentale de l'organisation des materiaux argileux : Hydratation, gonflement et structuration au cours de la dessiccation et de la re´humectation. INRA.

Tinnacher, R.M., Holmboe, M., Tournassat, C., Bourg, I.C., Davis, J.A., 2016. Ion adsorption and diffusion in smectite: Molecular, pore, and continuum scale views. Geochimica et Cosmochimica Acta 177, 130–149. https://doi.org/10.1016/j.gca.2015.12.010

Titiloye, J.O., Skipper, N.T., 2001. Molecular dynamics simulation of methane in sodium montmorillonite clay hydrates at elevated pressures and temperatures. Molecular Physics 99, 899–906. https://doi.org/10.1080/00268970010028863

Tournassat, C., Appelo, C.A.J., 2011. Modelling approaches for anion-exclusion in compacted Na-bentonite. Geochimica et Cosmochimica Acta 75, 3698–3710. https://doi.org/10.1016/j.gca.2011.04.001

Tournassat, C., Bourg, IanC., Holmboe, M., Sposito, G., Steefel, CarlI., 2016. Molecular Dynamics Simulations of Anion Exclusion in Clay Interlayer Nanopores. clays clay miner 64, 374–388. https://doi.org/10.1346/CCMN.2016.0640403

Tournassat, C., Neaman, A., Villiéras, F., Bosbach, D., Charlet, L., 2003. Nanomorphology of montmorillonite particles: Estimation of the clay edge sorption site density by low-pressure gas adsorption and AFM observations. American Mineralogist 88, 1989–1995. https://doi.org/10.2138/am-2003-11-1243

Tournassat, C., Steefel, C.I., 2019. Reactive Transport Modeling of Coupled Processes in Nanoporous Media. Reviews in Mineralogy and Geochemistry 85, 75–109. https://doi.org/10.2138/rmg.2019.85.4

Tournassat, C., Steefel, C.I., 2015. Ionic Transport in Nano-Porous Clays with Consideration of Electrostatic Effects. Reviews in Mineralogy and Geochemistry 80, 287–329. https://doi.org/10.2138/rmg.2015.80.09

Underwood, T.R., Bourg, I.C., 2020. Large-Scale Molecular Dynamics Simulation of the Dehydration of a Suspension of Smectite Clay Nanoparticles. J. Phys. Chem. C 124, 3702–3714. https://doi.org/10.1021/acs.jpcc.9b11197

Van Loon, L.R., Baeyens, B., Bradbury, M.H., 2005. Diffusion and retention of sodium and strontium in Opalinus clay: Comparison of sorption data from diffusion and batch sorption measurements, and geochemical calculations. Applied Geochemistry 20, 2351–2363. https://doi.org/10.1016/j.apgeochem.2005.08.008

Van Loon, L.R., Glaus, M.A., Müller, W., 2007. Anion exclusion effects in compacted bentonites: Towards a better understanding of anion diffusion. Applied Geochemistry 22, 2536–2552. https://doi.org/10.1016/j.apgeochem.2007.07.008

Van Loon, L.R., Mibus, J., 2015. A modified version of Archie's law to estimate effective diffusion coefficients of radionuclides in argillaceous rocks and its application in safety analysis studies. Applied Geochemistry 59, 85–94. https://doi.org/10.1016/j.apgeochem.2015.04.002

Van Loon, L.R., Soler, J.M., Jakob, A., Bradbury, M.H., 2003. Effect of confining pressure on the diffusion of HTO, 36Cl− and 125I− in a layered argillaceous rock (Opalinus Clay): diffusion perpendicular to the fabric. Applied Geochemistry 18, 1653–1662. https://doi.org/10.1016/S0883-2927(03)00047-7

Van Loon, L.R., Soler, J.M., Müller, W., Bradbury, M.H., 2004. Anisotropic Diffusion in Layered Argillaceous Rocks: A Case Study with Opalinus Clay. Environ. Sci. Technol. 38, 5721–5728. https://doi.org/10.1021/es049937g

Vasseur, G., Djeran-Maigre, I., Tessier, D., Velde, B., 1995. Evolution of structural and physical parameters of clays during experimental compaction 14.

Velde, B., 1996. Compaction trends of clay-rich deep-sea sediments. Marine Geology 133, 193–201. https://doi.org/10.1016/0025-3227(96)00020-5

Velde, B., Meunier, A., 2008. Fundamentals of Clay Mineral Crystal Structure and Physicochemical Properties, in: The Origin of Clay Minerals in Soils and Weathered Rocks. Springer Berlin Heidelberg, Berlin, Heidelberg, pp. 3–73. https://doi.org/10.1007/978-3-540-75634-7_1

Viennet, J.-C., Hubert, F., Ferrage, E., Tertre, E., Legout, A., Turpault, M.-P., 2015. Investigation of clay mineralogy in a temperate acidic soil of a forest using X-ray diffraction profile modeling: Beyond the HIS and HIV description. Geoderma 241–242, 75–86. https://doi.org/10.1016/j.geoderma.2014.11.004

Villieras, F., Cases, J.M., Francois, M., Michot, L.J., Thomas, F., 1992. Texture and surface energetic heterogeneity of solids from modeling of low-pressure gas adsorption isotherms. Langmuir 8, 1789–1795. https://doi.org/10.1021/la00043a018

Villieras, F., Michot, L.J., Bardot, F., Cases, J.M., François, M., Rudziński, W., 1997. An Improved Derivative Isotherm Summation Method to Study Surface Heterogeneity of Clay Minerals. Langmuir 13, 1104–1117. https://doi.org/10.1021/la9510083

Waseda, Y., Matsubara, E., Shinoda, K., 2011. X-Ray Diffraction Crystallography. Springer Berlin Heidelberg, Berlin, Heidelberg. https://doi.org/10.1007/978-3-642-16635-8

Wenk, H.-R., Kanitpanyacharoen, W., Voltolini, M., 2010. Preferred orientation of phyllosilicates: Comparison of fault gouge, shale and schist. Journal of Structural Geology 32, 478–489.

Wenk, Voltolini, Mazurek, Loon, V.L.R., Vinsot, 2008. Preferred Orientations and Anisotropy in Shales: Callovo-Oxfordian Shale (France) and Opalinus Clay (Switzerland). Clays Clay Miner. 56, 285–306. https://doi.org/10.1346/CCMN.2008.0560301

Wilson, M.J., 2013. Rock-forming Minerals, Sheet Silicates: Clay Minerals, Second. ed. Geological Society of London, London.

Wilson, M.J., 1999. The origin and formation of clay minerals in soils: past, present and future perspectives. Clay miner. 34, 7–25. https://doi.org/10.1180/000985599545957

Wittebroodt, C., Savoye, S., Frasca, B., Gouze, P., 2012. Diffusion of HTO, 36ClÀ and 125IÀ in Upper Toarcian argillite samples from Tournemire: Effects of initial iodide concentration and ionic strength. Applied Geochemistry 27, 1432–1441.

Xiang, Y., Al, T., Scott, L., Loomer, D., 2013. Diffusive anisotropy in low-permeability Ordovician sedimentary rocks from the Michigan Basin in southwest Ontario. Journal of Contaminant Hydrology 155, 31–45.

Yang, W., Zheng, Y., Zaoui, A., 2015. Swelling and diffusion behaviour of Na-vermiculite at different hydrated states. Solid State Ionics 282, 13–17. https://doi.org/10.1016/j.ssi.2015.09.007

Zhai, Z., Wang, X., Jin, X., Sun, L., Li, J., Cao, D., 2014. Adsorption and Diffusion of Shale Gas Reservoirs in Modeled Clay Minerals at Different Geological Depths. Energy Fuels 28, 7467–7473. https://doi.org/10.1021/ef5023434

Zhou, H., Chen, M., Zhu, R., Lu, X., Zhu, J., He, H., 2020. Coupling between clay swelling/collapse and cationic partition. Geochimica et Cosmochimica Acta 285, 78–99. https://doi.org/10.1016/j.gca.2020.07.007

Appendices

Appendix 1: Through Diffusion results of HDO, Sr2+ and Cl- diffusing through < 0.1 µm Ca-vermiculite samples.

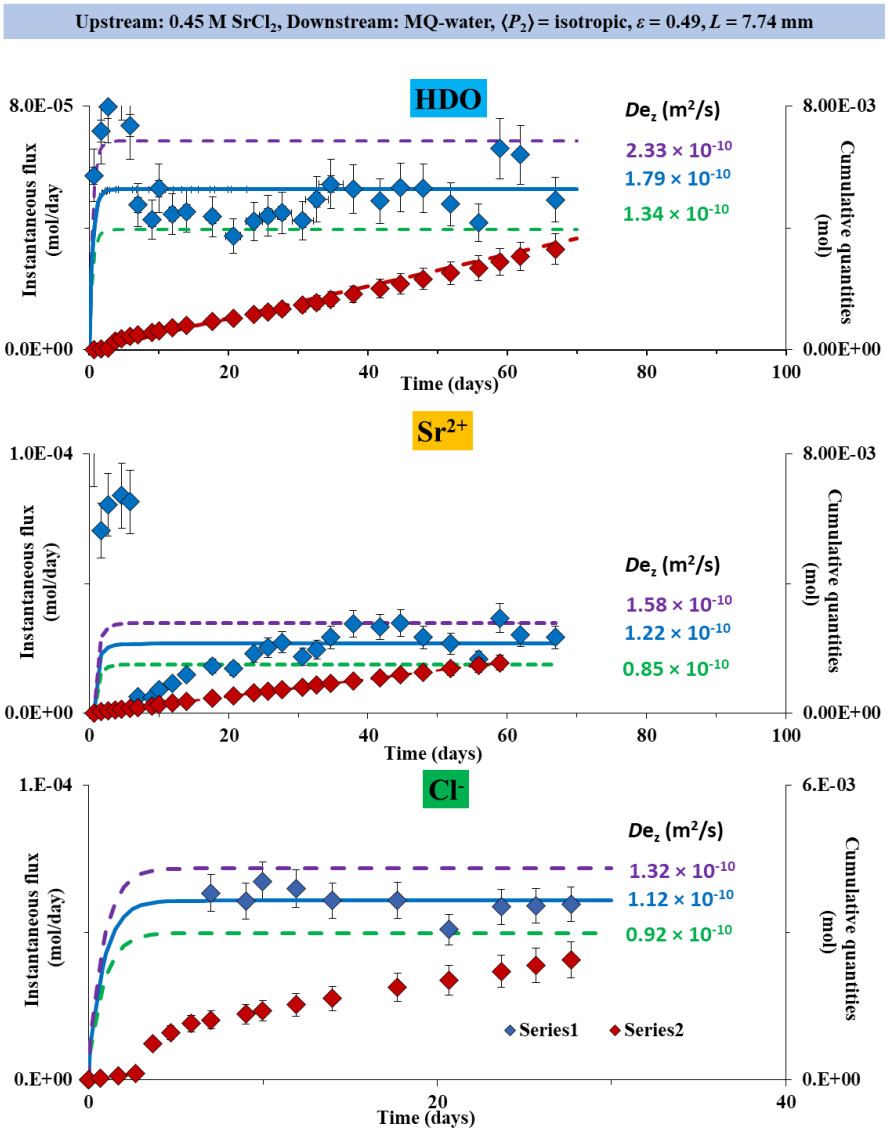


Fig. A.1. *Experimental instantaneous flux (blue diamonds) and cumulative quantities (red diamonds) of HDO, Sr^{2+} and Cl^{-} diffusing through < 0.1 µm Ca-vermiculite samples. The solid blue lines correspond to the fit of the experimental flux, whereas dotted lines are simulated flux curves calculated by considering the error range in the diffusion parameters. Dashed lines correspond to simulated cumulative curves by considering the diffusion parameters interpreting the average experimental flux. $\langle P_2 \rangle$ is the order parameter representing the degree of anisotropy in particles preferred orientation (see text for details). ε is the total porosity value (%). L is the sample thickness in mm. All De values are corrected from possible temperature variations and are reported for 21˚C*

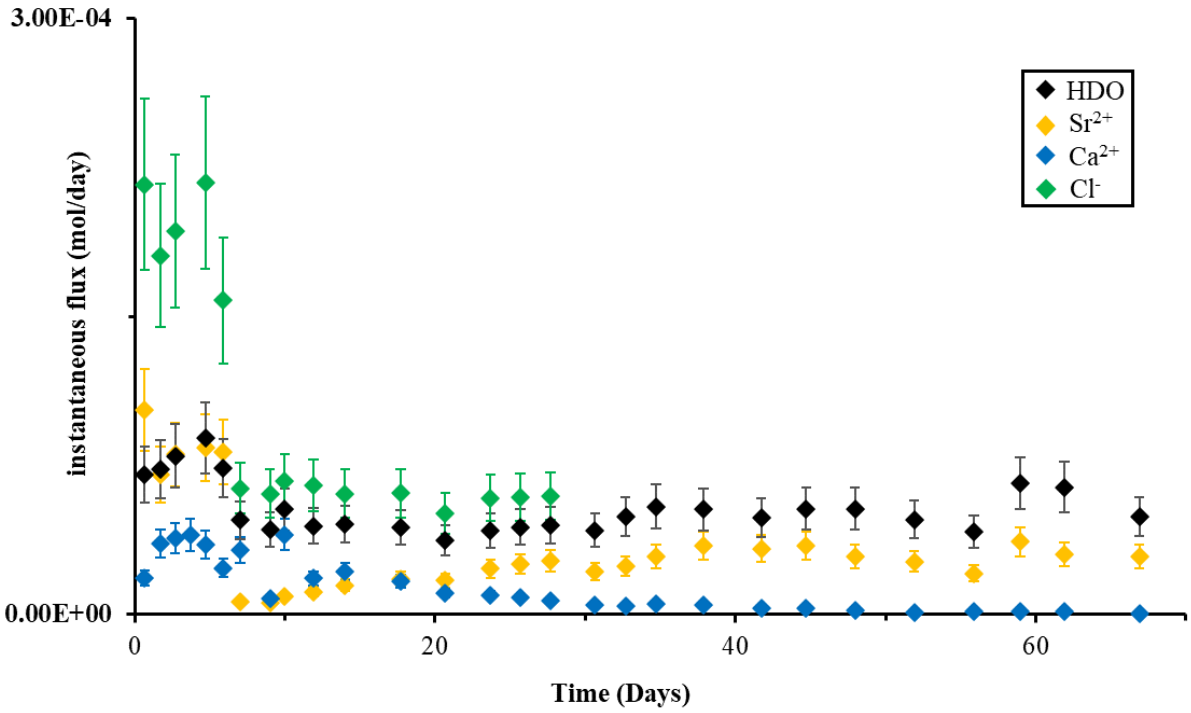


Fig. A.2. *Experimental instantaneous fluxes of HDO, Sr^{2+}, Ca^{2+} and Cl^{-} diffusing through < 0.1 µm Ca-vermiculite samples. Experimental conditions are in the description of Fig. A1*

Appendix 2: Article: Connecting molecular simulations and laboratory experiments for the study of time-resolved cation-exchange process in the interlayer of swelling clay minerals.

Emmanuel Tertre, Baptiste Dazas, Ali Asaad, Eric Ferrage, Brian Gregoire,

Fabien Hubert, Alfred Delville, Frederick Delay

Applied Clay Science 200 (2021) 105913

Contents lists available at ScienceDirect

Applied Clay Science

journal homepage: www.elsevier.com/locate/clay

Research Paper

Connecting molecular simulations and laboratory experiments for the study of time-resolved cation-exchange process in the interlayer of swelling clay minerals

Emmanuel Tertre [a,*], Baptiste Dazas [a], Ali Asaad [a], Eric Ferrage [a], Brian Grégoire [a], Fabien Hubert [a], Alfred Delville [b], Frédérick Delay [c]

[a] Université de Poitiers/CNRS, UMR 7285 IC2MP, Equipe HydrASA, 5 rue Albert Turpain, 86073 Poitiers cedex 9, France
[b] Université d'Orléans/CNRS, UMR 7374 ICMN, 45071 Orléans, France
[c] Université de Strasbourg/CNRS, UMR 7517 LHyGeS, 1 rue Blessig, 67000 Strasbourg, France

ARTICLE INFO

Keywords:
Vermiculite
Cation
Interlayer of clay mineral
Finite-volume model for diffusion
Self-diffusion coefficient
Up-scaling

ABSTRACT

In the context of element migration in clay-rich media, self-diffusion coefficients of interlayer cations in swelling clay minerals obtained from molecular simulations are rarely used by macroscopic models predicting cation-exchange processes. Based on experiments and simulations, this study aims at (i) making a connection between molecular and sample scale processes to predict the dynamics of cation-exchange reactions between the interlayer space of millimetre disks of vermiculite and aqueous reservoirs, and (ii) assessing the role played by both self-diffusion and selectivity coefficients on this process.

Time-resolved cation exchange experiments were performed using Ca-saturated vermiculite disks immersed in aqueous reservoirs with different NaCl or $SrCl_2$ salinities. The results were reproduced via a finite-volume model constrained by (i) cation self-diffusion coefficients calculated by molecular dynamics simulations and (ii) interlayer selectivity coefficients drawn from "batch" cation-exchange isotherms.

Results showed that considering the averaged values for both the cation-exchange selectivity coefficients and self-diffusion coefficients of the slowest interlayer cation led to good agreement between the experiments and simulations, validating the modelling strategy for the connection between the molecular and laboratory time scales. A sensitivity test regarding the influence of the two input parameters on the overall results was then performed. This study underlined a constrained upscaling strategy to better assess the role played by different intrinsic parameters of the clay/water systems (molecular self-diffusion coefficients in the interlayer space vs. selectivity coefficient) on the diffusion of cations during cation-exchange reaction in clay-rich media.

1. Introduction

Diffusion is the main transport process of water and chemical species in shales and engineered clay-rich barriers considered for the storage of nuclear wastes (see reviews of Bourg et al., 2003 and Charlet et al., 2017 among others). In addition, due to the high compaction of these environments, diffusion in the interlayer spaces of the swelling clay minerals is one of the principal processes controlling the migration of water and cations (Glaus et al., 2007). In this context, numerous models based on a continuum approach coupling diffusion and adsorption/desorption processes are available to describe the reactive transport of cations in compacted clayey porous media (Appelo and Wersin, 2007; Birgersson and Karnland, 2009; Jougnot et al., 2009; Appelo et al., 2010; Tachi and Yotsuji, 2014; Tachi et al., 2014; Tournassat and Steefel, 2015; Tinnacher et al., 2016). Among them, the most exhaustive models (Appelo and Wersin, 2007; Appelo et al., 2010; Tachi and Yotsuji, 2014; Tachi et al., 2014; Tournassat and Steefel, 2015; Tinnacher et al., 2016) account for the reduced mobilities of cations (as compared to bulk water) near the negative surfaces of clay particles (such as interlayer surfaces), as indicated by molecular dynamic simulation studies (Marry and Turcq, 2003; Tournassat et al., 2009; Michot et al., 2012; Tinnacher et al., 2016 among others). These models typically consider a unique pore size value (usually, within the nanometre range) and differ from each other in the way they describe the geometry of the electrical double layer (i.e.,

* Corresponding author.
E-mail address: emmanuel.tertre@univ-poitiers.fr (E. Tertre).

https://doi.org/10.1016/j.clay.2020.105913
Received 9 April 2020; Received in revised form 26 October 2020; Accepted 28 October 2020
Available online 12 November 2020
0169-1317/© 2020 Elsevier B.V. All rights reserved.

presence of the Stern layer or not, in addition to the diffuse ion swarm) and the evolution of the electrical potential from the surface to the nanopore centre. These models present the great advantages, over empirical models (i.e., those based on the Fick's first law) to (i) provide the coupling between transport and chemical processes (i.e., sorption reactions via selectivity coefficients), and (ii) to constrain the diffusion process at the sample scale using mobility determined at the molecular scale (Tournassat and Steefel, 2019). Applications of these reactive transport codes coupling transport and chemical processes, as Phreeqc® (Parkhurst and Appelo, 2013) or CrunchFlow MC (now CrunchClay; Steefel et al., 2015), were proved to be extremely efficient at describing the transport of multi-species in complex heterogeneous and charged clay porous materials submitted to various chemical and physical perturbations (e.g., sorption, dissolution/precipitation, change of porosity distribution due to salinity gradient).

However, at the scale of an individual clay particle (i.e., dispersed system), the situation differs for the specific case of time-resolved ion-exchange processes. One study tried to connect molecular and sample scales to predict cation-exchange rates at the interface between the interlayer of swelling clay minerals and aqueous reservoirs (Tertre et al., 2015). This was made possible using millimetre-sized vermiculite disks initially Ca-saturated and immersed in NaCl solutions with different salinities. Vermiculite does not display osmotic swelling, contrary to smectitic clays commonly used in macroscopic diffusion experiments (see Glaus et al., 2007 among others). This sample thus keeps a constant hydration state, allowing to derive self-diffusion coefficients from computational methods such as molecular simulations. By coupling molecular dynamic (MD) simulations at the molecular scale and Brownian dynamic (BD) simulations at the sample scale, authors indicated that the experimental data of the dynamics of the Na^{+}-for-Ca^{2+} ion exchange reaction at the interface between the interlayer of the clay mineral and the bulk reservoir were well reproduced (Tertre et al., 2015). In this previous study, it was also shown that for aqueous reservoirs with high salinities the diffusion during cation-exchange reactions was only driven by the sole self-diffusion coefficients of interlayer cations leading to the generation of interlayer gradients varying with the Na^{+}/Ca^{2+} interlayer occupancy and diffusion time. Notably, the integration of BD into continuum approaches is difficult, even though the technique is powerful to assess the influence of the geometry of the porous media on the macroscopic diffusion (Dabat et al., 2020). As an alternative, Tournassat and Steefel (2015) used a model based on continuous equations and properties of negative surfaces to successfully interpret the experimental dataset previously reported in Tertre et al. (2015). However, the interlayer diffusion coefficients of cations reported by Tournassat and Steefel (2015) were found to vary with the salinity of the aqueous reservoir. These molecular diffusion coefficients are thus apparent and cannot be considered as self-diffusion coefficients (i.e., depending only on the environment of the confined probe in the interlayer space at thermodynamic equilibrium) commonly derived from molecular simulations. Accordingly, the question remains open regarding the ability of continuum approaches to connect the molecular self-diffusion coefficients derived from molecular simulations at short timescales with laboratory experiments timescales for cation-exchange reactions in a single clay disk immersed in different aqueous reservoirs.

In this context, the aim of this present work is firstly to assess, within the framework of continuous approaches, the possibility to account for molecular self-diffusion coefficients to predict the dynamics of the cation-exchange reaction in the case of a single disk immersed in aqueous reservoirs. For this purpose a simple finite-volume model constrained by (i) interlayer self-diffusion coefficients stemming from MD simulations and (ii) interlayer selectivity coefficients, describing interlayer exchange, is used to simulate cation-exchange rates as a function of the diffusion time for a millimetre-sized particle immersed in an aqueous reservoir characterized by different concentrations. Secondly, the roles played by both self-diffusion and selectivity coefficients on the dynamics of the cation-exchange are assessed by the confrontation of predicted data with the experimental dataset. This includes Sr^{2+}-for-Ca^{2+} and Na^{+}-for-Ca^{2+} ion-exchange data obtained with millimetre vermiculite disks. Finally, the sensitivity of the proposed model to self-diffusion and selectivity coefficients values used is evaluated, which introduces a discussion on the parameters required to predict the dynamics of the cation-exchange process in diffusion models.

2. Experimental method and modelling

2.1. Cation-exchange experiments on individual vermiculite disks

Experiments were performed according to the method detailed in Tertre et al. (2015). Briefly, thin disks of Ca-vermiculite (5 mm in diameter; ≈ 0.6–0.7 mm in thickness), obtained by punching large monocrystal pieces of vermiculite from Santa Olalla (Huelva, Spain), were immersed in aqueous reservoirs of NaCl and $SrCl_2$ at different initial concentrations, and the release of Ca from the disk to the solution was measured with respect to time. The solid/solution ratio used for these experiments is equal to 0.12 $g_{hydrated\text{-}solid}/kg_{water}$ (i.e., typically 30 mg of hydrated solid in 250 mL of aqueous solution), corresponding to $1.05x10^{-4}$ mol_{Ca}/kg_{water} considering a cationic exchange capacity (CEC) of 175 meq/100 $g_{hydrated\text{-}solid}$ in agreement with the value reported for this parameter in the literature (Dzene et al., 2016). Experimental results are expressed in terms of the % Ca (relative to the CEC) released in solution as a function of the diffusion time. Aqueous concentrations of Ca cations were measured using an atomic absorption spectrophotometer (Varian AA240FS) with all samples analyzed in 2% HNO_3 solutions. To take into account possible interferences during analyses due to the extreme saline conditions used, $LaCl_3$ and KCl solutions were added in the samples. As recommended by Lajunen and Peramaki (2004), amounts of these added solutions were chosen in order to have final concentrations in the samples equal to 1 and 2 g/kg_{water} for $LaCl_3$ and KCl, respectively. In this present study, Sr^{2+}-for-Ca^{2+} data were obtained for three contrasted initial aqueous $SrCl_2$ concentrations (i.e., 10^{-2}, $2x10^{-4}$, and $3x10^{-5}$ mol/kg_{water}). To increase the number of available experimental data, additional Na^{+}-for-Ca^{2+} data were also collected using NaCl initial concentrations equal to $5x10^{-2}$ and $3x10^{-3}$ mol/kg_{water}, completing the Na^{+}-for-Ca^{2+} experimental data set reported in Tertre et al. (2015) for NaCl initial concentrations equal to 1, $5x10^{-2}$ and $3x10^{-3}$ mol/kg_{water}. The pH was measured throughout the experiments and was found to be fairly constant at approximately 5.9 ± 0.15. Finally, no change in sample disk integrity (i.e., dissolution) was observed during the experimental timespan.

2.2. Self-diffusion coefficients obtained by microscopic simulations

Self-diffusion coefficients of interlayer cations were obtained for different interlayer Ca^{2+}/Sr^{2+} and Ca^{2+}/Na^{+} occupancies by MD simulations. These calculations were based on molecular clay configurations derived from Grand Canonical Monte Carlo (GCMC) simulations representative of the hydrated clay mineral used for the experiment. These coefficients will be compared for the purpose of validation in the results and discussion section to data reported in the literature for other hydrated clay structures.

2.2.1. Grand Canonical Monte Carlo (GCMC) simulations

A molecular structure was first obtained by GCMC (Delville, 1991; Allen and Tildesley, 1994). This structure is composed of 3 clay layers, each made of 60 unit cells (i.e., 10 and 6 along the a and b unit-cell parameters, respectively), leading to simulation cells large enough (53.2 Å x 55.26 Å x 44.76 Å) to study the radial diffusion of confined cations. The chemical composition of the unit cell used for the calculation is:

$$\left[Si_{5.65}Al_{2.35}Mg_{5.32}Al_{0.58}Fe^{+III}_{0.1}O_{20}(OH)_4\right]\left(Ca_xSr_yNa_z\right), XH_2O$$

where $2x + 2y + z = 1.67$, with 1.67 corresponding to the structural charge of the unit cell. It should be noted that the structural formula used was adapted from that proposed in the literature by Argüelles et al. (2010) for a by-hydrated Mg-structure:

$$\left[Si_{5.66}Al_{2.34}Mg_{4.92}Al_{0.60}Fe^{+II}_{0.44}Ti_{0.04}O_{20}(OH)_4\right](Mg_{0.76}Ca_{0.06}Na_{0.04}), 7.63H_2O.$$

The purpose was to homogenize the number of substituted atoms between the 3 layers as well as counterions while maintaining the overall charge and charge localization. *X* is the number of confined water molecules per unit cell determined at a prescribed temperature ($T = 298$ K) and a water chemical potential ($p/p_0 = 1$) representative of water-saturated conditions. This value has been set to 10.0, 10.35 and 9.6 for Ca, Sr and Na by-hydrated end-members, respectively. Finally, note that simulation cells are directly in contact with the periodic boundaries leading then to cells mimicking «infinite» layer.

The thickness of the clay layer used for the calculations was fixed to 14.92 Å, corresponding to the value proposed by de la Calle and Suquet (1988) for a Ca-vermiculite layer immersed in water. This value was used irrespective of the equivalent fraction of Ca^{2+} (i.e., XCa) in the layers during exchange with either Sr^{2+} or Na^+, since the values reported in the literature for the thicknesses of clay layers saturated with Ca^{2+}, Sr^{2+} and Na^+ for water saturated conditions are very close (14.92, 15.20 and 14.85 Å, respectively; de la Calle and Suquet, 1988). It should be noted that XCa is defined as $XCa = \frac{[Ca]_{sorbed}}{CEC}$ where $[Ca]_{sorbed}$ is the Ca concentration sorbed in the vermiculite in meq/100 $g_{\text{hydrated solid}}$, as expressed for the CEC (see Section 2.1).

In GCMC simulations, the interactions between the different atoms were described using the ClayFF model (Cygan et al., 2004) modified by Ferrage et al. (2011) for the clay layer, and the flexible water SPC model. The Lennard-Jones potentials of the interlayer Ca^{2+} and Na^+ cations were taken from Cygan et al. (2004), while for Sr^{2+} cations, the potentials used were derived from data in the literature (Aaqvist, 1990), as suggested by Ngouana Wakou (2014). Ewald summation (Heyes, 1994) with 3D periodic boundary conditions was used to reproduce the long-range coulombic potential.

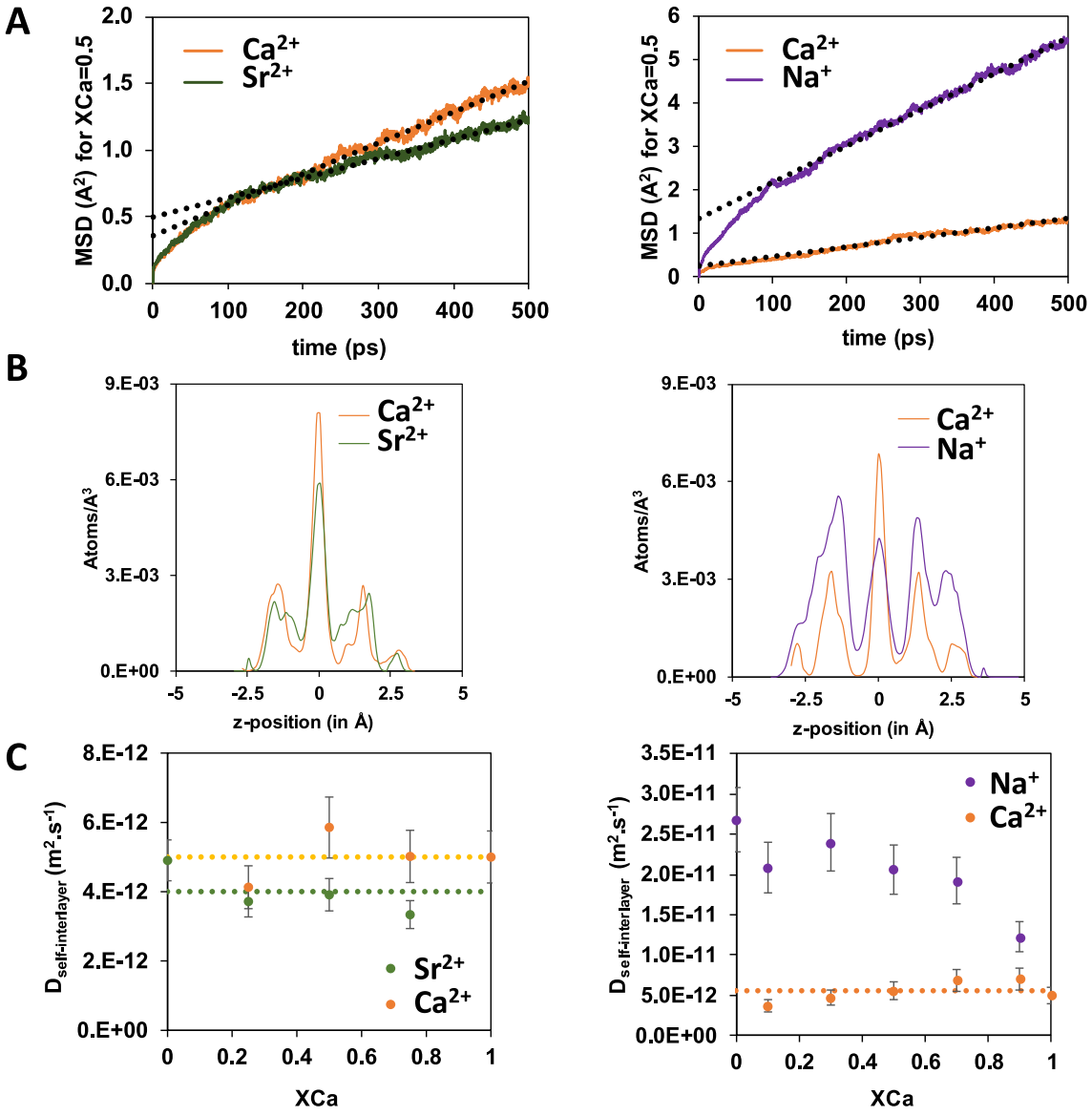


Fig. 1. Results from GCMC and MD simulations. (A) Asymptotic slope of the radial mean squared displacement obtained for the cations with XCa = 0.5. (B) Interlayer atomic density profiles (in atoms/Å^3) of cations for XCa = 0.5. (C) Variation of the self-diffusion coefficients of cations as a function of XCa. XCa is the equivalent fraction of Ca^{2+} in the interlayer. In Fig. 1C, dashed lines represent the average self-diffusion coefficients of Ca^{2+} and Sr^{2+} over a XCa range from 0 to 1. Left and right columns report on the data for Sr^{2+}-for-$Ca^{2+}$and Na^+-for-Ca^{2+} exchanges, respectively.

2.2.2. Molecular dynamic (MD) simulations

Self-diffusion coefficients of calcium, strontium and sodium were determined by MD simulations, which started from a prior equilibrium configuration obtained by GCMC simulations. Calculations were performed by using the LAMMPS software (Plimpton, 1995). It should be noted that when two types of cations are considered in the interlayer (i.e., Ca^{2+} and Sr^{2+} or Ca^{2+} and Na^{+}), the water content used in the structural model has been adjusted using the LAMMPS integrated GCMC algorithm. The microcanonical (NVE, in which N, V and E represent the number of particles, volume and energy, respectively) ensemble was applied for the simulation. A Verlet algorithm (Allen and Tildesley, 1994) was used to obtain the trajectories of the confined cations. The elementary time step employed for the calculations was fixed to 0.5 fs (as in Michot et al., 2012), while the total simulation time of the MD calculations exceeds 2 ns. To stabilize the temperature ($T = 298$ K) that would otherwise vary over the simulation time, a weakly coupled Berendsen thermostat was used (Berendsen et al., 1984). From the 3D local motions of atoms, the self-diffusion coefficients of the cations (i.e., $D_{self\text{-}interlayer}$) parallel to the clay surface are obtained from the asymptotic slope of the radial mean squared displacement (see Fig. 1A) defined in the basal plane of the layers according to:

$$D_{self-interlayer} = \frac{1}{4N}\lim_{t\to\infty}\frac{\left(\sum_{i=1}^{N}(x_i(0)-x_i(t))^2+\sum_{i=1}^{N}(y_i(0)-y_i(t))^2\right)}{t} \quad (1)$$

where N is the total number of diffusing cations and t is the diffusion time (s). To reduce the statistical noise, calculations were performed by considering four non-overlapping trajectories with a duration of 500 ps extracted from the complete run performed over 2 ns of total simulation time. Finally, self-diffusion coefficients issued from these calculations are dependent only on the environment of the probe in the interlayer space, and are representative of the mobilities of the cations in the interlayer of the bi-hydrated vermiculite, irrespective of the chemical composition of the aqueous reservoir with which vermiculite layers could be in contact.

2.3. Finite-volume model to simulate the macroscopic exchange rate

The finite-volume model proposed here to predict the macroscopic dynamics of the cation exchange processes is constrained by the radial self-diffusion coefficients calculated by MD. These coefficients were extracted from the analysis of the ionic trajectories obtained with Eq. (1), and were averaged over the whole atomic structure of the clay/water interface, thus taking into account water and ionic layering (see Fig. 1B) and 3D local mobility of the various atoms. Then, radial-self diffusion coefficients implicitly take into account the limited ionic motions in the direction perpendicular to the clay surface, as reported by Michot et al. (2012). As a consequence, the proposed finite-volume model can simply consider residual 2D macroscopic diffusion of neutral probes freely diffusing on the surface of a structureless cylindrical section with perfect radial symmetry. In this geometrical configuration, the motion of the probe is described by the one-dimensional radial component of the diffusion equation.

2.3.1. Generalities

Radial-cylindrical diffusion with infinite radial symmetry of a probe (i.e., a cation in our case) in a disk can be written as:

$$\frac{\partial C(r,t)}{\partial t} - \frac{1}{r}\frac{\partial}{\partial r}\left(r\,D\frac{\partial C(r,t)}{\partial r}\right) = 0 \quad (2)$$

where $C(r, t)$ [ML^{-3}] is the concentration of the probe at a distance r from the centre of the disk at time t and D [L^2T^{-1}] is the diffusion coefficient of the probe in the disk. In this study, D will be taken as the molecular self-diffusion coefficient calculated by MD. From a general standpoint, solving Eq. 2 by relying upon a finite-volume formalism states that for any elementary volume V within the disk, Eq. 2 can be integrated over the volume V:

$$\int\frac{\partial C}{\partial t}dV - \int\frac{1}{r}\frac{\partial}{\partial r}\left(rD\frac{\partial C}{\partial r}\right)dV = 0 \quad (3)$$

where $r^{-1}\partial/\partial r(r\ldots)$ is the divergent operator in cylindrical coordinates with infinite radial symmetry, and by using the Ostrogradski theorem, Eq. 3 can be rewritten as:

$$\int\frac{\partial C}{\partial t}dV - \int D\frac{\partial C}{\partial r}.n_\Gamma d\Gamma = 0 \quad (4)$$

where Γ is the contour boundary of the volume V and n_Γ is the outer normal to the boundary.

Considering the discretisation of the disk with a radial spatial step Δ_r in concentric cylindrical rings; a ring indexed by i is bound by cylindrical walls located in $(i-1)\Delta_r$ and $i\Delta_r$. The volume of the ring is $\pi e((i\Delta_r)^2 - ((i-1)\Delta_r)^2)$, where e is the thickness of the disk, the diffusing surface-areas of the contours of the ring being $2\pi ei\Delta r$ with a positive outer normal n_Γ, and $2\pi e(i-1)\Delta r$ with a negative outer normal. By assuming that a uniform mean concentration C_i can be defined over the ring i, using a first-order approximation for the spatial derivatives $\partial C/\partial r$, and considering a uniform diffusion coefficient D over the disk, Eq. 4 can be discretized as:

$$\frac{C_i^{n+1}-C_i^n}{\Delta t}\pi e\left((i\Delta_r)^2-((i-1)\Delta_r)^2\right) - D2\pi e(i\Delta_r)\frac{C_{i+1}^n-C_i^n}{\Delta_r} + D2\pi e(i-1)\Delta_r\frac{C_i^n-C_{i-1}^n}{\Delta_r} = 0 \quad (5)$$

where n is the index over the time coordinate discretized at step Δt. An explicit scheme over time discretizing the spatial derivatives at time $n\Delta t$ is employed. Rearranging Eq. 5 results in:

$$\frac{C_i^{n+1}-C_i^n}{\Delta t}2\Delta_r^2\left(i-\frac{1}{2}\right) = 2Di\left(C_{i+1}^n-C_i^n\right) - 2D(i-1)\left(C_i^n-C_{i-1}^n\right) \quad (6a)$$

i.e.,

$$C_i^{n+1} = C_i^n + \frac{\Delta t\ 2D}{2(\Delta_r)^2\left(i-\frac{1}{2}\right)}\left[i\left(C_{i+1}^n-C_i^n\right)-(i-1)\left(C_i^n-C_{i-1}^n\right)\right] \quad (6b)$$

By denoting $Ne = \frac{D\Delta t}{(\Delta_r)^2}$ (the Von Neumann stability criterion for diffusion; Charney et al., 1950), the concentration of the probe in the i concentric ring at time $(n+1)\Delta t$ from those at time $n\Delta$t is:

$$C_i^{n+1} = \left[\frac{i2Ne}{2i-1}\right]C_{i+1}^n + \left[\frac{(i-1)2Ne}{2i-1}\right]C_{i-1}^n + [1-2Ne]C_i^n \quad (7)$$

It should be noted that to preserve numerical stability, the Von Neumann criterion must be less than 0.5 for the explicit scheme in Eq. 7 to be stable and not subjected to spurious oscillations. It is noteworthy that in Eq. (5) the thickness e of the clay particle could be dropped, then rendering the one-dimensional radial diffusion logically independent of the thickness of the particle. However, in general cases, e could be kept in Eq. (5), because one could envision clay particles with non-uniform

thickness, or simply boundary conditions at the interface between the particle and the aqueous reservoir that need to be calculated as a" free" diffusive flux. In that case, the volumes of the clay disk and the reservoir would influence the boundary condition. Finally, note that the preceding reasons also motivate the choice of an explicit numerical solution to simulate the macroscopic diffusion instead of an analytical solution.

2.3.2. Input parameters

Since the limited ionic mobility in the direction perpendicular to the clay surface is included in the derivation of the radial self-diffusion coefficient evaluated by MD simulations (see introduction of Section 2.3), the macroscopic clay particle is represented in the framework of a finite-volume model by using a simple flat disk with a diameter equal to 5 mm, as used for the experiments. This approximation is justified by results obtained from X-ray diffraction measurements (Walker, 1961; Reed and Scott, 1962 among others) showing that cation exchange reactions occurring in the interlayer of coarse clay particles (i.e. > 10 μm) operate via a radial interlayer diffusion front inside the clay particles. Then, assumption is made that diffusion front moves in the whole particle (i.e., in all layers located in the clay particle) at the same velocity in the radial direction irrespective of the ionic interfacial content. This last approximation is compatible with the results obtained by MD numerical simulations displayed in Fig. 1C exhibiting a limited variation of the radial ionic mobility as a function of the ionic composition of the clay/water interface.

Input parameters of the finite-volume model are as follows: (i) the self-diffusion coefficient, representative of the mobilities of cation inside the particle and generating an interlayer gradient during exchange with the aqueous reservoir, and (ii) the amount of Ca located in the disk and fully exchanged at an infinite time (i.e., amount of initial reactive Ca). Self-diffusion coefficients of interlayer cations were calculated by MD simulations for the structure representative of the clay used experimentally (see Section 2.2) and for different Ca^{2+}/Na^{+} and Ca^{2+}/Sr^{2+} interlayer occupancies (i.e., XCa value). Furthermore, amounts of initial reactive Ca were calculated from total amounts of Ca exchanged (i.e., released) at infinite time predicted by means of interlayer selectivity coefficients previously published in Tertre et al. (2013) and Dzene et al. (2016). These total amounts were calculated with the Phreeqc® software (Parkhurst and Appelo, 1999) associated to the thermodynamic database proposed by Johnson et al. (1992) for aqueous species, assuming thermodynamic equilibrium between the solid and aqueous phases with an initial chemical composition representative of the experiments (solid/solution ratio and initial aqueous concentrations for Na^{+}, Ca^{2+}, Sr^{2+} and Cl^{-} ions). These calculations were performed by considering (i) an interlayer CEC equal to 175 meq/100 $g_{hydrated\text{-}solid}$ as proposed by Dzene et al. (2016) for the same by-hydrated Ca-vermiculite as the one used in this study, and (ii) decimal logarithms of selectivity coefficients (Gaines Thomas convention; Gaines and Thomas, 1953) equal to 0 and 0.1, as proposed by Dzene et al. (2016) and Tertre et al. (2013) describing the exchange in "batch" experiments of Ca^{2+}-for-Sr^{2+} and Ca^{2+}-for-Na^{+}, respectively. As an example, the selectivity coefficient is defined in the case of the Ca^{2+}-for-Na^{+} exchange as follow:

$$Kc\left(Na^{+}/Ca^{2+}\right) = \frac{E_{Ca2+}\left[Na^{+}\right]_{aq.}^{2}\gamma_{Na+}^{2}}{\left(E_{Na+}\right)^{2}\left[Ca^{2+}\right]_{aq.}\gamma_{Ca2+}} \quad (8)$$

where E_{Na+} and E_{Ca2+} are the equivalent fractions of Na^{+} and Ca^{2+} adsorbed in the interlayer, respectively, and, γ_{Na+} and γ_{Ca2+} are the activity coefficients for Na^{+} and Ca^{2+} aqueous species calculated by using the Davies approximation (Davies, 1962). Brackets indicate the

Table 1
Chemical compositions of the initial solutions used in the experiments and those predicted at infinite time with Phreeqc® software (Parkhurst and Appelo, 1999) assuming a thermodynamic equilibrium after ion-exchange reactions. These simulated data are converted in % of Ca (normalised to the sample CEC) released in solution at infinite time, and in amounts of initial reactive Ca in the vermiculite used as input parameters in the finite-volume model proposed.

Ion-exchange reactions	Initial chemical composition of the solution in contact with Ca-disk (concentrations are expressed in mol/kg_{water}) [a]	Predicted chemical composition of the solution at equilibrium (after ion-exchange reactions) (concentrations are expressed in mol/kg_{water}) [b] and [c]	% of Ca (normalised to the sample CEC), released in solution, and predicted at infinite time (see [b])	Amount of initial reactive Ca in the disk ($mmol_{Ca}/g_{hydrated\text{-}solid}$) [d]
Sr^{2+}-for-Ca^{2+}	$SrCl_2$ 10^{-2}	$[Sr^{2+}] = 9.9x10^{-3}$ $[Ca^{2+}] = 1.2x10^{-4}$ $[Cl^{-}] = 2.0x10^{-2}$	98	0.85
	$SrCl_2$ $2x10^{-4}$	$[Sr^{2+}] = 1.3x10^{-4}$ $[Ca^{2+}] = 6.8x10^{-5}$ $[Cl^{-}] = 4.0x10^{-4}$	65	0.57
	$SrCl_2$ $3x10^{-5}$	$[Sr^{2+}] = 6.8x10^{-6}$ $[Ca^{2+}] = 2.4x10^{-5}$ $[Cl^{-}] = 6.0x10^{-5}$	22	0.19
Na^{+}-for-Ca^{2+}	NaCl 1	$[Na^{+}] = 1.0x10^{0}$ $[Ca^{2+}] = 1.1x10^{-4}$ $[Cl^{-}] = 1.0x10^{0}$	100	0.88
	NaCl $5x10^{-2}$	$[Na^{+}] = 5.0x10^{-2}$ $[Ca^{2+}] = 1.0x10^{-4}$ $[Cl^{-}] = 5.0x10^{-2}$	97	0.85
	NaCl $3x10^{-3}$	$[Na^{+}] = 2.9x10^{-3}$ $[Ca^{2+}] = 4.1x10^{-5}$ $[Cl^{-}] = 3.0x10^{-3}$	39	0.34

[a] pH of all initial solutions used are equal to 5.9 ± 0.15.

[b] Calculations are performed assuming a thermodynamic equilibrium between initial solution and a mass of hydrated solid equal to 0.12 g for 1 kg_{water}. This solid/solution value is representative of experiments using millimetre Ca-disks, and is equivalent to consider a CEC for disk equal to 175 meq/100$g_{hydrated\text{-}solid}$ in agreement with published value for this parameter (Dzene et al., 2016). Calculations are performed using the Phreeqc® software (Parkhurst and Appelo, 1999) and previous models proposed by Dzene et al. (2016) and Tertre et al. (2013) predicting Sr^{2+}-for-$Ca^{2+}$and Ca^{2+}-for-Na^{+} interlayer exchange respectively in vermiculite. In these models, decimal logarithms of selectivity coefficients for Sr^{2+}-for-$Ca^{2+}$and Ca^{2+}-for-Na^{+} (Gaines Thomas convention; Gaines and Thomas, 1953) are equal to 0 and 0.1 respectively (see text for details).

[c] predicted pH of the solution after exchange reactions was close to initial one (± 0.1) even by taking into account the possible adsorption of H^{+} in the model. This data show that adsorption of H^{+} during Sr^{2+}-for-$Ca^{2+}$and Na^{+}-for-Ca^{2+} exchange reactions is negligible at the pH of the experiments performed in this study (i.e., around pH = 6) using millimetre-sized crystals.

[d] Amounts of initial reactive Ca located in the disk at time 0 were calculated by using the % of Ca (normalised to the sample CEC) released in solution and predicted at infinite time, the solid/solution ratio used for the experiment (i.e., 0.12 g/kg_{water}) and a CEC equal to 175 meq/100$g_{hydrated\text{-}solid}$ (Dzene et al., 2016).

concentrations of the species in solution at equilibrium (mol/kg_{water}).

Table 1 reports on the % of Ca (normalised to the sample CEC) released in solution and calculated at infinite time (i.e., thermodynamic equilibrium) for the different studied systems. Using CEC sample and solid/solution ratio, these values are then converted into the total amounts of Ca released in solution at infinite time and are assumed to be equal to the total amounts of reactive Ca initially located in the disk (see values in Table 1). For each system, this amount is then distributed between *i* concentric rings according to the spatial discretisation chosen for the disk (*i. e.* , Δ_r; see Section 2.3.1). Preliminary results reported in Supporting Material 1 (S.M.1; available online) showed that the simulated data were no longer dependent on the number of the concentric rings when this number was above 8 (see Fig. S.M.1). These data were obtained by considering an interlayer diffusion coefficient equal to $5.0x10^{-12}$ $m^2{\cdot}s^{-1}$ (corresponding to the self-diffusion coefficient calculated by MD for Ca^{2+} when XCa = 1 for $Sr^{2+}$for-Ca^{2+} exchange; see Section section 3.1) and a % of Ca (normalised to sample CEC) released in solution at infinite time equal to 100%. According to these results, all subsequent calculations were performed by considering a spatial discretisation using 8 rings, corresponding to take a radial step of 0.3125 mm (Δ_r), with the whole reproducing the actual radius (i.e., 2.5 mm) of the particle used in the experiments. It should be noted that the initial amount of Ca present in each concentric ring was set up to keep a uniform concentration over the entire disk irrespective of the volume (surface in 2-D) of each ring. Then, using this method, the amount of initial Ca present in each ring varies in order to respect the variation of the surface between the different rings. Furthermore, it should be noted that considering an initial amount of Ca in the disk different from that calculated by assuming a full exchange at infinite time in some cases (see Table 1) can be viewed as an effect of a limitation existing at the clay/water interface due to too low of amounts of Na^+ or Sr^{2+} cations in the aqueous reservoir to exchange all Ca^{2+} cations at infinite time. Finally, whatever the diffusion time investigated and experiment simulated, the outer boundary condition of the disk (i.e., amount of Ca considered at the external part of the larger concentric ring) was set to zero, a value simulating an infinite dilution of the Ca released by the disk into a large aqueous reservoir.

3. Results and discussion

3.1. Simulation of molecular self-diffusion coefficients

Irrespective of the Ca^{2+}/Sr^{2+} and Ca^{2+}/Na^+ interlayer occupancies (i.e., XCa; see section 2.2.1) used to perform the GCMC simulations, two types of populations for the three types of cations investigated (i.e., Ca^{2+}, Sr^{2+} and Na^+) can be observed. Indeed, one cationic population is located in the middle plane of the interlayer (z-position close to 0 Å), while another one prevails close to the clay surface (at approximately 2 Å from the interlayer middle plane). This behaviour, in agreement with previous results (Tertre et al., 2015), is illustrated in Fig. 1B for the organization of Ca^{2+} and Sr^{2+} for XCa = 0.5 and for Ca^{2+} and Na^+ for XCa = 0.5, respectively. For each value of XCa tested, the self-diffusion coefficient of each cation was obtained from the averaged mean-squared displacements obtained over the different populations (see Fig. 1A). These values are reported as a function of XCa in Fig. 1C for Sr^{2+}/Ca^{2+} and Na^+/Ca^{2+}. Self-diffusion coefficients of both Ca^{2+} and Sr^{2+} cations can be considered as being independent of XCa during Sr^{2+}-for-Ca^{2+} exchange (see Fig. 1C) with average values (within one standard deviation) equal to $4.0 \pm 0.6x10^{-12}$ and $5.0 \pm 0.6x10^{-12}$ $m^2{\cdot}s^{-1}$ for Sr^{2+} and Ca^{2+}, respectively. On the other hand, during Na^+-for-Ca^{2+} exchange, the self-diffusion coefficient of Na^+ is divided by approximately a factor 2 when XCa increases from 0 to 1, with the self-diffusion coefficient of Ca^{2+} being for its part rather constant at $5.5 \pm 1.9x10^{-12}$ $m^2{\cdot}s^{-1}$ (see Fig. 1C). The latter value, up to the addition of its standard deviation, is in good agreement with the $8 \pm 1.2x10^{-12}$ $m^2{\cdot}s^{-1}$ average value proposed by Tertre et al. (2015) for Ca^{2+} in the interlayer of a similar bihydrated structure.

3.2. Comparison between experimental data and prediction of the finite-volume model

The finite-volume model proposed in this study is based only on a single diffusion coefficient (see Eq. 2 and definition of the Von Neumann stability criterion in section 2.3.1). Firstly, assumption is made that, irrespective of the pair of cations studied, exchange can be depicted by using a self-diffusion coefficient corresponding to the average value of the slowest cation present in the system (i.e., within the range of XCa investigated, Sr^{2+} in the Sr^{2+}-for-Ca^{2+} exchange and Ca^{2+} in the Na^+-for-Ca^{2+} exchange, see section 3.1). These assumptions suggest that the slowest interlayer cation controls the dynamics of ion-exchange between the interlayer of the swelling clay mineral and the aqueous reservoir. With this assumption, the interlayer diffusion coefficients *D* used in Eq. 2 are set to $4.0 \pm 0.6x10^{-12}$ and $5.5 \pm 1.9x10^{-12}$ $m^2{\cdot}s^{-1}$ (see Fig. 1C) to describe Sr^{2+}-for-Ca^{2+} and Na^+-for-Ca^{2+} exchanges, respectively. Calculations of radial diffusion by the finite-volume model accounting for both of the above diffusion coefficients and a uniform initial concentration of Ca in the disk (see Table 1) are compared to experimental data in Fig. 2A and B for the cases of Sr^{2+}-for-Ca^{2+} and Na^+-for-Ca^{2+} exchanges and for different salinities of the aqueous reservoir. It should be noted that logarithm representations are used in Fig. 2 to better analyse the entire time-range investigated. As expected, the % Ca released in solution increases with both the salinity of the aqueous reservoir and diffusion time. It should be noted that for the Sr^{2+}-for-Ca^{2+} experiment, a salinity reservoir equal to 10^{-2} mol/kg_{water} in $SrCl_2$ allows to reach a complete release in the aqueous solution of the confined calcium at infinite time, while for Na^+-for-Ca^{2+}, the complete release is obtained for a salinity of the aqueous reservoir dramatically higher at 1 mol/kg_{water} NaCl. This behaviour is in agreement with selectivity coefficients previously published and describing the adsorption of these cations in swelling clay minerals (Wild and Keay, 1964).

As far as the Sr^{2+}-for-Ca^{2+} exchange is concerned, a good agreement is obtained between experimental and predicted data irrespective of the salinity of the aqueous reservoir tested. Regarding the Na^+-for-Ca^{2+} exchange, a good agreement is also obtained for the lowest salinity condition (i.e., $3x10^{-3}$ mol/kg_{water}), whereas the model overestimates by approximately 20% and underestimates by approximately 15% the data measured for the intermediate (i.e., $5x10^{-2}$ mol/kg_{water}) and highest (i.e., 1 mol/kg_{water}) salinity conditions, respectively. Then, based on self-diffusion coefficients obtained by MD and selectivity coefficients classically obtained from "batch" data at equilibrium, the maximum difference between the experimental and simulated data is only 20%, which is very satisfying because the diffusion model makes the link between the molecular and millimetre-scale processes. This upscaling approach based on continuous equations and consisting of predicting the dynamics of the cation-exchange reaction at the macroscopic scale seems to be rather robust. In the following, the results from tests of sensitivity are presented to collect more insights into the parameters (i.e., self-diffusion coefficient and selectivity coefficient) controlling the dynamics of the macroscopic ion-exchange rates.

3.3. Sensitivity of the finite-volume model to the self-diffusion coefficients and selectivity coefficients applied for Na^+-for-Ca^{2+} exchange

Simulated data are dependent on the averaged values chosen for both self-diffusion and cation-exchange selectivity coefficients used as input parameters in the finite-volume model. In this section, the sensitivity of the simulated data to these two non-coupled coefficients is then discussed, especially by fixing one of the coefficients and by varying the other one. For self-diffusion, the calculations were performed for the Na^+-for-Ca^{2+} exchange because the self-diffusion coefficients of both Ca^{2+} and Sr^{2+} are almost the same considering the standard deviations associated with their mean values (i.e., Ca^{2+} with $5.0 \pm 0.6x10^{-12}$ and

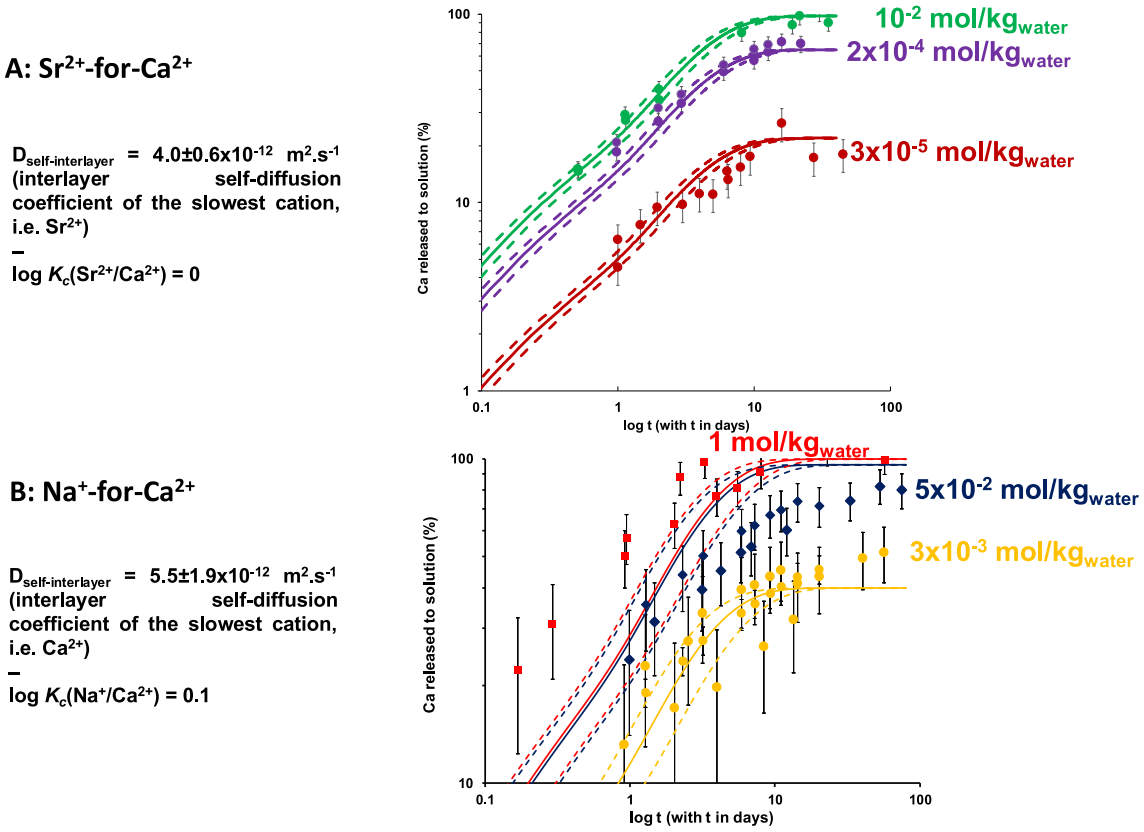


Fig. 2. Evolution over the diffusion time of the experimental % of Ca released in the solution normalised to the sample CEC (symbols) and compared with the simulations by the finite-volume model (solid and dashed lines). The average value over the XCa range of the self-diffusion coefficient of the slowest cation was used for the simulations. Solid lines report on calculations with this mean value, while dashed lines draw the envelope associated with coefficients defined up to their standard deviation. (A) Sr^{2+}-for-Ca^{2+}; (B) Na^{+}-for-Ca^{2+}.

Sr^{2+} with $4.0 \pm 0.6 \times 10^{-12}$ $m^2 \cdot s^{-1}$). In turn, this characteristic prohibits the detection of significant differences between data simulated by considering the average values of both cations or of the smallest ones (comparison not shown). Regarding selectivity coefficients, sensitivity calculations are also performed for the Na^{+}-for-Ca^{2+} exchange because the average value over the XCa range of the $\log K_c(Ca^{2+}/Sr^{2+})$ allows for interpreting the dynamics of the Sr^{2+}-for-Ca^{2+} exchange in millimetre disks for all salinity conditions investigated. It is however reminded that the average value of the $\log K_c(Na^{+}/Ca^{2+})$ overestimates by approximately 20% the experimental data obtained for intermediate salinity conditions (i.e., 5×10^{-2} mol/kg_{water}) (see discussion in Section 3.2).

3.3.1. *Sensitivity to self-diffusion coefficients*

For the 1 mol/kg_{water} NaCl condition, a maximum deviation between experimental and simulated data of 15% (see Fig. 2B) can be observed, especially for short diffusion times (i.e., <2 days). This part of the simulated curve is highly sensitive to the self-diffusion coefficient used in the calculation. This value was previously assumed to be equal to the average value of the self-diffusion coefficient of the slowest cation (i.e., Ca^{2+}) involved in the studied system over the entire XCa range investigated (i.e., $5.5 \pm 1.9 \times 10^{-12}$ $m^2 \cdot s^{-1}$). To test the sensitivity of the simulated data to this parameter, two additional calculations were performed for the 1 mol/kg_{water} and 3×10^{-3} mol/kg_{water} salinity conditions by using self-diffusion coefficients equal to 1.3×10^{-11} and 2.1×10^{-11} $m^2 \cdot s^{-1}$. The value of 1.3×10^{-11} corresponds to averaging between the diffusion coefficients of both Ca^{2+} and Na^{+} over the XCa range, while the value 2.1×10^{-11} corresponds to averaging the diffusion of the most mobile cation (i.e., Na^{+} in this case) over the XCa range (see Fig. 1C). The comparison between the simulated curves and experimental data is presented in Fig. 3. On the one hand, the self-diffusion

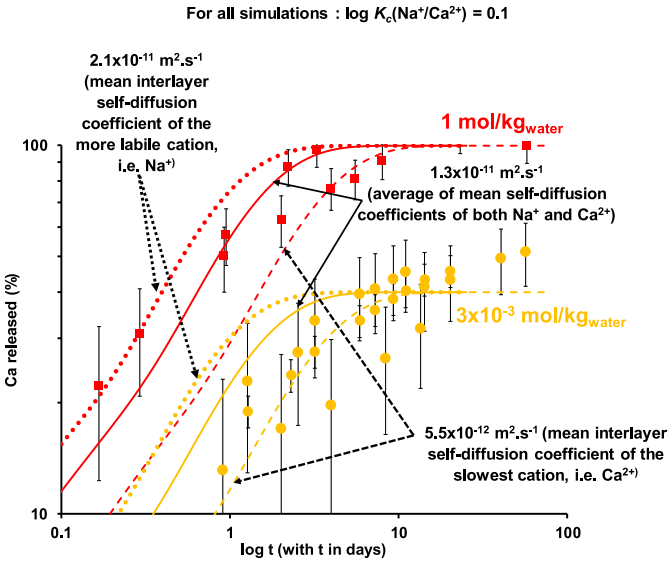


Fig. 3. Effect of the self-diffusion coefficient value used in the finite-volume model to predict Na^{+}-for-Ca^{2+} dynamic exchange with millimetre disks. Simulated data (lines) are performed for the 1 mol/kg_{water} and 3×10^{-3} mol/kg_{water} NaCl conditions and are compared to the experimental data (symbols).

coefficient equal to 1.3×10^{-11} $m^2 \cdot s^{-1}$ is able to interpret experimental data obtained with 1 mol/kg_{water} and 3×10^{-3} mol/kg_{water} salinity conditions (by accounting for uncertainties in the experimental data) for all diffusion times investigated. On the other hand, the value of 2.1×10^{-11}

$m^2 \cdot s^{-1}$ interprets experimental data obtained for the 1 mol/kg_{water} salinity condition at short times but not at intermediate times (i.e., a few days), and it systematically overestimates the data measured for the $3x10^{-3}$ mol/kg_{water} salinity condition at diffusion times smaller than a few days (see Fig. 3). Therefore, choosing the $1.3x10^{-11}$ $m^2 \cdot s^{-1}$ value, corresponding to the average value of the self-diffusion coefficients of both cations, appears to be the best option to interpret the entire set of experimental data for all of the salinities experienced in the aqueous reservoir.

These results highlight that for an exchange involving two cations with significantly different molecular mobilities, the average value of both interlayer diffusion coefficients, irrespective of the XCa value, is certainly the best compromise. However, it worth noting that interlayer diffusion coefficients of both Ca^{2+} and Na^+ only differ by a factor of 2.3. In the case of competitions between other types of cations such as Cs^+ and Na^+ for which mobility contrast is enhanced due to significant variation in the interlayer structures of the two-end members (Bourg and Sposito, 2010; Porion et al., 2015 among others), the average value could eventually render flawed results.

3.3.2. *Sensitivity to the selectivity coefficient*

In section 3.2, calculations were performed by considering that the selectivity coefficient describing ion-exchange in the interlayer of vermiculite was independent of both the particle size and the physico-chemical parameters (e.g., compositions of both the clay interlayer and aqueous composition at equilibrium). It should be noted however, that even though this parameter was found to be independent of the size fraction in the case of the Sr^{2+}-for-Ca^{2+} for three size fractions (i.e., 0.1–0.2, 1–2 and 10–20 μm; Dzene et al., 2016), the question of variability with the particle size remains in the case of the Na^+-for-Ca^{2+} exchange since the authors (Tertre et al., 2013) worked only on a < 150 μm size fraction. To assess the validity of such an assumption, additional data were obtained in this present study in batch experiments with a coarser size fraction of vermiculite (i.e., 50–150 μm). These data were obtained by following a methodology detailed in Tertre et al. (2011) and are reported in S.M.2 with the associated interpretation. These data allow for confirming the independence of the interlayer selectivity coefficient in the case of the Na^+-for-Ca^{2+} exchange with the particle size (i.e., $\log K_c(Na^+/Ca^{2+}) = 0.1$ using the Gaines Thomas convention). In addition, these data also show that a high uncertainty exists in the $\log K_c(Na^+/Ca^{2+})$ value for physicochemical conditions close to homoionic solution (i.e., for $\{Na^+\}_{aq.} > 0.999$ with $\{Na^+\}_{aq.}$ the equivalent fraction of Na^+ in solution at equilibrium) since a range of $\log K_c(Na^+/Ca^{2+})$ values from 0.1 to 1.3 is able to interpret experimental data for such conditions (see details in S.M.2). This behaviour differs from that considering a unique selectivity coefficient value to predict Ca^{2+}-for-Na^+ interlayer exchange, irrespective of the physicochemical conditions used (e.g., for $0 < \{Na^+\}_{aq.} < 1$).

In Fig. 4, the prediction of the finite-volume model parameterized with the highest possible interlayer selectivity coefficient (i.e., $\log K_c(Na^+/Ca^{2+}) = 1.3$) describing Ca^{2+}-for-Na^+ exchange in "batch conditions" when $\{Na\}_{aq.} > 0.999$ (corresponding to the $5x10^{-2}$ mol/kg_{water} NaCl condition in this study) is compared to the experimental data. Calculations were performed by considering the average self-diffusion coefficient of the slowest cation in the whole XCa range (i.e., Ca^{2+} with $D_{self\text{-}interlayer} = 5.5x10^{-12}$ $m^2 \cdot s^{-1}$), as for the data reported in Fig. 2. In Fig. 4, a good agreement can be observed between experimental and simulated data for this $\{Na\}_{aq.} > 0.999$ condition. This behaviour confirms the observation previously discussed regarding the limitation associated with the use of the same selectivity coefficient to describe the ion-exchange reaction irrespective of the physico-chemical conditions. This limitation is emphasized, especially when the system is close to that of homoionic solid and aqueous phases and even for a pair of cations allowed to maintain the same interlayer hydration during ion-exchange reactions (i.e., by-hydrated structure in our case). Furthermore, for the 1 M NaCl condition, simulated data using a $\log K_c(Na^+/Ca^{2+})$ value equal to 1.3 are perfectly superimposed to those simulated with the average selectivity coefficient previously tested (i.e., $\log K_c(Na^+/Ca^{2+}) = 0$) (see Fig. 4). For their part, experimental data obtained at the lowest salinity (i.e., $3x10^{-3}$ mol/kg_{water}) can be interpreted only by relying upon an average selectivity coefficient value of $\log K_c(Na^+/Ca^{2+}) = 0.1$. This observation is in agreement with the usual methodology reputed to lower uncertainties (Tournassat et al., 2007; Tertre et al., 2011) and consistent to obtain selectivity coefficients for systems far removed from homoionic conditions (in both solid and aqueous phases).

These sensitivity calculations confirm the robustness of the approach proposed in this work, employing an average selectivity coefficient between the two cations over the XCa range investigated under the acceptation that a maximum deviation of 20% between experimental and simulated data is tolerable. It is worth noting that these sensitivity calculations, based on the consideration of a unique selectivity coefficient, fully ignore potential effects related to the release of Ca^{2+} cations in the aqueous reservoir due to the ongoing ion-exchange process. This is an implicit property of the simple model used here, in contrast to existing more sophisticated coupled models, which would likely lead to

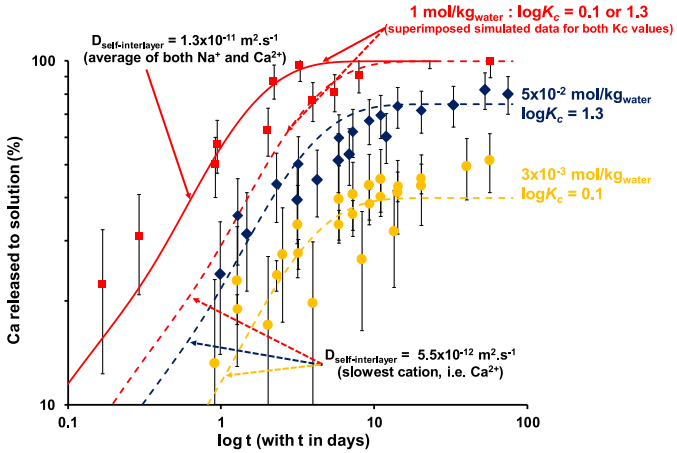


Fig. 4. Effects of a $\log K_c(Na^+/Ca^{2+})$ equal to 1.3 (i.e., the highest possible selectivity coefficient interpreting batch data for $\{Na\}_{aq.} > 0.999$; see Fig. S.M.2B and details in S.M.2) on simulations of exchange rates versus the diffusion time via the finite-volume model for disks immersed in $5x10^{-2}$ mol/kg_{water} NaCl solution. Dots correspond to experimental data (Fig. 2). All dashed lines represent simulated data using the average self-diffusion coefficient of the slowest cation in the entire XCa range (i.e., Ca^{2+} with $D_{self\text{-}interlayer} = 5.5x10^{-12}$ $m^2 \cdot s^{-1}$). The solid line reports simulated data for the 1 mol/kg_{water} salinity condition using a self-diffusion coefficient as the mean between mean coefficients of both Na^+ and Ca^{2+} (i.e., $1.3x10^{-11}$ $m^2 \cdot s^{-1}$; see text for details).

an overestimation of the calculated ion-exchange rate compared to experimental data. As seen from the good agreement between the experiments and simulations, this effect is likely to be considered as marginal for the experimental conditions used here.

4. Concluding remarks and perspectives

The results obtained in this study showed that self-diffusion coefficients obtained by molecular dynamic simulations can successfully be used to interpret cation-exchange laboratory experiments despite the large gap, in terms of timescale, between the two methods. Moreover, this study allowed to assess with a finite-volume model based on a continuous diffusion equation and a single diffusion coefficient the role played by both self-diffusion coefficients and selectivity coefficients in the dynamics of the ion-exchange reaction between the interlayer of individual swelling clay mineral particles and aqueous reservoirs characterized by contrasted chemical compositions. The results showed that the dynamics of a macroscopic exchange was mainly ruled by the interlayer mobility of the slowest cation in the ion-exchange investigated. Cation-exchange selectivity coefficient appeared to be independent of the particle size when the hydration state of the clay particle interlayer is kept constant during the exchange reaction. This behaviour was previously reported in the case of Sr^{2+}-for-Ca^{2+} exchange in batches for three vermiculite size fractions (0.1–0.2, 1–2 and 10–20 μm; Dzene et al., 2016)). It was extended here to the Ca^{2+}-for-Na^{+} exchange, with data obtained using a < 150 μm size fraction able to interpret data obtained with millimetre particles. This notwithstanding, sensitivity calculations showed a noticeable uncertainty in the selectivity coefficient for conditions close to a homoionic system (in both solid and aqueous phases). Consequently, even for two cations preserving the structure of the interlayer space during their exchange in water saturated conditions, using a unique selectivity coefficient to describe the ion-exchange reaction irrespective of the chemical composition of the system remains questionable. Finally, MD simulations showed that the self-diffusion coefficient of an interlayer cation could vary as a function of its occupancy in the interlayer (i.e., the case of Na^{+} in the present study). These data can be, at least qualitatively, interesting for reactive transport models coupling chemistry to transport in order to assess the role played by the different parameters in the global diffusion process investigated.

The interpretation raised from this study were based using a large range of salinities for the aqueous reservoir (from approximately a few 10^{-5} to 1 mol/kg_{water}) and for two pairs of cations differing by their charge (i.e., divalent/divalent cations and monovalent/divalent cations) allowing to keep the interlayer structure unchanged during exchange (i.e., by-hydrated structure in water saturated conditions). Then, possible perspective of this work could be related to the study of the exchange for a cationic duo inducing a change in the structure (e.g, hydration state) of the interlayers of vermiculite during ion-exchange reactions (e.g., Cs^{+}-for-Na^{+}; Dzene et al., 2015, 2017), thus impacting then self-diffusion and selectivity coefficients. Furthermore, extension of the proposed model to other types of swelling clay minerals, as smectites, would likely imply to change the input parameters, such as self-diffusion coefficients and selectivity coefficients, due to the different layer charges of these minerals. This modelling approach could thus help in assessing the role played by layer charge on the kinetics of cation-exchange process, especially for smectites for which the experiments as those proposed in this study are impossible due to their small particle sizes. Finally, the results obtained in this present study here, for diluted systems (i.e., low solid/solution ratio), could be taken into account in reactive transport models devoted to simulating ion-exchange reactions during the diffusion of cations in porous clay media (i.e., high solid/solution ratio), for which the proportion of interlayer porosity can be known.

Declaration of Competing Interest

The authors declare that they have no known competing financial interests or personal relationships that could have appeared to influence the work reported in this paper.

Acknowledgements

Hugo Petit (IC2MP/HydrASA, Poitiers, France) is thanked for his experimental contribution to the Ca^{2+}-for-Na^{+} isotherm measurement performed with the 50-150 μm size fraction. The authors are grateful to the EC2CO CNRS/INSU BIOHEFECT project (Project DIFFMATARG) and the European Union (ERDF) and “Région Nouvelle Aquitaine” for providing the financial support for this study.

Appendix A. Supplementary data

Supplementary data to this article can be found online at https://doi.org/10.1016/j.clay.2020.105913.

References

Aaqvist, J., 1990. Ion-water interaction potentials derived from free energy perturbation simulations. J. Phys. Chem. 94, 8021–8024. https://doi.org/10.1021/j100384a009.
Allen, M.P., Tildesley, D.J., 1994. Computer Simulation of Liquids. Clarendon Press, Oxford.
Appelo, C.A.J., Wersin, P., 2007. Multicomponent diffusion modeling in clay systems with application to the diffusion of tritium, iodide, and sodium in Opalinus clay. Environ. Sci. Technol. 41, 5002–5007. https://doi.org/10.1021/es0629256.
Appelo, C.A.J., Van Loon, L.R., Wersin, P., 2010. Multicomponent diffusion of a suite of tracers (HTO, Cl, Br, I, Na, Sr, Cs) in a single sample of Opalinus clay. Geochim. Cosmochim. Acta 74, 1201–1219. https://doi.org/10.1016/j.gca.2009.11.013.
Argüelles, A., Leoni, M., Blanco, J.A., Marcos, C., 2010. Semi-ordered crystalline structure of the Santa Olalla vermiculite inferred from X-ray powder diffraction. Am. Mineral. 95, 126–134. https://doi.org/10.2138/am.2010.3249.
Berendsen, H.J.C., Postma, J.P.M., Van Gunsteren, W.F., DiNola, A., Haak, J.R.J., 1984. Molecular dynamics with coupling to an external bath. J. Chem. Phys. 81, 3684–3690. https://doi.org/10.1063/1.448118.
Birgersson, M., Karnland, O., 2009. Ion equilibrium between montmorillonite interlayer space and an external solution – Consequences for diffusional transport. Geochim. Cosmochim. Acta 73, 1908–1923. https://doi.org/10.1016/j.gca.2008.11.027.
Bourg, I.C., Sposito, G., 2010. Connecting the molecular scale to the continuum scale for diffusion processes in smectite-rich poroux media. Environ. Sci. Techn. 44, 2085–2091. https://doi.org/10.1021/es903645a.
Bourg, I.C., Bourg, A.C.M., Sposito, G., 2003. Modeling diffusion and adsorption in compacted bentonite: a critical review. J. Contam. Hydrol. 61, 293–302. https://doi.org/10.1016/S0169-7722(02)00128-6.
Charlet, L., Alt-Epping, P., Wersin, P., Gilbert, B., 2017. Diffusion transport and reaction in clay rocks: a storage (nuclear waste, CO_2, H_2), energy (shale gas) and water quality issue. Adv. Water Res. 106, 39–59. https://doi.org/10.1016/j.advwatres.2017.03.019.
Charney, J.G., Fjortoft, R., Von Neumann, J., 1950. Numerical integration of the barometric vorticity equation. Tellus 2, 237–254. https://doi.org/10.1111/j.2153-3490.1950.tb00336.x.
Cygan, R.T., Liang, J.J., Kalinichev, A.G., 2004. Molecular models of hydroxide, oxyhydroxide and clay phases and the development of a general force field. J. Phys. Chem. B 108, 1255–1266. https://doi.org/10.1021/jp0363287.
Dabat, T., Porion, P., Hubert, F., Paineau, E., Dazas, B., Grégoire, B., Tertre, E., Delville, A., Ferrage, E., 2020. Influence of preferred orientation of clay particles on the diffusion of water in kaolinite porous media at constant porosity. Appl. Clay Sci. https://doi.org/10.1016/j.clay.2019.105354. In press.
Davies, C.W., 1962. Ion Association. Butterworth, London.
de la Calle, C., Suquet, H., 1988. Vermiculite. In: Bailey, S.W. (Ed.), Hydrous Phyllosilicates (Exclusive of Micas), Reviews in Mineralogy Volume, vol. 19. Mineralogical Society of America, Chantilly, VA, pp. 455–496.
Delville, A., 1991. Modeling the clay-water interface. Langmuir 7, 547–555. https://doi.org/10.1021/la00051a022.
Dzene, L., Tertre, E., Hubert, F., Ferrage, E., 2015. Nature of the sites involved in the process of cesium desorption from vermiculite. J. Colloid Interface Sci. 455, 254–260. https://doi.org/10.1016/j.jcis.2015.05.053.
Dzene, L., Ferrage, E., Hubert, F., Delville, A., Tertre, E., 2016. Experimental evidence of the contrasting reactivity of external vs. interlayer adsorption sites on swelling clay minerals: the Case of Sr^{2+}-for-Ca^{2+} exchange in vermiculite. Appl. Clay Sci. 132-133, 205–215. https://doi.org/10.1016/j.clay.2016.06.007.
Dzene, L., Verron, H., Delville, A., Michot, L.J., Robert, J.L., Tertre, E., Hubert, F., Ferrage, E., 2017. Influence of tetrahedral layer charge on the fixation of cesium in synthetic smectite. J. Phys. Chem. C 121, 23422–23435. https://doi.org/10.1021/acs.jpcc.7b06308.
Ferrage, E., Sakharov, B.A., Michot, L.J., Delville, A., Bauer, A., Lanson, B., Grangeon, S., Frapper, G., Jiménez-Ruiz, M., Cuello, G.J., 2011. Hydration properties and interlayer organization of water and ions in synthetic Na-smectite with tetrahedral layer charge. Part 2. Toward a precise coupling between molecular simulations and

diffraction data. J. Phys. Chem. C 115, 1867–1881. https://doi.org/10.1021/jp105128r.
Gaines, G.L., Thomas, H.C., 1953. Adsorption studies on clay minerals. II. A formulation of the thermodynamics of exchange adsorption. J. Chem. Phys. 21, 714. https://doi.org/10.1063/1.1698996.
Glaus, M.A., Baeyens, B., Bradbury, B., Jakob, A., Van Loon, L.R., Yaroshchuk, A., 2007. Diffusion of ^{22}Na and ^{85}Sr in montmorillonite: evidence of interlayer diffusion being the dominant pathway at high compaction. Environ. Sci. Technol. 41, 478–485. https://doi.org/10.1021/es061908d.
Heyes, D.M., 1994. Pressure tensor of partial-charge and point-dipole lattices with bulk and surface geometries. Phys. Rev. B Cond. Matt. 49, 755–764. https://doi.org/10.1103/PhysRevB.49.755.
Johnson, J.W., Oelkers, E.H., Helgeson, H.C., 1992. SUPCRT92: a software package for calculating the standard molars thermodynamic properties of minerals, gases, aqueous species and reactions from 1 to 5000 bars and 0 to 1000°C. Comput. Geosci. 18, 899–947. https://doi.org/10.1016/0098-3004(92)90029-Q.
Jougnot, D., Revil, A., Leroy, P., 2009. Diffusion of ionic tracers in the Callovo-Oxfordian clay–rock using the Donnan equilibrium model and the formation factor. Geochim. Cosmochim. Acta 73, 2712–2726. https://doi.org/10.1016/j.gca.2009.01.035.
Lajunen, L.H.J., Peramaki, P., 2004. Spectrochemical Analysis by Atomic Absorption and Emission. Cambridge Royal Society of Chemistry.
Marry, V., Turcq, P., 2003. Microscopic simulations of interlayer structure and dynamics in bihydrated heteroionic montmorillonites. J. Phys. Chem. B 107, 1832–1839. https://doi.org/10.1021/jp022084z.
Michot, L.J., Ferrage, E., Jimenez-Ruiz, M., Boehm, M., Delville, A., 2012. Anisotropic features of water and ion dynamics in synthetic Na- and Ca-smectites with tetrahedral layer charge. A combined quasi-elastic neutron-scattering and molecular dynamics simulations study. J. Phys. Chem. C 116, 16619–16633. https://doi.org/10.1021/jp304715m.
Ngouana Wakou, B.F., 2014. Modélisation moléculaire de l'hydratation, de la Structure, et de la mobilité des Ions et de l'eau dans l'espace Interfoliaire et à la Surface d'une argile smectitique (Ph.D. Thesis from Ecole des Mines de Nantes (in French)).
Parkhurst, D.L., Appelo, C.A.J., 1999. Phreeqc2 User's Manual and Program, US Geological Survey. Available at: https://www.usgs.gov/software/phreeqc-version-3.
Parkhurst, D.L., Appelo, C.A.J., 2013. Description of Input and Examples for PHREEQC Version 3 - a Computer Program for Speciation, Batch-Reaction, One-Dimensional Transport, and Inverse Geochemical Calculations. U.S. Geological Survey Techniques and Methods. book 6, chap. A43, 497 p., available at. http://pubs.usgs./gov/tm/06/a43/.
Plimpton, S., 1995. Fast parallel algorithms for short-range molecular dynamics. J. Comp. Phys. 117, 1–19. https://lammps.sandia.gov.
Porion, P., Warmont, F., Faugère, A.M., Rollet, A.L., Dubois, E., Marry, V., Michot, L.J., Delville, A., 2015. 133Cs nuclear magnetic resonance relaxometry as a probe of the mobility of cesium cations confined within dense clay sediments. J. Phys. Chem. C 119, 15360–15372. https://doi.org/10.1021/acs.jpcc.5b03880.
Reed, M.G., Scott, A.D., 1962. Kinetics of potassium release from biotite and muscovite in sodium tetraphenylboron solutions. Soil Sci. Soc. Proc. 26, 437–440.
Steefel, C.I., Appelo, C.A.J., Arora, B., Jacques, D., Kalbacher, T., Kolditz, O., Lagneau, V., Lichtner, P.C., Mayer, K.U., Meeussen, J.C.L., Molins, S., Moulton, D., Shao, H., Simunek, J., Spycher, N., Yabusaki, S.B., Yeh, G.T., 2015. Reactive transport codes for subsurface environmental simulation. Comput. Geosci. 19, 445–478. https://doi.org/10.1007/s10596-014-9443-x.
Tachi, Y., Yotsuji, K., 2014. Diffusion and sorption of Cs+, Na+, I- and HTO in compacted sodium montmorillonite as a function of porewater salinity: integrated sorption and diffusion model. Geochim. Cosmochim. Acta 132, 75–93. https://doi.org/10.1016/j.gca.2014.02.004.
Tachi, Y., Yotsuji, K., Suyama, T., Ochs, M., 2014. Integrated sorption and diffusion model for bentonite. Part 2. Porewater chemistry, sorption and diffusion modeling in compacted systems. J. Nucl. Sci. Technol. 51, 1–14. https://doi.org/10.1080/00223131.2014.914453.
Tertre, E., Prêt, D., Ferrage, E., 2011. Influence of the ionic strength and solid/solution ratio on Ca(II)-for-Na^+ exchange in montmorillonite. Part 1: Chemical measurements, thermodynamic modeling and implications for trace elements geochemistry. J. Colloid Interface Sci. 353, 248–256. https://doi.org/10.1016/j.jcis.2010.09.039.
Tertre, E., Hubert, F., Bruzac, S., Pacreau, M., Ferrage, E., Prêt, D., 2013. Ion-exchange reactions on clay minerals coupled with advection/dispersion processes. Application to Na^+/Ca^{2+} exchange on vermiculite: Reactive-transport modeling, batch and stirred flow-through reactor experiments. Geochim. Cosmochim. Acta 112, 1–19. https://doi.org/10.1016/j.gca.2013.02.028.
Tertre, E., Delville, A., Prêt, D., Hubert, F., Ferrage, E., 2015. Cation diffusion in the interlayer space of swelling clay minerals - a combined macroscopic and microscopic study. Geochim. Cosmochim. Acta 149, 251–267. https://doi.org/10.1016/j.gca.2014.10.011.
Tinnacher, R.M., Holmboe, M., Tournassat, C., Bourg, I.A., Davis, J.A., 2016. Ion adsorption and diffusion in smectite: molecular, pore and continuum scale views. Geochim. Cosmochim. Acta 177, 130–149. https://doi.org/10.1016/j.gca.2015.12.010.
Tournassat, C., Steefel, C.I., 2015. Ionic transport in nanoporous clays with consideration of electrostatic effects. Rev. Mineral. Geochem. 80, 287–330. https://doi.org/10.2138/rmg.2015.80.09.
Tournassat, C., Steefel, C.I., 2019. Modeling diffusion processes in the presence of a diffuse layer at charged mineral surfaces: a benchmark exercise. Comput. Geosci. https://doi.org/10.1007/s10596-019-09845-4.
Tournassat, C., Gailhanou, H., Crouzet, C., Braibant, G., Gautier, A., Lassin, A., Blanc, P., Gaucher, E.C., 2007. Two cation exchange models for direct and inverse modelling of solution major cation composition in equilibrium with illite surfaces. Geochim. Cosmochim. Acta 71, 1098–1114. https://doi.org/10.1016/j.gca.2006.11.018.
Tournassat, C., Chapron, Y., Leroy, P., Boulahya, F., 2009. Comparison of molecular dynamics simulations with triple layer and modified Gouy-Chapman models in a 0.1 M NaCl –montmorillonite system. J. Colloid Interface Sci. 339, 533–541. https://doi.org/10.1016/j.jcis.2009.06.051.
Walker, G.G., 1961. Vermiculite Minerals. Ch. 7 in the X-ray Identification and Crystals Structures of Clay Minerals (G. Brown, ed.). Mineralogical Society, London.
Wild, A., Keay, J., 1964. Cation exchange equilibria with vermiculite. J. Soil Sci. 15, 135–144. https://doi.org/10.1111/j.1365-2389.1964.tb02214.x.

Appendix 3: Article: Water and Ion Dynamics in Confined Media: A Multi-Scale Study of the Clay/Water Interface

Patrice Porion, Ali Asaad, Thomas Dabat, Baptiste Dazas, Alfred Delville, Eric Ferrage, Fabien Hubert, Mónica Jiménez-Ruiz, Laurent J. Michot, Sébastien Savoye, and Emmanuel Tertre

colloids and interfaces

MDPI

Review

Water and Ion Dynamics in Confined Media: A Multi-Scale Study of the Clay/Water Interface

Patrice Porion [1,*], Ali Asaad [2], Thomas Dabat [2], Baptiste Dazas [2], Alfred Delville [1,*], Eric Ferrage [2], Fabien Hubert [2], Mónica Jiménez-Ruiz [3], Laurent J. Michot [4], Sébastien Savoye [5] and Emmanuel Tertre [2]

1 Interfaces, Confinement, Matériaux et Nanostructures (ICMN), UMR 7374, CNRS, Université d'Orléans, 1b Rue de la Férollerie, CS 40059, CEDEX 2, F-45071 Orléans, France
2 IC2MP, UMR 7285, CNRS, Université de Poitiers, 5 Rue Albert Turpain, Bât. B8, TSA 51106, CEDEX 9, F-86073 Poitiers, France; ali.asaad@univ-poitiers.fr (A.A.); thomas.dabat@univ-poitiers.fr (T.D.); baptiste.dazas@univ-poitiers.fr (B.D.); eric.ferrage@univ-poitiers.fr (E.F.); fabien.hubert@univ-poitiers.fr (F.H.); emmanuel.tertre@univ-poitiers.fr (E.T.)
3 Institut Laue-Langevin, 71 Avenue des Martyrs, CS 20156, CEDEX 9, F-38042 Grenoble, France; jimenez@ill.fr
4 Laboratoire PHENIX, UMR 8234, CNRS, Sorbonne Université, UPMC, 4 Place Jussieu, CEDEX 5, F-75252 Paris, France; laurent.michot@sorbonne-universite.fr
5 Université Paris-Saclay, CEA, Service d'Etude du Comportement des Radionucléides, F-91191 Gif-sur-Yvette, France; sebastien.savoye@cea.fr
* Correspondence: patrice.porion@cnrs-orleans.fr (P.P.); alfred.delville@cnrs-orleans.fr (A.D.)

Abstract: This review details a large panel of experimental studies (Inelastic Neutron Scattering, Quasi-Elastic Neutron Scattering, Nuclear Magnetic Resonance relaxometry, Pulsed-Gradient Spin-Echo attenuation, Nuclear Magnetic Resonance Imaging, macroscopic diffusion experiments) used recently to probe, over a large distribution of characteristic times (from pico-second up to days), the dynamical properties of water molecules and neutralizing cations diffusing within clay/water interfacial media. The purpose of this review is not to describe these various experimental methods in detail but, rather, to investigate the specific dynamical information obtained by each of them concerning these clay/water interfacial media. In addition, this review also illustrates the various numerical methods (quantum Density Functional Theory, classical Molecular Dynamics, Brownian Dynamics, macroscopic differential equations) used to interpret these various experimental data by analyzing the corresponding multi-scale dynamical processes. The purpose of this multi-scale study is to perform a bottom-up analysis of the dynamical properties of confined ions and water molecules, by using complementary experimental and numerical studies covering a broad range of diffusion times (between pico-seconds up to days) and corresponding diffusion lengths (between Angstroms and centimeters). In the context of such a bottom-up approach, the numerical modeling of the dynamical properties of the diffusing probes is based on experimental or numerical investigations performed on a smaller scale, thus avoiding the use of empirical or fitted parameters.

Keywords: dynamics; interface; clay; Inelastic and Quasi-Elastic Neutron Scattering; Nuclear Magnetic Resonance relaxometry; Pulsed-Gradient Spin-Echo attenuation; Magnetic Resonance Imaging; macroscopic diffusion experiments; self-diffusion coefficient; multi-scale modeling

check for updates

Citation: Porion, P.; Asaad, A.; Dabat, T.; Dazas, B.; Delville, A.; Ferrage, E.; Hubert F.; Jiménez-Ruiz, M.; Michot, L.J.; Savoye, S.; Tertre, E. Water and Ion Dynamics in Confined Media: A Multi-Scale Study of the Clay/Water Interface. *Colloids Interfaces* **2021**, *5*, 34. https://doi.org/10.3390/colloids5020034

Academic Editors: Giuseppe Loglio and Reinhard Miller

Received: 18 March 2021
Accepted: 9 June 2021
Published: 15 June 2021

Publisher's Note: MDPI stays neutral with regard to jurisdictional claims in published maps and institutional affiliations.

Copyright: © 2021 by the authors. Licensee MDPI, Basel, Switzerland. This article is an open access article distributed under the terms and conditions of the Creative Commons Attribution (CC BY) license (https://creativecommons.org/licenses/by/4.0/).

1. Introduction

Among colloids, clays are ubiquitous materials exhibiting a large variety of physico-chemical properties, such as adsorption of water and polar molecules [1–3], high specific surface area [3], electric surface charge [3], swelling [4], gelling [5], thixotropy, and surface acidity exploited in numerous industrial processes, including waste storing [6,7], cosmetic and paint industries, drilling, cracking, and heterogeneous catalysis [8]. Optimizing these various applications requires a detailed analysis of the impact of the clay composition on the dynamical processes implied in these applications. For that purpose, numerous dynamical studies have been performed to probe, over a broad dynamical range, the mobility of

ions [9,10] and molecules [11–13] physisorbed at the clay/water interface. As illustrated in Figure 1, we selected to use a complementary set of experiments, including Inelastic Neutron Scattering (INS) [14–19], Quasi-Elastic Neutron Scattering (QENS) [12,20–30], Nuclear Magnetic Resonance (NMR) relaxometry [31–49], Pulsed-Gradient Spin-Echo (PGSE) attenuation [11,50–52], Magnetic Resonance Imaging (MRI) [51], and macroscopic diffusion experiments as Out-Diffusion (OD) [53,54] or Through-Diffusion (TD) [55] experiments, because they probe complementary time-scales (see Figure 1). These experiments allow investigating a broad dynamical range (from few pico-seconds to few days) and quantifying the impact of the clay/water interface on the dynamics of the interfacial molecular and ionic probes.

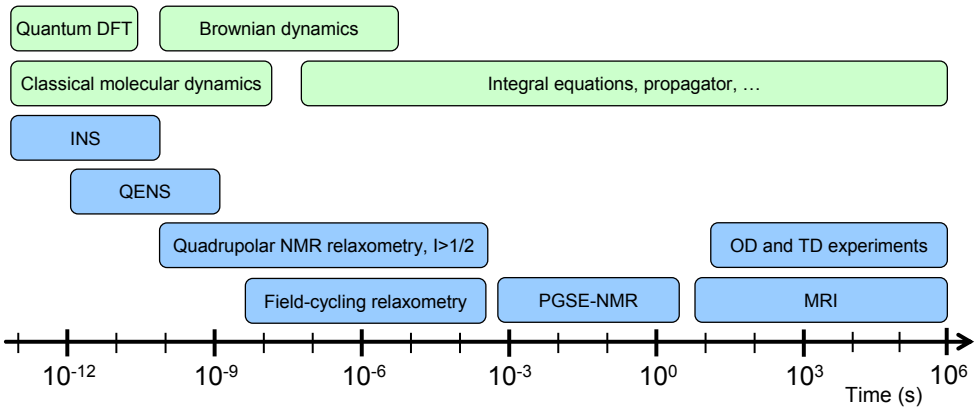


Figure 1. Schematic view of the time-scales probed by the various experimental methods (blue) and the numerical modeling (green).

Furthermore, as illustrated in Figure 2, the use of swelling clays, such as Na^+-saturated montmorillonite, allows probing a broad range of interlayer separations [4] varying between a limited number of hydration layers for layer-to-layer distances smaller than 20 Å, in the so-called crystalline swelling regime [2,56,57], and a large continuum of layer-to-layer distances (between 40 Å and 70 Å), in the so-called osmotic swelling regime. By contrast, Ca^{2+}-saturated montmorillonite only exhibits crystalline swelling (see Figure 2) because inter-ionic correlation forces strongly reduce the swelling pressure of these charged interfaces [58,59]. For that reason, these dynamical experiments require the use of purified clay samples to avoid coexistence of swollen and unswollen phases within heterogeneous samples.

For that purpose, some of the dynamical studies presented here were performed with synthetic clays (laponite and saponite) in order to avoid impurities within the clay network. In the case of natural clays (kaolinite, beidellite, and vermiculite), the samples were purified according to standard procedures [60] and size separated by centrifugation. Under such conditions, clay/water interfaces are well characterized systems and ideal to investigate the influence of charged interfaces on the thermodynamical and dynamical properties of confined fluids.

Finally, numerical modeling is required to relate the organization of these clay/water interfaces and the dynamical information extracted from the various experimental data obtained by INS, QENS, PGSE, MRI, and macroscopic diffusion experiments (see Figure 1). In that context, an atomic description of the clay/water interface is required for modeling the structural and dynamical properties of these interfacial systems probed in the crystalline swelling regime. For that purpose, quantum calculations are used to directly determine the dynamical properties of confined ions and water molecules by using ab initio DFT quantum methods [61,62]. Quantum calculations are also useful to evaluate atomic properties of the clay network, such as atomic partial charges, by using semi-empirical [63] or ab initio [64] quantum calculations. These parameters are further exploited in classical statistical treatments of the clay/water interfaces by using classical Monte Carlo (MC) simulations and Molecular Dynamics (MD) to investigate the structural and dynam-

ical properties of the confined ions and water molecules within the crystalline swelling regime [2,12,17,28,40,41,46,63–66]. By contrast, in the so-called osmotic regime, one may easily neglect the atomic structure of the clay network and the solvent molecules by using classical Brownian Dynamics (BD) in order to determine the effective mobility [67] of the neutralizing counterions in the presence of structureless charged surfaces [68]. In the same context, numerical integration of differential equations can also be used to study the mobility of diffusing probes at the macroscopic scale (Refs. [54,69], and references therein).

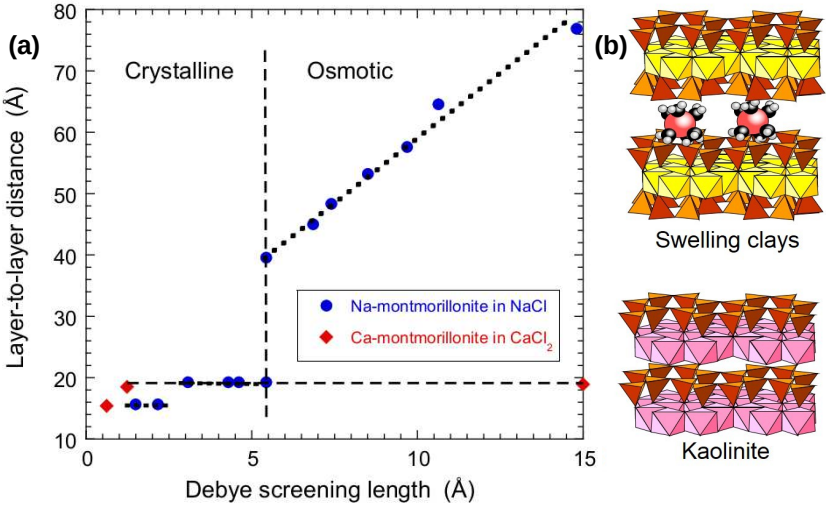


Figure 2. (**a**) X-ray diffraction measurements of the swelling of montmorillonite neutralized either by Na^+ (blue) or by Ca^{2+} (red) counterions and dispersed, respectively, in NaCl or $CaCl_2$ aqueous solutions. The data are issue from Ref. [4]; (**b**) Structures of kaolinite and swelling clays (montmorillonite, laponite, saponite, beidellite, and vermiculite).

In the present review, these techniques are described following a path of increasing probed time-scales, together with the associated numerical methods, in order to highlight the methodology used to get information regarding the multi-scale properties of clay/water interfaces. The purpose of that study is to exploit such a multi-scale analysis of the dynamical properties of ions and water molecules diffusing within clay sediments in order to develop a bottom-up approach of such complex interfacial dynamical processes. In such analysis, we avoid to use fitted parameters derived from empirical models by performing realistic numerical modeling exploiting structural or dynamical properties, such as average residence time or local mobility, extracted from preliminary studies performed on a smaller scale.

2. Multi-Scale Approaches for Studies of Water and Ions Dynamics in Clay Systems

2.1. Inelastic Neutron Scattering

The intensity of the INS spectra is directly proportional to the so-called Generalized Density of States, labeled $GDOS(\omega)$, that is the density of states of a system taking into account the scattering cross section of the various atoms:

$$GDOS(\omega) = \sum_j \frac{\sigma_j}{M_j} g_j(\omega), \quad (1)$$

where M_j and σ_j are, respectively, the atomic mass and the cross section of the atom labeled j. An important point is that the scattering cross section of Hydrogen is almost 2 order of magnitude that of the other atoms of the clay (Si, Al, O), so the $GDOS(\omega)$ gives mainly information on the vibrational modes of the H atoms. For the hydrated systems, the simulated spectra were calculated with Density Functional Theory Molecular Dynamics simulations since the confined water molecules remain liquids and, thus, disordered

compared to monocrystalline clay network. After solving classical Newton equations, the $GDOS(\omega)$ was approximated by evaluating the velocity auto-correlation function of the atoms:

$$g_j(\omega) = \sqrt{\frac{1}{2\pi}} \int_{-\infty}^{+\infty} e^{-i\omega t} \sum_j \frac{\langle \vec{v}_j(0) \cdot \vec{v}_j(t) \rangle}{\langle \vec{v}_j(0) \cdot \vec{v}_j(0) \rangle} dt, \quad (2)$$

where $\vec{v}_j(t)$ is the instantaneous velocity of atom j. Before comparing the predictions obtained from the ab initio MD simulations with experimental data, the contributions from the dry clay network is subtracted [18]. The resulting spectra are displayed in Figure 3 for two hydration states corresponding, respectively, to the formation of one and two hydration layers [70]. In both longitudinal and perpendicular directions, the agreements between predicted $g_{H-water}(\omega)$ and experimental spectra are semi-quantitative with a fair matching of the characteristic frequencies (see Figure 3), partially validating the use of the above-mentioned approximation in the treatment of such local motions of the confined water molecules.

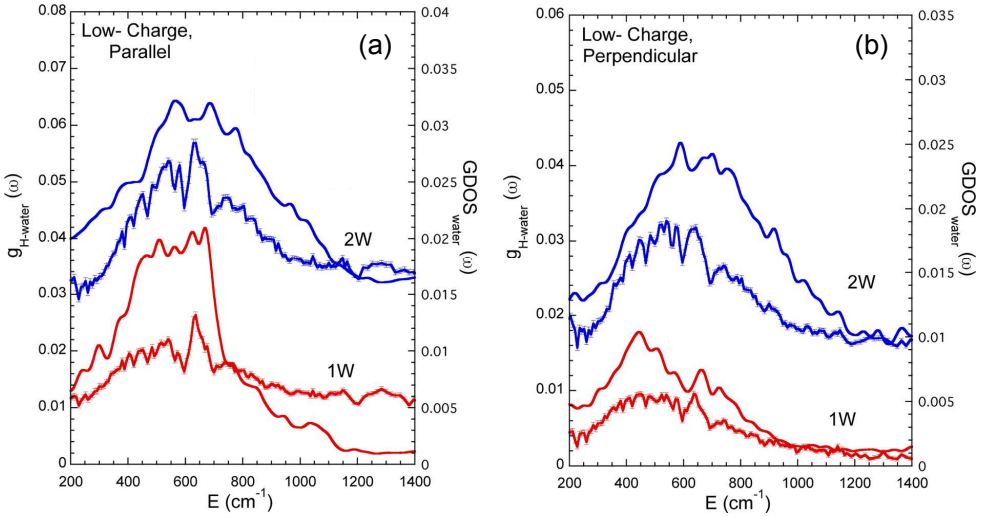


Figure 3. Comparison between the experimental $GDOS_{water}(\omega)$ and simulated $g_{H-water}(\omega)$, see Equation (2), for INS spectra of hydrated saponite sediments along the directions parallel (**a**) and perpendicular (**b**) to the clay layers (see text). Reprinted with permission from Ref. [18]. Copyright (2017) American Chemical Society.

2.2. Quasi-Elastic Neutron Scattering

Quasi-Elastic Neutron Scattering (QENS) experiments are performed [12,28] to probe the diffusive motions of the confined water molecules and their orientational dependence regarding the clay surface. These measurements are performed with the same saponite synthetic clay at various hydration states and neutralized by sodium or calcium counterions. Since the dynamical range probed by these QENS measurement extend up to a few hundred pico-seconds (see Figure 1), the molecular modeling of the clay/water interface is performed by using the classical CLAYYFF force field [64], with a minor correction of its Lennard/Jones parameters introduced to improve the agreement between the structure of the clay/water interface obtained by X-Ray and neutron scattering experiments and simulated data [2,57,70]. Grand Canonical Monte Carlo (GCMC) simulations [71] are first performed to determine the number of confined water molecules as a function of the experimentally fixed water chemical potential [12,28] and the layer-to-layer distance previously determined by X-Ray Scattering (XRS) [70]. The mobility of the confined water molecules and neutralizing sodium or calcium counterions is then modeled by performing numerical simulations of Molecular Dynamics (MD) [72] (see Figure 4), starting from an equilibrium configuration previously determined by GCMC simulations.

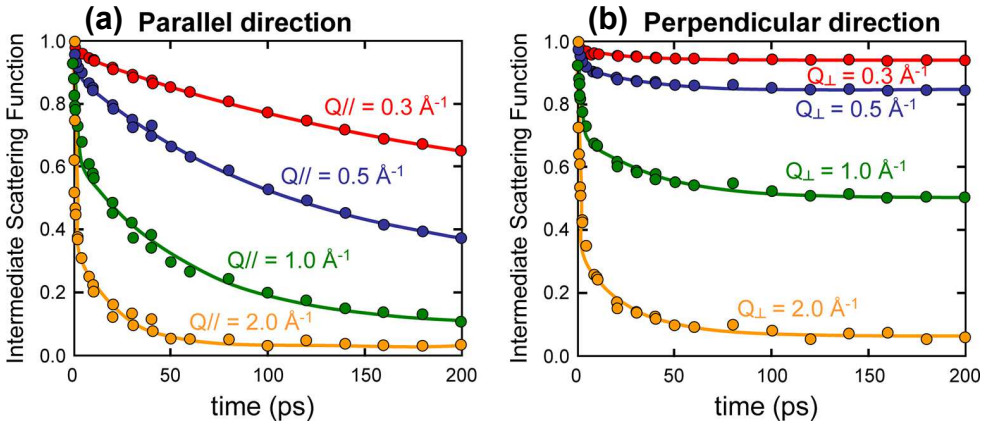


Figure 4. Time evolution of the Intermediate Scattering Function, in Equation (3), evaluated by numerical simulations of Molecular Dynamics for hydrated samples of saponite neutralized by Na^+ counterions, along the directions parallel (**a**) and perpendicular (**b**) to the clay layers. Reprinted with permission from Ref. [28]. Copyright (2012) American Chemical Society.

The QENS spectra displayed in Figure 5 are directly evaluated from the Fourier Transform of the Intermediate Scattering Function (ISF):

$$F_s(\vec{Q}_\alpha, t) = \frac{1}{2N_w} \sum_{j=1}^{N_w} \sum_{nh=1}^{2} \exp\left[i\, \vec{Q}_\alpha \cdot (\vec{r}_{i,nh}(0) - \vec{r}_{i,nh}(t)) \right], \quad (3)$$

convoluted by the spectral resolution of INS experimental set-up [28]. As displayed in Figure 5, an excellent agreement is obtained in all cases between the experimental spectra and the simulated numerical data. As a consequence, one may be quite confident in the validity of the water mobility determined by these numerical simulations on a time-scale slightly shorter than nano-second. The water self-diffusion coefficients displayed in Table 1 are obtained by integrating the velocity auto-correlation function [73] of the water molecules,

$$D_\alpha = \lim_{\tau \to +\infty} \int_0^\tau \langle \vec{v}_\alpha(0) \cdot \vec{v}_\alpha(\tau) \rangle \, d\tau, \quad (4)$$

allowing to determine the local water mobility in the direction parallel and perpendicular to the clay surface [74]. In Figure 5, the wave numbers q probed by these QENS experiments vary between 0.3 and 1.8 $Å^{-1}$, thus restricting the corresponding diffusion length between 21 and 3.5 Å. Furthermore, the same QENS measurements probe a limited dynamical range characterized by a spectral window of 0.25 meV with a resolution of 0.0025 meV (see Figure 5), corresponding to maximum diffusion times of 132 ps. By taking into account the order of magnitude of the apparent mobility of the confined water displayed in Table 1, this maximum diffusion period restricts the order of magnitude of the probed diffusion length to typically a few Angstroms. Furthermore, as displayed in Figure 4, the time-scale probed by the QENS measurements totally matches the dynamical range probed by MD numerical simulations. As a consequence, the agreement between these QENS experimental data and the numerical results obtained by MD simulations depends not only on the quality of the numerical model used in that study but also on the matching between the time-scales and diffusion-ranges probed by both experimental and numerical methods. As a consequence, the self-diffusion coefficients reported here in the direction perpendicular to the clay surface quantifies only the local mobility of the confined water molecules and does not correspond to macroscopic displacements totally impeached by the confining clay platelets (see Figure 6a). By contrast, the water mobility of the water molecules quantified by the same QENS measurements in the direction parallel to the clay surface can be used to determine the order of magnitude of the residence time of the same water molecules (labeled τ_C in Figure 6a) confined in the interlamellar space

between two clay platelets. As displayed in Table 1, confinement under low electrostatic coupling (i.e., for 0.8 electron per unit cell) simply reduces the water mobility by a factor ten by comparison with bulk water. By contrast, at higher electrostatic coupling (i.e., for 1.4 electron per unit cell), the water mobility may be reduced by two orders of magnitude. These numerical results illustrate how geometric and energetic constraints can significantly modify the dynamics of confined water molecules.

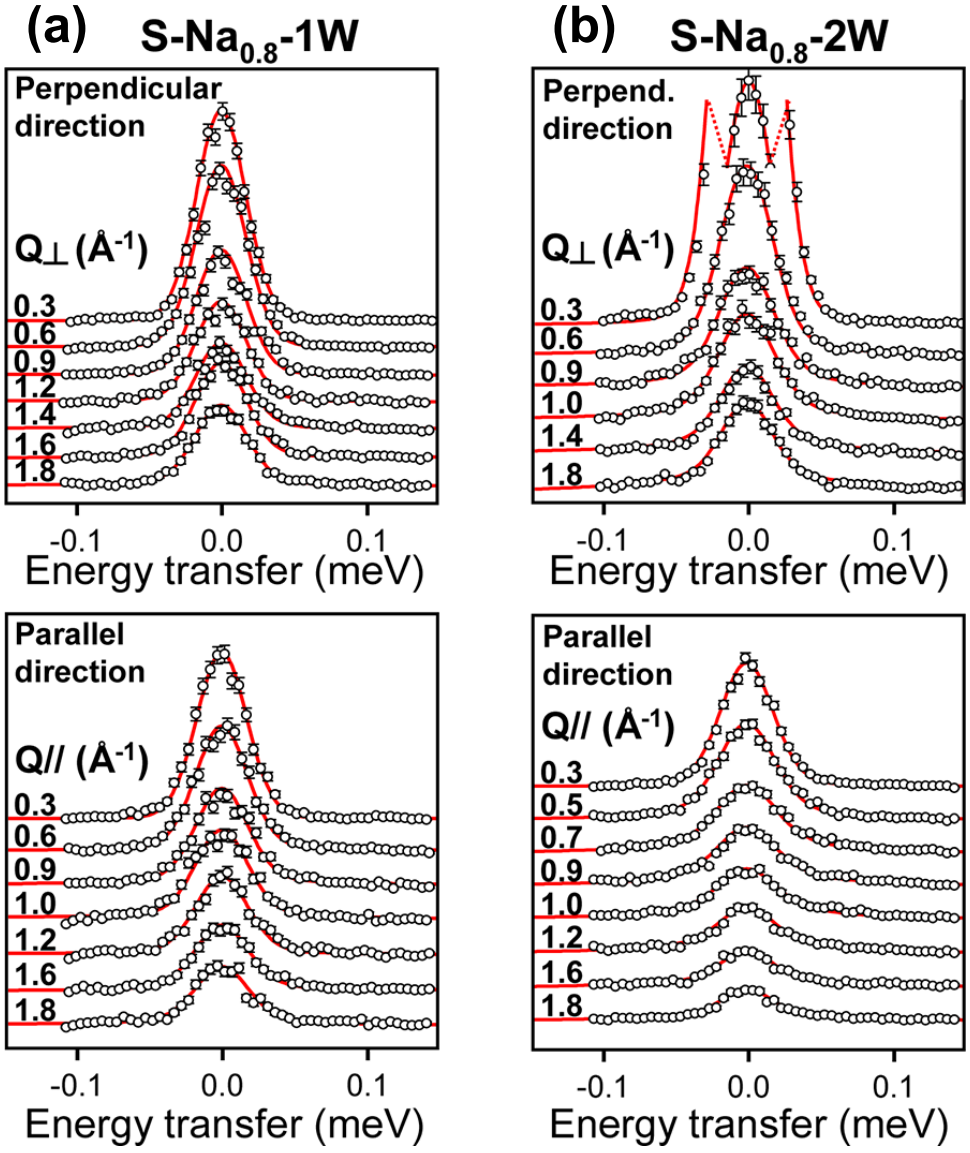


Figure 5. Direct comparison between experimental Quasi-Elastic Neutron Scattering spectra (open circles) and their numerical counterpart (red line) evaluated by MD simulations. Data were obtained for low-charge (0.8 e/uc) synthetic saponite in the direction parallel (**bottom**) or perpendicular (**top**) to the clay layer and for (**a**) mono-hydrated state and (**b**) bi-hydrated state. Reprinted with permission from Ref. [28]. Copyright (2012) American Chemical Society.

Table 1. Water dynamical parameters, $D_{//}$ and $D_{\perp}$, respectively, the self-diffusion coefficient defined in the direction parallel and perpendicular to the clay surface, deduced from MD simulations for all samples investigated at 300 K. The data are from Table 3 in the Ref. [28] with permission from Ref. [28]. Copyright (2012) American Chemical Society.

Sample	$D_{//}$ (10^{-10} $m^2 \cdot s^{-1}$)	$D_{\perp}$ (10^{-10} $m^2 \cdot s^{-1}$)
Na^+-saponite 0.8 e/uc-1W	2.4 ± 0.20	
Na^+-saponite 0.8 e/uc-2W	7.2 ± 0.50	3.0 ± 1.0
Na^+-saponite 1.4 e/uc-1W	0.6 ± 0.05	
Na^+-saponite 1.4 e/uc-2W	3.1 ± 0.10	2.0 ± 0.5
Ca^{2+}-saponite 0.8 e/uc-1W	1.6 ± 0.20	
Ca^{2+}-saponite 0.8 e/uc-2W	6.5 ± 0.30	3.0 ± 1.0
Ca^{2+}-saponite 1.4 e/uc-1W	0.3 ± 0.05	
Ca^{2+}-saponite 1.4 e/uc-2W	2.4 ± 0.10	2.0 ± 0.5

2.3. Nuclear Magnetic Resonance Relaxometry

In the last decade, Nuclear Magnetic Resonance (NMR) relaxometry appeared as a powerful tool [75,76] to investigate dynamics of fluids under confinement by measuring the frequency variation of the NMR relaxation rates. Usual NMR spectrometers allow to measure easily the relaxation of the nuclear magnetization in the direction parallel and perpendicular to the static magnetic field, leading, respectively, to the longitudinal and transverse relaxation rates. For bulk liquids, these two independent measurements lead to the same relaxation rates. By contrast, the transverse relaxation rates of confined fluids largely exceed their longitudinal counterpart due to their large frequency variations. The purpose of NMR relaxometry is to probe that frequency variation of the relaxation rates in order to extract dynamical information on the molecular motions (rotation and diffusion) inducing the fluctuations of the magnetic coupling monitoring the NMR relaxation processes. For I = 1/2 spin nuclei [35,75,76], field-cycling NMR spectrometers are perfectly appropriate to perform such investigations since the order of magnitude of the probed relaxation rates is generally compatible with the time required to switch the magnetic field of these spectrometers (typically, milli-seconds). As an example, field cycling NMR relaxometry measurements were only performed with dilute dispersions of synthetic clays [37]. By contrast, the same field cycling spectrometers become inefficient for quadrupolar nuclei (spin I > 1/2) because of the large enhancement of their relaxation rates under confinement. In that context, spin-locking relaxation measurement [77–80] is a powerful tool since it may be performed with usual spectrometer and is simply limited by the short dead time required to generate a sequence of NMR pulses (typically, micro-seconds).

Furthermore, a complete understanding of the NMR relaxation processes requires a quantum analysis of the spin. For I = 1/2 spin nuclei, this is easily performed by using the four Pauli matrices [75] to describe the three independent states of the magnetization (M_x, M_y and M_z) completed by the unit operator, in order to obtain a complete basis set. For quadrupolar nuclei (spin I > 1/2), this basis set becomes incomplete and new operators must be added [81] (five for I = 1 spin nuclei like ^{2}H, twelve for I = 3/2 spin nuclei like ^{7}Li or ^{23}Na and up to sixty for I = 7/2 spin nuclei like ^{133}Cs). These supplementary operators describe new quantum states, also called coherences, accessible to the nuclear magnetization by using specific pulse sequences [82–84]. By measuring the corresponding multi-quanta relaxation rates [85], it becomes possible to separately identify the contributions from the different relaxation mechanisms of confined quadrupolar nuclei [10,41,43,44,51,80,86]. Finally, by performing selective multi-quanta spin-locking relaxation measurements [85], one can extract dynamical information on confined fluids from the frequency variations of the relaxation rates of these additional coherences.

In the case of heavy water, the electrostatic field gradient felt by the deuterium atom is oriented along the $\overrightarrow{OD}$ director. As a consequence, the NMR relaxation rate of these deuterium atoms may be determined by the correlation time describing the reorientation of that $\overrightarrow{OD}$ director by reference with the static magnetic field. In bulk water, that correlation

time is about 3.6 pico-seconds, leading to a NMR relaxation rate of 2.4 s^{-1}. By applying the same analysis to the NMR relaxation rate of confined water molecules, the measured relaxation rate (typically, 10^4 s^{-1}; see Figure 7) requires reorientation correlation time of the $\overrightarrow{OD}$ director with an order of magnitude of 15 nano-seconds, i.e., three order of magnitude larger than the value measured by QENS (see Michot et al. [12]). That interpretation is, thus, invalid since it neglects the influence of confinement on the specific orientation of the confined water molecules (see Figure 6d), leading to the splitting of the deuterium resonance line (see Figures 6b,c). As a consequence, the decorrelation of the electric field gradient felt by the confined water molecules is incomplete until they remain confined inside the interlamellar space of the same clay sediment (see Figure 6a). By contrast, after desorption from one oriented micro-domain, the residual quadrupolar coupling vanishes and the long-time decrease of the correlation function monitoring the water quadrupolar coupling is then driven by the water residence time τ_C, as displayed in Figure 6a.

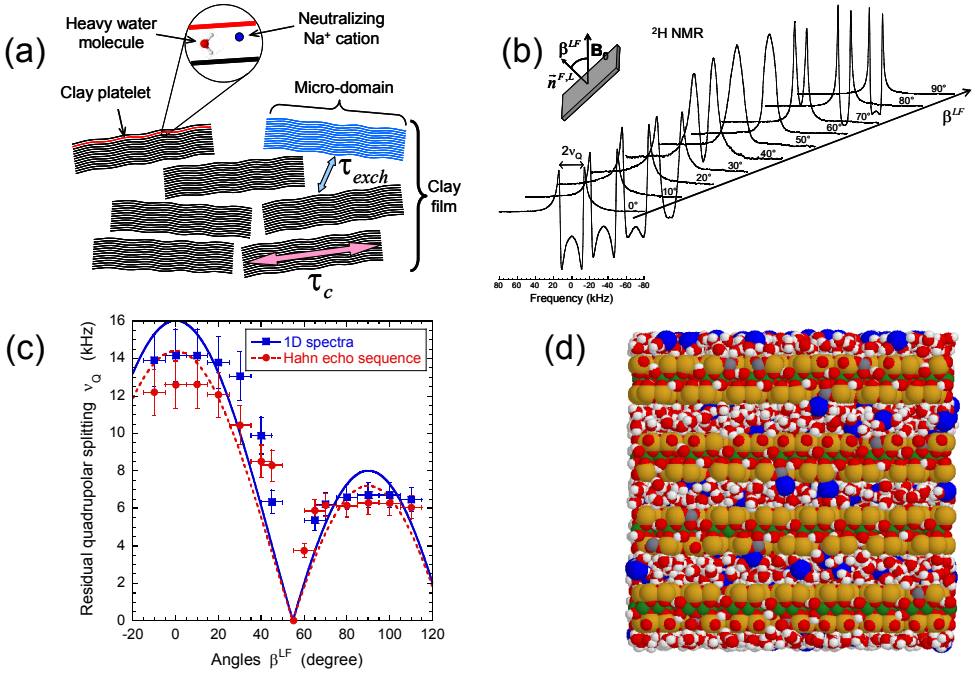


Figure 6. (**a**) Schematic view of the multi-scale organization of the hydrated clay-sediment induced by the coexistence of various micro-domains resulting from the stacking of hydrated clay platelets; (**b**) variation of the ^{2}H NMR spectra of the confined water molecules as a function of the sediment orientation in the static magnetic field; (**c**) variation of the residual quadrupolar splitting (see Equation (5)), extracted from the spectra displayed in Figure 6b; (**d**) snapshot illustrating one equilibrium configuration obtained by Grand Canonical Monte Carlo simulations of the water molecules and neutralizing Na^+ counterions confined between fragments of saponite platelets. Reprinted with permission from Ref. [80]. Copyright (2014) American Chemical Society.

In that context, a first set of ^{2}H multi-quanta spin-locking relaxometry experiments were performed to determine the average residence time of water molecules confined within the interlamellar space of clay platelets forming aggregates (Figure 6a) of dense sediments of Na^+-beidellite clay [80]. As illustrated in Figure 6b, the apparent splitting ν_Q of the ^{2}H resonance line varies as a function of the sediment orientation β^{LF} into the static magnetic field, according to the expected relationship (Figure 6c):

$$\nu_Q(\beta^{LF}) = \frac{3\cos^2\beta^{LF} - 1}{2}\nu_Q(0), \quad (5)$$

where β^{LF} is the angle between the direction of the static magnetic field and the normal $\vec{n}$ to the surface of the clay film. This residual splitting of the ^{2}H NMR resonance line results from the specific orientation of the confined water molecules as illustrated by an equilibrium configuration of the confined ions and water molecules obtained by Grand Canonical Monte Carlo simulations (Figure 6d).

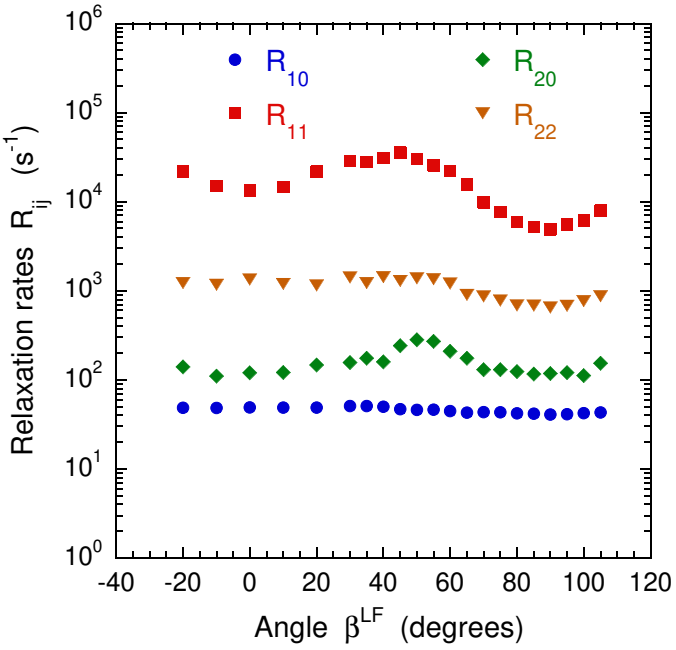


Figure 7. Variation of the relaxation rate of the T_{10}, $T_{11}(a,s)$, T_{20}, and $T_{22}(a,s)$ coherences, noted R_{10}, $R_{11}(a,s)$, R_{20}, and $R_{22}(a,s)$, respectively, as a function of the orientation β^{LF} of the clay film into the static magnetic field. Reprinted with permission from Ref. [80]. Copyright (2014) American Chemical Society.

By measuring the specific relaxation rates of the so-called $T_{10}(s)$, $T_{11}(a,s)$, T_{20}, and $T_{22}(a,s)$ coherences [82] of this I = 1 spin nucleus as a function of the sediment orientation into the static magnetic field (Figure 7), it becomes possible to quantify the relative contributions of the quadrupolar and heteronuclear dipolar NMR relaxation mechanisms [80]. Three specific angles (0°, 30°, and 90°) are then selected to determine the time evolution of four independent coherences (labeled $T_{11}(s)$, $T_{21}(a)$, $T_{21}(s)$, and $T_{22}(a)$ [82–84] under spin-locking conditions by applying an irradiation field of calibrated irradiation power ω_1. For I = 1/2 spin nuclei, such spin-locking relaxometry measurements probe only a single angular velocity ($2\,\omega_1$) for each irradiation power [77–79]. By contrast, in the presence of a residual quadrupolar coupling (ω_Q), I = 1 spin nuclei probe three different angular velocities:

$$k_1 = \sqrt{\omega_Q^2 + 4\,\omega_1^2}\,, \quad k_2 = \frac{\omega_Q + \sqrt{\omega_Q^2 + 4\,\omega_1^2}}{2} \quad \text{and} \quad k_3 = \frac{-\omega_Q + \sqrt{\omega_Q^2 + 4\,\omega_1^2}}{2}, \quad (6)$$

for a single irradiation power ω_1 [82].

Some raw data are displayed in Figure 8 in addition to their Fourier transforms illustrating the specific angular velocities (k_1, k_2, and k_3) probed by these spin-locking relaxometry measurements. As also illustrated by Equation (6), the three apparent velocities (k_1, k_2 and k_3) vary as a function of the sediment orientation which modulates the residual quadrupolar splitting (ω_Q); see Equation (5). As a consequence, it becomes possible to investigate a broad dynamical range by using a limited number of irradiation powers ω_1 (see Figure 9). Figure 9 exhibits a transition between a plateau, at low angular velocities, and a power-law decrease, at high angular velocities [80]. By using the water self-diffusion

coefficient of the confined water molecules previously determined by QENS measurements under equivalent conditions (see Section 2.2), numerical simulations of Brownian Dynamics are performed to determine the average residence time of water molecules confined within the interlamellar space between two beidellite platelets. That residence time fully corresponds [43] to the critical time τ_C evaluated from the measured angular velocity ω_C ($\tau_C = 1/\omega_C$; see Figure 9). This result illustrates how multi-quanta spin-locking NMR relaxometry of quadrupolar nuclei largely extends up to $\sim 10^{-4}$ s, the time-scale previously probed by QENS measurements.

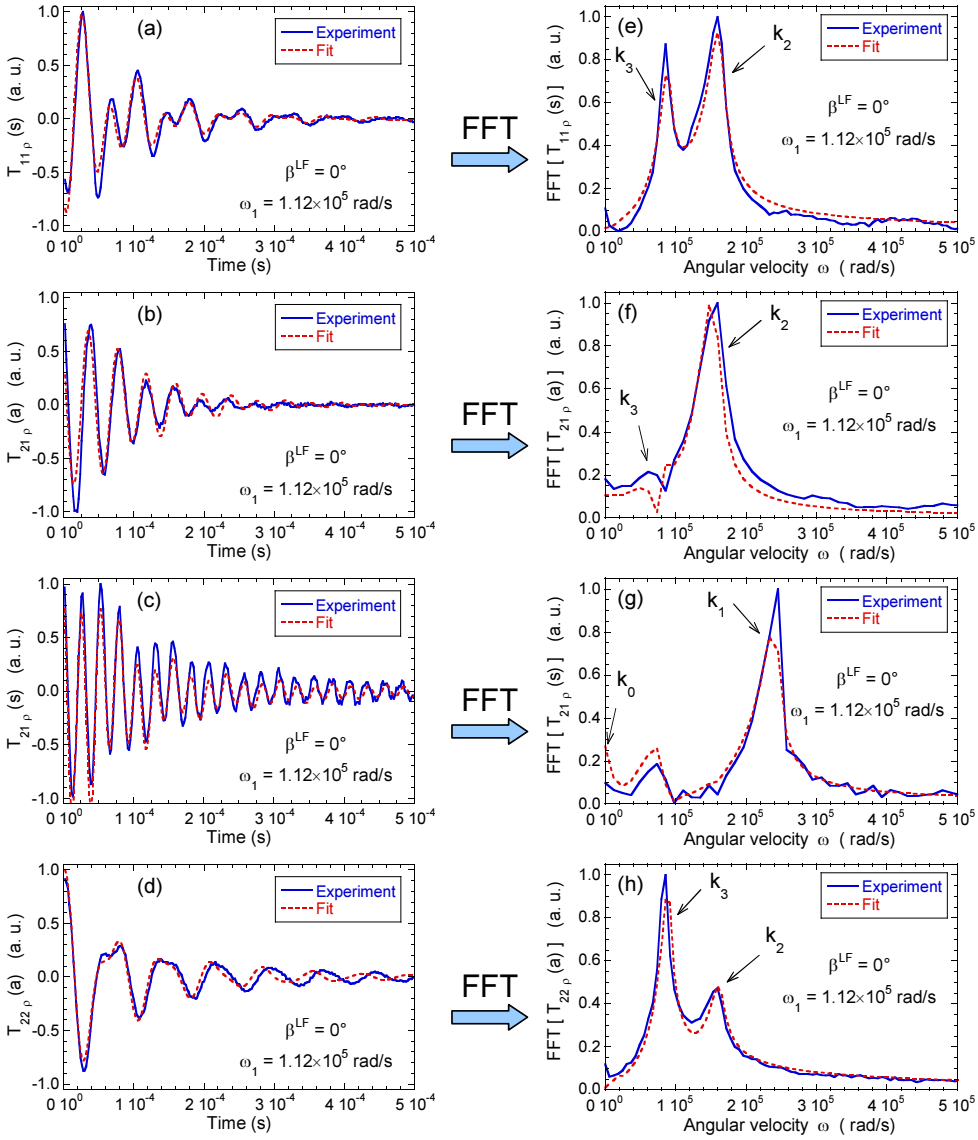


Figure 8. Time evolution of (**a**) $T_{11}(s)$; (**b**) $T_{21}(a)$; (**c**) $T_{21}(s)$ and (**d**) $T_{22}(a)$ coherences measured under spin-locking conditions, noted $T_{11\rho}(s)$, $T_{21\rho}(a)$, $T_{21\rho}(s)$ and $T_{22\rho}(a)$, respectively, and their Fourier transforms for (**e**) $T_{11}(s)$; (**f**) $T_{21}(a)$; (**g**) $T_{21}(s)$ and (**h**) $T_{22}(a)$ coherences (^{2}H NMR). These Fourier transforms better illustrate the contribution from the characteristic angular velocities k_i; see Equation (6). Reprinted with permission from Ref. [80]. Copyright (2014) American Chemical Society.

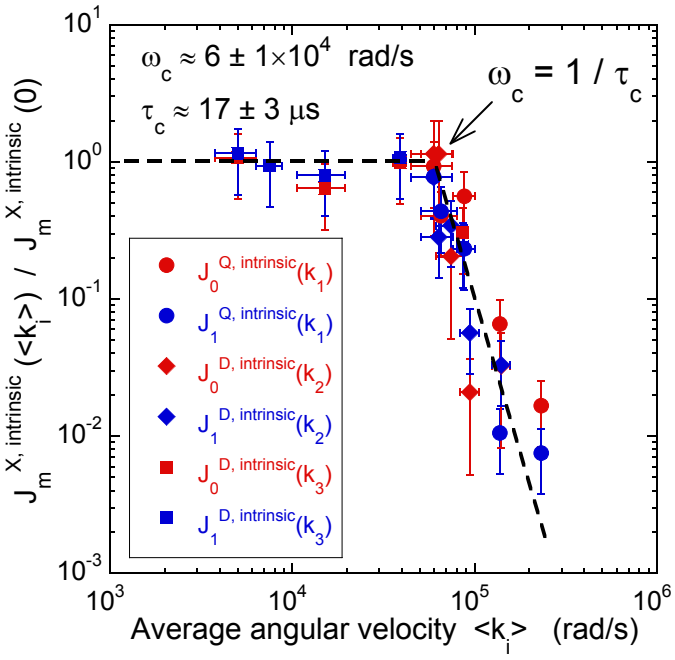


Figure 9. Dispersion curve determined from the variation of the quadrupolar and heteronuclear dipolar contributions to the relaxation of the $T_{11}(s)$, $T_{21}(a)$, $T_{21}(s)$, and $T_{22}(a)$, ^{2}H coherences measured under spin-locking conditions. Reprinted with permission from Ref. [80]. Copyright (2014) American Chemical Society.

The same spin-locking relaxometry measurements were performed by ^{7}Li NMR spectroscopy to study the mobility of lithium counterions within aqueous dispersions of synthetic laponite clays [10]. Dense dispersions are prepared by uni-axial oedometric compression; more details are given in the Supplementary Materials. Above the Isotropic/Nematic phase transition [5], the ^{7}Li NMR spectra exhibit a splitting of the resonance line (see Figure 10) that perfectly cancels at the so-called magic angle; see Equation (5). This behavior results from the occurrence of a single nematic phase, with a director parallel to the compression axis. Since ^{7}Li is a I=3/2 spin nucleus, six different angular velocities may now be probed by using ^{7}Li NMR relaxometry with a single irradiation power ω_1 [84] (see Figure 11):

$$\begin{aligned} \lambda_1 &= \sqrt{\omega_Q^2 + 2\omega_1\omega_Q + 4\omega_1^2} & \lambda_2 &= \sqrt{\omega_Q^2 - 2\omega_1\omega_Q + 4\omega_1^2} \\ \lambda_3 &= \omega_1 + \sqrt{\frac{\omega_Q^2 + 4\omega_1^2 + \lambda_1\lambda_2}{2}} & \lambda_4 &= \omega_1 + \sqrt{\frac{\omega_Q^2 + 4\omega_1^2 - \lambda_1\lambda_2}{2}}. \\ \lambda_5 &= \omega_1 - \sqrt{\frac{\omega_Q^2 + 4\omega_1^2 + \lambda_1\lambda_2}{2}} & \lambda_6 &= \omega_1 - \sqrt{\frac{\omega_Q^2 + 4\omega_1^2 - \lambda_1\lambda_2}{2}} \end{aligned} \quad (7)$$

As illustrated in Figure 12, a broad range of angular velocities is then investigated by using a limited number of angular velocities. Figure 12 also exhibits the dispersion curve of the NMR relaxation rates. Here, we also detect a transition between a low-frequency plateau and a high-frequency continuous decrease.

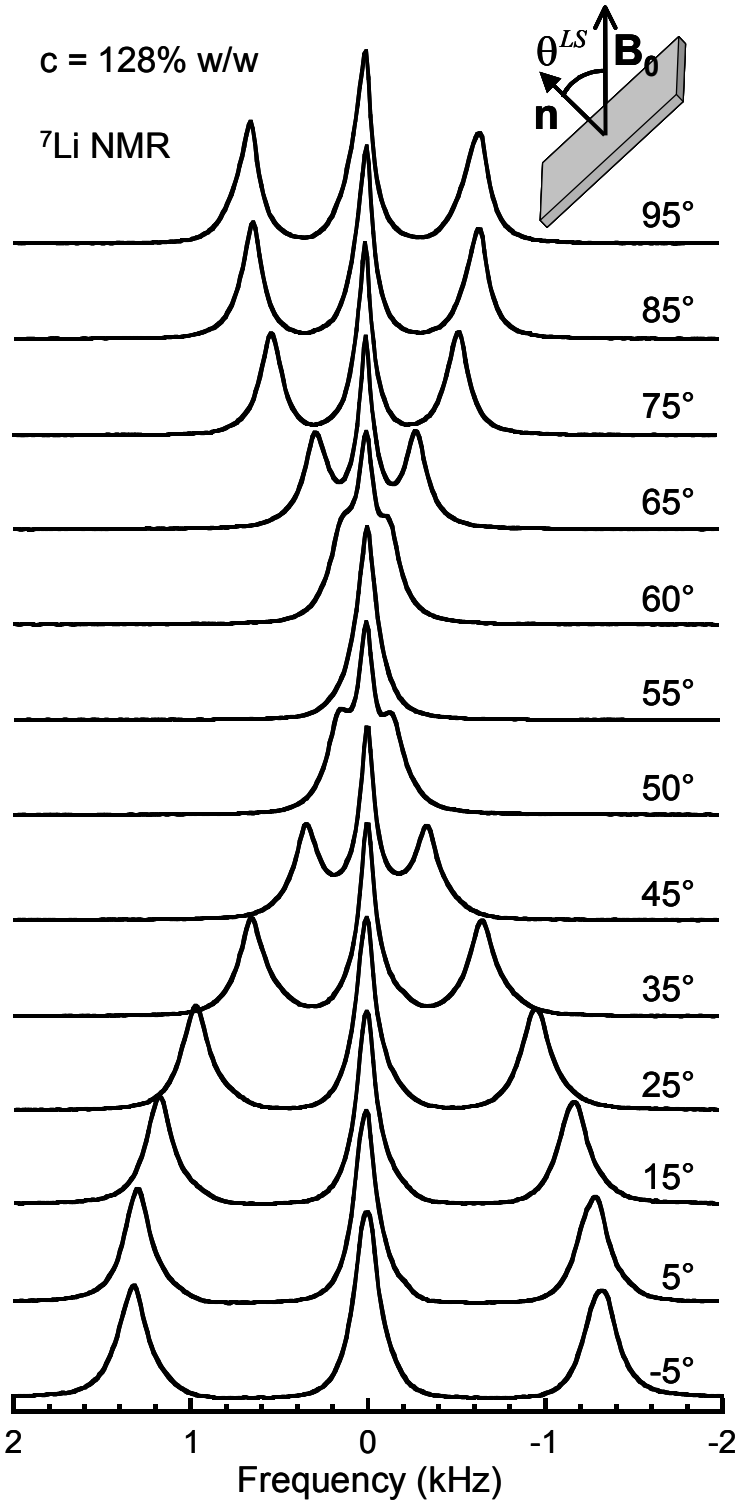


Figure 10. Variation of the ^{7}Li NMR spectra measured within laponite aqueous dispersion as a function of the orientation of the clay sample in the static magnetic field. Reprinted with permission from Ref. [10]. Copyright (2008) American Chemical Society.

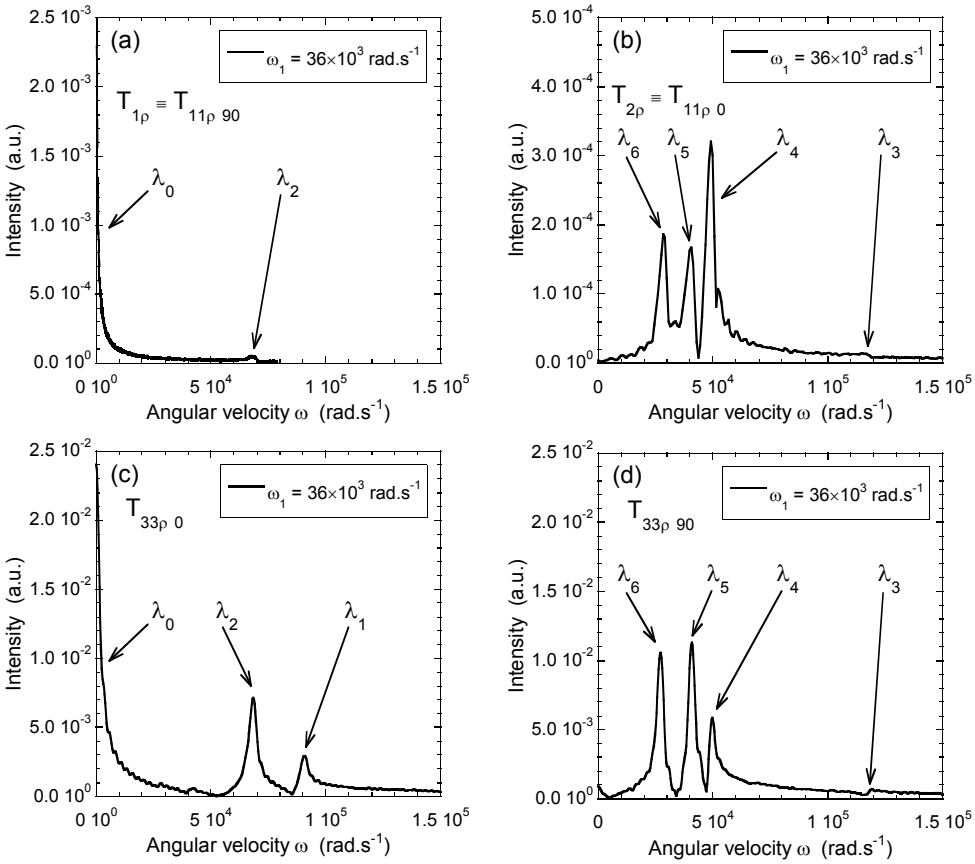


Figure 11. Fourier transform of the time evolution of the ^{7}Li coherences, (**a**) $T_{11}(a)$; (**b**) $T_{11}(s)$; (**c**) $T_{33}(s)$ and (**d**) $T_{33}(a)$, under spin-locking conditions, illustrating the whole set of characteristic angular velocities k_i; see Equation (7). Reprinted with permission from Ref. [41]. Copyright (2009) American Chemical Society.

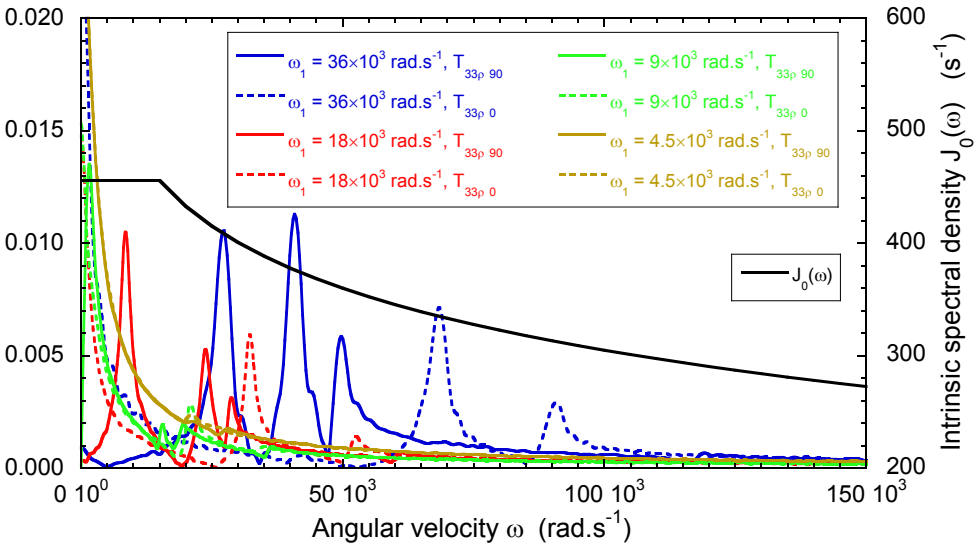


Figure 12. Illustration of the frequency domain probed by time evolution of the $T_{33}(a,s)$ coherences under spin-locking conditions, leading to the dispersion curve of the ^{7}Li NMR relaxation rate. Reprinted with permission from Ref. [41]. Copyright (2009) American Chemical Society.

Numerical simulations of Brownian Dynamics (BD) are then required to interpret these results. In order to reproduce ionic condensation on the clay surface, a mean force potential [73] is evaluated from preliminary Monte Carlo simulations of the distribution (see Figure 13) of thousands Lithium counterions neutralizing the negative charge of an isolated laponite platelet. By using the weak overlap approximation [68], BD simulations are further performed for modeling lithium diffusion within a collection of partially oriented laponite platelets. As illustrated in Figure 14, the decorrelation of the memory function, induced by the fluctuations of the quadrupolar relaxation mechanism [41], evolves according to a t^{-1} power law for diffusion time longer than 10^2 ns. This behavior results from the strong electrostatic coupling between the highly charged clay platelet and the lithium counterions trapped in the so-called condensation layer (see Figure 14). This phenomenon is responsible for the low frequency logarithmic decrease of the ^{7}Li NMR relaxation rates displayed in Figure 12. As a consequence, two different confinements may be detected by NMR relaxometry within such solid/liquid interfacial systems, induced either by geometrical constraints, as in the case of water molecules adsorbed within the interlamellar space of dense sediments, or by energetic coupling, as in the case of ionic condensation within dilute clay dispersions.

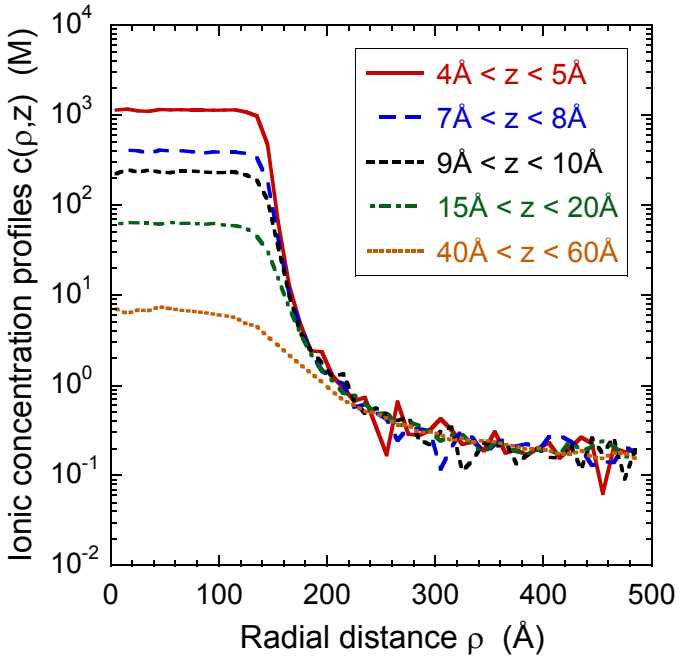


Figure 13. Ionic concentration profiles evaluated by Monte Carlo numerical simulations illustrating Li^+ ions condensation around an isolated laponite platelet. Reprinted with permission from Ref. [41]. Copyright (2009) American Chemical Society.

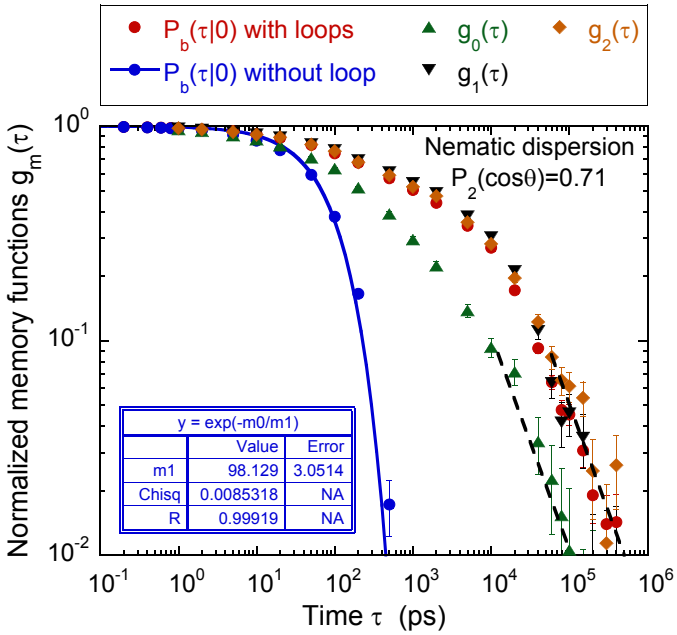


Figure 14. Numerical modeling of the memory function quantifying the decorrelation of the quadrupolar coupling felt by Li^+ counterions diffusing within a dense sediment resulting from the collection of partially oriented laponite platelets. Reprinted with permission from Ref. [41]. Copyright (2009) American Chemical Society.

2.4. Pulsed-Gradient Spin-Echo Attenuation

Attenuation of the NMR signal measured after an echo pulse-sequence encoded by using gradients of the static magnetic field leads to dynamical information on the mobility of the NMR probes in the direction parallel to the applied field gradient [87]. These attenuation measurements directly probe the Intermediate Scattering Function; see Equation (1) in the Supplementary Materials for wave-vectors q defined by the relationship:

$$q = \frac{\gamma \delta G}{\pi}, \tag{8}$$

where γ is the gyromagnetic ratio of the NMR nucleus (2.6752×10^8 rad/s for ^{1}H and 1.037×10^8 rad/s for ^{7}Li), and δ is the duration of the applied field gradient and G its strength; see Figure S2 in the Supplementary Materials for more details.

Because of the maximum strength of the applied field gradient (typically, G_{max} = 1.6 T/m) and its duration (typically, δ = 500 µs), the maximum resolution defined as resolution$_{max} = 1/q_{max}$ is not better than 15 µm, thus corresponding to macroscopic mobility measurements. Since the magnetic field gradient may be applied along any direction within the sample, ^{1}H PGSE NMR measurements were first performed to detect the Isotropic/Nematic phase transition of laponite aqueous dispersions [11,50,88] by measuring the anisotropy of the water self-diffusion tensor. These measurements were possible thanks to the great anisotropy of the laponite platelets (diameter∼300 Å, thickness∼10 Å). As illustrated in Figure 15, the Isotropic/Nematic transition of these laponite suspensions does not vary as a function of the neutralizing monovalent counterions and is well reproduced by numerical simulations of Brownian Dynamics mimicking water diffusion within a collection of partially oriented hard disks [50].

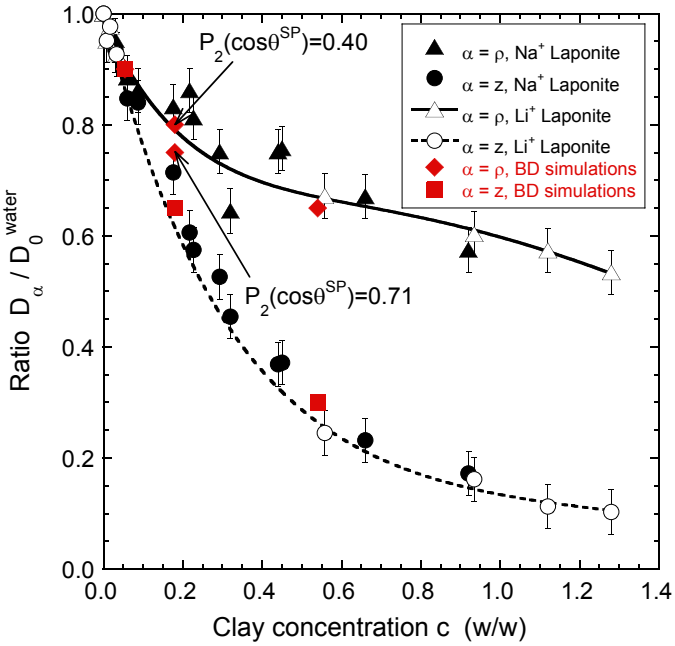


Figure 15. Influence of the clay concentration on the water self-diffusion tensor measured within laponite aqueous dispersion by using ^{1}H NMR Pulsed-Gradient Spin-Echo attenuation. Reprinted with permission from Ref. [50]. Copyright (2008) American Chemical Society.

The same PGSE measurements were performed by ^{7}Li NMR spectroscopy within aqueous dispersions of laponite platelets neutralized by lithium counterions. By contrast with the continuous decrease of the measured water mobility normalized by the bulk water mobility, Figure 16 exhibits a strong initial decrease of the lithium mobility by reference to its value measured within simple LiCl aqueous solutions. This phenomenon is the fingerprint of the ionic condensation of the lithium counterions at the surface of the highly charged laponite platelets. Numerical simulations of Brownian Dynamics may reproduce that phenomenon by including an effective mean force potential as described previously (see Figure 13). While these BD simulations agree perfectly with experimental data at low clay concentrations (see Figure 16), large differences appear at higher concentrations because of the limitation of the weak overlap approximation [68] implied in these BD simulations [50].

Because of the time scale required to build these magnetic field gradients (typically, 60 μs), such PGSE measurements become inefficient to measure the mobility of water molecules or counterions confined within the interlamellar space of clay aggregates due to the corresponding enhancement of their transverse relaxation rates. A last illustration of the use of ^{1}H PGSE concerns the analysis of anisotropy of water diffusion in compacted clay samples made of micrometer-sized kaolinite particles [51,52]; see the Supplementary Materials for more details. Since kaolinite is unswelling clay, these measurements are appropriate to detect the macroscopic mobility of the water molecules diffusing around the clay particles, leading to the so-called tortuosity factor [89,90]. In addition, this mobility is also strongly impacted by the preferential orientation of lamellar particles in the system (see Figures 18 and 19) [52]. These properties can be quantified based on X-Ray Scattering technique on bi-dimensional detector plate (2D-XRS) (see Figure 17) and the analysis of intensity distribution along the diffraction ring of the 001 reflection [52]. This measurement allows extracting the order parameter $\langle P_2 \rangle$ through the second order Legendre polynomial function [91], a parameter ranging from 0 for isotropic organization of particle to 1 if particles are perfectly oriented. The influence of preferred orientation for a constant porosity value can reveal a reduction of water mobility by a factor 2 when increasing anisotropy in particle orientation (see Figure 18). Such anisotropy in water mobility is well highlighted using ^{1}H PGSE-NMR technique and can be quantitatively reproduced by DB simulations

using virtual porous media mimicking the size, shape, and orientation of the particles in the porous media (see Figure 18). By accounting for the self-diffusion of water probes in the interparticle volume and elastic collisions with particle interfaces, the simulated data are found to well reproduce experimental measurements (see Figures 18 and 19), thus allowing to decouple the contribution of porosity and particle orientation on the overall water diffusion process.

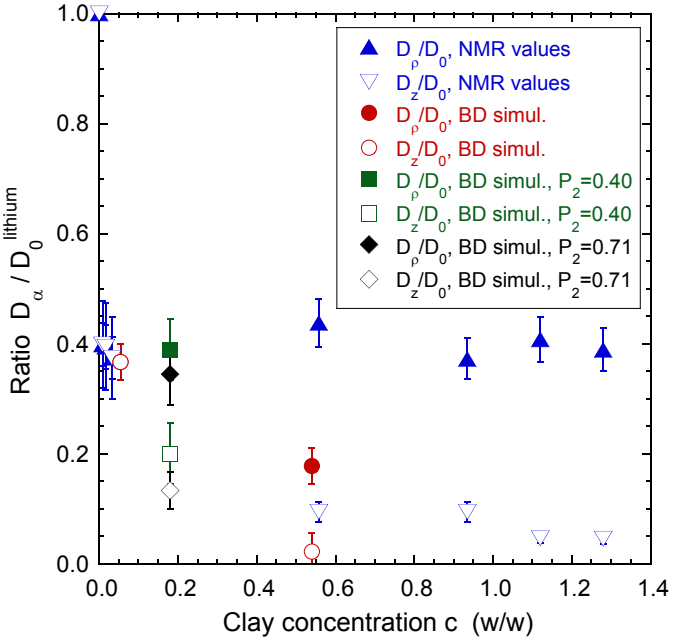


Figure 16. Influence of the clay concentration on the lithium ions self-diffusion tensor measured within laponite aqueous dispersion by using ^{7}Li NMR Pulsed-Gradient Spin-Echo attenuation. Reprinted with permission from Ref. [50]. Copyright (2008) American Chemical Society.

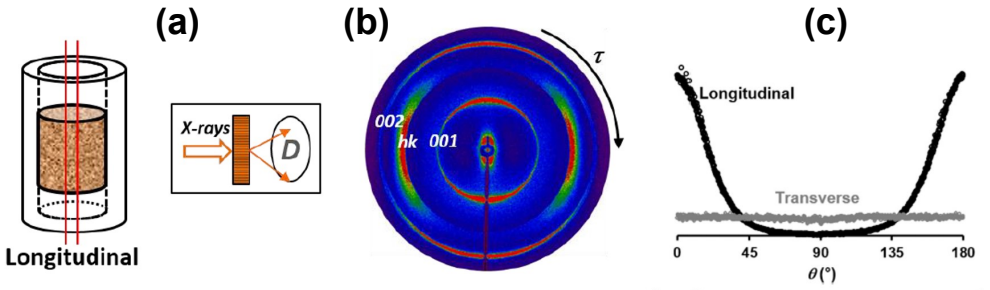


Figure 17. Determination of the orientation distribution functions of kaolinite particles within centrifuged clay samples by using 2D X-Ray Scattering patterns analysis. The longitudinal direction corresponds to the compression axis of the clay sample. (**a**) Schematic view of the experimental setup; (**b**) experimental 2D-XRS patterns and (**c**) orientation distribution functions (ODF) from the angular scan of the 001 reflection extracted from the 2D-XRS patterns. Reprinted from Ref. [52]. Copyright (2020), with permission from Elsevier.

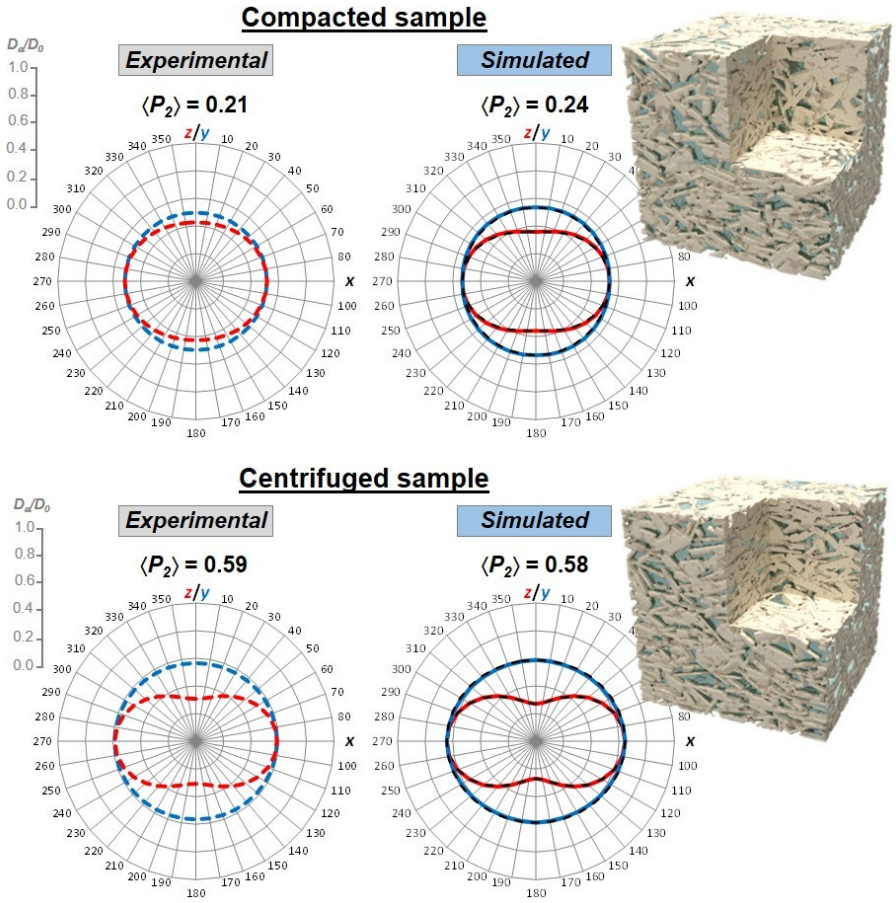


Figure 18. Components of the water self-diffusion tensor measured by ^{1}H NMR PGSE attenuation within compressed and centrifugated kaolinite clay samples. Numerical simulations of Brownian Dynamics are used to simulate the water self-diffusion tensor within virtual porous media, shown as inserts, mimicking these clay samples (see text). Reprinted from Ref. [52]. Copyright (2020), with permission from Elsevier.

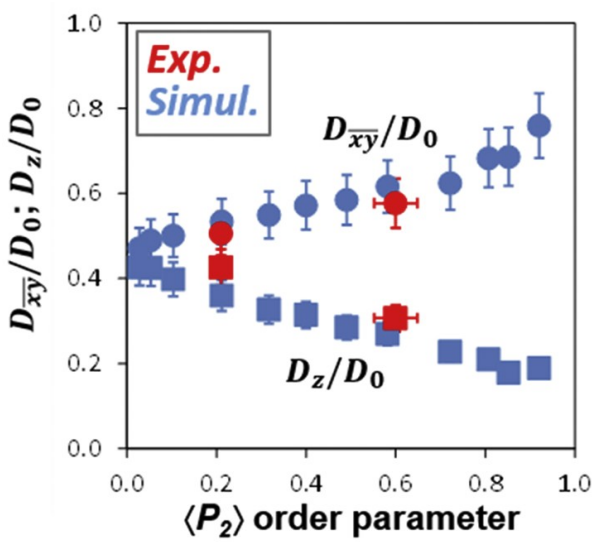


Figure 19. Influence of the preferred orientation of particles $\langle P_2 \rangle$ on the water self-diffusion tensor measured (red) and simulated (blue) within a collection of clay samples with the same porosity. The z-direction is perpendicular to the preferred alignment of clay platelets. Reprinted from Ref. [52]. Copyright (2020), with permission from Elsevier.

2.5. Magnetic Resonance Imaging

Magnetic Resonance Imaging (MRI) experiments were also performed by using ^{1}H NMR spectroscopy to obtain long time-scale information on the macroscopic mobility of water molecules within clay porous media made of kaolinite particles [51]; see the Supplementary Materials for more details. The experimental conditions are selected to probe a total length of 25 mm. The porosity of the dry kaolinite sample (ϕ_{dry} = 0.52) is evaluated by helium pycnometry [51]. The clay sample is initially saturated with bulk water, leading to a total length (noted L_1) of 12.3 mm (see Figure 20a). The MRI experiment starts just after the addition of a limited amount of heavy water (length L_2 = 7 mm) on the top of the hydrated clay sediment, leading to a total length (L = 19.3 mm) fitting the experimental window. As illustrated in Figure 20a, the ^{1}H water concentration profiles exhibit some attenuation of the ^{1}H NMR signal at the bottom of the clay sample because a significant section of the clay sample (5.3 mm) is located outside the optimal detection area of the detection coil. We also detect alterations of the water concentration profile near the clay/heavy water interfacial area, further limiting the useful length of the hydrated sample to 5 mm. By integrating the ^{1}H NMR signal over the corresponding limited area (see Figure 21), we obtain information of the long time-scale, $\tau \approx (40 \pm 2) \times 10^3$ s, implied in this exchange between bulk and heavy water. Numerical simulation are performed [51] to fully validate that analysis (see Figures 20b and 21) by using the porosity of the dry clay sample and the water mobility previously measured by ^{1}H PGSE attenuation measurements (see Section 2.4 above). That result clearly illustrates how MRI experiments may be used as complementary tool to probe the mobility of confined molecules over a broad macroscopic time-scale (from minutes up to day).

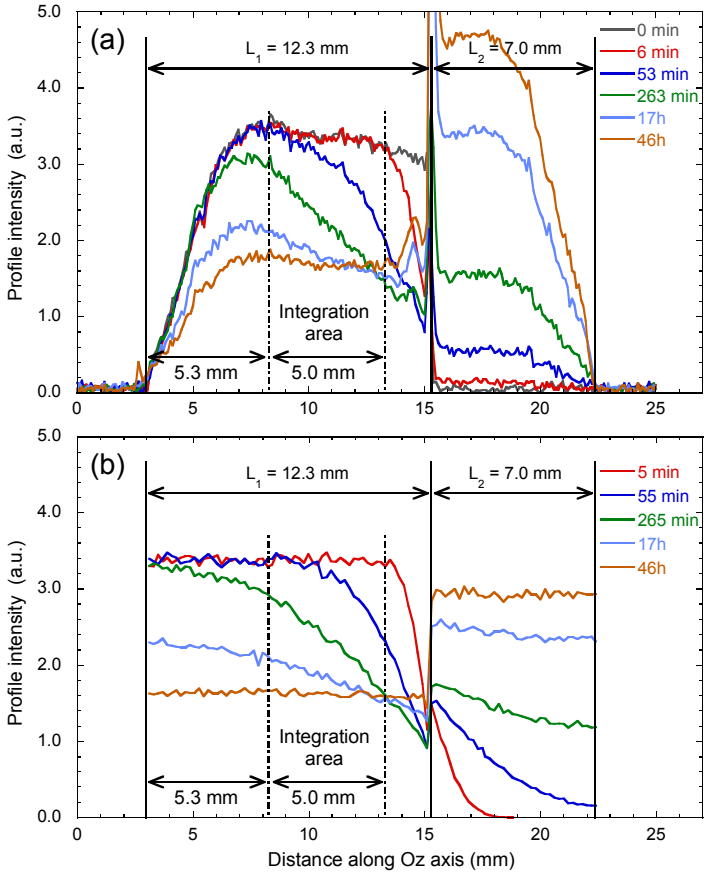


Figure 20. Time evolution of the water concentration profiles within water saturated kaolinite sample after addition of external heavy water. The experimental profiles are obtained by using ^{1}H Magnetic Resonance Imaging (**a**) and compared to numerical data obtained by Brownian Dynamics (**b**). Reprinted with permission from Ref. [51]. Copyright (2018) American Chemical Society.

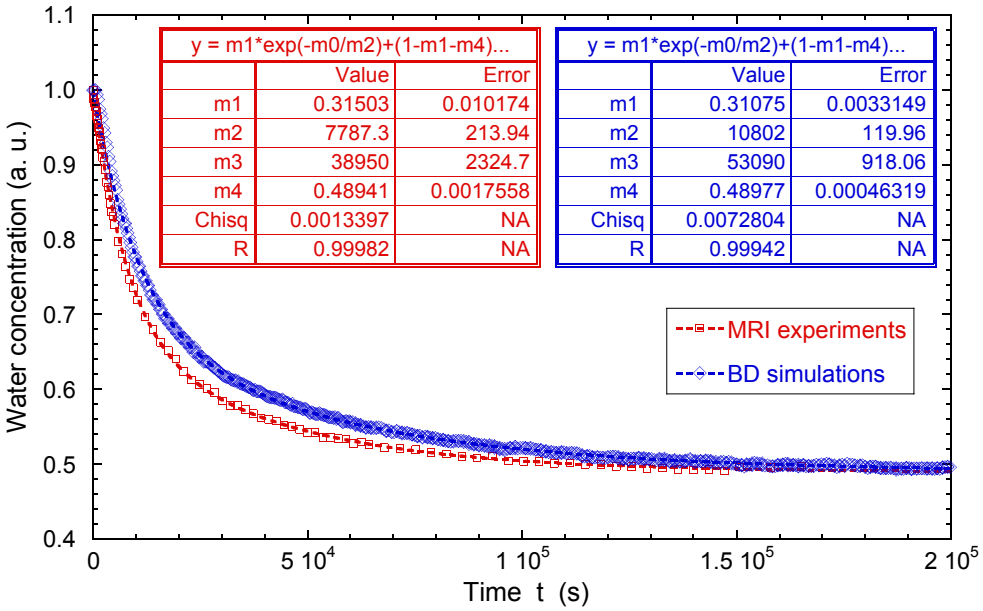


Figure 21. Direct comparison of the time evolutions of the measured and simulated numbers of confined water molecules. Experimental and numerical data are fitted by a biexponential law: $f(t) = m_1 \exp(-t/m_2) + (1 - m_1 - m_4) \exp(-t/m_3) + m_4$, where m_i are constants. Reprinted with permission from Ref. [51]. Copyright (2018) American Chemical Society.

2.6. Macroscopic Diffusion Experiments

Out-Diffusion experiments were performed to determine the time-scale characterizing the exchange between Ca^{2+}, initially located in the interlayer of vermiculite disks and neutralizing its charge, and Na^+ or Sr^{2+}, present in aqueous solutions [53,54] (see Figure 22 and the Supplementary Materials for more details). Firstly, the resulting exchange rates between these counterions were well predicted by BD simulations using self-diffusion coefficients for interlayer and aqueous bulk cations, calculated from preliminary MD simulations and the geometry of both aqueous reservoir and vermiculite disks (see Figure 22a) in the case of the Ca^{2+}/Na^+ exchange [53]. The results of this study showed that the time-evolution of the concentration gradient of interlayer Ca^{2+} was the main driving force interpreting exchange rates measured at all aqueous reservoir salinity investigated, while limitation at the solid/liquid interface, due to diffusion in the aqueous reservoir, can acts as a limiting factor to interpret exchange rates measured at low salinity conditions. As displayed in Figure 22b, the same experimental data were also well reproduced by a classical finite-volume model based on continuous differential equations, constrained by a self-diffusion coefficient of the slowest interlayer cation. That approach uses also selectivity coefficients obtained independently in batch and describing the ionic exchange at thermodynamic equilibrium (see Ref. [54] for more details). Using the two numerical approaches (BD and classical finite-volume model based on continuous differential equations), data were always based on self-diffusion coefficients obtained from preliminary numerical simulations of Molecular Dynamics (MD) without the use of any fitted parameter [53,54]. As displayed in Figure 22, the agreement between experimental and numerical data validates the use of self-diffusion coefficients obtained from MD simulations to predict the dynamic of the exchange between interlayer cations and aqueous ones over several days (up to 20 days) and then the multi-scale approaches proposed.

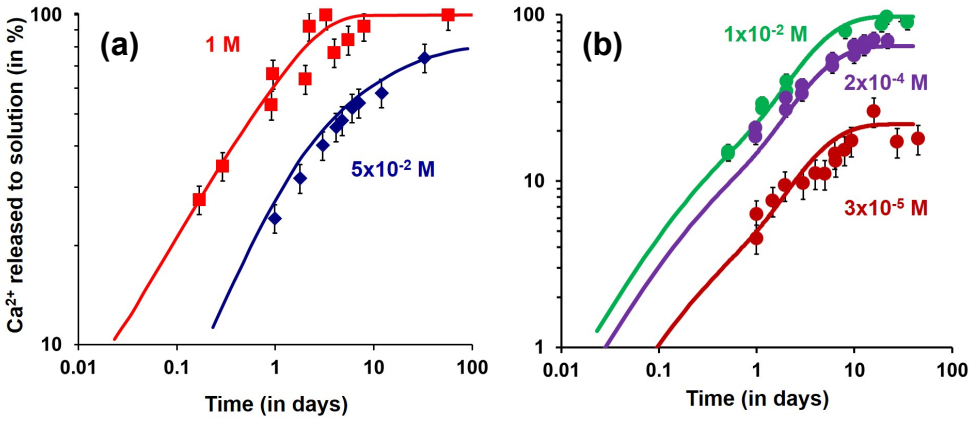


Figure 22. Macroscopic diffusion measurements of the (**a**) Ca^{2+}-for-Na^{+} and (**b**) Ca^{2+}-for-Sr^{2+} exchange within single centimeter-sized vermiculite disks. The continuous lines are obtained by (**a**) BD simulations and (**b**) a finite-volume model, both taking into account interlayer self-diffusion coefficients obtained by MD simulations. The numerical value annotated next to each curve corresponds to the salinity of the aqueous reservoir. Reprinted from Refs. [53,54]. Copyright (2015 and 2021), with permission from Elsevier.

As a second illustration of long-time diffusion process, Through-Diffusion experiments are commonly used to measure the flux of a tracer, traversing a compacted sample and to extract an effective diffusion coefficient. Such effective diffusion coefficient is directly linked to the pore diffusion parameter commonly derived from NMR measurements probing only the porosity accessible for the investigated probe. A large number of experiments were performed in literature to investigate the influence of porosity on the diffusion of water and ions in porous media made of clayey particles [69,92–94]. Water diffusion coefficients obtained using Through-Diffusion experiments and PGSE-NMR analyses performed with compacted kaolinite samples, characterized by the same porosity and preferential particle orientation, revealed similar results (see Figure 23), despite the different time scale probed by the two methods (i.e., ms for PGSE-NMR versus several days for Through-Diffusion [52]). This finding provides interesting information regarding representative time and length scales for the investigation of water dynamics in clay porous media. Moreover, this consistency allows taking advantage of both techniques for the study of clay/water interfaces. On the one hand PGSE-NMR cannot be used when sample contains paramagnetic elements, whereas Through-Diffusion is insensitive to the chemical composition of the sample. On the other hand, PGSE-NMR provides the full tensor of water dynamics whereas Through-Diffusion experiments requires to be repeated when changing the direction of diffusion probed. For the analysis of clay porous media with both interparticle and interlayer porosity (dual porosity media), Through-Diffusion was successfully applied on vermiculite to investigate the role played by the different types of porosities and preferential orientation of particle on water dynamics [55,94]. Among the large set of different numerical methods to interpret the experimental data [69,95,96], Asaad et al. [55] used BD simulations on representative virtual porous media to mimic the diffusion of water probes in both interparticle and interlayer volume, using self-diffusion coefficients extracted from MD simulations. The good agreement between experiments and simulations (see Figure 23) allowed highlighting the marginal role of interlayer volume on the flux of water tracer traversing samples, and the similar role of preferential orientation of particle when dealing with single or dual porosity media.

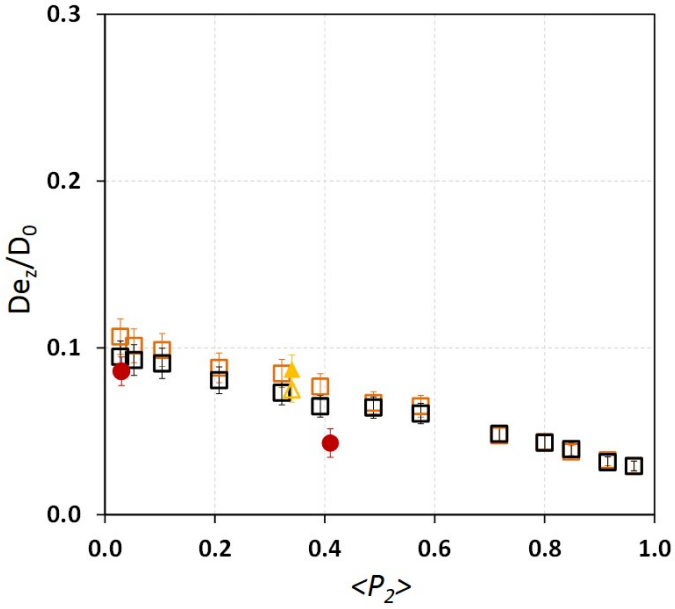


Figure 23. Influence of the particle orientation and interlayer porosity on the apparent mobility of water molecules (i.e., effective diffusion coefficient) diffusing through clay porous media in the direction perpendicular to the preferred orientation of the clay particles. Data are normalized to the self-diffusion coefficient of water in bulk solution. The data obtained for kaolinite (single porosity of ∼0.26) by ^{1}H NMR PGSE attenuation (empty yellow triangle) and TD experiments (full yellow triangle) are taken from Asaad et al. [55] and Tertre et al. [94], respectively. TD data obtained for vermiculite (dual porosity) for a similar interparticle porosity are shown as full red circles [55]. Experimental data are compared with results from BD simulations (empty squares) taking into account interlayer diffusion (orange symbols) or only the mobility in the interparticle volume (black symbols) [55]. Reprinted from Ref. [55]. Copyright (2021), with permission from Elsevier.

3. Conclusions

This review focuses on dynamical properties of the water molecules and neutralizing counterions confined within clay particles. By exploiting a large panel of complementary experimental studies, it becomes possible to investigate a large time scale varying between pico-second and days, implying local motions, as well as macroscopic displacements, within the clay aggregates. In addition to these experimental studies, we also performed multi-scale modeling of these clay/water interfacial systems in order to better extract dynamical information from the raw experimental data and further validate the conclusions of our analysis. This allowed deriving a complete bottom-up analysis of the dynamical properties of ions and water molecules confined within dense clay sediments. In that context, the interpretation of such complex dynamical phenomena is based on numerical modeling exploiting realistic models and dynamical information (residence time, local mobility) extracted from preliminary measurements performed on a smaller scale. Such complementary approaches should be useful for the analysis of other solid/liquid interfacial systems, such as cementeous and zeolitic materials, porous silicates, membranes and micelles, and aqueous dispersions of macromolecules and biopolymers.

Supplementary Materials: This Supplementary Material details the materials and the experimental methods presented in this review. The following are available at https://www.mdpi.com/article/10.3390/colloids5020034/s1.

Author Contributions: Conceptualization, P.P., A.D., E.F. and E.T.; investigation, P.P., A.A., T.D., B.D., A.D., E.F., F.H., M.J.-R., L.J.M., S.S. and E.T.; writing—original draft preparation, A.D.; writing—review and editing, P.P., A.D., E.F. and E.T.; visualization, P.P.; funding acquisition, A.D., E.F. and L.J.M. All authors have read and agreed to the published version of the manuscript.

Funding: The NMR spectrometers used in that study were purchased thanks to grants from Région Centre (France). This study was partially supported by grants from the CNRS Interdisciplinary Project "Nucléaire, Energie, Environnement, Déchets, Société (NEEDS)" through its "Milieux Poreux (MiPor)" Program, which provided financial support for the Projects MultiDyn, TransReac, and Darius.

Acknowledgments: The authors cordially thank A.M. Faugère for technical assistance with the NMR spectrometers and Ph. Badets for devising NMR specific probe (ICMN, Orléans, France).

Conflicts of Interest: The authors declare no conflict of interest.

Abbreviations

The following abbreviations are used in this manuscript:

BD	Brownian Dynamics
DFT	Density Functional Theory
GCMC	Grand Canonical Monte Carlo
GDOS	Generalized Density Of States
INS	Inelastic Neutron Scattering
MC	Monte Carlo
MD	Molecular Dynamics
MRI	Magnetic Resonance Imaging
NMR	Nuclear Magnetic Resonance
OD	Out-Diffusion
ODF	Orientation Distribution Function
PGSE	Pulsed-Gradient Spin-Echo
QENS	Quasi-Elastic Neutron Scattering
TD	Through-Diffusion
XRS	X-Ray Scattering

References

1. Li, H.; Teppen, B.J.; Johnston, C.T.; Boyd, S.A. Thermodynamics of nitroaromatic compound adsorption from water by smectite clay. *Environ. Sci. Technol.* **2004**, *38*, 5433–5442, doi:10.1021/es035054y.
2. Ferrage, E.; Sakharov, B.A.; Michot, L.J.; Delville, A.; Bauer, A.; Lanson, B.; Grangeon, S.; Frapper, G.; Jiménez-Ruiz, M.; Cuello, G.J. Hydration properties and interlayer organization of water and ions in synthetic Na-smectite with tetrahedral layer charge. Part 2. Toward a precise coupling between molecular simulations and diffraction data. *J. Phys. Chem. C* **2011**, *115*, 1867–1881, doi:10.1021/jp105128r.
3. Fripiat, J.; Cases, J.; François, M.; Letellier, M. Thermodynamic and microdynamic behavior of water in clay suspensions and gels. *J. Colloid Interface Sci.* **1982**, *89*, 378–400, doi:10.1016/0021-9797(82)90191-6.
4. Norrish, K. The swelling of montmorillonite. *Discuss. Faraday Soc.* **1954**, *18*, 120–134, doi:10.1039/DF9541800120.
5. Mourchid, A.; Delville, A.; Lambard, J.; Lécolier, E.; Levitz, P. Phase diagram of colloidal dispersions of anisotropic charged particles: Equilibrium properties, structure, and rheology of Laponite suspensions. *Langmuir* **1995**, *11*, 1942–1950, doi:10.1021/la00006a020.
6. Pusch, R. Highly compacted sodium Bentonite for isolating rock-deposited radioactive waste products. *Nucl. Technol.* **1979**, *45*, 153–157, doi:10.13182/NT79-A32305.
7. Charlet, L.; Alt-Epping, P.; Wersin, P.; Gilbert, B. Diffusive transport and reaction in clay rocks: A storage (nuclear waste, CO_2, H_2), energy (shale gas) and water quality issue. *Adv. Water Resour.* **2017**, *106*, 39–59, doi:10.1016/j.advwatres.2017.03.019.
8. Buyukdagli, S.; Blossey, R. Dipolar correlations in structured solvents under nanoconfinement. *J. Chem. Phys.* **2014**, *140*, 234903, doi:10.1063/1.4881604.
9. Porion, P.; Faugère, A.M.; Lécolier, E.; Gherardi, B.; Delville, A. ^{23}Na Nuclear quadrupolar relaxation as a probe of the microstructure and dynamics of aqueous clay dispersions: An application to Laponite gels. *J. Phys. Chem. B* **1998**, *102*, 3477–3485, doi:10.1021/jp9801673.
10. Porion, P.; Faugère, A.M.; Delville, A. ^{7}Li NMR spectroscopy and multiquantum relaxation as a probe of the microstructure and dynamics of confined Li^+ cations: An application to dense clay sediments. *J. Phys. Chem. C* **2008**, *112*, 9808–9821, doi:10.1021/jp8010348.
11. Porion, P.; Rodts, S.; Al-Mukhtar, M.; Faugère, A.M.; Delville, A. Anisotropy of the solvent self-diffusion tensor as a probe of nematic ordering within dispersion of nano-composite. *Phys. Rev. Lett.* **2001**, *87*, 208302, doi:10.1103/PhysRevLett.87.208302.
12. Michot, L.J.; Delville, A.; Humbert, B.; Plazanet, M.; Levitz, P. Diffusion of water in a synthetic clay with tetrahedral charges by combined neutron time-of-flight measurements and molecular dynamics simulations. *J. Phys. Chem. C* **2007**, *111*, 9818–9831, doi:10.1021/jp0690446.

13. Porion, P.; Michot, L.J.; Faugère, A.M.; Delville, A. Influence of confinement on the long-range mobility of water molecules within clay aggregates: A ^{2}H NMR analysis using spin-locking relaxation rates. *J. Phys. Chem. C* **2007**, *111*, 13117–13128, doi:10.1021/jp073393y.
14. Jiménez-Ruiz, M.; Ferrage, E.; Delville, A.; Michot, L.J. Anisotropy on the collective dynamics of water confined in swelling clay minerals. *J. Phys. Chem. A* **2012**, *116*, 2379–2387, doi:10.1021/jp201543t.
15. White, C.E.; Kearley, G.J.; Provis, J.L.; Riley, D.P. Structure of kaolinite and influence of stacking faults: Reconciling theory and experiment using inelastic neutron scattering analysis. *J. Chem. Phys.* **2013**, *138*, 194501, doi:10.1063/1.4804306.
16. Cygan, R.T.; Daemen, L.L.; Ilgen, A.G.; Krumhansl, J.L.; Nenoff, T.M. Inelastic neutron scattering and molecular simulation of the dynamics of interlayer water in smectite clay minerals. *J. Phys. Chem. C* **2015**, *119*, 28005–28019, doi:10.1021/acs.jpcc.5b08838.
17. Michot, L.J.; Ferrage, E.; Delville, A.; Jiménez-Ruiz, M. Influence of layer charge, hydration state and cation nature on the collective dynamics of interlayer water in synthetic swelling clay minerals. *Appl. Clay Sci.* **2016**, *119*, 375–384, doi:10.1016/j.clay.2015.11.005.
18. Jiménez-Ruiz, M.; Ferrage, E.; Blanchard, M.; Fernandez-Castanon, J.; Delville, A.; Johnson, M.R.; Michot, L.J. Combination of inelastic neutron scattering experiments and ab initio quantum calculations for the study of the hydration properties of oriented saponites. *J. Phys. Chem. C* **2017**, *121*, 5029–5040, doi:10.1021/acs.jpcc.6b11836.
19. Gates, W.P.; Seydel, T.; Bordallo, H.N. Layer charge effects on anisotropy of interlayer water and structural OH dynamics in clay minerals probed by high-resolution neutron spectroscopy. *Appl. Clay Sci.* **2021**, *201*, 105928, doi:10.1016/j.clay.2020.105928.
20. Cebula, D.J.; Thomas, R.K.; White, J.W. Diffusion of water in Li-Montmorillonite studied by quasielastic neutron scattering. *Clays Clay Miner.* **1981**, *29*, 241–248, doi:10.1346/CCMN.1981.0290401.
21. Tuck, J.J.; Hall, P.L.; Hayes, M.H.B.; Ross, D.K.; Hayter, J.B. Quasi-elastic neutron-scattering studies of intercalated molecules in charge-deficient layer silicates. Part 2—High-resolution measurements of the diffusion of water in montmorillonite and vermiculite. *J. Chem. Soc. Faraday Trans. I* **1985**, *81*, 833–846, doi:10.1039/F19858100833.
22. Poinsignon, C. Protonic conductivity and water dynamics in swelling clays. *Solid State Ionics* **1997**, *97*, 399–407, doi:10.1016/S0167-2738(97)00020-9.
23. Swenson, J.; Bergman, R.; Longeville, S. A neutron spin-echo study of confined water. *J. Chem. Phys.* **2001**, *115*, 11299–11305, doi:10.1063/1.1420728.
24. Mamontov, E. Comment on "Quasielastic neutron scattering of two-dimensional water in a vermiculite clay" [J. Chem. Phys. 113, 2873 (2000)] and "A neutron spin-echo study of confined water" [J. Chem. Phys. 115, 11299 (2001)]. *J. Chem. Phys.* **2004**, *121*, 9193–9194, doi:10.1063/1.1797091.
25. Malikova, N.; Cadéne, A.; Marry, V.; Dubois, E.; Turq, P.; Zanotti, J.M.; Longeville, S. Diffusion of water in clays - microscopic simulation and neutron scattering. *Chem. Phys.* **2005**, *317*, 226–235, doi:10.1016/j.chemphys.2005.04.035.
26. Malikova, N.; Cadène, A.; Marry, V.; Dubois, E.; Turq, P. Diffusion of water in clays on the microscopic scale: Modeling and experiment. *J. Phys. Chem. B* **2006**, *110*, 3206–3214, doi:10.1021/jp056954z.
27. Skipper, N.T.; Lock, P.A.; Titiloye, J.O.; Swenson, J.; Mirza, Z.A.; Howells, W.S.; Fernandez-Alonso, F. The structure and dynamics of 2-dimensional fluids in swelling clays. *Chem. Geol.* **2006**, *230*, 182–196, doi:10.1016/j.chemgeo.2006.02.023.
28. Michot, L.J.; Ferrage, E.; Jiménez-Ruiz, M.; Boehm, M.; Delville, A. Anisotropic features of water and ion dynamics in synthetic Na- and Ca-smectites with tetrahedral layer charge. A combined Quasi-Elastic Neutron-Scattering and Molecular Dynamics simulations study. *J. Phys. Chem. C* **2012**, *116*, 16619–16633, doi:10.1021/jp304715m.
29. Marry, V.; Dubois, E.; Malikova, N.; Breu, J.; Haussler, W. Anisotropy of water dynamics in clays: Insights from molecular simulations for experimental QENS analysis. *J. Phys. Chem. C* **2013**, *117*, 15106–15115, doi:10.1021/jp403501h.
30. Berg, M.C.; Dalby, K.N.; Tsapatsaris, N.; Okhrimenko, D.V.; Sørensen, H.O.; Jha, D.; Embs, J.P.; Stipp, S.L.S.; Bordallo, H.N. Water mobility in chalk: A quasielastic neutron scattering study. *J. Phys. Chem. C* **2017**, *121*, 14088–14095, doi:10.1021/acs.jpcc.7b01998.
31. Korb, J.; Xu, S.; Jonas, J. Confinement effects on dipolar relaxation by translational dynamics of liquids in porous silica glasses. *J. Chem. Phys.* **1993**, *98*, 2411–2422, doi:10.1063/1.464169.
32. Koziol, P.; Nelson, S.; Jonas, J. Low-dimensional effects on frequency dependence of proton NMR relaxation in liquid cyclohexane confined to porous glasses. *Chem. Phys. Lett.* **1993**, *201*, 383–386, doi:10.1016/0009-2614(93)85087-5.
33. Stapf, S.; Kimmich, R.; Seiter, R.O. Proton and deuteron field-cycling NMR relaxometry of liquids in porous glasses: Evidence for Lévy-walk statistics. *Phys. Rev. Lett.* **1995**, *75*, 2855–2858, doi:10.1103/PhysRevLett.75.2855.
34. Levitz, P. From Knudsen diffusion to Levy walks. *Europhys. Lett.* **1997**, *39*, 593–598, doi:10.1209/epl/i1997-00394-5.
35. Korb, J.P.; Whaley-Hodges, M.; Bryant, R.G. Translational diffusion of liquids at surfaces of microporous materials: Theoretical analysis of field-cycling magnetic relaxation measurements. *Phys. Rev. E* **1997**, *56*, 1934–1945, doi:10.1103/PhysRevE.56.1934.
36. Zavada, T.; Kimmich, R. The anomalous adsorbate dynamics at surfaces in porous media studied by nuclear magnetic resonance methods. The orientational structure factor and Lévy walk. *J. Chem. Phys.* **1998**, *109*, 6929–6939, doi:10.1063/1.477260.
37. Zavada, T.; Kimmich, R.; Grandjean, J.; Kobelkov, A. Field-cycling NMR relaxometry of water in synthetic saponites: Lévy walks on finite planar surfaces. *J. Chem. Phys.* **1999**, *110*, 6977–6981, doi:10.1063/1.478603.
38. Levitz, P.; Korb, J.P.; Bryant, R.G. Molecular diffusion in disordered interfacial media as probed by pulsed field gradients and nuclear magnetic relaxation dispersion. *J. Chim. Phys.* **1999**, *96*, 1494–1505, doi:10.1051/jcp:1999225.
39. Kimmich, R.; Anoardo, E. Field-cycling NMR relaxometry. *Prog. Nucl. Magn. Reson. Spectrosc.* **2004**, *44*, 257–320, doi:10.1016/j.pnmrs.2004.03.002.

40. Porion, P.; Michot, L.J.; Faugère, A.M.; Delville, A. Structural and dynamical properties of the water molecules confined in dense clay sediments: A study combining ^{2}H NMR spectroscopy and multiscale numerical modeling. *J. Phys. Chem. C* **2007**, *111*, 5441–5453, doi:10.1021/jp067907p.
41. Porion, P.; Faugère, A.M.; Delville, A. Long-time scale ionic dynamics in dense clay sediments measured by the frequency variation of the ^{7}Li multiple-quantum NMR relaxation rates in relation with a multiscale modeling. *J. Phys. Chem. C* **2009**, *113*, 10580–10597, doi:10.1021/jp9007625.
42. Korb, J.P. Nuclear magnetic relaxation of liquids in porous media. *New J. Phys.* **2011**, *13*, 035016, doi:10.1088/1367-2630/13/3/035016.
43. Porion, P.; Michot, L.J.; Warmont, F.; Faugère, A.M.; Delville, A. Long-time dynamics of confined water molecules probed by ^{2}H NMR multiquanta relaxometry: An application to dense clay sediments. *J. Phys. Chem. C* **2012**, *116*, 17682–17697, doi:10.1021/jp305577g.
44. Porion, P.; Warmont, F.; Faugère, A.M.; Rollet, A.L.; Dubois, E.; Marry, V.; Michot, L.J.; Delville, A. ^{133}Cs Nuclear Magnetic Resonance relaxometry as a probe of the mobility of cesium cations confined within dense clay sediments. *J. Phys. Chem. C* **2015**, *119*, 15360–15372, doi:10.1021/acs.jpcc.5b03880.
45. Zaburdaev, V.; Denisov, S.; Klafter, J. Lévy walks. *Rev. Mod. Phys.* **2015**, *87*, 483–530, doi:10.1103/RevModPhys.87.483.
46. Porion, P.; Faugère, A.M.; Rollet, A.L.; Dubois, E.; Marry, V.; Michot, L.J.; Delville, A. Influence of strong confinement on the structure and dynamics of liquids: A study of the clay/water interface exploiting ^{2}H NMR spectroscopy and spin-locking relaxometry. *J. Phys. Chem. C* **2018**, *122*, 16830–16841, doi:10.1021/acs.jpcc.8b05089.
47. Bowers, G.M.; Loring, J.S.; Schaef, H.T.; Cunniff, S.S.; Walter, E.D.; Burton, S.D.; Larsen, R.K.; Miller, Q.R.S.; Bowden, M.E.; Ilton, E.S.; Kirkpatrick, R.J. Chemical trapping of CO_2 by clay minerals at reservoir conditions: Two mechanisms observed by in situ high-pressure and -temperature experiments. *ACS Earth Space Chem.* **2019**, *3*, 1034–1046, doi:10.1021/acsearthspacechem.9b00038.
48. Bowers, G.M.; Loring, J.S.; Walter, E.D.; Burton, S.D.; Bowden, M.E.; Hoyt, D.W.; Arey, B.; Larsen, R.K.; Kirkpatrick, R.J. Influence of smectite structure and hydration on supercritical methane binding and dynamics in smectite pores. *J. Phys. Chem. C* **2019**, *123*, 29231–29244, doi:10.1021/acs.jpcc.9b08875.
49. Nanda, R.; Bowers, G.M.; Loganathan, N.; Burton, S.D.; Kirkpatrick, R.J. Temperature dependent structure and dynamics in smectite interlayers: ^{23}Na MAS NMR spectroscopy of Na-hectorite. *RSC Adv.* **2019**, *9*, 12755–12765, doi:10.1039/C9RA01056D.
50. Porion, P.; Faugère, A.M.; Delville, A. ^{1}H and ^{7}Li NMR pulsed gradient spin echo measurements and multiscale modeling of the water and ionic mobility within aqueous dispersions of charged anisotropic nanoparticles. *J. Phys. Chem. C* **2008**, *112*, 11893–11900, doi:10.1021/jp802928n.
51. Porion, P.; Ferrage, E.; Hubert, F.; Tertre, E.; Dabat, T.; Faugère, A.M.; Condé, F.; Warmont, F.; Delville, A. Water mobility within compacted clay samples: Multi-scale analysis exploiting ^{1}H NMR Pulsed Gradient Spin Echo and Magnetic Resonance Imaging of water density profiles. *ACS Omega* **2018**, *3*, 7399–7406, doi:10.1021/acsomega.8b01083.
52. Dabat, T.; Porion, P.; Hubert, F.; Paineau, E.; Dazas, B.; Grégoire, B.; Tertre, E.; Delville, A.; Ferrage, E. Influence of preferred orientation of clay particles on the diffusion of water in kaolinite porous media at constant porosity. *Appl. Clay Sci.* **2020**, *184*, 105354, doi:10.1016/j.clay.2019.105354.
53. Tertre, E.; Delville, A.; Prêt, D.; Hubert, F.; Ferrage, E. Cation diffusion in the interlayer space of swelling clay minerals—A combined macroscopic and microscopic study. *Geochim. Cosmochim. Acta* **2015**, *149*, 251–267, doi:10.1016/j.gca.2014.10.011.
54. Tertre, E.; Dazas, B.; Asaad, A.; Ferrage, E.; Grégoire, B.; Hubert, F.; Delville, A.; Delay, F. Connecting molecular simulations and laboratory experiments for the study of time-resolved cation-exchange process in the interlayer of swelling clay minerals. *Appl. Clay Sci.* **2021**, *200*, 105913, doi:10.1016/j.clay.2020.105913.
55. Asaad, A.; Hubert, F.; Ferrage, E.; Dabat, T.; Paineau, E.; Porion, P.; Savoye, S.; Gregoire, B.; Dazas, B.; Delville, A.; Tertre, E. Role of interlayer porosity and particle organization in the diffusion of water in swelling clays. *Appl. Clay Sci.* **2021**, *207*, 106089, doi:10.1016/j.clay.2021.106089.
56. Rinnert, E.; Carteret, C.; Humbert, B.; Fragneto-Cusani, G.; Ramsay, J.D.F.; Delville, A.; Robert, J.L.; Bihannic, I.; Pelletier, M.; Michot, L.J. Hydration of a synthetic clay with tetrahedral charges: A multidisciplinary experimental and numerical study. *J. Phys. Chem. B* **2005**, *109*, 23745–23759, doi:10.1021/jp050957u.
57. Dazas, B.; Ferrage, E.; Delville, A.; Lanson, B. Interlayer structure model of tri-hydrated low-charge smectite by X-ray diffraction and Monte Carlo modeling in the Grand Canonical ensemble. *Am. Mineral.* **2014**, *99*, 1724–1735, doi:10.2138/am.2014.4846.
58. Pellenq, R.J.M.; Caillol, J.M.; Delville, A. Electrostatic attraction between two charged surface: A (N,V,T) Monte Carlo simulation. *J. Phys. Chem. B* **1997**, *101*, 8584–8594, doi:10.1021/jp971273s.
59. Delville, A.; Gasmi, N.; Pellenq, R.J.M.; Caillol, J.M.; Van Damme, H. Correlations between the stability of charged interfaces and ionic exchange capacity: A Monte Carlo study. *Langmuir* **1998**, *14*, 5077–5082, doi:10.1021/la9802872.
60. Michot, L.J.; Bihannic, I.; Porsch, K.; Maddi, S.; Baravian, C.; Mougel, J.; Levitz, P. Phase diagrams of Wyoming Na-montmorillonite clay. Influence of particle anisotropy. *Langmuir* **2004**, *20*, 10829–10837, doi:10.1021/la0489108.
61. Boek, E.S.; Sprik, M. Ab Initio molecular dynamics study of the hydration of a sodium smectite clay. *J. Phys. Chem. B* **2003**, *107*, 3251–3256, doi:10.1021/jp0262564.
62. Suter, J.L.; Boek, E.S.; Sprik, M. Adsorption of a sodium ion on a smectite clay from constrained ab initio Molecular Dynamics simulations. *J. Phys. Chem. C* **2008**, *112*, 18832–18839, doi:10.1021/jp075946a.
63. Delville, A. Modeling the clay water interface. *Langmuir* **1991**, *7*, 547–555, doi:10.1021/la00051a022.

64. Cygan, R.T.; Liang, J.J.; Kalinichev, A.G. Molecular models of hydroxide, oxyhydroxide, and clay phases and the development of a general force field. *J. Phys. Chem. B* **2004**, *108*, 1255–1266, doi:10.1021/jp0363287.
65. Marry, V.; Dubois, E.; Malikova, N.; Durand-Vidal, S.; Longeville, S.; Breu, J. Water dynamics in Hectorite clays: Influence of temperature studied by coupling neutron spin echo and molecular dynamics. *Environ. Sci. Technol.* **2011**, *45*, 2850–2855, doi:10.1021/es1031932.
66. Abramov, A.; Iglauer, S. Application of the CLAYFF and the DREIDING force fields for modeling of alkylated quartz surfaces. *Langmuir* **2019**, *35*, 5746–5752, doi:10.1021/acs.langmuir.9b00527.
67. van Gunsteren, W.F.; Berendsen, H.J.C.; Rullmann, J.A.C. Stochastic dynamics for molecules with constraints—Brownian dynamics of n-alkanes. *Mol. Phys.* **1981**, *44*, 69–95, doi:10.1080/00268978100102291.
68. Israelachvili, J.N. *Intermolecular and Surface Forces*, 1st ed.; Academic Press: New York, NY, USA, 1985.
69. Tournassat, C.; Steefel, C.I. Reactive transport modeling of coupled processes in nanoporous media. *Rev. Mineral. Geochem.* **2019**, *85*, 75–109, doi:10.2138/rmg.2019.85.4.
70. Dazas, B.; Lanson, B.; Delville, A.; Robert, J.L.; Komarneni, S.; Michot, L.J.; Ferrage, E. Influence of tetrahedral layer charge on the organization of interlayer water and ions in synthetic Na-saturated smectites. *J. Phys. Chem. C* **2015**, *119*, 4158–4172, doi:10.1021/jp5123322.
71. Adams, D.J. Chemical potential of hard-sphere fluids by Monte Carlo methods. *Mol. Phys.* **1974**, *28*, 1241–1252, doi:10.1080/00268977400102551.
72. Allen, M.P.; Tildesley, D.J. *Computer Simulation of Liquids*; Clarendon Press: Oxford, UK, 1994.
73. Hansen, J.P.; McDonald, I.R. *Theory of Simple Liquids*, 2nd ed.; Academic Press: London, UK, 1990.
74. Schoen, M.; Cushman, J.H.; Diestler, D.J.; Rhykerd Jr, C.L. Fluids in micropores. II. Self-Diffusion in a simple classical fluid in a slit pore. *J. Chem. Phys.* **1988**, *88*, 1394–1406, doi:10.1063/1.454211.
75. Kimmich, R. *NMR: Tomography, Diffusometry, Relaxometry*, 1st ed.; Springer: Berlin, Germany, 1997.
76. Korb, J.P. Multiscale nuclear magnetic relaxation dispersion of complex liquids in bulk and confinement. *Prog. Nucl. Magn. Reson. Spectrosc.* **2018**, *104*, 12–55, doi:10.1016/j.pnmrs.2017.11.001.
77. Delville, A.; Letellier, M. Structure and dynamics of simple liquids in heterogeneous condition: An NMR study of the clay-water interface. *Langmuir* **1995**, *11*, 1361–1367, doi:10.1021/la00004a050.
78. Korb, J.P.; Malier, L.; Cros, F.; Xu, S.; Jonas, J. Surface dynamics of liquids in nanopores. *Phys. Rev. Lett.* **1996**, *77*, 2312–2315, doi:10.1103/PhysRevLett.77.2312.
79. Fleury, M.; Canet, D. Water orientation in smectites using NMR nutation experiments. *J. Phys. Chem. C* **2014**, *118*, 4733–4740, doi:10.1021/jp4118503.
80. Porion, P.; Faugère, A.M.; Delville, A. Structural and dynamical properties of water molecules confined within clay sediments probed by deuterium NMR spectroscopy, multiquanta relaxometry, and two-time stimulated echo attenuation. *J. Phys. Chem. C* **2014**, *118*, 20429–20444, doi:10.1021/jp506312q.
81. Bowden, G.J.; Hutchison, W.D.; Khachan, J. Tensor operator formalism for multiple-quantum NMR. 2. Spins-3/2, spin-2, and spin-5/2 and general I. *J. Magn. Reson.* **1986**, *67*, 415–437, doi:10.1016/0022-2364(86)90379-3.
82. van der Maarel, J.R.C. The relaxation dynamics of spin I=1 nuclei with a static quadrupolar coupling and a radio-frequency field. *J. Chem. Phys.* **1993**, *99*, 5646–5653, doi:10.1063/1.465959.
83. van der Maarel, J.R.C. Thermal relaxation and coherence dynamics of spin 3/2. I. Static and fluctuating quadrupolar interactions in the multipole basis. *Concepts Magn. Reson. Part A* **2003**, *19*, 97–116, doi:10.1002/cmr.a.10087.
84. van der Maarel, J.R.C. Thermal relaxation and coherence dynamics of spin 3/2. II. Strong radio-frequency field. *Concepts Magn. Reson. Part A* **2003**, *19A*, 117–133, doi:10.1002/cmr.a.10088.
85. Porion, P.; Delville, A. Multi-Quanta spin-locking Nuclear Magnetic Resonance relaxation measurements: An analysis of the long-time dynamical properties of ions and water molecules confined within dense clay sediments. *Magnetochemistry* **2017**, *3*, 35, doi:10.3390/magnetochemistry3040035.
86. Porion, P.; Faugère, A.M.; Delville, A. Multiscale water dynamics within dense clay sediments probed by ^{2}H multiquanta NMR relaxometry and two-time stimulated echo NMR spectroscopy. *J. Phys. Chem. C* **2013**, *117*, 26119–26134, doi:10.1021/jp4093354.
87. Callaghan, P.T. *Principles of Nuclear Magnetic Resonance Microscopy*; Clarendon Press: Oxford, UK, 1991.
88. Porion, P.; Al-Mukhtar, M.; Faugère, A.M.; Pellenq, R.J.M.; Meyer, S.; Delville, A. Water self-diffusion within nematic dispersion of nanocomposites: A multiscale analysis of ^{1}H pulsed gradient spin-echo NMR measurements. *J. Phys. Chem. B* **2003**, *107*, 4012–4023, doi:10.1021/jp022161q.
89. Latour, L.L.; Mitra, P.P.; Kleinberg, R.L.; Sotak, C.H. Time-dependent diffusion coefficient of fluids in porous media as a probe of surface-to-volume ratio. *J. Magn. Reson. Ser. A* **1993**, *101*, 342–346, doi:10.1006/jmra.1993.1056.
90. Latour, L.L.; Kleinberg, R.L.; Mitra, P.P.; Sotak, C.H. Pore-size distributions and tortuosity in heterogeneous porous media. *J. Magn. Reson. Ser. A* **1995**, *112*, 83–91, doi:10.1006/jmra.1995.1012.
91. Dabat, T.; Hubert, F.; Paineau, E.; Launois, P.; Leforest, C.; Grégoire, B.; Dazas, B.; Tertre, E.; Delville, A.; Ferrage, E. A general orientation distribution function for clay-rich media. *Nat. Commun.* **2019**, *10*, 5456, doi:10.1038/s41467-019-13401-0.
92. Bourg, I.C.; Bourg, A.C.; Sposito, G. Modeling diffusion and adsorption in compacted bentonite: A critical review. *J. Contam. Hydrol.* **2003**, *61*, 293–302, doi:10.1016/S0169-7722(02)00128-6.

93. Bourg, I.C.; Tournassat, C. Chapter 6 - Self-Diffusion of Water and Ions in Clay Barriers. In *Natural and Engineered Clay Barriers*; Tournassat, C., Steefel, C.I., Bourg, I.C., Bergaya, F., Eds.; Elsevier: Amsterdam, The Netherlands, 2015; Volume 6: Developments in Clay Science, pp. 189–226, doi:10.1016/B978-0-08-100027-4.00006-1.
94. Tertre, E.; Savoye, S.; Hubert, F.; Prêt, D.; Dabat, T.; Ferrage, E. Diffusion of water through the dual-porosity swelling clay mineral vermiculite. *Environ. Sci. Technol.* **2018**, *52*, 1899–1907, doi:10.1021/acs.est.7b05343.
95. Churakov, S.V.; Gimmi, T. Up-scaling of molecular diffusion coefficients in clays: A two-step approach. *J. Phys. Chem. C* **2011**, *115*, 6703–6714, doi:10.1021/jp112325n.
96. Tyagi, M.; Gimmi, T.; Churakov, S.V. Multi-scale micro-structure generation strategy for up-scaling transport in clays. *Adv. Water Resour.* **2013**, *59*, 181–195, doi:10.1016/j.advwatres.2013.06.002.